

Molecular mechanisms underlying cardiac neural crest
development in avian embryos

Thesis by
Shashank Gandhi

In Partial Fulfillment of the Requirements for
the Degree of
Doctor of Philosophy

The logo for the California Institute of Technology (Caltech), featuring the word "Caltech" in a bold, orange, sans-serif font.

CALIFORNIA INSTITUTE OF TECHNOLOGY
Pasadena, California

2021
(Defended May 4, 2021)

© 2021

Shashank Gandhi

ORCID: 0000-0002-4081-4338



ACKNOWLEDGMENTS

“Life is what happens to you while you’re busy making other plans.”

– John Lennon

When I look back at my life’s journey so far, this quote from John Lennon hits close to home. Growing up in India, I never thought I would one day become a scientist. But here I am today, compiling this thesis and attempting to acknowledge the contributions of the many people who played an important role in helping me stand where I am now.

First and foremost, I want to thank my parents, Mr. Laxmi Narain Gandhi and Mrs. Bimla Gandhi. I would not be here today if it were not for their sacrifices and hard work in ensuring that I had every opportunity I needed to succeed in life. None of this would have been possible without their unconditional love and support. I would also like to thank my brothers Sachin and Manish, sister-in-law Shweta, and niece Grisha for their love and support throughout the years, and my in-laws, Mr. William Perry and Mrs. Gina Perry, for welcoming me into their family.

My scientific journey in the US began in New York when I was enrolled as a master’s student at New York University. It is most certainly an understatement to say that my time at NYU made me the person I am today, both on a personal and professional level. It started with Lionel Christiaen giving me, someone with no molecular biology experience whatsoever, the opportunity to conduct my master’s thesis research in his lab. There, then-postdoctoral researcher (and now professor!) Alberto Stolfi took me on as his young padawan and taught me the technical skills I needed to succeed as a scientist. His training continues to help me even today, and I am most grateful for his mentorship both inside and outside the lab. I would be remiss not to mention members of the Christiaen lab who have stayed in touch with me since then, especially Claudia and Nikki, for their friendship.

I came to Caltech with a different career path in mind, but unfortunate circumstances surrounding my last rotation left me battered. My confidence was at an all-time low, and I briefly considered dropping out of grad school, naively thinking that not having a lab to join after being tricked into doing a second rotation in the same lab (and a fourth rotation overall) was an ominous sign that I was not meant to become a scientist after all. That incident later on proved to be both a blessing in disguise and a critical turning point in my PhD. A senior graduate student at the time, Ravi Nath, advised me to talk to a professor who he said had a track record of being an excellent mentor. He suggested I meet with her before making any rash decisions, as she was sure to empathize with my situation. That professor was none other than my thesis advisor, Marianne Bronner, who ended up offering me a position in her lab without asking me to do a formal rotation. I came in with no external funding and was ineligible to apply for federal grants or fellowships as an international student, and yet, she showed faith in me and took me on as one of her graduate students. Over the years, Marianne instilled in me the confidence I needed to come up with my own ideas to work on in the lab. At the same time, she helped me realize the importance of maintaining a healthy work-life balance. I often found myself being sent back home to sleep if she discovered me in the lab early in the morning wearing the same clothes as the previous day. She was always eager to make hands-on contributions to experiments in the lab, and to this day, members of the lab, including myself, continue to rely on her expertise when a project requires tricky injections in an embryo. Even during the pandemic, between her endless Zoom meetings, Marianne always made time to meet with me, sometimes on just a few minutes' notice. In fact, Marianne has often pointed out how spoiled I have become after years of receiving her edits and comments on my manuscripts within a matter of days, sometimes overnight! If I can manage to be only half as efficient as she has been, I would consider myself a successful scientist. I have cherished every single one of my interactions with Marianne over the course of my PhD. I look up to her in many ways, and she will continue to be a role model throughout my career.

While I have been very fortunate to collaborate with several current and former members of the Bronner lab, there are a few people whom I would like to particularly mention for their contributions to my professional and personal development: Max Ezin—my mentor, friend, and closest collaborator. I have learned so much from Max, and her unique storytelling style and sense of humor made every interaction enjoyable. Max was not afraid to call me out on my actions and life choices, especially when I failed to take care of my injuries. *Je voudrais remercier vous pour votre support, Max!* Felipe Vieceli, who trained me in chick embryology techniques when I first joined the lab and eventually became a close collaborator and friend. Erica Hutchins, who was always willing to nerd out with me about everything Star Wars, and often treated the lab with her delicious baked goods. I especially appreciated Erica’s honesty and the scientific rigor with which she approached her work. Erica is also the individual who shared with me the best joke I have ever heard: “What’s the internal temperature of a Tauntaun? *Lukewarm.*” Megan Martik, who thinks about science in a way similar to how I have approached my graduate work. She was always happy to provide feedback on my manuscripts and fellowship applications, which as it turns out, I will continue to seek at UC Berkeley where she’s starting her own lab! Meyer Barembaum—senior scientist in the lab who was always willing to share his experience and wisdom with me, including his *in situ* probes on several occasions. And finally, a big shout out to Johanna Tan-Cabugao, Constanza Gonzalez, and David Mayorga. Because of their hard work, I never had to worry about ordering reagents, making plates and solutions, or dealing with bureaucracy surrounding travel reimbursements, leaving me with more time to focus on doing the best science I possibly could.

I would also like to express my gratitude towards the faculty members who supported me at Caltech. In particular, my thesis advisory committee members, Ellen Rothenberg, Matt Thomson, Joe Parker, and Magdalena Zernicka-Goetz, provided valuable insights and feedback on my work and wrote letters of recommendation to support my various fellowship applications. I would especially like to thank Ellen, who served as the chair of my thesis committee. Even short conversations with Ellen always

left me energized. Most importantly, Ellen helped me to better appreciate my accomplishments with her infectious enthusiasm every time I shared a piece of good news. I would also like to acknowledge Matt Thomson for his guidance and support while I was preparing my fellowship applications. Finally, although she was not officially a member of my thesis advisory committee, Dianne Newman provided invaluable advice and support during my time at Caltech.

I would also like to thank the undergraduate students I had the privilege to mentor over the course of my PhD—Alexa Lauinger, Krystyna Maruszko, Donald Siu, Ciannah Correa, and Jens Bager Christensen. Not only did they make valuable hands-on contributions to several of my published works, but their patience and honesty also enabled me to become a better teacher and mentor.

Most of my graduate work would not have been possible without the help and technical support from the Caltech and Beckman Institute core facilities. I would especially like to thank Rochelle Diamond, Jamie Tijeria, and Diana Perez with the Fluorescence-Activated Cell Sorting facility, Igor Antoshechkin with the Millard and Muriel Jacobs Genetics and Genomics Laboratory, Sisi Chen and Jong Park with the Single Cell Profiling and Engineering Center of the Beckman Institute, Grace Shin and Maayan Schwarzkopf with Molecular Technologies, and Giada Spigolon and Andres Collazo with the Biological Imaging Facility of the Beckman Institute for their expertise and contributions to my projects. In the last few years of my PhD, I was fortunate to interact with Fan Gao, Director of the Bioinformatics Resource Center of the Beckman Institute. Fan has continued to play an instrumental role in several of my projects, and I have tremendously benefitted from my conversations with him.

No one's graduate school experience in Caltech's Biology and Biological Engineering division is complete without the administrative support from Liz Ayala and Raina Beaven. From as early as planning my travel for the in-person interview at Caltech

to figuring out the deadlines and paperwork for graduation, I am indebted to Liz for her assistance and guidance.

Caltech is a very small school, and I was fortunate to find friends outside of the lab who not only shared my passion for science, but who were also kind and welcoming towards me as I continued to find my “home away from home” in the US. I won't try to name all of them here, but I hope you all know how grateful I am for your friendship. In addition, even though I have lived in the US for the last 8 years, friends from my childhood have continued to stay in touch and on several occasions have provided a much needed escape from the day-to-day grind of grad school. For that, I would like to thank Arjun Gupta and Ankit Sharma.

Pursuing a PhD can be extremely challenging, especially in times when the experiments don't work or a fellowship application is rejected. Having an outlet to destress is vital, and for me, playing cricket became that outlet. I was lucky to find people who shared my passion for cricket, including members of the Caltech Cricket Club, Hollywood Cricket Club, and the LA Mighty Cricket Club. I would especially like to thank Piyush Agram, who first introduced me to cricket in Southern California, Ankit Parmar, who made me feel welcome at the Hollywood Cricket Club and helped me navigate the politics of playing professional cricket in the US, and Shahid Jalil, who backed me up as a player for his team, the LA Mighty Cricket Club. Even after I move away from Southern California, I will continue to cherish the relationships I have established with several members of these cricket teams.

Finally, I am ever so grateful for my wife, Dr. Elena Perry. I met Elena at graduate student orientation back in Fall 2015. Not many people know this, but Elena took a year off from her undergrad to study abroad in Korea. When she was interviewing for grad school at one of her top choices, there was a big storm in Boston that weekend, which swayed her away from going to grad school on the east coast. On the other hand, while I had a productive time during my master's at NYU, I was not very fond of New York City

back then, and desperately wanted to leave. So deciding where to get my PhD, at NYU or Caltech, was not a difficult choice. The reason why I am mentioning this is because all these things had to happen exactly like they did for Elena and me to come to Caltech and sit next to each other in Justin Bois' Python bootcamp. A few weeks later, we would find ourselves taking Justin's Data Analysis class together, working on assignments in the same group. To a certain degree, we do owe our relationship to Justin. If it weren't for his hard assignments on Bayesian statistics, we wouldn't have spent as much time around each other, all the while getting to know and appreciate one another. Elena, I am really fortunate to have met you. We have had quite a few adventures around the world, from drinking champagne on top of the Eiffel Tower to sleeping in a hammock in the middle of the Amazon Rainforest. And there's no other person I can imagine with whom I'd rather share these experiences. Over the years, you have helped me address and weed out flaws in my personality that have affected my professional and personal relationships. It was your support that carried me during the turbulent time I had in my first year. The Covid-19 pandemic has made me appreciate your presence in my life even more. Especially related to my PhD, you have never shied away from helping me, whether it was advice on what kind of statistical test to use for my data, or making plots for me using your ggplot expertise. Traveling with you to New York even made me fall in love with the city, which I didn't think was possible, another testament to how my life is better when you're in it. I can probably go on and on, but I will just say this – Elena, you are my pillar of strength. Every day spent with you is a blessing, and I am eagerly looking forward to what the future has in store for us. I love you.

ABSTRACT

The neural crest is a multipotent, vertebrate-specific stem cell population that gives rise to diverse cell types in the developing embryo, including craniofacial cartilage, enteric ganglia, and cardiac septa. Neural crest cells that originate from a given axial level in the embryo give rise to a characteristic array of progeny and follow distinct pathways from those arising at other levels. One of these subpopulations, called the cardiac neural crest, originates in the dorsal hindbrain and migrates into the developing heart, where it forms the aorticopulmonary septum, cardiac ganglion, and part of the interventricular septum. Mutations in or loss of these cells causes heart defects that are among the most common birth defects in the general population. For my thesis, I sought to identify the mechanisms that underlie the formation of neural crest cells, and confer cardiac neural crest cells with their unique developmental potential.

To enable interrogation of epistatic relationships between key neural crest genes during neural crest induction and crest specification, I first optimized the CRISPR-Cas9 system for genome editing in gastrula and neurula-stage chicken embryos. I then further improved the CRISPR toolbox by devising an all-in-one single-plasmid strategy that harnesses the self-cleavage properties of ribozymes for the simultaneous delivery of Cas9, gRNAs, and fluorescent reporters in transfected cells. This has enabled live tracking of wildtype and mutant neural crest cells as they migrate to their terminal locations.

Prior to their induction at the neural plate border, precursors in the neural plate border are transcriptionally primed toward multiple cell fates, including neural tube, neural crest, epidermis, and placode. While this priming has been thought to involve epigenetic regulation, chromatin remodeler genes have been overlooked in the context of neural crest formation given their concomitant expression in surrounding cell types. By combining single-cell transcriptional profiling of the early chick embryonic hindbrain with temporally-controlled knockouts, I uncovered a novel bimodal mechanism whereby the chromatin

remodeler gene *Hmga1* first regulates *Pax7*-dependent neural crest induction at the neural plate border, and later modulates Wnt signaling in the dorsal neural tube to control neural crest delamination. These results established *Hmga1* as a direct regulator of neural crest induction and emigration.

Finally, given that amongst distinct neural crest subpopulations designated as cranial, cardiac/vagal, and trunk, only cardiac crest has the ability to contribute to heart development, and that neither trunk nor cranial neural crest subpopulations can rescue the loss of cardiac crest, I investigated the genetic logic that imbues cardiac crest with its unique ability to form cardiovascular derivatives. To this end, I combined surgical ablations, bulk and single-cell transcriptional profiling, RNA labeling, CRISPR-Cas9-mediated gene editing, transcription factor binding motif mutation analysis, and transgenic tissue grafting approaches to uncover and characterize a cardiac-neural-crest-specific subcircuit comprised of the transcription factors *Sox8*, *Tgif1*, and *Ets1*. I demonstrated that ectopic expression of this subcircuit in trunk neural crest cells reprogrammed them towards a cardiac-crest-like fate, and transplanting these reprogrammed cells in place of ablated cardiac crest restored cardiac-crest-like migration patterns and rescued outflow tract septation defects.

Taken together, my thesis work has not only built a genome engineering toolbox for a key model system in developmental biology, but has also expanded our understanding of the genetic circuits that govern the formation of the cardiac neural crest and underlie its unique ability to contribute to the heart.

PUBLISHED CONTENT AND CONTRIBUTIONS

1. **Gandhi, S.**, Bronner, M.E. (2021). Seq your destiny: Neural crest fate determination in the genomic era. In press. *Annual Reviews of Genetics*.

S.G. wrote the paper with input from M.E.B.

2. **Gandhi, S.#**, Li, Y., Tang, W., Christensen, J.B., Urrutia, H.A., Vieceli, F.M., Piacentino, M.L., and Bronner, M.E.# (2021). A single-plasmid approach for genome editing coupled with long-term lineage analysis in chick embryos. *Development* 148, dev.193565. (# co-corresponding authors)

S.G. conceptualized and developed the method, designed the experiments, generated experimental data, performed analyses, and wrote the paper, all with input from Y.L., W.T., J.B.C., H.A.U., F.M.V., M.L.P., and M.E.B.

3. Li, Y., Gonzalez, W., Andreev, A., Tang, W., **Gandhi, S.**, Cunha, A., Prober, D., Lois, C., Bronner, M.E. (2020). Macropinocytosis-mediated membrane recycling via microtubules drives neural crest migration by delivering F-actin to the lamellipodium. *Proceedings of the National Academy of Sciences*, 117 (44), 27400-27411.

S.G. assisted Y.L. with generation of experimental data.

4. **Gandhi, S.#**, Hutchins, E.J., Maruszko, K., Park, J.H., Thomson, M., Bronner, M.E.# (2020). Bimodal function of chromatin remodeler *Hmga1* in neural crest induction and Wnt-dependent emigration. *eLife* 2020;9:e57779. (# co-corresponding authors)

S.G. conceived the project, designed the experiments, generated experimental data, performed analyses, and wrote the paper, all with input from E.J.H., K.M., J.H.P, M.T., and M.E.B.

5. **Gandhi, S.**, Ezin, M., and Bronner, M.E. (2020). Reprogramming axial level identity to rescue neural-crest-related congenital heart defects. *Developmental Cell* 53, 300-315.e4. doi: [10.1016/j.devcel.2020.04.005](https://doi.org/10.1016/j.devcel.2020.04.005)

S.G. conceived the project, designed the experiments, generated experimental data, performed analyses, and wrote the paper, all with input from M.E. and M.E.B.

6. Martik, M.L., **Gandhi, S.**, Uy, B.R., Gillis, J.A., Green, S.A., Simões-Costa, M., and Bronner, M.E. (2019). Evolution of the new head by gradual acquisition of neural crest regulatory circuits. *Nature* 574, 675–678. doi: [10.1038/s41586-019-1691-4](https://doi.org/10.1038/s41586-019-1691-4)

S.G. conceived the bioinformatics pipeline for data analysis, wrote and tested the code, generated experimental data for Figure 3, and helped with writing the paper.

7. Tang, W., Li, Y., **Gandhi, S.**, and Bronner, M.E. (2019). Multiplex clonal analysis in the chick embryo using retrovirally-mediated combinatorial labeling. *Developmental Biology* 450, 1–8. doi: [10.1016/j.ydbio.2019.03.007](https://doi.org/10.1016/j.ydbio.2019.03.007)

S.G. generated a subset of molecular constructs and helped with writing the paper.

8. Tani-Matsuhana, S.*, Viecei, F.M.*, **Gandhi, S.**, Inoue, K., and Bronner, M.E. (2018). Transcriptome profiling of the cardiac neural crest reveals a critical role for MafB. *Developmental Biology* 444, S209–S218. doi: [10.1016/j.ydbio.2018.09.015](https://doi.org/10.1016/j.ydbio.2018.09.015)
*equal contribution

S.G. generated experimental data, assembled figures, and helped with writing the paper.

9. **Gandhi, S.**, and Bronner, M.E. (2018). Insights into neural crest development from studies of avian embryos. *International Journal of Developmental Biology* 62, 179–190. doi: [10.1387/ijdb.180038sg](https://doi.org/10.1387/ijdb.180038sg)

S.G. wrote the paper with input from M.E.B.

10. **Gandhi, S.**, Piacentino, M.L., Viecei, F.M., and Bronner, M.E. (2017). Optimization of CRISPR/Cas9 genome editing for loss-of-function in the early chick embryo. *Developmental Biology* 432, 86–97. doi: [10.1016/j.ydbio.2017.08.036](https://doi.org/10.1016/j.ydbio.2017.08.036)

S.G. conceptualized and developed the method, generated experimental data, and wrote the manuscript, all with input from M.E.B. and all other authors.

TABLE OF CONTENTS

Acknowledgments	iii
Abstract	ix
Published Content and Contributions	xi
Table of Contents	xiii
List of Figures	xix
Chapter 1: Introduction.....	1
1.1 A brief history of the neural crest.....	2
1.2 Thesis overview	2
1.3 References.....	6
Chapter 2: Neural crest development in avian embryos.....	8
2.1 Introduction	9
2.2 Induction of the neural crest in avian embryos.....	10
2.3 Neural crest migration pathways along the body axis of the chick embryo	13
2.4 Regionalization along the Anterior-Posterior axis	16
2.5 Multipotent or fate-restricted?	18
2.6 Experimental strategies to study neural crest development	20
2.6.1 Neural crest lineage tracing.....	21
2.6.2 Crestospheres	23
2.6.3 Antisense morpholinos	24
2.7 Conclusions	25
2.8 References.....	26
Chapter 3: Evolution of the neural crest.....	38
3.1 Introduction	39
3.2 Results and discussion	40

3.2.1 Lamprey lacks a full cranial neural crest subcircuit.....	40
3.2.2 Skates add Ets1 to the cranial neural crest subcircuit	41
3.2.3 Further elaboration of the neural crest subcircuit.....	43
3.2.4 Lamprey neural crest is more trunk-like	43
3.3 Conclusions	47
3.4 Acknowledgments.....	48
3.5 Author contributions.....	48
3.6 Funding.....	48
3.7 Materials and methods	48
3.8 References.....	52
3.9 Supplementary figures.....	56
Chapter 4: CRISPR-Cas9-mediated gene knockouts in avian embryos.....	60
4.1 Introduction	61
4.2 Results and discussion.....	63
4.2.1 Optimizing CRISPR-Cas9 components for application in chick embryos.....	63
4.2.2 CRISPR-Cas9-mediated knockout of key neural crest genes	65
4.2.3 Establishing epistatic relations using CRISPR-Cas9	70
4.2.4 Rapid screening of gRNAs using a Cas9-integrated chicken DF-1 fibroblast cell line.....	75
4.3 Conclusions	76
4.4 Acknowledgments.....	77
4.5 Author contributions.....	77
4.6 Funding.....	78
4.7 Materials and methods	78
4.8 References.....	83

Chapter 5: A combinatorial approach for gene editing and lineage tracing.....	91
5.1 Introduction	92
5.2 Results and discussion	93
5.2.1 Single-plasmid approach to deliver CRISPR components.....	93
5.2.2 Single-plasmid strategy can efficiently perturb function across species.....	95
5.2.3 Early effects of loss of <i>Sox10</i> using single-plasmid approach	97
5.2.4 Using single-plasmid approach for live imaging	99
5.2.5 Incorporating CRISPR components into RIA retroviruses	101
5.2.6 Targeting <i>Sox10</i> in neural crest derivatives using RIA-CRISPR retroviruses ..	103
5.2.7 Targeting Pax6 in the chick retina	105
5.2.8 Targeting Pax7 in the neural crest and presomitic mesoderm.....	110
5.2.9 Coupling RIA-CRISPR retrovirus-mediated perturbation with clonal lineage analysis	113
5.3 Conclusions	116
5.4 Acknowledgments.....	116
5.5 Author contributions.....	117
5.6 Funding	117
5.7 Materials and methods	117
5.8 References.....	124
 Chapter 6: Plasticity at the neural plate border.....	 131
6.1 Introduction	132
6.2 Results	134
6.2.1 Single-cell RNA-seq of early migrating hindbrain neural crest reveals novel transcriptional regulators	134
6.2.2 <i>Hmga1</i> is expressed in the neural plate, neural plate border, and neural crest cells.....	137
6.2.3 <i>Hmga1</i> is necessary for neural crest specification.....	139

6.2.4 <i>Hmga1</i> regulates expression of <i>Pax7</i> in neural crest precursors in the neural plate border.....	141
6.2.5 <i>Hmga1</i> is not required for expression of neural plate border genes <i>Msx1</i> or <i>Tfap2a</i>	145
6.2.6 <i>Hmga1</i> and <i>Pax7</i> rescue the effects of losing <i>Hmga1</i> on neural crest specification	146
6.2.7 <i>Hmga1</i> activates Wnt signaling to mediate neural crest emigration	149
6.3 Discussion.....	153
6.4 Acknowledgments.....	158
6.5 Author contributions.....	158
6.6 Funding	158
6.7 Materials and methods	159
6.8 References.....	169
6.9 Supplementary figures.....	177
 Chapter 7: Cardiac neural crest plasticity in heart development	 182
7.1 Graphical abstract.....	183
7.2 Introduction	184
7.3 Results	185
7.3.1 Ablation of the chick cardiac neural crest results in cardiovascular defects	185
7.3.2 Population level transcriptome analysis reveals genes enriched in the cardiac neural crest	187
7.3.3 Single-cell RNA-seq reveals heterogeneity in migrating cardiac crest	188
7.3.4 Transcription factor <i>Tgif1</i> is required for cardiac neural crest specification.....	191
7.3.5 <i>Tgif1</i> is necessary for proper outflow tract septation.....	193
7.3.6 HCR and scRNA-seq reveal coexpression of <i>Tgif1</i> with <i>Ets1</i> and <i>Sox8</i>	195
7.3.7 <i>Sox8</i> , <i>Tgif1</i> and <i>Ets1</i> comprise a transcriptional cascade important for cardiac neural crest identity.....	197

7.3.8 Reprogrammed trunk neural crest cells exhibit cardiac crest-like migratory behavior	201
7.3.9 Reprogrammed trunk neural crest acquires cardiac ectomesenchymal potential	203
7.4 Discussion.....	206
7.5 Acknowledgments.....	210
7.6 Author contributions.....	210
7.7 Funding.....	210
7.8 Materials and methods	211
7.9 References.....	220
7.10 Supplementary figures.....	229
 Chapter 8: Concluding remarks	 233
8.1 Introduction	234
8.2 The neural crest.....	236
8.3 Plasticity at the neural plate border	239
8.4 Specification of the cardiac neural crest in the dorsal hindbrain.....	241
8.5 Molecular recipe for neural crest cell fate.....	243
8.5.1 Cranial neural crest.....	244
8.5.2 Cardiac neural crest.....	246
8.5.3 Vagal neural crest.....	247
8.6 To go with your heart or your gut?.....	248
8.7 Epigenomic regulation of neural crest cell fate.....	251
8.7.1 Non-coding RNAs	252
8.7.2 RNA-binding proteins	253
8.8 Genomics and neural crest cell fate	254
8.8.1 Acquisition of neural crest identity	254
8.8.2 Acquisition of a broad developmental potential.....	258

8.8.2.1 The retention model.....	258
8.8.2.2 The reacquisition model	260
8.9 Conclusions	262
8.10 References	263
Appendix A: Protocol for cloning gRNAs downstream of the U6 promoter	280
Appendix B: Molecular cloning of single-CRISPR plasmid.....	284
Appendix C: Synthesizing high-titer RIA retroviruses	290
Appendix D: Dissociating embryonic tissue into a single-cell suspension	295

LIST OF FIGURES

Chapter 2

<i>Number</i>	<i>Page</i>
1. Illustration demonstrating various stages of neural crest development.....	10
2. Neural crest derivatives along the Anterior-Posterior axis in chick embryos.....	17

Chapter 3

<i>Number</i>	<i>Page</i>
1. Lamprey cranial neural crest lacks most components of a chick “cranial crest circuit”	40
2. Nodes of an early cranial-specific circuit were acquired in and restricted to the cranial neural crest progressively throughout gnathostome evolution	42
3. Tissue-specific RNA-seq comparisons between lamprey and chicken reveal ancestral neural crest had a more trunk-like identity	44
4. Model of the evolution of neural crest axial levels during vertebrate evolution	45
5. Heterochronic shifts of cranial specific gene regulatory nodes from later neural crest derivatives to an early specification program happened gradually throughout gnathostome evolution	56
6. Expression of cranial circuit genes in the neural crest of the little skate	57
7. Pharyngeal neural crest derivative expression of cranial circuit orthologues in stage 25 <i>Leucoraja erinacea</i> embryos.....	58
8. Expression of cranial circuit genes in the neural crest of the zebrafish.....	59
9. Expression of cranial circuit orthologues in pharyngeal neural crest derivatives of 3dpf <i>Danio rerio</i> embryos.....	59

Chapter 4

<i>Number</i>	<i>Page</i>
1. Optimizing individual CRISPR-Cas9 components for application in chick embryos.....	64
2. CRISPR-Cas9-mediated knockout of Pax7	66
3. CRISPR-Cas9-mediated knockout of Sox10	69
4. Application of CRISPR-Cas9 to study epistatic relationships.....	71
5. CRISPR-Cas9 allows investigation of direct gene regulatory interactions.....	73
6. Construction of a Cas9-DF-1 fibroblast cell line to validate gRNAs	76

Chapter 5

<i>Number</i>	<i>Page</i>
1. Optimizing delivery of CRISPR components in chick embryo	94
2. Single CRISPR plasmid efficiently perturbs function across multiple species	96
3. Electroporation-mediated early knockout of <i>Sox10</i> using single CRISPR plasmid	98
4. Live imaging application of the single CRISPR plasmid.....	100
5. Incorporating single CRISPR plasmid into RIA retroviruses.....	102
6. RIA retrovirus-mediated knockout of <i>Sox10</i> in neural crest derivatives	104
7. Targeting <i>Pax6</i> in the developing chick retina using RIA-CRISPR retrovirus	107
8. Targeting <i>Pax7</i> in the dermomyotome and hindlimb using RIA-CRISPR retrovirus.	111
9. Proof-of-principle experiment to show application of RIA-CRISPR retroviruses for clonal analysis	114

Chapter 6

<i>Number</i>	<i>Page</i>
1. Single-cell (sc) RNA-seq of hindbrain neural crest reveals known and novel transcriptional regulators.....	135
2. <i>Hmga1</i> is expressed in the neural plate, neural plate border, and premigratory and migratory neural crest cells	138
3. <i>Hmga1</i> knockout results in loss of neural crest specification	140
4. The effects of <i>Hmga1</i> knockout on neural crest specification are Pax7-dependent	143
5. Ectopic expression of <i>Hmga1</i> or <i>Pax7</i> rescues cranial neural crest specification	147
6. <i>Hmga1</i> activates Wnt signaling pathway in delaminating neural crest cells	150
7. Current model for <i>Hmga1</i> function in chick neural crest development.....	154
8. Quality of single cell RNA-seq dataset.....	177
9. Identification of novel genes expressed in the neural crest.....	178
10. Overlapping expression of <i>Hmga1</i> and <i>Pax7</i> in the neural crest visualized in individual channels.....	179
11. Knocking out <i>Hmga1</i> in gastrula stage embryos	180
12. <i>Hmga1</i> knockout does not affect neural crest cell proliferation and apoptosis	180
13. <i>Hmga1</i> regulates <i>Wnt1</i> expression in premigratory cranial neural crest cells	181

Chapter 7

<i>Number</i>	<i>Page</i>
1. Chick cardiac neural crest ablation results in cardiovascular abnormalities	186
2. Bulk and single cell transcriptional profiling of cardiac neural crest	189
3. <i>Tgif1</i> is critical for cardiac neural crest specification and outflow tract septation	192
4. <i>Tgif1</i> is coexpressed with Sox8 and Ets1 in migrating cardiac neural crest	196

5. <i>Sox8, Tgif1 and Ets1</i> comprise a transcriptional cascade important for cardiac crest identity	198
6. Reprogrammed trunk neural crest cells exhibit cardiac crest-like migratory behavior	202
7. Reprogrammed trunk neural crest acquires cardiac ectomesenchymal potential	204
8. Effect of ablations on cardiovascular development, and quality control on bulk and single cell RNA-seq data.....	229
9. Role of <i>Tgif1</i> in cardiac neural crest	230
10. Identification of cardiac neural crest subcircuit genes	231
11. Investigation of functional relationships between cardiac neural crest subcircuit genes and identification of downstream targets	232

Chapter 8

<i>Number</i>	<i>Page</i>
1. Early stages of neural crest development.....	235
2. Rostrocaudal arrangement of neural crest populations.....	237
3. Transcriptional subcircuits and neural crest identity	245
4. Application of high-throughput sequencing technologies to deciphering gene regulatory networks.....	255

Chapter 1

Introduction

1.1 A brief history of the neural crest

The neural crest is a transient, multipotent stem cell population unique to vertebrates. The history of neural crest research dates back 150 years, when the Swiss anatomist, Wilhelm His, Sr., identified a region at the border of the neural tube and the non-ectoderm in early stage chick embryos that differentiated into the cranial and spinal ganglia (His W., 1868; Trainor et al., 2003). This cell population, which he named *Zwischenstrang* (the intermediate cord) was later referred to as the neural crest. Early grafting experiments in amphibians gave the first insights into the developmental potential of these cells. Subsequently, lineage tracing experiments in avian embryos using various methods of marking the neural crest greatly enhanced our understanding of the pathways of migration and derivatives they formed. These initially involved radioactive labeling (Chibon, 1967; Weston, 1963), but were revolutionized by the advent of the quail-chick chimeric grafts (Le Douarin, 1980) which allowed Le Douarin and colleagues to map neural crest migratory pathways, derivatives, and their axial level of origin (Le Douarin, 1973; Le Douarin and Teillet, 1973, 1974). As an amniotic system, the chick embryo has been a particularly valuable organism for understanding these questions, sharing similarities with humans both at the morphological and nucleotide level. Their stem cell-like regenerative properties, long-range migratory capabilities, and experimental malleability have made neural crest cells an excellent model system to study developmental potential and cell-fate decisions (Dupin and Sommer, 2012; Smith, 1990; Tucker, 2004). Therefore, understanding how the neural crest develops can help us gain insights into how cells behave differently depending on their position and function in the organism.

1.2 Thesis overview

In Chapter 2, I discuss the mechanisms underlying neural crest specification, migration, and differentiation in avian embryos, and highlight the genetic tools that were available to study these biological processes in chick embryos at the time I began working on this thesis.

In Chapter 3, in collaboration with postdoctoral researcher Dr. Megan Martik, I address the question of how evolution of the neural crest impacted the vertebrate body plan. Contribution of the neural crest towards the craniofacial architecture of vertebrates led to the genesis of the “new head hypothesis” (Gans and Northcutt, 1983), according to which the possession of distinct craniofacial derivatives enabled diversification of the brain and acquisition of predatory behavior in vertebrates, as compared to filter feeding chordates (Le Douarin, 2004). We examine the molecular circuits that control neural crest development along the anteroposterior axis of a jawless vertebrate, the sea lamprey. Gene expression analyses show that the lamprey cranial neural crest lacks most components of an amniote cranial-specific transcriptional circuit that confers the ability to form craniofacial cartilage onto other neural crest populations (Simões-Costa and Bronner, 2016). Consistent with this, hierarchical clustering reveals that the transcriptional profile of the lamprey cranial crest is more similar to the amniote trunk crest. Intriguingly, analysis of the cranial neural crest in little skate and zebrafish embryos demonstrates that the cranial-specific transcriptional circuit emerged via gradual addition of network components to the neural crest of gnathostomes, which subsequently became restricted to the cephalic region. Our results indicate that the ancestral neural crest at the base of vertebrates possessed a trunk-like identity, and we propose that the emergence of the cranial neural crest, by progressive assembly of a novel axial-level-specific regulatory circuit, allowed for the elaboration of the New Head during vertebrate evolution.

In Chapter 4, I present an optimized CRISPR-Cas9 method for targeted gene knockouts in chicken embryos that is reproducible, robust, and specific. By employing a three-fold strategy to modify CRISPR reagents, we significantly improve the efficiency of gene knockouts when compared to previous iterations of this tool. We start by flanking Cas9 protein with two nuclear localization signal sequences to improve its nuclear localization. Second, we use a modified guide RNA (gRNA) scaffold that obviates premature termination of transcription and unstable Cas9-gRNA interactions. Third, we use a chick-specific U6 promoter that yields 4-fold higher gRNA expression than the previously utilized human U6. For rapid screening of gRNAs for *in vivo* applications, we

also generate a chicken fibroblast cell line that constitutively expresses Cas9-GFP. As proof of principle, we target Pax7 and Sox10 via electroporation in the neural crest. These key transcription factors have known functions in neural crest development, and the results show that CRISPR/Cas9-mediated deletions cause loss of their respective proteins and transcripts, as well as putative downstream targets. CRISPR-Cas9 has made genome editing possible in virtually any organism, including those not previously amenable to genetic manipulations, and here we implement it for efficient loss-of-function experiments in early avian embryos.

In Chapter 5, I present a combinatorial approach for lineage analysis and CRISPR-Cas9-mediated genome editing that employs replication-incompetent avian (RIA) retroviruses to study experimentally perturbed cells in an otherwise normal environment in several tissues of the chick embryo. To achieve this, we have engineered a plasmid that encodes Cas9 protein, gene-specific guide RNA (gRNA), and a fluorescent marker within the same construct. Using transfection- and electroporation-based approaches, we show that this construct can be used to perturb gene function in early embryos as well as human cell lines. Importantly, incorporation of this cistronic construct into RIA retroviruses enabled long-term lineage analysis of mutant cells. We demonstrate the application of our newly-engineered reagents by perturbing β -catenin *in vitro* and *Sox10*, *Pax6*, and *Pax7* in the neural crest, retina, and neural tube and segmental plate *in vivo*, respectively. This work finally makes it possible to challenge a cell's developmental potential and interrogate the role of particular genes in developmental processes by enabling their knockout in permanently-labeled cells in living embryos.

In Chapter 6, I characterize the chromatin remodeler gene *Hmga1* as an important regulator of neural crest formation at the neural plate border. We combine single-cell RNA sequencing with high resolution *in situ* hybridization to show that *Hmga1* is highly expressed prior to neural crest induction and is retained during chick neural crest specification, delamination, and migration. Temporally-controlled CRISPR-Cas9-mediated knockouts uncovered two distinct roles for *Hmga1* in neural crest development. At the neural plate border, *Hmga1* regulates Pax7-dependent neural crest lineage

specification. At premigratory stages, a second role manifests where *Hmga1* loss reduces cranial crest emigration from the dorsal neural tube independent of *Pax7*. Interestingly, this is rescued by stabilized β -catenin, thus implicating *Hmga1* as a canonical Wnt activator. Together, our results show that *Hmga1* functions in a bimodal manner during neural crest development to regulate specification at the neural plate border, and subsequent emigration from the neural tube via canonical Wnt signaling.

In Chapter 7, I probe the molecular mechanisms underlying the cardiac neural crest's unique developmental potential. The cardiac neural crest arises in the hindbrain, then migrates to the heart and contributes to critical structures, including the outflow tract septum. Chick cardiac crest ablation results in failure of this septation, phenocopying the human heart defect Persistent Truncus Arteriosus (PTA), which trunk neural crest fails to rescue. We first report laterality differences in cardiovascular defects resulting from unilateral cardiac neural fold ablations. We resolve the heterogeneity within the migratory cardiac neural crest using single-cell RNA sequencing and report the earlier-than-expected onset of gene expression associated with their ectomesenchymal differentiation potential. Using loss-of-function analyses, we establish regulatory relationships of cardiac neural crest genes and explore their role in heart development. Accordingly, we find that one of these genes, *Tgif1*, functions in a cardiac neural crest subcircuit important for specification and proper outflow tract septation. Finally, we show that ectopic expression of a cardiac crest-specific subcircuit, comprised of *Sox8*, *Tgif1*, and *Ets1*, is sufficient to reprogram trunk neural crest cells, enabling them to migrate to the heart and rescue the effects of a cardiac crest ablation, which they cannot normally do. Taken together, our results help elucidate the genetic properties of this unique neural crest lineage in the formation and function of the heart, helping uncover potential target genes involved in cardiovascular birth defects, and provide a molecular recipe for generating ectomesenchymal derivatives of the cardiac crest for the purposes of regenerative medicine.

Finally, in Chapter 8, I provide concluding remarks on my thesis work and discuss how genomic approaches have provided new insights into old questions in neural crest biology, especially those that elucidate transcriptional and post-transcriptional mechanisms governing neural crest formation and establishment of axial level identity.

1.3 References

Chibon, P. (1967). Marquage nucléaire par la thymidine tritiée des dérivés de la crête neurale chez l'Amphibien Urodèle *Pleurodeles waltlii* Michah. *J. Embryol. Exp. Morphol.* *18*, 343–358.

Le Douarin, N.M. (1973). A biological cell labeling technique and its use in experimental embryology. *Dev. Biol.* *30*, 217–222.

Le Douarin, N.M. (1980). The ontogeny of the neural crest in avian embryo chimaeras. *Nature* *286*, 663–669.

Le Douarin, N.M. (2004). The avian embryo as a model to study the development of the neural crest: A long and still ongoing story. *Mech. Dev.* *121*, 1089–1102.

Le Douarin, N.M., and Teillet, M.A. (1973). The migration of neural crest cells to the wall of the digestive tract in avian embryo. *J. Embryol. Exp. Morphol.* *30*, 31–48.

Le Douarin, N.M., and Teillet, M.A. (1974). Experimental analysis of the migration and differentiation of neuroblasts of the autonomic nervous system and of neurectodermal mesenchymal derivatives, using a biological cell marking technique. *Dev. Biol.* *41*, 162–184.

Dupin, E., and Sommer, L. (2012). Neural crest progenitors and stem cells: From early development to adulthood. *Dev. Biol.* *366*, 83–95.

Gans, C., and Northcutt, R.G. (1983). Neural crest and the origin of vertebrates: a new head. *Science* *220*, 268–273.

Simões-Costa, M., and Bronner, M.E. (2016). Reprogramming of avian neural crest axial identity and cell fate. *Science* 352, 1570–1573.

Smith, J. (1990). The avian neural crest as a model system for the study of cell lineages. *Int. J. Dev. Biol.* 34, 157–162.

Trainor, P.A., Melton, K.R., and Manzanares, M. (2003). Origins and plasticity of neural crest cells and their roles in jaw and craniofacial evolution. *Int. J. Dev. Biol.* 47, 541–553.

Tucker, R.P. (2004). Neural crest cells: a model for invasive behavior. *Int. J. Biochem. Cell Biol.* 36, 173–177.

Weston, J.A. (1963). A radioautographic analysis of the migration and localization of trunk neural crest cells in the chick. *Dev. Biol.* 6, 279–310.

Chapter 2

Neural crest development in avian embryos

A modified version of this chapter was published as:

Gandhi, S., and Bronner, M.E. (2018). Insights into neural crest development from studies of avian embryos. *Int. J. Dev. Biol.* 62, 179–190.

<https://doi.org/10.1387/ijdb.180038sg>

2.1 Introduction

The neural crest is a multipotent and highly migratory cell type that contributes to many of the defining features of vertebrates, including the skeleton of the head and most of the peripheral nervous system. Induced at the border of the neural plate and the non-neural ectoderm, this cell population initially resides in the elevating neural folds as neurulation progresses, and then within the dorsal neural tube [Figure 1]. Shortly after neural tube closure in avian embryos, neural crest cells undergo an epithelial-to-mesenchymal transition (EMT), losing their cell-cell contacts and transforming into a migratory cell type, distinct from both neural tube and the epidermal cells (Bronner and Simões-Costa, 2016; Le Douarin and Kalcheim, 1999; Hall, 2009; Sauka-Spengler and Bronner-Fraser, 2008; Steventon et al., 2005). Post EMT, these cells migrate extensively throughout the embryo along distinct pathways, exhibiting both collective and individual cell migration behavior in response to environmental cues and morphogenetic signals. They subsequently give rise to numerous cell types, including melanocytes of the skin, craniofacial cartilage and bones, smooth muscle, Schwann cells, and sensory and autonomic neurons of the peripheral nervous system (Le Douarin and Kalcheim, 1999; Le Douarin and Teillet, 1971; Dupin et al., 2006; Grenier et al., 2009; Hall, 2009; Kirby and Hutson, 2010; Minoux and Rijli, 2010; Theveneau and Mayor, 2011). Despite the fact that the neural crest is derived from the ectoderm, it has been referred to as the fourth germ layer due to its ability to migrate long distances and differentiate into such a plethora of derivatives (Le Douarin and Dupin, 2014; Hall, 2000; Shyamala et al., 2015).

150 years after the discovery of the neural crest, avian embryos have been one of the most important model organisms for studying neural crest development. Past and emerging technologies continue to improve the resolution with which we can examine important questions of neural crest development, with modern avian molecular embryology continuing to make important contributions. In this chapter, I describe aspects of neural crest induction, migration, and axial level differences, highlighting what is known about the underlying gene regulatory mechanisms.

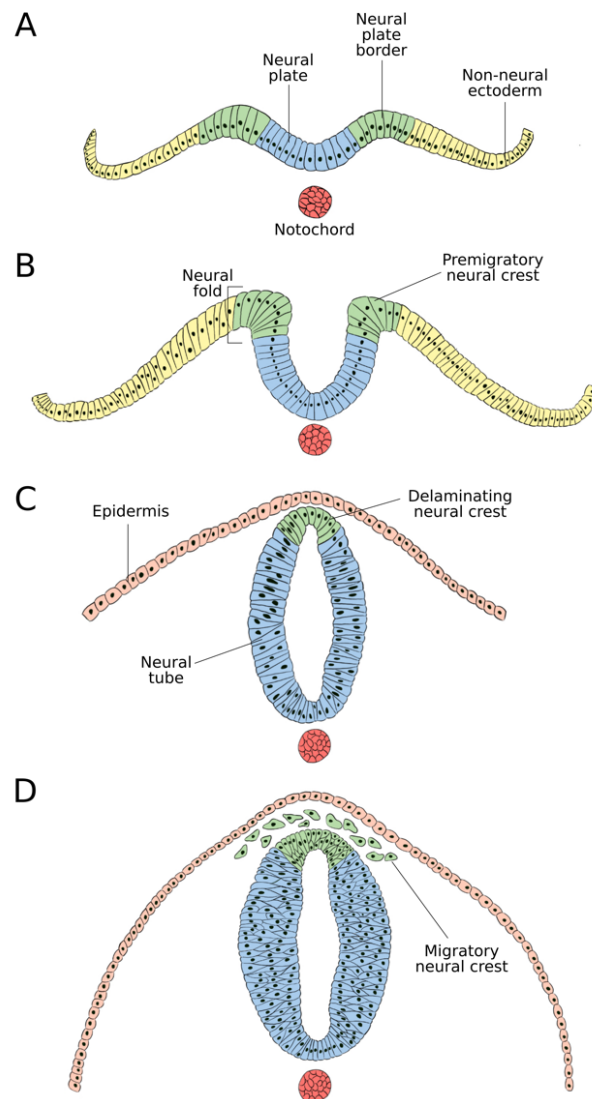


Figure 1. Illustration demonstrating various stages of neural crest development. **A.** The neural crest is a transient population of multipotent cells found in vertebrates. Neural crest cells are specified at the border between the neural plate (blue) and non-neural ectoderm (yellow) at the gastrula stage. **B.** During neurulation, the neural plate border elevates to form the neural folds containing premigratory neural crest cells. **C-D.** As the neural folds fuse to form the neural tube, neural crest cells undergo an epithelial-to-mesenchymal transition (EMT), delaminate from the dorsal neural tube, and migrate extensively to various parts of the developing embryo where they differentiate into a plethora of derivatives.

2.2 Induction of the neural crest in avian embryos

Until the mid-2000s, the prevailing view of neural crest induction was that interactions between the non-neural surface ectoderm, neural plate, and/or underlying mesoderm resulted in specification of neural crest precursors via signaling interactions

between tissues (Basch et al., 2004; Gammill and Bronner-Fraser, 2002; Monsoro-Burq et al., 2003; Takahashi et al., 2007). Moreover, multiple juxtaposition studies performed in both avian and amphibian embryos highlighted the role of the epidermis in specifying neural crest cells. However, most of the early experiments in chick embryos were performed after the neural tube had already formed. In 2006, Basch et al. (2006) presented a revised view on the specification and induction of the neural crest precursors. They hypothesized that regions of the epiblast were already induced to become presumptive neural crest during gastrulation, better matching experimental evidence in frog and zebrafish. The comparatively slow development of the chick embryo enabled more refined analysis of the timing of neural crest induction. By characterizing the expression level of the paired box transcription factor Pax7 in gastrulating chick embryos, Basch et al. (2006) concluded that the neural plate border region was already fated to become neural crest prior to completion of gastrulation, and that cells from this domain incorporate into the neural folds, and ultimately, the migratory neural crest. Dissection of the Pax7 expressing domain from the epiblast followed by explantation in a neutral environment was sufficient to give rise to migratory neural crest, identified by staining for the migratory cell-surface antigen HNK1. Finally, using molecular markers for mesoderm, they also demonstrated that the neural crest was specified without any interaction between the neural plate border region expressing Pax7, and the underlying mesoderm. These results not only characterized Pax7 as an early neural plate border marker, but also placed the initiation of neural crest specification at or before gastrulation. More recently, Roellig et al. (2017) have expanded this viewpoint by resolving the co-expression pattern of transcription factors including Pax7, Sox2, and Six1 in the neural plate border at a single-cell level.

The specification of neural crest cells has been described as a multistep process involving Fibroblast Growth Factor (FGF), Bone Morphogenetic Protein (BMP), and the Wnt signaling cascades, with additional contributions by Notch/Delta, Retinoic Acid (RA), Hedgehog, and endothelin signaling (Barenbaum and Bronner-Fraser, 2005; Basch et al., 2004; Knecht and Bronner-Fraser, 2002; Steventon et al., 2009). Of these, FGF

signaling, which arises from the surrounding mesoderm, acts in conjunction with Wnt signaling to repress BMP signaling during the first half of neural crest induction (Stuhlmiller and García-Castro, 2012). In the second half, inhibition of FGF signaling allows for the activation of BMP signaling, which together with Wnt signaling, activate a pool of transcription factors referred to as Neural Plate Border (NPB) specifiers. These NPB specifiers, including transcription factors Pax3/7, Msx1/2, Pax7, Zic1, Gbx2, and Tfap2, play an important role in establishing the interface between the neuroepithelium and the surface ectoderm (Grocott et al., 2012; Khudyakov and Bronner-Fraser, 2009). Once the NPB is established, the NPB specifier genes activate another set of transcription factors called the Neural Crest Specifier genes such as FoxD3, Sox9, Snail, and Sox10 (Simões-Costa and Bronner, 2013, 2015; Simões-Costa et al., 2014). Of these, the transcription factor Forkhead Box protein D3 (FoxD3) appears to be expressed first, and is required for the subsequent onset of other neural crest specifier genes (Labosky and Kaestner, 1998; Sasai et al., 2001; Sauka-Spengler and Bronner-Fraser, 2008; Stewart et al., 2006). FoxD3 is expressed in both premigratory and some migratory neural crest cells, and regulates their epithelial-to-mesenchymal transition, thereby controlling emigration (Fairchild et al., 2014; Kos et al., 2001). However, detailed genomic analysis has revealed that the expression of FoxD3 in the cranial versus the trunk axial level is tightly regulated by direct transcriptional input into two different enhancers, NC1 and NC2, from different transcription factors, hence establishing a direct interactional network between the neural plate border specifier genes and their downstream neural crest specifier target genes (Simões-Costa et al., 2012). Interestingly, the NC1 enhancer governs the expression of FoxD3 in the premigratory cranial neural crest, while the NC2 enhancer is initially active in the trunk neural crest. In contrast, the neural crest specifier gene Sox10 is expressed as neural crest cells prepare to emigrate and then maintained in the migratory population (Betancur et al., 2010). It also directly or indirectly regulates the activity of proteins like Rho GTPases that are actively involved in actin reorganization, thus contributing to cell membrane fluidity, and ultimately, cell migration (Liu and Jessell, 1998; Sit and Manser, 2011), which has been discussed in detail below. Later, Sox10

plays an important role in differentiation of neural crest cells into specific neuronal cell types (Carney et al., 2006; Kim et al., 2003).

Contrary to the induction model of neural crest specification, a recent study in *Xenopus* embryos has proposed that neural crest cells retain multipotency from an early blastula to the neurula stage (Buitrago-Delgado et al., 2015). Interestingly, this model seems consistent with findings in avian embryos, where expression of the earliest neural plate border marker Pax7 was observed in distinct regions of epiblast between stages 3 and 4 (Basch et al., 2006).

2.3 Neural crest migration pathways along the body axis of the chick embryo

Following delamination from the dorsolateral part of the neural tube, neural crest cells undergo a change in their transcriptional landscape, assuming a state distinct from both the neural tube and the epidermis. This migratory state is marked by a reduction in cell-cell adhesion and enhanced interactions with the extracellular matrix. In chick embryos, the process of delamination overlaps with neural tube closure (Le Douarin and Kalcheim, 1999; Duband and Thiery, 1982; Théveneau et al., 2007), and differs along the rostral-caudal axis. In the rostral part of the embryo, the cranial neural crest cells undergo EMT as a collective event, resulting in the delamination of numerous cells concurrently. They then follow distinct streams and migrate extensively with leader cells pioneering the pathways followed by closely-associated follower cells. In contrast, trunk neural crest cells delaminate by leaving the neural tube one cell at a time in a drip-like fashion and start migrating immediately after detaching from the tube. Interestingly, neural crest migration in the trunk is tightly linked with differentiation of the somites (Sela-Donenfeld and Kalcheim, 1999). As neural crest cells first leave the neural tube, they migrate between the neural tube and the adjacent epithelial somite. The somites subsequently undergo an epithelial-mesenchymal transition to form the dermomyotome and sclerotome, at which point trunk neural crest cells invade the sclerotome and migrate throughout the anterior half of each sclerotome resulting in their segmental migration (Bronner-Fraser, 1986; Rickmann et al., 1985). In the chick, neural crest cells typically begin to delaminate about

five somite lengths above the last formed somite. The caudal trunk neural crest delaminates almost a day after the completion of neurulation (Osorio et al., 2009).

Neural crest migration is a dynamic process. For example, the chick cranial neural crest cells emigrate from the dorsal neural tube immediately after its closure in a rostral-caudal wave, with cells at the midline of the caudal forebrain and midbrain emerging prior to those adjacent to the hindbrain. Not only are there differences in the migratory properties of cells originating from different axial levels, but the leader and trailer cells can also exhibit differences in migration rates and directionality. At the hindbrain level, these differences correlate with segmentation of the rhombomeres (Kulesa and Fraser, 1998, 2000; Kulesa and Gammill, 2010; Lumsden et al., 1991). Neural crest cells migrating towards branchial arch 1 and 3 exhibit collective cell migration with high directionality, where the leader cell moves at a speed similar to the cells following in the chain. In contrast, cells migrating into branchial arch 2 display more directed, individual cell movement with low cell-cell contacts, albeit at much slower migration speeds (Kulesa and Fraser, 2000). The neural crest cells that originate from rhombomeres 3 and 5 migrate from the dorsal midline of the neural tube, following a diagonal cellular trajectory in a caudo- or rostro-lateral manner before migrating laterally away from the neural tube, thus avoiding inhibitory environments immediately lateral to r3 and r5. Interestingly, these cells end up getting stalled as they reach the lateral-most extent of the neural tube. Eventually, they either merge with their neighboring stream from rhombomere 4 migrating towards the second branchial arch, or they remain stationary, suggesting that the microenvironment adjacent to r3 is inhibitory for neural crest migration, thus establishing a neural crest cell-free zone. However, cells that merge with their neighboring stream maintain filipodial contacts with the leader cells, allowing them to alter the direction of their migration towards the second branchial arch (Kulesa and Fraser, 1998, 2000).

Trunk neural crest migration is restricted to two major migratory pathways – ventral and dorsolateral. In the chick, neural crest cells first migrate ventrally, since repressors such as Slit ligands, endothelin-3, and ephrinB1 are initially expressed along the dorsolateral pathway, thus restricting neural crest cells to follow a ventral migratory

pathway and migrate through the inhibitor-free anterior part of the sclerotome (Harris and Erickson, 2007). The posterior sclerotome, on the other hand, expresses members of ephrin and semaphorin families, along with inhibitory Extracellular Matrix (ECM) molecules, Versicans, and F-spondin (Newgreen and Gooday, 1985; Newgreen et al., 1986). The underlying mechanism of repression arises from the interaction between the migratory neural crest receptors *eph* and *neuropilin2* and their antagonistic ligands EphrinB and Semaphorin, respectively. Indeed, when neural crest cells from the trunk axial level were cultured in dishes containing fibronectin-coated matrices with alternating ephrin stripes, the cells moved along the regions with no ephrin, while completely avoiding ephrin coated stripes (Davy and Soriano, 2007; Krull et al., 1997; Wang and Anderson, 1997). Migration of these cells is also controlled temporally in a chemotactic fashion by the levels of Stromal cell-derived factor 1 (SDF1) along the ventro-dorsal axis (Kasemeier-Kulesa et al., 2010). Neural crest cells that differentiate within the sclerotome give rise to the dorsal root ganglia, with high levels of Notch leading to a glial fate, while high levels of Notch's ligand Delta lead to a neuronal fate. Expression of the chemokine (C-X-C motif) receptor 4 drives the first wave of ventrally-migrating trunk neural crest cells towards the dorsal aorta (Saito et al., 2012). Cells that lack the expression of CXCR4 continue to migrate and give rise to sympathoadrenal cells that then condense to form sympathetic ganglia as well as the adrenal medulla. BMP signaling from the dorsal aorta influences these cells to become sympathoadrenal while interactions with presumptive adrenal cortical cells influence further differentiation into the adrenal medulla (Saito and Takahashi, 2015).

The second migratory pathway, the dorsolateral pathway, is followed by neural crest cells that are fate-restricted to become pigment cell progenitors in a FoxD3-dependent manner (Tosney, 2004). Low levels of FoxD3 allow proper regulation of MITF, a transcription factor necessary for the differentiation of neural crest cells into melanocytes (Thomas and Erickson, 2009). Once the pigment precursors are specified, ephrin mediates the increase in levels of its receptor, EphB2, on the surface of these

cells, facilitating their migration through regions that initially inhibited the migration of multipotent trunk neural crest cells.

2.4 Regionalization along the anterior-posterior axis

Neural crest cells migrate long distances in response to both environmental cues and various signaling cascades (Kulesa and Gammill, 2010). Once they reach their final destination, the cells can differentiate into a wide array of cell types. The pioneering work of Le Douarin and colleagues showed that the neural crest can be categorized into four unique, albeit overlapping regions along the body axis in avian embryos, based on their axial level of origin [Figure 2]. The cranial neural crest, also known as the cephalic neural crest, includes the forebrain, midbrain and the anterior hindbrain region; the vagal neural crest spans from the posterior hindbrain region to somite 7; the trunk neural crest comprises somite 8 – 28; and the lumbosacral neural crest represents the region posterior of somite 28. Within the vagal neural crest, there is another subpopulation called the cardiac neural crest that arises from the neural tube adjacent to the mid otic-placode to somite 3. The cranial neural crest contributes to the craniofacial skeleton, and the glia and neurons of the cranial ganglia (D'amico-Martel and Noden, 1983; Le Douarin and Kalcheim, 1982). The vagal neural crest populates the gut, and the neurons and glia of the enteric nervous system. The cardiac neural crest gives rise to the cardiac outflow tract and the pharyngeal arches, and is the only neural crest subpopulation that contributes to proper cardiovascular development (Stoller and Epstein, 2005). The trunk neural crest cells form the dorsal root ganglia, sympathetic ganglia, and the adrenal medulla. Finally, the lumbosacral neural crest also contributes to the enteric nervous system. Interestingly, regardless of the axial identity, neural crest cells also differentiate into melanocytes, neurons, and glia (Le Douarin and Kalcheim, 1982).

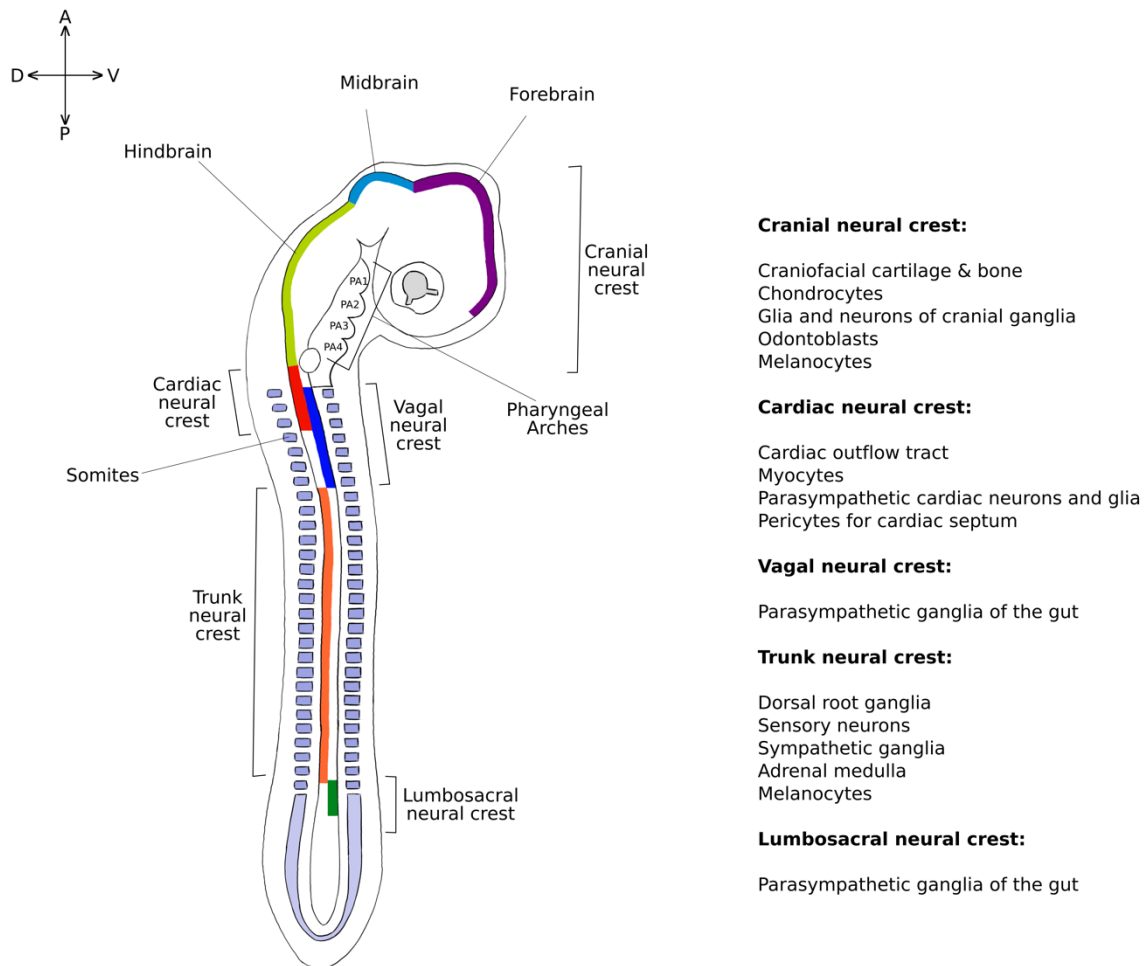


Figure 2. Neural crest derivatives along the anterior-posterior axis in chick embryos. Neural crest subpopulations have been designated based on their axial level of origin along the anterior-posterior axis. Cranial neural crest cells migrate from the cranial neural tube into the pharyngeal arches and give rise to craniofacial cartilage and bone, as well as glia and neurons of the cranial ganglia. The cardiac neural crest arises from the neural tube adjacent to the mid-otic region to somite 3 (marked in red), and plays a key role in cardiac outflow tract septation. Vagal neural crest spans from adjacent to somite 1 through 7 (marked in blue), and together with the lumbosacral neural crest, arising from the region posterior to somite 28 (marked in dark green), form the parasympathetic ganglia of the enteric nervous system. Trunk neural crest arises from the neural tube adjacent to somite 7 through 28 (marked in orange), and contributes to dorsal root and sympathetic neurons and glia, melanocytes, and the adrenal medulla. A summary of the main derivatives formed by the entire neural crest population is listed.

Axial level differences in differentiative ability are highlighted by transplantation experiments performed in chick embryos, where cranial and trunk neural crest cells were exchanged. Cranial neural crest cells give rise to the craniofacial skeleton, and happens to be the only neural crest population capable of doing so. When these cells were transplanted to the trunk, they not only compensated for the absence of trunk neural crest cells, but also differentiated into cartilage nodules (Le Douarin and Teillet, 1974; Le Lievre

et al., 1980). In contrast, trunk neural crest cells failed to give rise to any cartilage when transplanted to the cranial level, even though they contributed to the neurons and glia of the cranial ganglia (Nakamura and Ayer-Le Lievre, 1982). Indeed, genomic analysis revealed that the endogenous levels of the neural crest specifier genes *FoxD3* and *Sox10* are controlled by different set of enhancers at the cranial and trunk axial levels (Betancur et al., 2010, 2011; Simões-Costa et al., 2012). Not only that, but the transcriptional inputs these enhancers receive from their upstream genes are also different at the two axial levels (Simões-Costa et al., 2012). Taken together, these results suggest that there are intrinsic differences between the developmental fate of the two populations.

Recently, it has been possible to “reprogram” neural crest axial identity by tweaking the underlying genetic circuitry. Simões-Costa and Bronner revealed a cranial crest-specific subcircuit by performing transcriptional profiling of the migratory crest from the cranial and trunk axial levels (Simões-Costa and Bronner, 2016). They discovered that ectopic expression of a subset of this subcircuit in the trunk, the transcription factors *Sox8*, *Tfap2b*, and *Ets1*, was sufficient to alter the fate and identity of trunk neural crest into “cranial-like” cells. The altered identity was assessed by testing the ability of the trunk neural crest cells to activate *Sox10e2*, an enhancer that governs the expression of *Sox10* selectively in the migratory cranial neural crest cells (Betancur et al., 2010). To investigate the effect on trunk neural crest cell fate, they transplanted cells expressing the three factors from GFP donor embryos into wild-type chick embryos. Following incubation until embryonic day 7, they observed that cells transfected with the cranial neural crest-specific subcircuit had successfully differentiated into chondrocytes. The control group, on the other hand, did not form any part of the cartilage, suggesting that expression of the three transcription factors was sufficient to drive the population of the trunk neural crest towards a craniofacial derivative fate.

2.5 Multipotent or fate-restricted?

The advent of vertebrates has been suggested to overlap with the appearance of two cell types, neural crest cells and ectodermal placodal cells (Gans and Northcutt, 1983;

Gee, 1997; Glenn Northcutt, 2005), which contribute to the facial skeleton, cranial ganglia and sense organs. As the craniofacial skeleton and peripheral nervous system of the head are defining features of vertebrates, this suggests that the ability of neural crest cells to differentiate into a multitude of cell types played an important role in the evolution of vertebrates. This raises the intriguing question: how are neural crest cells able to differentiate into such diverse cell types? Over the last several decades, many hypotheses have been formulated to address this question.

Multiple studies performed over the last three decades support the idea that the neural crest is a multipotent population with the ability to give rise to many or all potential derivatives. The first piece of evidence *in vivo* came from Bronner-Fraser and Fraser when they injected fluorescent Dextran molecules into individual trunk and cranial neural crest cells before their delamination and migration (Bronner-Fraser and Fraser, 1988; Serbedzija et al., 1994). They observed that the progeny of the injected cells were capable of differentiating into several cell types such as sensory neurons, Schwann cells, and melanocytes, thus suggesting that a part of the migratory trunk neural crest was multipotent. They also reported the possibility of a common precursor for both the central nervous system (neural tube) and the peripheral nervous system (neural crest). Around the same time, Baroffio et al. (1988) successfully cultured cranial neural crest cells obtained from quail embryos and reported that the cells exhibited a wide developmental potential, corroborating the *in vivo* results obtained by Bronner-Fraser and Fraser. In addition, other clonogenic culture studies of neural crest cells reported that their lineage decision was directly influenced by the growth factors used in the culture medium (Lahav et al., 1998).

On the other hand, there is some evidence suggesting that the neural crest may be a heterogeneous mixture of fate-restricted cells. For example, Nitzan et al. (2013) have proposed that premigratory neural crest cells are unipotent and arranged in the dorsal neural tube in a spatiotemporal pattern in chick embryos that correlates with the derivatives they will form.

It is important to note that the techniques used in the above-mentioned studies suffered from some major drawbacks. First, *in vivo* lineage tracing experiments using fluorescent Dextran only allowed for the characterization of neural crest derivatives based on visualization of a lineage marker that is transient and diluted with each cell division. Second, clonal analysis *in vitro* requires growing cells in a culture medium outside the context of the developing embryo. However, Baggiolini et al. (2015) used a confetti mouse model to trace neural crest cells and their derivatives *in vivo*, allowing them to achieve permanent lineage labeling at single-cell resolution and in an intact endogenous environment of the embryo. Using this model, they traced nearly 100 neural crest cells, both premigratory and migratory, and demonstrated that almost 75% of these cells gave rise to multiple derivatives comprising of the dorsal root ganglia, melanocytes, sympathetic ganglia, and Schwann cells. While they observed that a small proportion of the cells gave rise to a single derivative, the vast majority of the trunk neural crest cells were multipotent, suggesting that the neural crest is primarily a multipotent population and thereby confirming the work in chick embryos done by Bronner-Fraser and Fraser some 25 years earlier.

2.6 Experimental strategies to study neural crest development

Some of the earliest experiments performed in developmental biology relied on ablation and grafting experiments to decrypt the puzzle that was the developing embryo. After Wilhelm Roux first published his ablation technique, Hans Spemann used it to investigate the role of tissue interactions in eye development. At the time, the process of lens formation was not thoroughly understood. By destroying the optic vesicle before it associated with the overlying ectoderm, Spemann demonstrated the importance of the interactions between the optic vesicle and the ectoderm in inducing proper lens development.

In the 19th century, the ablation technique was adapted to the chick embryo to address a diverse array of questions. It was through the ablation of the cardiac neural crest that the contribution of this population of neural crest cells to proper cardiovascular

development was highlighted (Besson et al., 1986; Kirby and Waldo, 1995; Kirby et al., 1985; Nishibatake et al., 1987). However, these experiments only revealed some of the developmental capabilities of the neural crest tissue. Moreover, it was difficult to conclude whether the presence or absence of structures after neural crest ablation indicated their site of origin. However, technical breakthroughs in biology have made it possible to address such questions in much finer detail. Here, we discuss some of the experimental techniques that are currently available to study neural crest development in chick embryos.

2.6.1 Neural crest lineage tracing

One of the biggest technical challenges in neural crest biology was the ability to distinguish a neural crest cell from its neighbors while it migrated through mesenchymal regions in the embryo. As a result, cell marking techniques that would allow investigators to trace individual cells were highly sought after. Radioactive labeling of nuclei with tritiated thymidine followed by transplantation of labeled tissue in a host embryo allowed Weston (1963) and Chibon (1967) to follow migration of these cells in avian and amphibian embryos, respectively (Chibon, 1967; Weston, 1963). The technique was soon adapted in a number of studies (Johnston, 1966; Noden, 1975, 1978; Weston and Butler, 1966). However, the levels of tritiated thymidine diluted with each cell division event, making this technique appropriate for only short-term tracing of neural crest cells. Moreover, the method was also prone to giving false labeling of non-neural crest cells, as the radioactive label from a dead cell could spread to its neighbors. Therefore, it was important to look for alternative strategies for neural crest labeling.

In the 1960s, Le Douarin devised the elegant quail-chick chimeras as a method to label cells and follow the long-term fate of neural crest cells, allowing her to trace neural crest pathways of migration and characterize their numerous derivatives (Le Douarin, 1969, 1973). This technique was based on the difference in the heterochromatin state of chick and quail embryos, which could be labeled with a simple histological Feulgen stain. These experiments not only made it possible to follow the migratory pathways of these

cells throughout the embryo, but also provided valuable insights into the extensive nature of neural crest derivatives. Using this approach, Douarin categorized the derivatives of the neural crest at different axial levels in chick embryos, leading to important observations regarding differences in properties of neural crest cells derived from different axial levels.

To confirm these results using methods that did not require interspecies transplantation, the next generation of labeling methods made use of fluorescently labeled large molecules such as Lysinated Rhodamine Dextran (LRD) and vital dyes such as Dil (1,1'-dioctadecyl-3,3,3',3'-tetramethylindocarbocyanide perchlorate). While these labeling methods were still transient, they offered several advantages over radioactive labeling. For example, both LRD and Dil were not prone to leak, hence reducing false labeling of tissues surrounding neural crest cells. They both were transferred to their daughter cells for a few generations, allowing tracking of migration at single cell resolution, albeit for short intervals. Most importantly, using these dyes to label cells and track their migration within the same embryo circumvented the need for grafting labeled cells in a host embryo, making their application much simpler than their predecessors. These techniques were instrumental in demonstrating the multipotent nature of neural crest cells not only in avian embryos (Artinger et al., 1995; Bronner-Fraser and Fraser, 1988; Lumsden et al., 1991; Serbedzija et al., 1989, 1990, 1994), but also in mammalian systems (Osugi-Yamashita et al., 1996). These labeling techniques gave valuable insights into the developmental potential of neural crest cells. However, given their transient nature, it was not possible to trace a single neural crest cell to the tissue to which it contributed later on during development. Hence, it was necessary to establish techniques that would not only allow labeling of single cells, but would also ensure long-range tracking of their migratory pathway.

With their ability to generate double-stranded DNA that stably integrate into the host cell genome, retroviruses offer an easy and effective alternative to classical cell labeling techniques described above. Replication Competent and Incompetent Avian Retroviruses (RCAS/RIA) have long been used to permanently label single cells and their

progeny by expressing reporter genes through the viral promoter (Frank and Sanes, 1991; Murai et al., 2015; Price et al., 1987; Sanes, 1989; Sanes et al., 1986). Injecting the viruses at different developmental stages at precise locations in the embryo allows spatiotemporal control over the labeling of neural crest cells at different axial levels. Pseudotyping the virus envelope protein ensures that the infection is limited to chicken cells. Moreover, these viruses have also been used to mis-express endogenous genes in neural crest cells (Eames et al., 2004).

2.6.2 Crestospheres

Methods employing *in vitro* culturing of neural crest cells were already established in the 1970s. However, it was not possible until very recently to successfully culture premigratory neural crest cells in their multipotent and self-renewal state (Cohen and Konigsberg, 1975). After they migrate from the neural tube, neural crest cells have a limited ability to self-renew for a few cell cycles (Stemple and Anderson, 1992; Trentin et al., 2004), and thus rapidly transit from stem cells to progenitor cells. However, more recently, Kerosuo et al. (2015) have successfully optimized conditions to culture premigratory neural crest cells as “crestospheres,” enabling long term self-renewal and retention of multipotency of the premigratory neural crest cells.

Premigratory neural crest cells express a suite of neural crest specifier genes including FoxD3, Sox9, Snail2, and Sox10 (Simões-Costa and Bronner, 2015; Simões-Costa et al., 2014). Kerosuo et al. (2015) tested various culture conditions that not only enabled proper expression of these transcription factors, but also promoted the maintenance of their self-renewal properties and stemness. Using a cocktail of growth factors that included epidermal growth factor, basic FGF, and RA, they found optimal conditions to culture premigratory neural crest cells in their multipotent state, as judged by the expression of neural crest marker genes in the cultured crestospheres. Interestingly, this medium also enabled culturing of crestospheres from entire neural tube tissue, suggesting that the correct proportion of growth factors supported culturing of neural crest at the cost of neural fate. Using these conditions, they successfully

maintained crestosphere cultures for as long as 5 weeks, albeit at a declining proliferation rate. By exposing them to specific differentiation media, they also demonstrated the differentiation potential of crestospheres into multiple neural crest derivatives.

Taken together, this technique of *in vitro* culturing of premigratory neural crest cells offers an interesting model to study neural crest development. Not only can the crestospheres be used to answer questions about the stem-cell-like behavior of neural crest cells, but they can also be used to investigate the role of certain environmental cues in cell migration and differentiation. By culturing crestospheres from GFP transgenic chick embryos and transplanting them back into wild type embryos, one could study the developmental potential of neural crest cells at single-cell resolution.

2.6.3 Antisense morpholinos

The concept of using antisense oligonucleotides to study gene expression was first proposed almost 20 years ago (Baker and Monia, 1999; Crooke, 1999). The antisense technology relied on the understanding of nucleic acid structure and the underlying mechanisms governing their hybridization. Synthetic oligonucleotides designed following these principles were capable of inhibiting protein translation via three different pathways; first, by disrupting ribosome assembly at the targeted mRNA; second, by blocking splice junctions through direct hindrance; third, by recruiting RNase H enzymes that degrade the target mRNA through recognition of the synthetic oligonucleotide-mRNA duplex. While the specificity of these oligonucleotides was a cause for concern, subsequent structural and chemical modifications of the oligonucleotides made this a useful technique for knockdown studies in different model systems including *Xenopus* (Heasman et al., 2000), zebrafish (Nasevicius and Ekker, 2000; Yang et al., 2001), and sea urchins (Howard et al., 2001).

Antisense morpholino oligonucleotides were first implemented in avian embryos for gene knockdowns when Kos et al. (2001) demonstrated the role of FoxD3 in maintaining the neural crest-derived melanoblast lineage. Since then, the entire chick neural crest community has relied on morpholinos to interrogate the role of different genes

in neural crest development (Barembaum and Bronner, 2013; Basch et al., 2006; Betancur et al., 2010; Simões-Costa et al., 2015, 2012). Important controls for establishing specificity of morpholinos include rescue experiments and validating protein knockdown. However, given the disadvantages of using morpholinos, including rising concerns about non-specific effects (Gerety and Wilkinson, 2011), cost ineffectiveness, and inability to target non-coding regions, the community has turned to CRISPR/Cas9 technology for more robust gene knockouts, which I will discuss in the next few chapters.

2.7 Conclusions

In this chapter, I have summarized aspects of the history of neural crest studies in avian embryos and fundamental principles underlying neural crest development. The neural crest is a stem-cell-like population of cells that is responsible for the emergence of craniofacial cartilage and bones in vertebrates, effectively parting them from invertebrate chordates. Through a network of transcription factors and signaling cascades, different segments of neural crest development are tightly regulated. Lineage tracing experiments in chicks (Bronner-Fraser and Fraser, 1988) are highly concordant with recent work in confetti mice, where Baggiolini et al. (2015) demonstrated that most of the cells are multipotent and hence are capable of differentiating into a diverse array of derivatives. I have also highlighted some of the most common experimental techniques that have been used to unfold the mystery of neural crest development and the gene regulatory network underlying different modules of neural crest development, such as induction, specification, migration, and differentiation. While we currently have a description of direct or indirect interactions between different neural crest transcription factors, several questions remain unanswered. For example, multiple mechanistic studies looking into these genetic interactions have posed questions about how non-coding RNAs such as lncRNAs, miRNAs, or piRNAs fit into the neural crest development paradigm. Addressing these questions will not only allow for the expansion of the neural crest gene regulatory network, but will also increase its resolution.

2.8 References

Artinger, K.B., Fraser, S., and Bronner-Fraser, M. (1995). Dorsal and ventral cell types can arise from common neural tube progenitors. *Dev. Biol.* *172*, 591–601.

Baggiolini, A., Varum, S., Mateos, J.M., Bettosini, D., John, N., Bonalli, M., Ziegler, U., Dimou, L., Clevers, H., Furrer, R., et al. (2015). Premigratory and migratory neural crest cells are multipotent in vivo. *Cell Stem Cell* *16*, 314–322.

Baker, B.F., and Monia, B.P. (1999). Novel mechanisms for antisense-mediated regulation of gene expression. *Biochim. Biophys. Acta - Gene Struct. Expr.* *1489*, 3–18.

Barenbaum, M., and Bronner-Fraser, M. (2005). Early steps in neural crest specification. *Semin. Cell Dev. Biol.* *16*, 642–646.

Barenbaum, M., and Bronner, M.E. (2013). Identification and dissection of a key enhancer mediating cranial neural crest specific expression of transcription factor, *Ets-1*. *Dev. Biol.* *382*, 567–575.

Baroffio, A., Dupin, E., and Le Douarin, N.M. (1988). Clone-forming ability and differentiation potential of migratory neural crest cells. *Proc. Natl Acad. Sci. USA* *85*, 5325–5329.

Basch, M.L., García-Castro, M.I., and Bronner-Fraser, M. (2004). Molecular mechanisms of neural crest induction. *Birth Defects Res. Part C - Embryo Today Rev.* *72*, 109–123.

Basch, M.L., Bronner-Fraser, M., and García-Castro, M.I. (2006). Specification of the neural crest occurs during gastrulation and requires *Pax7*. *Nature* *441*, 218–222.

Besson, W.T., Kirby, M.L., Van Mierop, L.H.S., and Teabeaut, J.R. (1986). Effects of the size of lesions of the cardiac neural crest at various embryonic ages on incidence and type of cardiac defects. *Circulation* *73*, 360–364.

Betancur, P., Bronner-Fraser, M., and Sauka-Spengler, T. (2010). Genomic code for Sox10 activation reveals a key regulatory enhancer for cranial neural crest. *Proc. Natl Acad. Sci. USA* *107*, 3570–3575.

Betancur, P., Sauka-Spengler, T., and Bronner, M. (2011). A Sox10 enhancer element common to the otic placode and neural crest is activated by tissue-specific paralogs. *Development* *138*, 3689–3698.

Bronner-Fraser, M. (1986). Analysis of the early stages of trunk neural crest migration in avian embryos using monoclonal antibody HNK-1. *Dev. Biol.* *115*, 44–55.

Bronner-Fraser, M., and Fraser, S.E. (1988). Cell lineage analysis reveals multipotency of some avian neural crest cells. *Nature* *335*, 161–164.

Bronner, M.E., and Simões-Costa, M. (2016). The Neural Crest Migrating into the Twenty-First Century. *Curr. Top. Dev. Biol.* *116*, 115–134.

Buitrago-Delgado, E., Nordin, K., Rao, A., Geary, L., and LaBonne, C. (2015). Shared regulatory programs suggest retention of blastula-stage potential in neural crest cells. *Science* *348*, 1332–1335.

Carney, T.J., Dutton, K.A., Greenhill, E., Delfino-Machín, M., Dufourcq, P., Blader, P., and Kelsh, R.N. (2006). A direct role for Sox10 in specification of neural crest-derived sensory neurons. *Development* *133*, 4619–4630.

Chibon, P. (1967). Marquage nucléaire par la thymidine tritiée des dérivés de la crête neurale chez l'Amphibien Urodèle *Pleurodeles waltlii* Michah. *J. Embryol. Exp. Morphol.* *18*, 343–358.

Cohen, A.M., and Konigsberg, I.R. (1975). A clonal approach to the problem of neural crest determination. *Dev. Biol.* *46*, 262–280.

Crooke, S.T. (1999). Molecular mechanisms of action of antisense drugs. *Biochim. Biophys. Acta - Gene Struct. Expr.* *1489*, 31–44.

D'amico-Martel, A., and Noden, D.M. (1983). Contributions of placodal and neural crest cells to avian cranial peripheral ganglia. *Am. J. Anat.* 166, 445–468.

Davy, A., and Soriano, P. (2007). Ephrin-B2 forward signaling regulates somite patterning and neural crest cell development. *Dev. Biol.* 304, 182–193.

Le Douarin, N.M. (1969). Details of the interphase nucleus in Japanese quail (*Coturnix coturnix japonica*). *Bull. Biol. Fr. Belg.* 103, 435–452.

Le Douarin, N.M. (1973). A biological cell labeling technique and its use in experimental embryology. *Dev. Biol.* 30, 217–222.

Le Douarin, N.M., and Dupin, E. (2014). The Neural Crest, a Fourth Germ Layer of the Vertebrate Embryo: Significance in Chordate Evolution. In *Neural Crest Cells: Evolution, Development and Disease*, pp. 3–26.

Le Douarin, N.M., and Kalcheim, C. (1982). *The Neural Crest*.

Le Douarin, N.M., and Kalcheim, C. (1999). *The neural crest* (Cambridge University Press).

Le Douarin, N.M., and Teillet, M.A. (1971). Localization, by the method of interspecific grafts of the neural area from which adrenal cells arise in the bird embryo. *C. R. Acad. Sci. Hebd. Seances Acad. Sci. D.* 272, 481–484.

Le Douarin, N.M., and Teillet, M.A. (1974). Experimental analysis of the migration and differentiation of neuroblasts of the autonomic nervous system and of neurectodermal mesenchymal derivatives, using a biological cell marking technique. *Dev. Biol.* 41, 162–184.

Duband, J.L., and Thiery, J.P. (1982). Distribution of fibronectin in the early phase of avian cephalic neural crest cell migration. *Dev. Biol.* 93, 308–323.

Dupin, E., Creuzet, S., and Le Douarin, N.M. (2006). The contribution of the neural crest to the vertebrate body. In *Advances in Experimental Medicine and Biology*, pp. 96–119.

Eames, B.F., Sharpe, P.T., and Helms, J.A. (2004). Hierarchy revealed in the specification of three skeletal fates by Sox9 and Runx2. *Dev. Biol.* *274*, 188–200.

Fairchild, C.L., Conway, J.P., Schiffmacher, A.T., Taneyhill, L.A., and Gammill, L.S. (2014). FoxD3 regulates cranial neural crest EMT via downregulation of tetraspanin18 independent of its functions during neural crest formation. *Mech. Dev.* *132*, 1–12.

Frank, E., and Sanes, J.R. (1991). Lineage of neurons and glia in chick dorsal root ganglia: analysis in vivo with a recombinant retrovirus. *Development* *111*, 895–908.

Gammill, L.S., and Bronner-Fraser, M. (2002). Genomic analysis of neural crest induction. *Development* *129*, 5731–5741.

Gans, C., and Northcutt, R.G. (1983). Neural crest and the origin of vertebrates: a new head. *Science* *220*, 268–273.

Gee, H. (1997). *Before the backbone: views on the origin of the vertebrates* (Chapman & Hall).

Gerety, S.S., and Wilkinson, D.G. (2011). Morpholino artifacts provide pitfalls and reveal a novel role for pro-apoptotic genes in hindbrain boundary development. *Dev. Biol.* *350*, 279–289.

Glenn Northcutt, R. (2005). The new head hypothesis revisited. *J. Exp. Zool. Part B Mol. Dev. Evol.* *304B*, 274–297.

Grenier, J., Teillet, M.-A., Grifone, R., Kelly, R.G., and Duprez, D. (2009). Relationship between Neural Crest Cells and Cranial Mesoderm during Head Muscle Development. *PLoS One* *4*, e4381.

Grocott, T., Tambalo, M., and Streit, A. (2012). The peripheral sensory nervous system in the vertebrate head: A gene regulatory perspective. *Dev. Biol.* 370, 3–23.

Hall, B.K. (2000). The neural crest as a fourth germ layer and vertebrates as quadroblastic not triploblastic. *Evol. Dev.* 2, 3–5.

Hall, B.K. (2009). The neural crest and neural crest cells in vertebrate development and evolution (Boston, MA: Springer US).

Harris, M.L., and Erickson, C.A. (2007). Lineage specification in neural crest cell pathfinding. *Dev. Dyn.* 236, 1–19.

Heasman, J., Kofron, M., and Wylie, C. (2000). β Catenin Signaling Activity Dissected in the Early *Xenopus* Embryo: A Novel Antisense Approach. *Dev. Biol.* 222, 124–134.

Howard, E.W., Newman, L.A., Oleksyn, D.W., Angerer, R.C., and Angerer, L.M. (2001). SpKrl: a direct target of beta-catenin regulation required for endoderm differentiation in sea urchin embryos. *Development* 128, 365–375.

Johnston, M.C. (1966). A radioautographic study of the migration and fate of cranial neural crest cells in the chick embryo. *Anat. Rec.* 156, 143–155.

Kasemeier-Kulesa, J.C., McLennan, R., Romine, M.H., Kulesa, P.M., and Lefcort, F. (2010). CXCR4 controls ventral migration of sympathetic precursor cells. *J. Neurosci.* 30, 13078–13088.

Kerosuo, L., Nie, S., Bajpai, R., and Bronner, M.E. (2015). Crestospheres: Long-term maintenance of multipotent, premigratory neural crest stem cells. *Stem Cell Reports* 5, 499–507.

Khudyakov, J., and Bronner-Fraser, M. (2009). Comprehensive spatiotemporal analysis of early chick neural crest network genes. *Dev. Dyn.* 238, 716–723.

Kim, J., Lo, L., Dormand, E., and Anderson, D.J. (2003). SOX10 maintains multipotency and inhibits neuronal differentiation of neural crest stem cells. *Neuron* *38*, 17–31.

Kirby, M.L., and Hutson, M.R. (2010). Factors controlling cardiac neural crest cell migration. *Cell Adhes. Migr.* *4*, 609–621.

Kirby, M.L., and Waldo, K.L. (1995). Neural crest and cardiovascular patterning. *Circ. Res.* *77*, 211–215.

Kirby, M.L., Turnage, K.L., and Hays, B.M. (1985). Characterization of conotruncal malformations following ablation of “cardiac” neural crest. *Anat. Rec.* *213*, 87–93.

Knecht, A.K., and Bronner-Fraser, M. (2002). Induction of the neural crest: a multigene process. *Nat. Rev. Genet.* *3*, 453–461.

Kos, R., Reedy, M. V., Johnson, R.L., and Erickson, C.A. (2001). The winged-helix transcription factor FoxD3 is important for establishing the neural crest lineage and repressing melanogenesis in avian embryos. *Development* *128*, 1467–1479.

Krull, C.E., Lansford, R., Gale, N.W., Collazo, A., Marcelle, C., Yancopoulos, G.D., Fraser, S.E., and Bronner-Fraser, M. (1997). Interactions of Eph-related receptors and ligands confer rostrocaudal pattern to trunk neural crest migration. *Curr. Biol.* *7*, 571–580.

Kulesa, P.M., and Fraser, S.E. (1998). Neural crest cell dynamics revealed by time-lapse video microscopy of whole embryo chick explant cultures. *Dev. Biol.* *204*, 327–344.

Kulesa, P.M., and Fraser, S.E. (2000). In ovo time-lapse analysis of chick hindbrain neural crest cell migration shows cell interactions during migration to the branchial arches. *Development* *127*, 1161–1172.

Kulesa, P.M., and Gammill, L.S. (2010). Neural crest migration: Patterns, phases and signals. *Dev. Biol.* *344*, 566–568.

Labosky, P.A., and Kaestner, K.H. (1998). The winged helix transcription factor Hfh2 is expressed in neural crest and spinal cord during mouse development. *Mech. Dev.* 76, 185–190.

Lahav, R., Dupin, E., Lecoin, L., Glavieux, C., Champeval, D., Ziller, C., and Le Douarin, N.M. (1998). Endothelin 3 selectively promotes survival and proliferation of neural crest-derived glial and melanocytic precursors in vitro. *Proc. Natl Acad. Sci. USA* 95, 14214–14219.

Le Lièvre, C.S., Schweizer, G.G., Ziller, C.M., and Le Douarin, N.M. (1980). Restrictions of developmental capabilities in neural crest cell derivatives as tested by in vivo transplantation experiments. *Dev. Biol.* 77, 362–378.

Liu, J.P., and Jessell, T.M. (1998). A role for rhoB in the delamination of neural crest cells from the dorsal neural tube. *Development* 125, 5055–5067.

Lumsden, A., Sprawson, N., and Graham, A. (1991). Segmental origin and migration of neural crest cells in the hindbrain region of the chick embryo. *Development* 113, 1281–1291.

Minoux, M., and Rijli, F.M. (2010). Molecular mechanisms of cranial neural crest cell migration and patterning in craniofacial development. *Development* 137, 2605–2621.

Monsoro-Burq, A.-H., Fletcher, R.B., and Harland, R.M. (2003). Neural crest induction by paraxial mesoderm in *Xenopus* embryos requires FGF signals. *Development* 130, 3111–3124.

Murai, H., Tadokoro, R., Sakai, K.I., and Takahashi, Y. (2015). In ovo gene manipulation of melanocytes and their adjacent keratinocytes during skin pigmentation of chicken embryos. *Dev. Growth Differ.* 57, 232–241.

Nakamura, H., and Ayer-Le Lievre, C.S. (1982). Mesectodermal capabilities of the trunk neural crest of birds. *J. Embryol. Exp. Morphol.* 70, 1–18.

Nasevicius, A., and Ekker, S.C. (2000). Effective targeted gene 'knockdown' in zebrafish. *Nat. Genet.* *26*, 216–220.

Newgreen, D.F., and Gooday, D. (1985). Control of the onset of migration of neural crest cells in avian embryos - Role of Ca⁺⁺-dependent cell adhesions. *Cell Tissue Res.* *239*, 329–336.

Newgreen, D.F., Scheel, M., and Kastner, V. (1986). Morphogenesis of sclerotome and neural crest in avian embryos - In vivo and in vitro studies on the role of notochordal extracellular material. *Cell Tissue Res.* *244*, 299–313.

Nishibatake, M., Kirby, M.L., and Van Mierop, L.H.S. (1987). Pathogenesis of persistent truncus arteriosus and dextroposed aorta in the chick embryo after neural crest ablation. *Circulation* *75*, 255–264.

Nitzan, E., Pfaltzgraff, E.R., Labosky, P.A., and Kalcheim, C. (2013). Neural crest and Schwann cell progenitor-derived melanocytes are two spatially segregated populations similarly regulated by Foxd3. *Proc. Natl Acad. Sci. USA* *110*, 12709–12714.

Noden, D.M. (1975). An analysis of the migratory behavior of avian cephalic neural crest cells. *Dev. Biol.* *42*, 106–130.

Noden, D.M. (1978). The control of avian cephalic neural crest cytodifferentiation. I. Skeletal and connective tissues. *Dev. Biol.* *67*, 296–312.

Osorio, L., Teillet, M.-A., and Catala, M. (2009). Role of noggin as an upstream signal in the lack of neuronal derivatives found in the avian caudal-most neural crest. *Development* *136*, 1717–1726.

Osumi-Yamashita, N., Ninomiya, Y., Doi, H., and Eto, K. (1996). Rhombomere formation and hind-brain crest cell migration from prorhombomeric origins in mouse embryos. *Dev. Growth Differ.* *38*, 107–118.

Price, J., Turner, D., and Cepko, C.L. (1987). Lineage analysis in the vertebrate nervous system by retrovirus-mediated gene transfer. *Proc. Natl Acad. Sci. USA* *84*, 156–160.

Rickmann, M., Fawcett, J.W., and Keynes, R.J. (1985). The migration of neural crest cells and the growth of motor axons through the rostral half of the chick somite. *J. Embryol. Exp. Morphol.* *90*, 437–455.

Roellig, D., Tan-Cabugao, J., Esaian, S., and Bronner, M.E. (2017). Dynamic transcriptional signature and cell fate analysis reveals plasticity of individual neural plate border cells. *ELife* *6*, e21620.

Saito, D., and Takahashi, Y. (2015). Sympatho-adrenal morphogenesis regulated by the dorsal aorta. *Mech. Dev.* *138*, 2–7.

Saito, D., Takase, Y., Murai, H., and Takahashi, Y. (2012). The dorsal aorta initiates a molecular cascade that instructs sympatho-adrenal specification. *Science* *336*, 1578–1581.

Sanes, J.R. (1989). Analysing cell lineage with a recombinant retrovirus. *Trends Neurosci.* *12*, 21–28.

Sanes, J.R., Rubenstein, J.L., and Nicolas, J.F. (1986). Use of a recombinant retrovirus to study post-implantation cell lineage in mouse embryos. *EMBO J.* *5*, 3133–3142.

Sasai, N., Mizuseki, K., and Sasai, Y. (2001). Requirement of FoxD3-class signaling for neural crest determination in *Xenopus*. *Development* *128*, 2525–2536.

Sauka-Spengler, T., and Bronner-Fraser, M. (2008). A gene regulatory network orchestrates neural crest formation. *Nat. Rev. Mol. Cell Biol.* *9*, 557–568.

Sela-Donenfeld, D., and Kalcheim, C. (1999). Regulation of the onset of neural crest migration by coordinated activity of BMP4 and Noggin in the dorsal neural tube. *Development* *126*, 4749–4762.

Serbedzija, G.N., Bronner-Fraser, M., and Fraser, S.E. (1989). A vital dye analysis of the timing and pathways of avian trunk neural crest cell migration. *Development* *106*, 809–816.

Serbedzija, G.N., Fraser, S.E., and Bronner-Fraser, M. (1990). Pathways of trunk neural crest cell migration in the mouse embryo as revealed by vital dye labelling. *Development* *108*, 605–612.

Serbedzija, G.N., Bronner-Fraser, M., and Fraser, S.E. (1994). Developmental potential of trunk neural crest cells in the mouse. *Development* *120*, 1709–1718.

Shyamala, K., Yanduri, S., Girish, H.C., and Murgod, S. (2015). Neural crest: The fourth germ layer. *J. Oral Maxillofac. Pathol.* *19*, 221–229.

Simões-Costa, M., and Bronner, M.E. (2013). Insights into neural crest development and evolution from genomic analysis. *Genome Res.* *23*, 1069–1080.

Simões-Costa, M., and Bronner, M.E. (2015). Establishing neural crest identity: a gene regulatory recipe. *Development* *142*, 242–257.

Simões-Costa, M., and Bronner, M.E. (2016). Reprogramming of avian neural crest axial identity and cell fate. *Science* *352*, 1570–1573.

Simões-Costa, M., McKeown, S.J., Tan-Cabugao, J., Sauka-Spengler, T., and Bronner, M.E. (2012). Dynamic and differential regulation of stem cell factor FoxD3 in the neural crest is encrypted in the genome. *PLoS Genet.* *8*, e1003142.

Simões-Costa, M., Tan-Cabugao, J., Antoshechkin, I., Sauka-Spengler, T., and Bronner, M.E. (2014). Transcriptome analysis reveals novel players in the cranial neural crest gene regulatory network. *Genome Res.* *24*, 281–290.

Simões-Costa, M., Stone, M., and Bronner, M.E. (2015). Axud1 Integrates Wnt Signaling and Transcriptional Inputs to Drive Neural Crest Formation. *Dev. Cell* *34*, 544–554.

Sit, S.-T., and Manser, E. (2011). Rho GTPases and their role in organizing the actin cytoskeleton. *J. Cell Sci.* *124*, 679–683.

Stemple, D.L., and Anderson, D.J. (1992). Isolation of a stem cell for neurons and glia from the mammalian neural crest. *Cell* *71*, 973–985.

Steventon, B., Carmona-Fontaine, C., and Mayor, R. (2005). Genetic network during neural crest induction: From cell specification to cell survival. *Semin. Cell Dev. Biol.* *16*, 647–654.

Steventon, B., Araya, C., Linker, C., Kuriyama, S., and Mayor, R. (2009). Differential requirements of BMP and Wnt signalling during gastrulation and neurulation define two steps in neural crest induction. *Development* *136*, 771–779.

Stewart, R.A., Arduini, B.L., Berghmans, S., George, R.E., Kanki, J.P., Henion, P.D., and Look, A.T. (2006). Zebrafish *foxd3* is selectively required for neural crest specification, migration and survival. *Dev. Biol.* *292*, 174–188.

Stoller, J.Z., and Epstein, J.A. (2005). Cardiac neural crest. *Semin. Cell Dev. Biol.* *16*, 704–715.

Stuhlmiller, T.J., and García-Castro, M.I. (2012). Current perspectives of the signaling pathways directing neural crest induction. *Cell. Mol. Life Sci.* *69*, 3715–3737.

Takahashi, K., Tanabe, K., Ohnuki, M., Narita, M., Ichisaka, T., Tomoda, K., and Yamanaka, S. (2007). Induction of pluripotent stem cells from adult human fibroblasts by defined factors. *Cell* *131*, 861–872.

Theveneau, E., and Mayor, R. (2011). Collective cell migration of the cephalic neural crest: The art of integrating information. *Genesis* *49*, 164–176.

Théveneau, E., Duband, J.-L., Altabef, M., Fauquette, W., and Pollet, I. (2007). *Ets-1* Confers Cranial Features on Neural Crest Delamination. *PLoS One* *2*, e1142.

Thomas, A.J., and Erickson, C. a (2009). FOXD3 regulates the lineage switch between neural crest-derived glial cells and pigment cells by repressing MITF through a non-canonical mechanism. *Development* *136*, 1849–1858.

Tosney, K.W. (2004). Long-Distance Cue from Emerging Dermis Stimulates Neural Crest Melanoblast Migration. *Dev. Dyn.* *229*, 99–108.

Trentin, A., Glavieux-Pardanaud, C., Le Douarin, N.M., and Dupin, E. (2004). Self-renewal capacity is a widespread property of various types of neural crest precursor cells. *Proc. Natl Acad. Sci. USA* *101*, 4495–4500.

Wang, H.U., and Anderson, D.J. (1997). Eph family transmembrane ligands can mediate repulsive guidance of trunk neural crest migration and motor axon outgrowth. *Neuron* *18*, 383–396.

Weston, J.A. (1963). A radioautographic analysis of the migration and localization of trunk neural crest cells in the chick. *Dev. Biol.* *6*, 279–310.

Weston, J.A., and Butler, S.L. (1966). Temporal factors affecting localization of neural crest cells in the chicken embryo. *Dev. Biol.* *14*, 246–266.

Yang, Z., Liu, N., and Lin, S. (2001). A zebrafish forebrain-specific zinc finger gene can induce ectopic d1x2 and d1x6 expression. *Dev. Biol.* *231*, 138–148.

Chapter 3

Evolution of the neural crest

A modified version of this chapter was published as:

Martik, M.L., Gandhi, S., Uy, B.R., Gillis, J.A., Green, S.A., Simões-Costa, M., and Bronner, M.E. (2019). Evolution of the new head by gradual acquisition of neural crest regulatory circuits. *Nature* 574, 675–678.

<https://doi.org/10.1038/s41586-019-1691-4>

3.1 Introduction

Gans and Northcutt's "New Head" hypothesis proposed that emergence of the vertebrate lineage was accompanied by the advent of the neural crest, an embryonic stem cell population that arises within the forming central nervous system (CNS) in all vertebrates (Gans and Northcutt, 1983; Glenn Northcutt, 2005). These cells subsequently leave the CNS, migrate to diverse locations, and differentiate into many derivatives including peripheral ganglia and craniofacial skeleton (Le Douarin, 1982; Le Douarin and Smith, 1988). As vertebrates evolved, neural crest cells contributed to morphological novelties like jaws, that enabled the expansion of vertebrates.

A pan-vertebrate neural crest gene regulatory network (GRN), invoking sequential deployment of signaling and transcriptional events, has been proposed to underlie formation of this unique cell type. Primarily studied at cranial levels, the core of the neural crest GRN is largely conserved across vertebrates, including the sea lamprey, *Petromyzon marinus*, a jawless (cyclostome) vertebrate. However, differences exist in utilization of key transcription factors, like *Ets1* and *Twist*, which are deployed later in the lamprey GRN than in amniotes (Nikitina et al., 2008; Sauka-Spengler et al., 2007), suggesting regulatory differences between cyclostomes and gnathostomes. Furthermore, some neural crest derivatives are novelties of gnathostomes, such as jaws at cranial levels, a vagal-derived enteric nervous system, and sympathetic ganglia at trunk levels (Green et al., 2017; Häming et al., 2011). This raises the intriguing possibility that network differences in axial regionalization of the neural crest may have contributed to the presence of these gnathostome cell types.

In jawed vertebrates, the neural crest is subdivided along the body axis into cranial, vagal, and trunk populations. In contrast, lamprey lack an intermediate vagal population, suggesting there are two major subdivisions: cranial and trunk (Le Douarin, 1982; Green et al., 2017). How axial identity in lamprey is controlled molecularly remains unknown. Avian embryos possess a "cranial-crest-specific" neural crest GRN subcircuit with ability to drive differentiation of trunk neural crest into ectomesenchymal derivatives (Simões-

Costa and Bronner, 2016). In this kernel, transcription factors *Brn3c*, *Lhx5*, and *Dmbx1* are expressed at the neural plate border and, in turn, activate expression of *Ets1* and *Sox8* in premigratory cranial neural crest [Figure 1A]. In contrast to their cranial-specific expression, *Tfap2b* and *Sox10* are pan-neural neural crest genes expressed all along the body axis (Betancur et al., 2010).

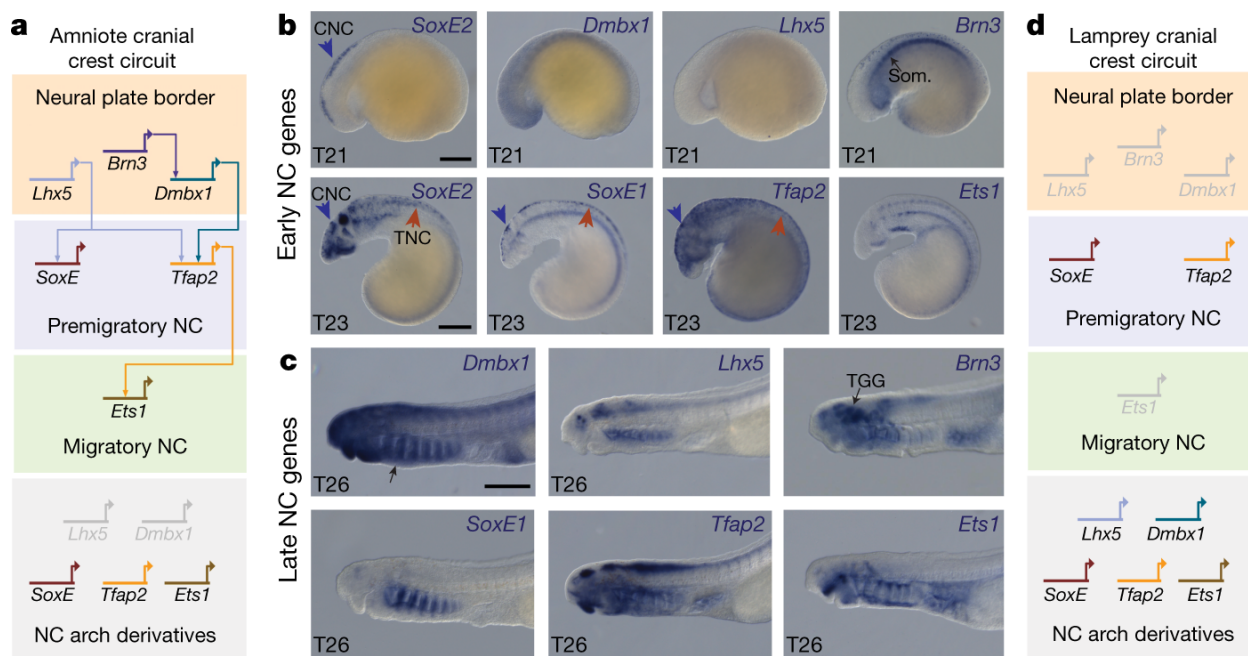


Figure 1. Lamprey cranial neural crest lacks most components of a chick “cranial crest circuit.” **a**, Biotapestry model of cranial neural crest-specific gene regulatory circuit that drives skeletal differentiation in amniotes. **b**, Expression of lamprey orthologues of amniote cranial neural crest-specific genes at T21 and T23. Blue arrows, expression in the cranial neural crest (CNC); red arrows, expression in the trunk neural crest (TNC). **c**, Late expression of cranial neural crest-specific orthologues in pharyngeal arch neural crest derivatives (black arrow). TGG, trigeminal ganglia. Scale bars, 250 μ m. Reproducible on $n \geq 5$ embryos per time point for $n \geq 10$ experiments.

3.2 Results and Discussion

3.2.1 Lamprey lacks a full cranial neural crest subcircuit

Here, we assessed whether this cranial subcircuit is a general feature of vertebrates by examining whether lamprey possesses a homologous spatiotemporal regulatory state. Taking a candidate approach, we analyzed the expression of cranial circuit orthologues in lamprey embryos at different developmental stages. In contrast to

amniotes, our results show that *Brn3*, *Lhx5*, *Dmbx1*, and *Ets1* appear to be absent from lamprey premigratory or migratory neural crest [Figure 1B]. The lack of most cranial-specific regulatory factors suggests a high degree of divergence between early regulatory states of lamprey and amniote neural crest. In contrast, lamprey *SoxE1* and *Tfap2* were robustly expressed in premigratory and migratory neural crest along the entire body axis [Figure 1B, Supplementary Figure 1A-D]. No *SoxE* family member was restricted in expression to the cranial neural crest as is *Sox8* in amniotes. Of note, lamprey *SoxE* transcription factors are homologous to gnathostome *Sox8/9/10*, and there is variation in *SoxE* paralog usage across gnathostomes (Haldin and LaBonne, 2010; Lee et al., 2016; McCauley and Bronner-Fraser, 2006). Consistent with the lack of restricted cranial-specific expression, ectomesenchymal derivatives have been previously reported as present at trunk levels in the lamprey dorsal fin (Häming et al., 2011).

How then did this regulatory subcircuit evolve? Intriguingly, genes from the cranial crest subcircuit are present in the genome and expressed later in pharyngeal arches populated by neural crest cells [Figure 1C,D, Supplementary Figure 1E-L]. An intriguing possibility is that these genes were expressed only in late neural crest derivatives of early vertebrates, followed by gradual co-option of components of this regulatory program to earlier developmental stages in gnathostomes. According to this scenario, genes involved in neural crest differentiation in early vertebrates were co-opted to the specification program of gnathostomes at all axial levels. With subsequent regulatory modifications, they became cranially restricted, possibly endowing the cranial neural crest with novel morphogenetic features while the trunk neural crest lost ability to make cranial-like derivatives (Green et al., 2015; Martik and Bronner, 2017).

3.2.2 Skates add *Ets1* to the cranial neural crest subcircuit

To explore this possibility, we examined candidate elements of the cranial neural crest subcircuit in the little skate *Leucoraja erinacea*, a Chondrichthyan gnathostome outgroup to the bony fishes. Of the *SoxE* genes, expression of *Sox9* and *Sox10*, as well as *Tfap2b* and *Ets1*, were present at all axial levels and not restricted to cranial crest

[Figure 2A, Supplementary Figure 2]. Since *Ets1* appears in the little skate migratory neural crest as in other gnathostomes, we conclude that this early node was a novelty acquired by the cranial neural crest GRN prior to divergence of cartilaginous and bony fishes [Figure 2A,B, Supplementary Figure 2]. Later, after neural crest cells migrated to and populated the pharyngeal arches, *SoxE*, *Tfap2b*, and *Ets1* were present within the arches [Supplementary Figure 3]. Trunk neural crest in the little skate produces ectomesenchymal dermal denticles, “cranial-like” derivatives, consistent with our observation that cranial subcircuit genes in the little skate are not restricted to the head but can drive differentiation of skeletogenic derivatives in the trunk (Gillis et al., 2017). In the fossil record, many stem-gnathostomes possessed extensive dermal armour, which has been retained, albeit with the dental component reduced and modified, within the

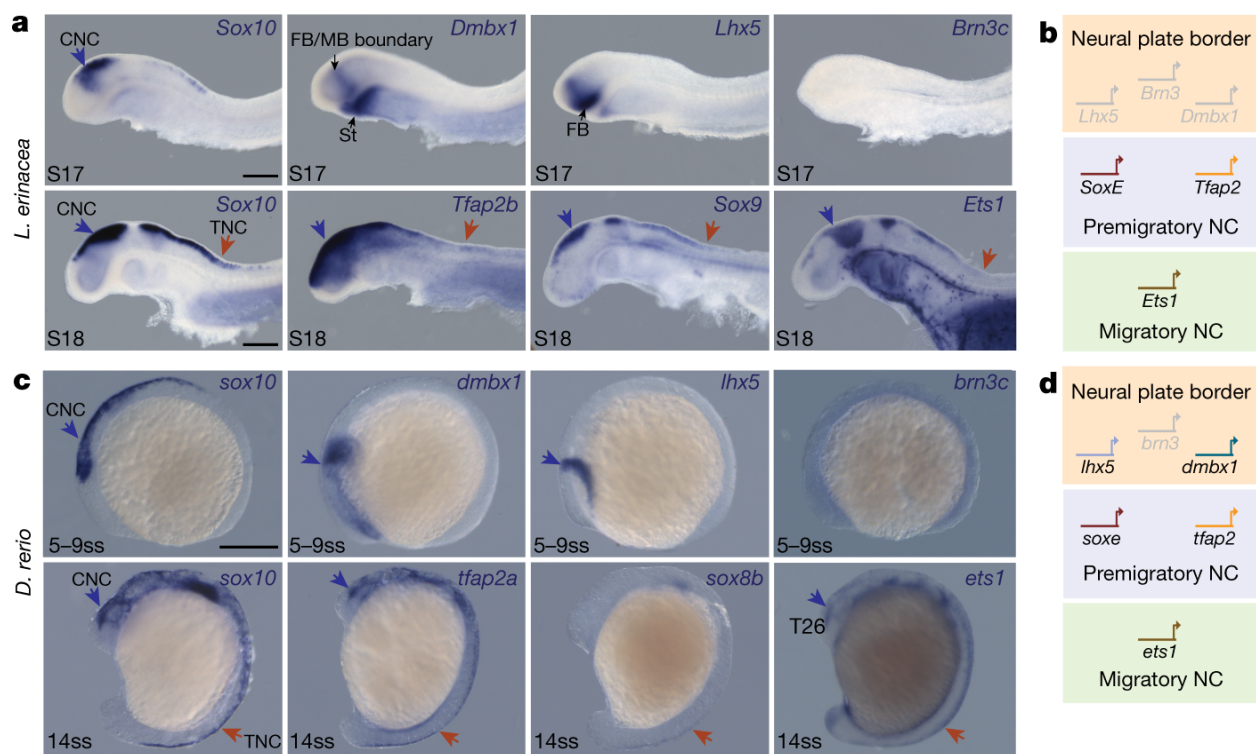


Figure 2. Nodes of an early cranial-specific circuit were acquired in and restricted to the cranial neural crest progressively throughout gnathostome evolution. **a**, Expression of cranial neural crest-specific orthologues in the little skate at stages (S) 17 and 18. Blue arrow, expression of orthologues in the cranial neural crest; red arrows, expression of orthologues in the trunk neural crest. **b**, Biotapestry model of the skate circuit with the addition of a novel node, *Ets1*. **c**, Expression of cranial neural crest-specific orthologues in the zebrafish at 5–9 somite stage (ss) and 14ss. **d**, Biotapestry model of the zebrafish circuit with the addition of novel early nodes, *lhx5* and *dmbx1*. FB/MB, forebrain/midbrain; St, stomodeum. Scale bars, 250 μ m. For skates, *in situ* hybridizations were reproducible on $n \geq 2$ embryos for $n \geq 2$ experiments. For zebrafish, *in situ* hybridizations were reproducible on $n \geq 5$ embryos per time point for $n \geq 10$ experiments.

gnathostome crown group (e.g. dermal denticles of chondrichthyans; dentinous scales of *Polypterus* and coelacanth). Thus, dental tissues in the post cranial dermal skeleton appear to be ancestral for gnathostomes.

3.2.3 Further elaboration of the neural crest subcircuit

Interestingly, in the teleost *Danio rerio*, *lhx5* and *dmbx1* are present in the early cranial circuit but absent from later pharyngeal arch derivatives [Figure 2C,D, Supplementary Figure 4, Supplementary Figure 5]. In addition, *sox8b*, *sox10*, *tfap2a*, and *ets1* are present in premigratory and migratory crest at all axial levels, though *brn3c* is missing [Figure 2C, Supplementary Figure 4]. Rather than restricted to the cranial crest, many of these factors also are present in the zebrafish trunk, raising the possibility that resolution of axial level potential may have arisen within sarcopterygians. Furthermore, *in situ* analysis of pharyngeal arch derivatives in both little skate and zebrafish lend support to temporal shifts of cranial specific regulatory nodes from later neural crest derivatives to an early specification program. With progressive loss of nodes from late derivatives and addition to an earlier program, this suggests that regulatory modifications arose gradually throughout gnathostome evolution [Supplementary Figure 1M].

3.2.4 Lamprey cranial neural crest is more trunk-like

Our candidate gene approach suggests that extensive changes occurred in the neural crest regulatory state between jawless and jawed vertebrates. To investigate further, we conducted a comparative transcriptome analysis of cranial and trunk neural crest subpopulations in lamprey and chicken [Figure 3]. Premigratory lamprey neural crest was obtained by microdissecting segments of cranial and trunk dorsal neural tubes at stages T21 and T23.5. For chick, premigratory neural crest populations were isolated using enhancers driving eGFP expression in cranial or trunk neural crest populations for FACS at stages HH9+ and HH18, respectively. After cDNA library preparation and sequencing, differential expression analysis revealed far fewer genes (1233 genes in lamprey compared with 2794 in chicken) significantly enriched in lamprey cranial versus trunk crest compared with chick cranial versus trunk [Figure 3A,3B].

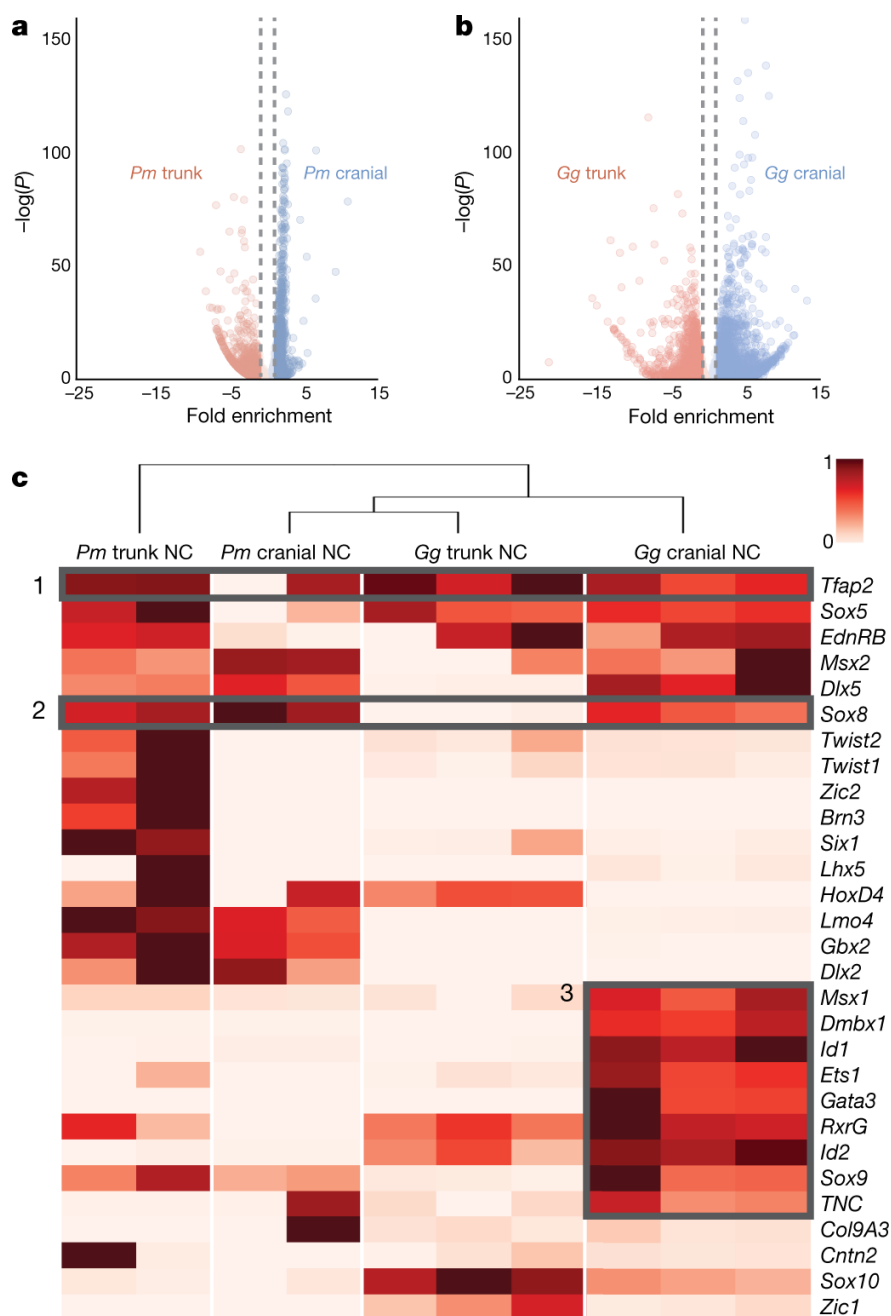


Figure 3. Tissue-specific RNA-seq comparisons between lamprey and chicken reveal that the ancestral neural crest had a more trunk-like identity. **a**, Volcano plot showing lamprey differential enrichments of cranial (blue) and trunk (red) genes by population RNA sequencing (RNA-seq; 100 embryos were dissected for each of $n = 2$ biological replicates; adjusted $P < 0.05$). **b**, Volcano plot showing enrichment of genes in the cranial (blue) versus the trunk (red) neural crest in chicken (≥ 15 heads and 5 trunks were dissected and prepared for FACS for each of $n = 3$ biological replicates; adjusted $P < 0.05$). **c**, Hierarchical clustering analysis of all RNA-seq libraries focused on the neural crest GRN reveals similarities and differences between axial levels among species.

To better understand how each library correlated to the others in an unbiased fashion, we mapped each to a common reference transcriptome, created by aligning proteomes using BLAT and compiling matching sequences as a consensus alignment between species for Bowtie mapping. We next performed hierarchical clustering analysis of all known neural crest GRN genes [Figure 3C]. Consistent with our previous *in situ* hybridization analysis [Figure 1B], *Tfap2* was enriched at all axial levels in both chicken and lamprey [Figure 3C’]; *Sox8* was enriched in chicken cranial neural crest but was in both cranial and trunk lamprey populations [Figure 3C’]. *Dmbx1* and *Ets1* were enriched in chick but not lamprey cranial datasets [Figure 3C’’].

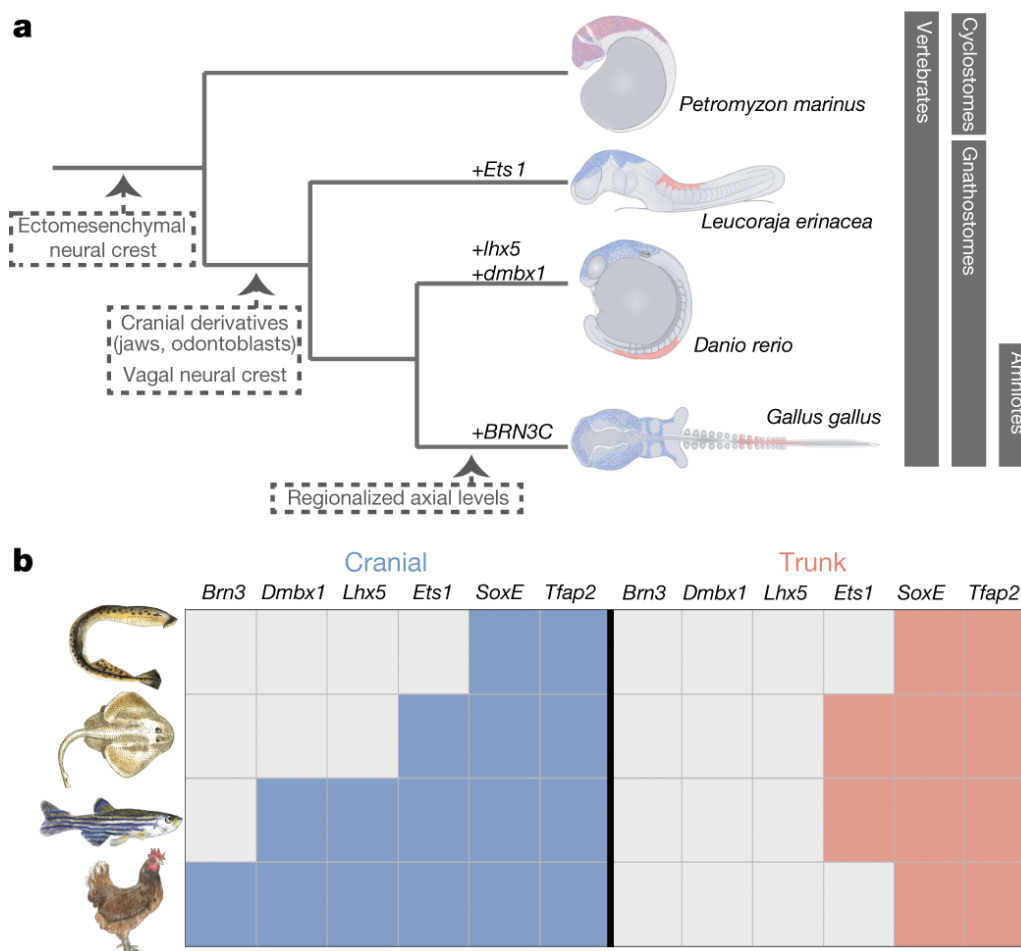


Figure 4. Model of the evolution of neural crest axial levels during vertebrate evolution. **a**, Our data suggest that the ancestral neural crest was a more uniform population of cells along the body axis that underwent gradual regulatory modifications during gnathostome evolution. **b**, Progressive restriction of the “cranial circuit genes” to the cranial axial level led to axial specialization of the neural crest regulatory program.

Interestingly, we found that lamprey cranial populations correlated more closely to chicken trunk than lamprey trunk libraries, suggesting that basal neural crest was “trunk-like” in its regulatory program [Figure 3C]. These results suggest that cyclostomes possess a simpler and more trunk-like cranial crest GRN, with potentially important implications for evolution of neural crest subpopulations [Figure 4A]. Accordingly, we speculate that the ancestral neural crest may have been relatively homogeneous and trunk-like. Throughout evolution of the vertebrate lineage, we propose that key transcription factors were progressively co-opted into an early, cranial-restricted circuit, whereas some features like skeletogenic potential were lost from the trunk.

These differences in axial-specific genes contrast with the deep conservation of the pan-neural crest program (Sauka-Spengler and Bronner-Fraser, 2008; Sauka-Spengler et al., 2007). Transcription factors like *SoxEs*, *Tfap2*, and *Id* may be the rudiment of a larger, more complex cranial crest GRN that was expanded during early vertebrate evolution with incorporation of novel players such as *Dmbx1*, *Brn3c*, *Ets1*, and *Lhx5*. Consistent with these findings, the basal chordate *Amphioxus* lacks expression at the neural plate border of genes like *Dmbx*, *Brn3*, *Ets*, as well as core neural crest genes like *SoxE*, *FoxD*, *Tfap2*, and *Id*, although these genes are expressed in other tissues (Meulemans and Bronner-Fraser, 2002; Takahashi and Holland, 2004; Wada et al., 2005; Yu et al., 2008). Our observations also show that some of these “novel” genes are expressed at later stages of neural crest formation, consistent with the possibility that elaboration of the GRN might have involved co-option of parts of differentiation programs to earlier portions of the network perhaps by acquisition of new regulatory elements responsible for their heterochronic shift (Davidson and Erwin, 2006). Thus, the pan-neural crest program was likely the ancestral molecular recipe to make neural crest, with the subsequent elaboration of axial-specific regulatory programs conferring important differences in developmental potential along the body axis. Given that many key neural crest derivatives are gnathostome innovations, we hypothesize that gain of these derivatives may be due to gene regulatory differences associated with axial-specific regulatory programs.

3.3 Conclusions

Taken together, our results suggest the following scenario to explain the evolution of neural crest subpopulations [Figure 4]. We suggest that the neural crest of early vertebrates was uniform and similar to amniote trunk populations, and that the division of the neural crest into cranial and trunk subpopulations occurred early in vertebrate evolution [Figure 4A]. Consistent with evolutionary expansion of neural crest cells in the vertebrate lineage, our molecular analysis of the cranial neural crest reveals surprising differences in lamprey compared with gnathostome counterparts [Figure 4B]. Given that the Hox code was already linked to segmentation of the CNS in basal vertebrates, posteriorizing influences of Hox genes and other factors may be sufficient to account for the subtle transcriptional differences observed between these two populations (Parker et al., 2014, 2016). We cannot rule out the possibility that cyclostomes lost neural crest subpopulations during the course of evolution. However, the relative scarcity of cranial-specific factors in the lamprey cranial crest might suggest that the gnathostome cranial neural crest GRN has undergone extensive elaboration from a regulatory standpoint. Thus, we propose that regionalization of the neural crest, with both emergence of new subpopulations and expansion of the cranial crest GRN, played a crucial part in vertebrate evolution as a key element for driving evolution and expansion of gnathostomes.

What does this mean for the “New Head” hypothesis? We posit that the neural crest component of the New Head, rather than arising *in toto* at the base of vertebrates, underwent continued regulatory modifications, evolving gradually during the course of vertebrate evolution. Our data suggest that early vertebrates possessed a relatively simple neural crest that initially arose as a fairly uniform population along the body axis and lacked region-restricted regulatory programming. During gnathostome evolution, the cranial neural crest appears to have gained regulatory complexity that modulated differentiation capacity, gaining some individual cell fates while restricting others. We propose that co-option of distinct genes into a cranial-specific module enabled this progressive specialization of neural crest regulatory programs, leading to unique axial populations and morphological novelties of the gnathostome body plan.

3.4 Acknowledgements

We thank Joanne Tan-Cabugao and Eli Grossman for technical assistance. We would also like to thank David Mayorga and Ryan Fraser for help with fish husbandry. We thank Brennah Martik for illustrating the adult animals for our expression matrices and acknowledge the Caltech Millard and Muriel Jacobs Genetics and Genomics Laboratory, in particular, Igor Antoshechkin for sequencing of our RNA-seq libraries. We thank Rochelle Diamond, Jamie Tijerina, and Patrick Cannon of the Caltech Flow Cytometry Cell Sorting Facility for cell sorting assistance.

3.5 Author Contributions

Project and analysis conception were designed by M.L.M., M.S.C., and M.E.B. Writing and interpretation was performed by M.L.M., S.G., B.R.U., J.A.G., S.A.G., M.S.C., M.E.B. Lamprey orthologue cloning and all *in situ* hybridization, imaging, and analysis was performed by M.L.M. Bioinformatics and chicken RNA-seq was performed by S.G. Lamprey embryo acquisition was performed by S.A.G. Cloning of skate orthologues and skate embryo acquisition was performed by J.A.G. Lamprey embryo dissections and library preparations were performed by B.R.U. and M.S.C.

3.6 Funding

This work is supported by NIH grant R01NS086907 and R35NS111564 to M.E.B. M.L.M. is supported by a Helen Hay Whitney Foundation postdoctoral fellowship. S.G. is supported by a graduate fellowship from the American Heart Association (18PRE34050063).

3.7 Materials and methods

3.7.1 Animal husbandry and embryo collection

Adult sea lamprey were obtained from the US Fish and Wildlife Service and Department of the Interior. Embryos were cultured according to previously published

protocols and staged according to Tahara staging methods (McCauley and Bronner-Fraser, 2006; Nikitina et al., 2009). All lamprey embryology work was completed in compliance with California Institute of Technology Institutional Animal Care and Use Committee (IACUC) protocol 1436. Skate eggs were obtained by the Marine Biological Laboratory (MBL) Marine Resource Center, and embryos were cultured as previously described (Gillis et al., 2017). All skate embryology work was compliant with animal protocols approved by the IACUC at the MBL. Adult zebrafish were maintained in the Beckman Institute Fish Facility at Caltech, and all animal and embryo work was compliant under approved IACUC protocol 1346. Fertilized chicken eggs were obtained from a local farm in Sylmar, CA.

3.7.2 Cloning of lamprey, skate, and zebrafish orthologues

RNA was extracted from desired embryo stages using the RNAqueous-Micro Kit (Thermo Fisher Scientific), and cDNA was synthesized using a SuperScript III Reverse Transcriptase Kit (Invitrogen). Gene specific primers were used to amplify probe template sequences found from transcriptome datasets. Nucleotide sequences were annotated and deposited on Genbank (BioProject # PRJNA497902).

3.7.3 *In situ* hybridization of lamprey, skate, and zebrafish embryos, sectioning, imaging, and biotapestry modeling

Whole mount *in situ* hybridization was performed using previously published protocols (Gillis et al., 2017; Green et al., 2017; Longabaugh et al., 2005; Simões-Costa et al., 2012). Cryosections of lamprey, skate, or zebrafish embryo *in situs* were sectioned at 18 μm with a *Microm* HM550 *cryostat*. *In situ* analysis of S25 skate embryos sections was performed using paraffin sections as follows: After fixation, embryos were embedded in paraffin and sections were prepared at 5 (skate) or 10 μm (lamprey) thickness on a Zeiss microtome. After paraffin removal with histosol, sections were hybridized with 1 ng/ μl anti-sense digoxigenin-labelled probes overnight at 70°C in a humidifying chamber. After hybridization, sections were washed with 50% formamide/50% 1X SSCT buffer followed by washes with MABT and a blocking step in 1% Roche blocking reagent. Sections were

then incubated overnight at room temperature with a 1:2000 dilution of anti-DIG-Alkaline Phosphatase antibody (Roche). After several washes with MABT, chromogenic color was developed using NBT/BCIP precipitation (Roche). Imaging was performed on a Zeiss AxioImager.M2 equipped with an Apotome.2. Gene network models were assembled using Biotapestry (Longabaugh et al., 2005).

3.7.4 Chicken embryo electroporation, dissociated, and cell sorting

Cranial and trunk neural crest cells were labeled using previously published neural crest enhancers FoxD3-NC1.1 and FoxD3-NC2, respectively (Simões-Costa et al., 2012). To isolate cranial neural crest cells, stage Hamburger Hamilton (HH) 4 embryos were bilaterally electroporated with FoxD3-NC1.1>eGFP and cultured *ex ovo* until stage HH9+ (Hamburger and Hamilton, 1951). For each biological replicate, at least 15 embryo heads were dissected in Ringers and washed thrice in chilled 1x PBS. For trunk neural crest cells, stage HH10 embryos were bilaterally electroporated with FoxD3-NC2>eGFP and cultured *in ovo* until stage HH18. Based on the expression of the reporter, five embryo trunks spanning the length of five somites were dissected in Ringers and washed thrice in chilled 1x PBS. The tissues were dissociated in Accumax (Innovative Cell Technologies, Inc.) for 15 minutes at 37°C and GFP+ cells were collected using Fluorescence Activated Cell Sorting.

3.7.5 Library preparation and sequencing

Chicken libraries were prepared using the SMART-Seq Ultra Low Input RNA Kit (Takara) according to the manufacturer's protocol. For lamprey embryos, tissue was dissected from the cranial dorsal neural tubes of T21 and trunk neural tube of T23.5 embryos. Total RNA was extracted using the RNAqueous kit (Ambion). RNA-seq was performed at 50 million reads on 2 biological replicates for both the T21 cranial and T23.5 trunk neural tube samples. Sequencing libraries were built according to Illumina standard protocols. SR50 sequencing was performed in a HiSeq Illumina machine. Databases have been deposited to NCBI (BioProject # PRJNA497902).

3.7.6 Statistical analysis of lamprey and chicken axial population RNA-seq

To identify orthologous genes between lamprey and chicken, the lamprey proteome obtained from SIMRbase (Smith et al., 2018) was aligned to the chicken proteome using the BLAT alignment software available on the UCSC genome browser (Karolchik et al., 2003; Kent, 2002). Briefly, every lamprey protein sequence was locally queried against the chicken proteome, following which regions with the longest alignment were matched to the respective chicken gene. Using this alignment-based approach, proteins with an alignment percentage score between 52-100 were identified as orthologues, and their respective cDNA sequences were obtained from the chicken and lamprey databases. Chicken cranial and trunk libraries were aligned to the chicken sequences, while the lamprey cranial and trunk libraries were aligned to the lamprey sequences using Bowtie2 (Langmead and Salzberg, 2012). Transcript counts were calculated using HTSeq-Count and differential gene expression analysis was performed using DESeq2 (Anders et al., 2015; Love et al., 2014). Using chicken gene annotations as a reference, we added the transcript counts for duplicated orthologues found in the lamprey genome to calculate an “aggregated” transcript count for each gene. These aggregated transcript counts were then normalized using the formula:

$$Z_i = \frac{T_i - \min(T)}{\max(T) - \min(T)}$$

where Z_i – Normalized transcript count,

T_i – Absolute transcript count.

A subset of genes previously identified as being part of the neural crest gene regulatory network (Martik and Bronner, 2017) was then isolated from the count matrix and plotted as a heatmap to obtain the gene expression matrix.

3.7.7 Data and code availability

All sequencing data is available online (NCBI BioProject# PRJNA497902). Sequences of *in situ* probe templates for Figures 1B, 1C, 2A, and 2C are available through this BioProject. All raw sequencing files for all RNA-seq libraries [Figure 3] are available through this BioProject as well. Code used to analyze sequencing datasets is available from the corresponding author upon request.

3.8 References

Anders, S., Pyl, P.T., and Huber, W. (2015). HTSeq—a Python framework to work with high-throughput sequencing data. *Bioinformatics* 31, 166–169.

Betancur, P., Bronner-Fraser, M., and Sauka-Spengler, T. (2010). Genomic code for Sox10 activation reveals a key regulatory enhancer for cranial neural crest. *Proc. Natl Acad. Sci. USA* 107, 3570–3575.

Davidson, E.H., and Erwin, D.H. (2006). Gene regulatory networks and the evolution of animal body plans. *Science* 311, 796–797.

Le Douarin, N.M. (1982). *The Neural Crest* (Cambridge University Press).

Le Douarin, N.M., and Smith, J. (1988). Development of the peripheral nervous system from the neural crest. *Annu. Rev. Cell Biol.* 4, 375–404.

Gans, C., and Northcutt, R.G. (1983). Neural crest and the origin of vertebrates: a new head. *Science* 220, 268–273.

Gillis, J.A., Alsema, E.C., and Criswell, K.E. (2017). Trunk neural crest origin of dermal denticles in a cartilaginous fish. *Proc. Natl Acad. Sci. USA* 114, 13200–13205.

Glenn Northcutt, R. (2005). The new head hypothesis revisited. *J. Exp. Zool. Part B Mol. Dev. Evol.* 304B, 274–297.

Green, S.A., Simões-Costa, M., and Bronner, M.E. (2015). Evolution of vertebrates as viewed from the crest. *Nature* 520, 474–482.

Green, S.A., Uy, B.R., and Bronner, M.E. (2017). Ancient evolutionary origin of vertebrate enteric neurons from trunk-derived neural crest. *Nature* 544, 88–91.

Haldin, C.E., and LaBonne, C. (2010). SoxE factors as multifunctional neural crest regulatory factors. *Int. J. Biochem. Cell Biol.* 42, 441–444.

Hamburger, V., and Hamilton, H.L. (1951). A series of normal stages in the development of the chick embryo. *J. Morphol.* 88, 49–92.

Häming, D., Simões-Costa, M., Uy, B., Valencia, J., Sauka-Spengler, T., and Bronner-Fraser, M. (2011). Expression of Sympathetic Nervous System Genes in Lamprey Suggests Their Recruitment for Specification of a New Vertebrate Feature. *PLoS One* 6, e26543.

Karolchik, D., Baertsch, R., Diekhans, M., Furey, T.S., Hinrichs, A., Lu, Y.T., Roskin, K.M., Schwartz, M., Sugnet, C.W., Thomas, D.J., et al. (2003). The UCSC Genome Browser Database. *Nucleic Acids Res.* 31, 51–54.

Kent, W.J. (2002). BLAT-The BLAST-Like Alignment Tool. *Genome Res.* 12, 656–664.

Langmead, B., and Salzberg, S.L. (2012). Fast gapped-read alignment with Bowtie 2. *Nat. Methods* 9, 357–359.

Lee, E.M., Yuan, T., Ballim, R.D., Nguyen, K., Kelsh, R.N., Medeiros, D.M., and McCauley, D.W. (2016). Functional constraints on SoxE proteins in neural crest development: The importance of differential expression for evolution of protein activity. *Dev. Biol.* 418, 166–178.

Longabaugh, W.J.R., Davidson, E.H., and Bolouri, H. (2005). Computational representation of developmental genetic regulatory networks. *Dev. Biol.* 283, 1–16.

Love, M.I., Huber, W., and Anders, S. (2014). Moderated estimation of fold change and dispersion for RNA-seq data with DESeq2. *Genome Biol.* 15.

Martik, M.L., and Bronner, M.E. (2017). Regulatory logic underlying diversification of the neural crest. *Trends Genet.* 33, 715–727.

McCauley, D.W., and Bronner-Fraser, M. (2006). Importance of SoxE in neural crest development and the evolution of the pharynx. *Nature* 441, 750–752.

Meulemans, D., and Bronner-Fraser, M. (2002). Amphioxus and lamprey AP-2 genes: Implications for neural crest evolution and migration patterns. *Development* 129, 4953–4962.

Nikitina, N., Sauka-Spengler, T., and Bronner-Fraser, M. (2008). Dissecting early regulatory relationships in the lamprey neural crest gene network. *Proc. Natl Acad. Sci. USA* 105, 20083–20088.

Nikitina, N., Bronner-Fraser, M., and Sauka-Spengler, T. (2009). Culturing lamprey embryos. *Cold Spring Harb. Protoc.* 4.

Parker, H.J., Bronner, M.E., and Krumlauf, R. (2014). Hox regulatory network of hindbrain segmentation is conserved to the base of vertebrates. *Nature* 514, 490–493.

Parker, H.J., Bronner, M.E., and Krumlauf, R. (2016). The vertebrate Hox gene regulatory network for hindbrain segmentation: Evolution and diversification: Coupling of a Hox gene regulatory network to hindbrain segmentation is an ancient trait originating at the base of vertebrates H. J. Parker et al. *BioEssays* 38, 526–538.

Sauka-Spengler, T., and Bronner-Fraser, M. (2008). Evolution of the neural crest viewed from a gene regulatory perspective. *Genesis* 46, 673–682.

Sauka-Spengler, T., Meulemans, D., Jones, M., and Bronner-Fraser, M. (2007). Ancient Evolutionary Origin of the Neural Crest Gene Regulatory Network. *Dev. Cell* 13, 405–420.

Simões-Costa, M., and Bronner, M.E. (2016). Reprogramming of avian neural crest axial identity and cell fate. *Science* *352*, 1570–1573.

Simões-Costa, M., McKeown, S.J., Tan-Cabugao, J., Sauka-Spengler, T., and Bronner, M.E. (2012). Dynamic and differential regulation of stem cell factor FoxD3 in the neural crest is encrypted in the genome. *PLoS Genet.* *8*, e1003142.

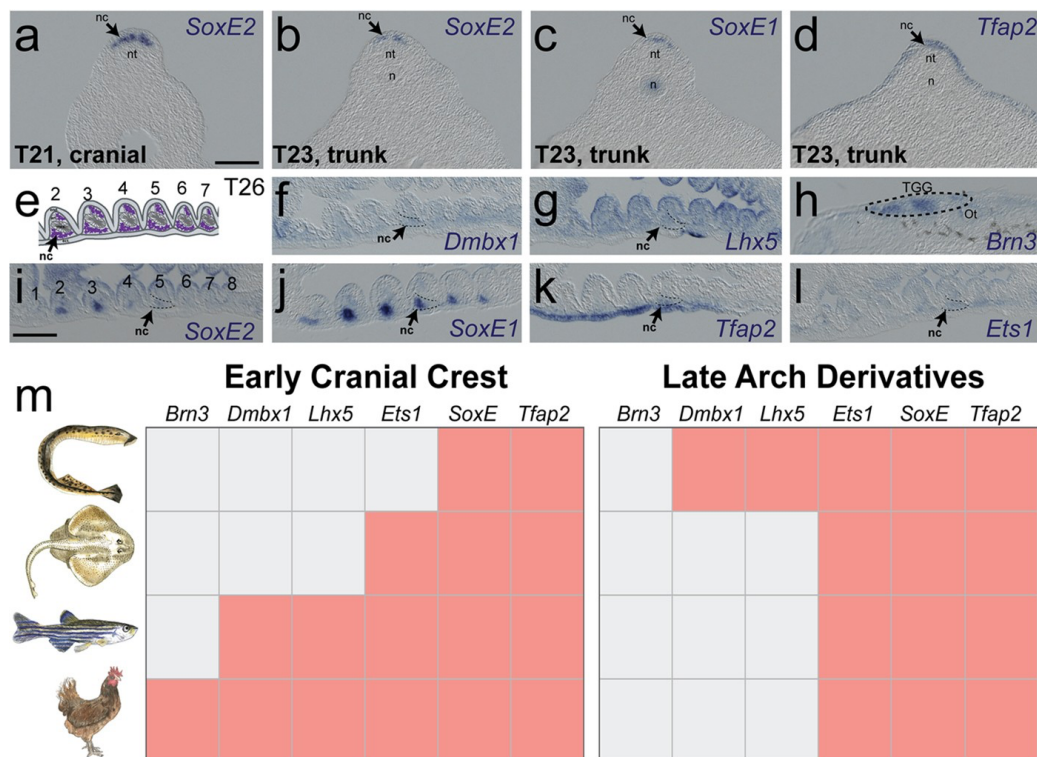
Smith, J.J., Timoshevskaya, N., Ye, C., Holt, C., Keinath, M.C., Parker, H.J., Cook, M.E., Hess, J.E., Narum, S.R., Lamanna, F., et al. (2018). The sea lamprey germline genome provides insights into programmed genome rearrangement and vertebrate evolution. *Nat. Genet.* *50*, 270–277.

Takahashi, T., and Holland, P.W.H. (2004). Amphioxus and ascidian Dmbx homeobox genes give clues to the vertebrate origins of midbrain development. *Development* *131*, 3285–3294.

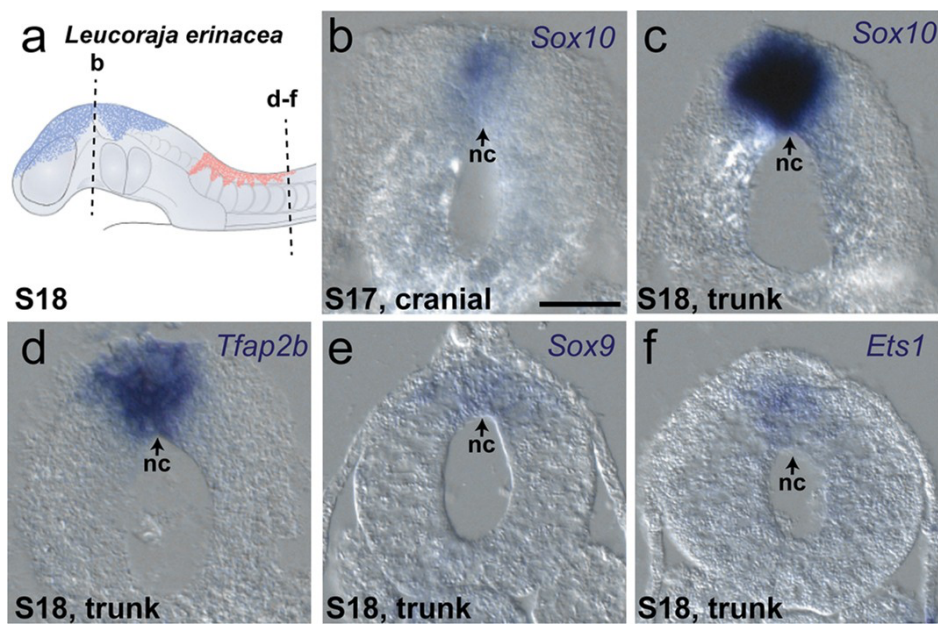
Wada, H., Kobayashi, M., and Zhang, S. (2005). Ets identified as a trans-regulatory factor of amphioxus Hox2 by transgenic analysis using ascidian embryos. *Dev. Biol.* *285*, 524–532.

Yu, J.K., Meulemans, D., McKeown, S.J., and Bronner-Fraser, M. (2008). Insights from the amphioxus genome on the origin of vertebrate neural crest. *Genome Res.* *18*, 1127–1132.

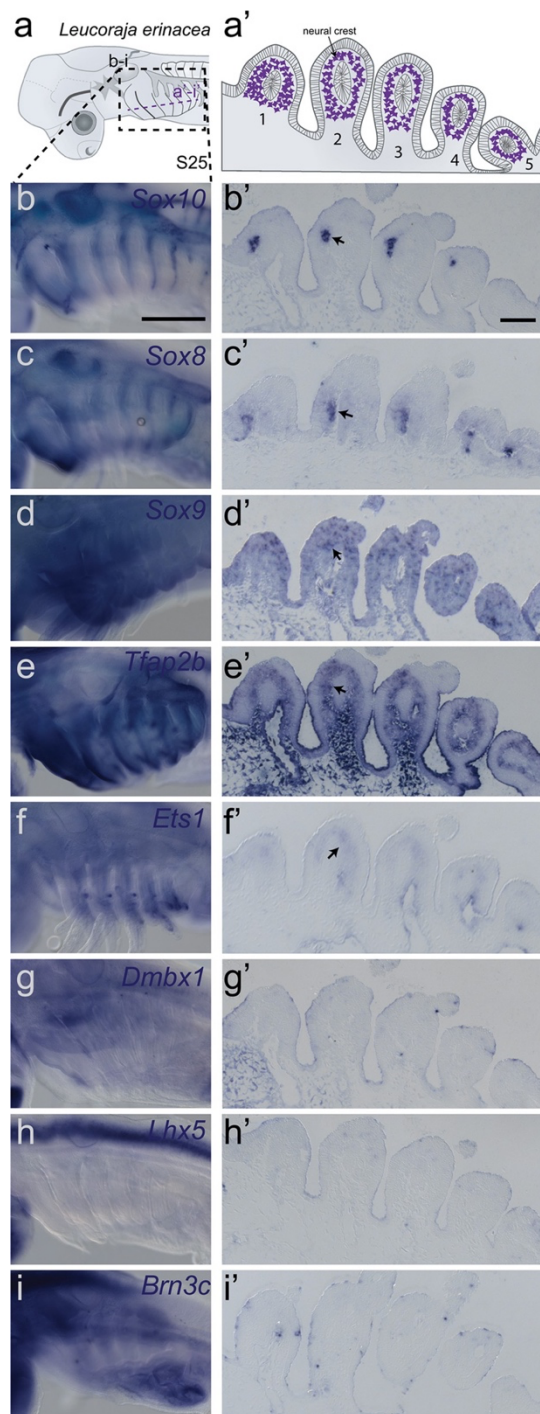
3.9 Supplementary Figures



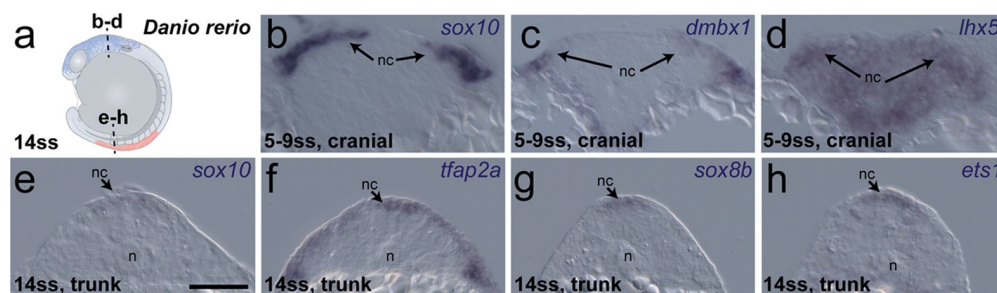
Supplementary Figure 1. Heterochronic shifts of cranial specific gene regulatory nodes from later neural crest derivatives to an early specification program happened gradually throughout gnathostome evolution. a-d, Expression of lamprey orthologues of amniote cranial specific genes at T21 (cranial) and T23 (trunk) in cross-section. **e,** Pharyngeal neural crest derivative expression in Tahara stage 26 *Petromyzon marinus* frontal section (illustration based on (Damas, 1944)). **f-l,** Cranial circuit orthologues are expressed in pharyngeal arch derivatives, with the exception of *Brn3* which is present in the neural crest-derived cranial sensory ganglia (Modrell et al., 2014) in lamprey frontal sections. **m,** Gene expression matrix summarizing the heterochronic shift of cranial crest specific circuit nodes. nc=neural crest, nt= neural tube, n=notochord, end.=endoderm, ect.=ectoderm, mes.=mesoderm. Scale bars= 100 μ m.



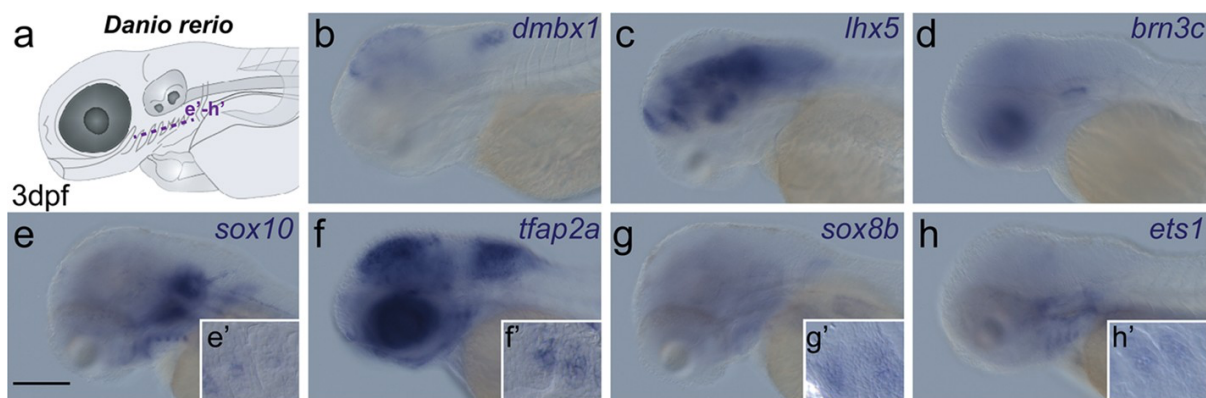
Supplementary Figure 2. Expression of cranial circuit genes in the neural crest of the little skate. **a**, Schematic of a stage 18 *Leucoraja erinacea* embryo with the neural crest illustrated as blue (cranial) and red (trunk). **b-f**, Cross-sections as depicted in **a**. nc=neural crest, scale bar= 50 μ m.



Supplementary Figure 3. Pharyngeal neural crest derivative expression of cranial circuit orthologues in stage 25 *Leucoraja erinacea* embryos. **a**, Dashed box on the illustration represents the region of the head for each embryo imaged in figures b-i, and the purple dashed line depicts the location of the frontal section for figures a'-i'. **b-f'**, Pharyngeal neural crest derivative expression of cranial circuit orthologues. **g-i'**, *Dmbx1*, *Lhx5*, and *Brn3c* are absent in pharyngeal arch derivatives at stage 25. b-i, scale bar=500µm. b'-i', scale bar= 100µm.



Supplementary Figure 4. Expression of cranial circuit genes in the neural crest of the zebrafish. **a**, Schematic of a 14ss *D. rerio* embryo with the NC illustrated as blue (cranial) and red (trunk). **b–h**, Cross-sections as shown in **a**. Scale bars, 50 μm .



Supplementary Figure 5. Expression of cranial circuit orthologues in pharyngeal neural crest derivatives of 3dpf *D. rerio* embryos. **a**, Schematic of head of zebrafish embryo at 3 days post fertilization (dpf). Purple dashed line depicts the location of the frontal sections for the insets in **e–h**. **e–h**, Expression of cranial circuit orthologues in pharyngeal arches. **b–d**, *Dmbx1*, *Lhx5*, and *Brn3c* are absent from pharyngeal arch derivatives at 3 dpf. Scale bar, 150 μm .

Chapter 4

CRISPR-Cas9-mediated gene knockouts in avian embryos

A modified version of this chapter was published as:

Gandhi, S., Piacentino, M.L., Vieceli, F.M., and Bronner, M.E. (2017). Optimization of CRISPR/Cas9 genome editing for loss-of-function in the early chick embryo. *Dev. Biol.* 432, 86–97.

<https://doi.org/10.1016/j.ydbio.2017.08.036>

4.1 Introduction

Chick embryos have long been used as a model organism to address important questions in developmental biology due to their accessibility to transplantation, surgical ablations, and other genetic perturbations. This has allowed researchers to regulate gene expression in a spatiotemporally controlled manner at diverse stages of development (Darnell and Schoenwolf, 2000; Streit et al., 2013). Traditionally, loss-of-function experiments have utilized anti-sense morpholinos (Corey and Abrams, 2001), dominant-negative constructs, or shRNAs (Sauka-Spengler and Barembaum, 2008). However, these techniques are transient, becoming diluted by cell proliferation during development, and there have been increasing concerns regarding possible lack of specificity due to either off-target effects or reagent toxicity (Eisen and Smith, 2008; Gerety and Wilkinson, 2011; Kok et al., 2015; Schulte-Merker and Stainier, 2014).

One alternative to these approaches is CRISPR-Cas9 (Clustered Regularly Interspaced Short Palindromic Repeats/CRISPR-Associated protein 9), a revolutionary technology that has enabled efficient knockout of target genes across a wide range of model organisms (Cong et al., 2013; Dickinson et al., 2013; Gagnon et al., 2014; Ren et al., 2014; Stolfi et al., 2014). CRISPR-Cas9 involves the formation of a complex between guide RNA (gRNA) and Cas9, an endonuclease enzyme derived from *Streptococcus pyogenes*, which then binds to specific targets in the genome. Once bound to genomic DNA, this complex introduces double-stranded breaks that are imperfectly repaired by Non-Homologous End Joining repair enzymes, often leading to a frame-shift insertion or deletion, and subsequent truncation and/or degradation of the target transcript (Jinek et al., 2012; Qi et al., 2013; Sternberg et al., 2014). Specificity is achieved through Watson-Crick base pairing between the protospacer domain of the gRNA and the target locus in the genome, together with recognition of a Protospacer Adjacent Motif (PAM) by Cas9. Not only does CRISPR-Cas9 offer high spatiotemporal specificity (Stolfi et al., 2014), but it also enables investigation of the roles of non-coding genetic elements such as enhancers and insulators in regulating gene expression during development (Diao et al., 2016; Han et al., 2014; Korkmaz et al., 2016; Lopes et al., 2016; Thakore et al., 2015).

In spite of all its advantages, the CRISPR-Cas9 system has not been fully optimized for application in chick embryos. Early attempts at implementation in avian embryos employed a tetracycline-inducible Cas9 system to perform gene editing of Pax7 using Tol-2 mediated integration at stages after neural tube closure (Véron et al., 2015). While useful, this approach functioned at low efficiency, particularly at early developmental stages (Bai et al., 2016; Oishi et al., 2016; Véron et al., 2015). Since then, several studies performed in other model systems have reported optimizations of individual CRISPR-Cas9 components, improving our understanding of this gene-editing technology (Chen et al., 2013; Doench et al., 2016; Gandhi et al., 2017; Port et al., 2014; Ren et al., 2014).

To extend the usefulness of this technique to the early chick embryo, we have adapted an optimized CRISPR-Cas9 system for efficient genome editing by implementing three modifications. First, we used a previously characterized Cas9 protein flanked with two nuclear localization sequences (NLS) for enhanced compartmentalization in the nucleus (Chen et al., 2013; Stolfi et al., 2014). Second, we used a modified gRNA “F+E” scaffold that has been shown to resolve issues including premature termination of RNA Polymerase-III-mediated transcription of the gRNA cassette and unstable interaction between Cas9 protein and transcribed gRNA (Chen et al., 2013; Orioli et al., 2011). Third, we improved gRNA expression by using a chick-specific U6 promoter that outperforms a human U6 promoter in chick embryos (Cong et al., 2013; Kudo and Sutou, 2005; Wise et al., 2007).

In the present study, we demonstrate the efficiency of this improved CRISPR-Cas9 system by performing functional testing in the avian neural crest. The neural crest is a multipotent cell population that originates at the neural plate border, then migrates extensively throughout the embryo to give rise to numerous cell types (Le Douarin and Kalcheim, 1982; Green et al., 2015; Simões-Costa and Bronner, 2015). We test the ability of our optimized CRISPR-Cas9 system to knock out key transcription factors in the neural crest, including the neural plate border specifier Pax7 (Basch et al., 2006), and the neural crest specifier Sox10 (Betancur et al., 2010; Carney et al., 2006). The results show that

our CRISPR-Cas9 system is robust and reproducible as a means for knocking out genes of interest in chicken embryos.

4.2 Results and Discussion

4.2.1 Optimizing CRISPR-Cas9 components for application in chick embryos

As a first step, we cloned a previously published human codon-optimized *spCas9* (Qi et al., 2013) flanked with an NLS sequence on both the N- and C-terminus under the regulation of the chicken beta-actin promoter (CAGG) (Alexopoulou et al., 2008) to ensure optimal nuclear localization of Cas9 protein *in vivo* [Figure 1A]. It was previously shown that two NLS sequences are necessary for proper nuclear localization of Cas9 protein (Chen et al., 2013). Co-electroporation of Cas9 (*CAGG>nls-Cas9-nls*) with *CAGG>H2B-RFP* and a control gRNA (*U6.3>Control.gRNA.f+e*), followed by immunostaining for Cas9 protein, demonstrated effective nuclear localization in transfected cells [Figure 1B-D]. Second, we cloned all protospacer sequences targeting genes of interest in a previously modified gRNA 'F+E' scaffold [Figure 1E] that contains a "flipped" (F) Adenine-Uracil pair downstream of the protospacer domain and an "extended" (E) Cas9 stem handle (Chen et al., 2013). These modifications were shown to improve RNA polymerase III-mediated gRNA transcription by minimizing the possibility of premature termination of transcription, as well as stabilize the interaction between Cas9 protein and the transcribed gRNA, respectively (Chen et al., 2013; Stolfi et al., 2014). Third, we tested different RNA Polymerase III-mediated promoters for their ability to drive gRNA expression in transfected cells *in vivo*. Although most CRISPR knockout experiments performed in mammalian systems have used a human U6 promoter to govern gRNA expression (Jinek et al., 2013; Mali et al., 2013; Wang et al., 2014), species-specific U6 promoters have been used in non-mammalian model organisms such as zebrafish, Ciona, and Drosophila (Ablain et al., 2015; Nishiyama and Fujiwara, 2008; Port et al., 2014). To that effect, we directly compared gRNA expression levels mediated by the standard human U6 (hU6) promoter with a chicken U6 (cU6.3) promoter.

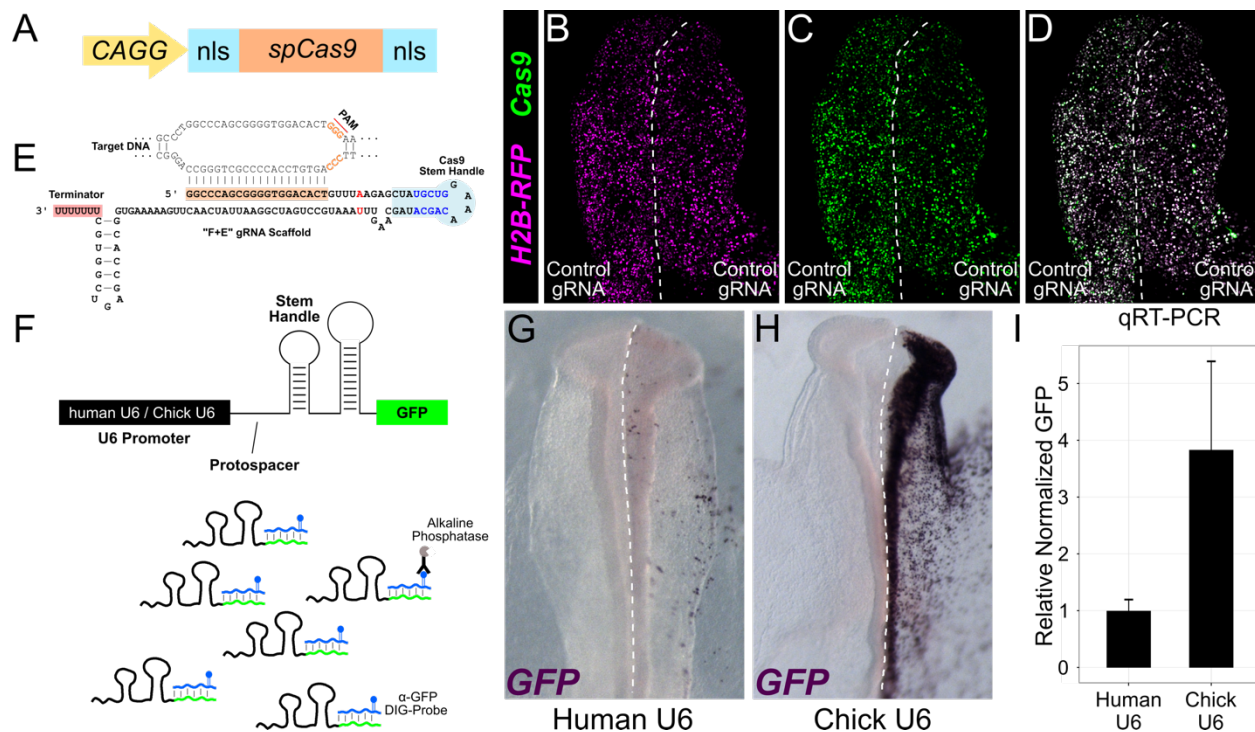


Figure 1. Optimizing individual CRISPR-Cas9 components for application in chick embryos. **A.** Schematic of the Cas9 construct used in this study. Cas9 flanked with two Nuclear Localization Signal (NLS) sequences was cloned under the regulation of the chicken beta actin promoter (*CAGG*). **B-D.** Gastrulating Hamburger Hamilton stage HH4 embryos co-electroporated with *CAGG>nls-Cas9-nls, U6.3>Control.gRNAf+e*, and *CAGG>H2B-RFP*, cultured *ex ovo* until stage HH9, and immunostained for Cas9 demonstrate efficient nuclear localization of Cas9 protein. Dotted line represents the midline of the neural tube. **E.** *Pax7.1* protospacer was cloned into a modified "F+E" scaffold. "F" (flip) modification is marked in red, "E" (extension) modification is marked in blue. Watson-Crick base pairing between the protospacer (highlighted in orange) and the target DNA strand is also shown. **F.** Design for the U6 promoter optimization assay. Human and chicken U6 promoters were tested for their ability to drive expression of a modified gRNA cassette in which the terminator domain was replaced with GFP (see Materials and methods for details). Transcripts synthesized through RNA Polymerase III-mediated transcription included the entire GFP sequence, which was then used for qualitative (*in situ* hybridization) and quantitative (qRT-PCR) assessment of promoter efficacy. DIG – Digoxigenin. **G-H.** The right side of stage HH4 chicken embryos was electroporated with the construct described in F. The embryos were cultured *ex ovo* until stage HH9-10, after which they were fixed and processed for *in situ* hybridization against GFP. The signal obtained in embryos electroporated with the chicken U6 promoter construct (n=3) was stronger than in embryos electroporated with the human U6 promoter construct (n=3). Dotted line represents the midline of the embryo. **I.** qRT-PCR primers specific to GFP were used to quantify the 4-fold increase in activity of the chicken U6 promoter relative to the human counterpart (n=3 for each group). Error bars represent standard error of the means.

To this end, we electroporated the right side of gastrulating chick embryos at Hamburger Hamilton stage 4 (HH4) (Hamburger and Hamilton, 1992) with different *U6-variant>bCat.gRNA.f+e.NoTermGFP* constructs [Figure 1F; see Materials and methods for details], and allowed embryos to develop until stage HH9-10. A reporter (*CAGG>H2B-RFP*) was co-electroporated to normalize electroporation variability between embryos.

Using *in situ* hybridization against GFP, we observed increased gRNA transcription with the chicken U6.3 promoter variant compared with the hU6 promoter [Figure 1G-H]. After isolating RNA and reverse-transcribing cDNA from three biological replicates electroporated with the two variants, we performed quantitative RT-PCR (qRT-PCR) using primers specific to GFP. The results confirmed our *in situ* hybridization analysis, showing that the chicken-specific U6.3 promoter resulted in a 4-fold increase in gRNA transcription compared to a human U6 promoter used in previous studies [Figure 1I]. The chicken U6.3 promoter variant also outperformed an additional chick U6 promoter (data not shown), demonstrating that intra-species variability should be considered when selecting promoters to drive expression of small RNA molecules. Taken together, our results identify chicken-specific U6.3 promoter as an improvement over previously used human U6 promoters for gRNA transcription, and highlight the importance of U6 promoter selection for subsequent loss-of-function studies.

In addition to improving the U6 promoter for delivery of gRNA, we incorporated a screening step into our gRNA design strategy to help eliminate the possibility of off-target effects. Multiple groups have previously highlighted design principles that correlate directly with the activity of the gRNA *in vivo* (Cho et al., 2014; Gandhi et al., 2017; Tsai et al., 2015). To simplify our gRNA design, we considered these principles and employed the MIT CRISPR program (<http://crispr.mit.edu>) for initial target site selection. When presented with multiple protospacer sequences, those with high scoring alignments outside the desired locus were discarded. As such, all gRNAs used for functional analysis in this study were designed to avoid off-target gRNA sites, thereby minimizing non-specific effects.

4.2.2 CRISPR-Cas9-mediated knockout of key neural crest genes

To establish proof of principle, we first used our optimized CRISPR system to target the transcription factor Pax7 in chick embryos. Pax7 is one of the earliest markers of the neural plate border, and its loss using a translation-blocking morpholino results in a significant decrease in neural crest markers such as *Snai2*, *Sox9*, and *FoxD3* (Basch

et al., 2006; Labosky and Kaestner, 1998; Simões-Costa and Bronner, 2015; Simões-Costa et al., 2012). We designed a gRNA targeting the splice acceptor site of the second exon of Pax7 [Figure 2A] and expressed it under the regulation of the optimized chicken U6.3 promoter (*U6.3>Pax7.1.gRNAf+e*).

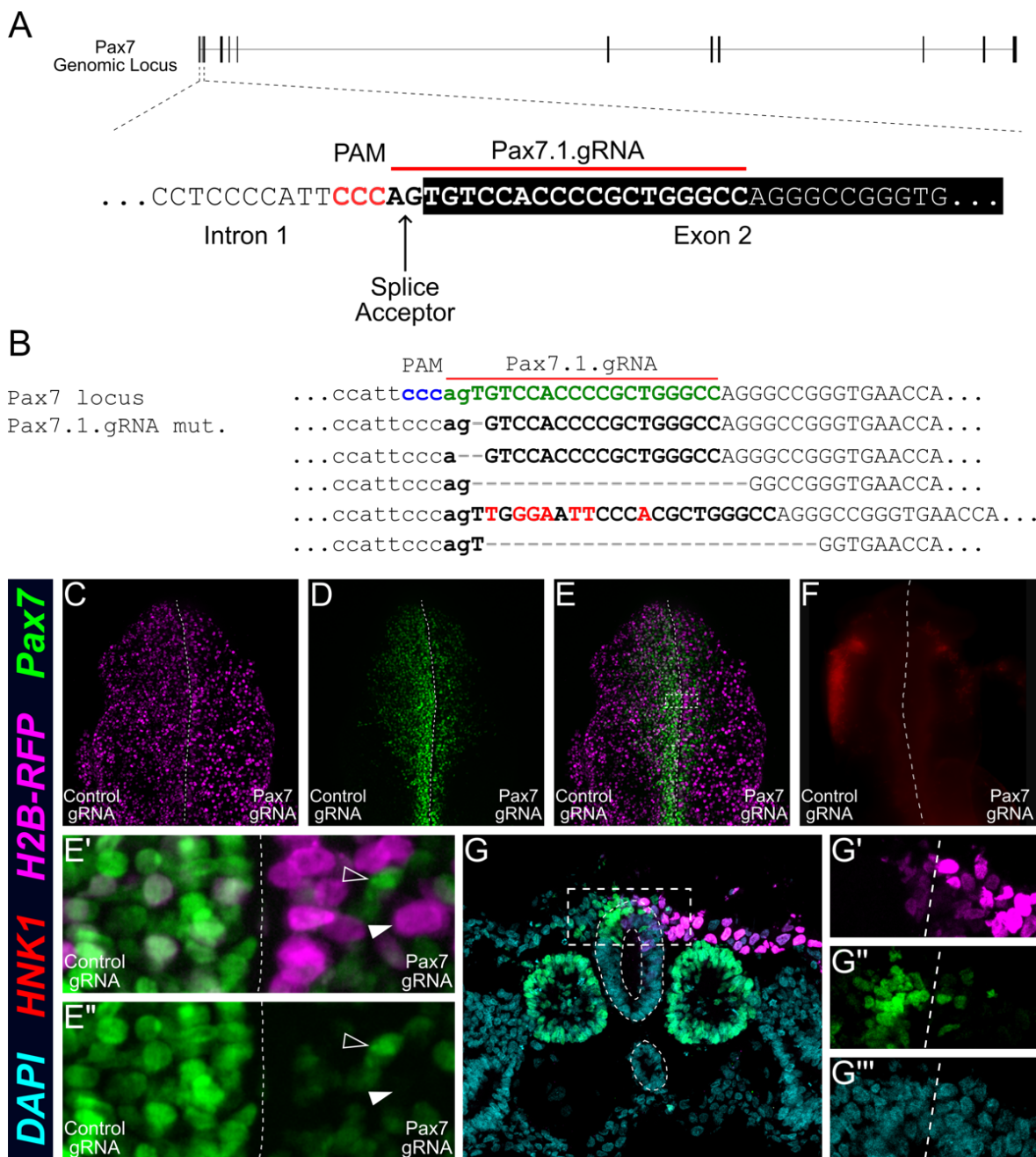


Figure 2. See next page for legend.

Figure 2. CRISPR-Cas9-mediated knockout of Pax7. **A.** (Top) The *G. gallus Pax7* gene contains 12 exons (black solid boxes). (Bottom) Nucleotide sequence surrounding the splice junction of exon 2 with the Protospacer Adjacent Motif (PAM) marked in red, and the *Pax7.1.gRNA* protospacer sequence highlighted with a red bar. **B.** Genotyping of Pax7 knockout cells isolated from HH10 chicken embryos following electroporation of Pax7-targeting CRISPR reagents identified multiple mutations that would result in a splicing error or frameshift in the predicted protein. **C.** Stage HH4 embryos were electroporated with *U6.3>Control.gRNAf+e* and *U6.3>Pax7.1.gRNAf+e* on the left and right side, respectively, along with *CAGG>nls-Cas9-nls* and *CAGG>H2B-RFP* on both sides, then cultured *ex ovo* until stage HH10. Dotted line represents midline of the neural tube. **D.** CRISPR-Cas9-mediated knockout of Pax7 resulted in a dramatic decrease in Pax7 protein level as assessed by immunostaining (n=21/21). **E.** Overlay of RFP (red) and Pax7 (green) channels revealed that all RFP+ (solid arrowhead) cells were Pax7-, indicating that all transfected cells lost Pax7 protein. Conversely, untransfected cells (E', E'') retained endogenous Pax7 expression (empty arrowhead), suggesting that the protein levels in transfected cells on the right side of the embryo were lost as a result of CRISPR-Cas9-mediated activity. **F.** Embryos were cultured until stage HH10 and immunostained for migratory neural crest expression of HNK1. HNK1 levels on the Pax7 knockout side were considerably reduced compared to the internal control, consistent with the role of Pax7 upstream of migratory neural crest formation. **G.** Another stage HH4 embryo unilaterally electroporated with *U6.3>Pax7.1.gRNAf+e*, *CAGG>nls-Cas9-nls* and *CAGG>H2B-RFP* on the right side was cultured *ex ovo* until stage HH9 and stained for RFP and Pax7. Nuclei were labeled using DAPI stain. Transverse sectioning through this embryo revealed a nearly complete loss of Pax7 expression in the neural tube (dotted line). The zoomed-in images of the dorsal neural tube show high transfection rate (RFP+ cells; G'), loss of Pax7 on the right side (Pax7- cells; G''), and unaffected nuclear morphology (DAPI+ nuclei, G''').

To confirm CRISPR-mediated genomic editing at the desired locus, we co-electroporated *U6.3>Pax7.1.gRNAf+e* along with *CAGG>nls-Cas9-nls* and *CAGG>H2B-RFP* bilaterally, and harvested embryos at stage HH10. Embryos were dissociated to isolate RFP+ cells by flow cytometry, which were then used to prepare genomic DNA for genotyping. The target locus was PCR-amplified and sequenced to identify CRISPR-induced mutations. As expected, a range of different insertion (red) and deletion (gray) mutations were identified in the gRNA target sequence [Figure 2B], demonstrating that the Cas9 protein used in this study can induce targeted genomic mutations. We next co-electroporated the Pax7-targeting gRNA (*U6.3>Pax7.1.gRNAf+e*) along with *CAGG>nls-Cas9-nls* and *CAGG>H2B-RFP* on the right side of gastrulating stage HH4 embryos, and then cultured these until developmental stage HH9+ [Figure 2C]. The left side was electroporated with a control gRNA that has no recognition sites in the chick genome (*U6.3>Control.gRNAf+e*) and served as an internal control. Immunostaining using a Pax7 antibody revealed downregulation of Pax7 protein level on the side electroporated with *Pax7.1* gRNA compared to the control side [Figure 2D], consistent with the anticipated splicing errors and/or frame shifts following Cas9-induced mutations. When overlaying RFP and Pax7 channels, we observed that all cells that were successfully transfected

with the H2B-RFP plasmid showed no detectable Pax7 protein compared to the control side, where transfected neural crest cells were double-positive for RFP and Pax7 [Figure 2E, E', E'']. This was particularly interesting because Pax7 is expressed in the neural plate border as early as stage HH4+ (Basch et al., 2006; Roellig et al., 2017). Given that several hours after electroporation are required for the production of Cas9 protein after electroporation (Stolfi et al., 2014), this suggests that the half-life of Pax7 protein is short enough for our CRISPR-Cas9 system to cause loss of Pax7 protein expression within 14 hours. To confirm that loss of Pax7 would manifest itself in a loss of the neural crest migration phenotype, we co-immunostained stage HH10 embryos for HNK1, a surface antigen that has traditionally been used as a marker for migratory neural crest cells (Basch et al., 2006). As expected, we saw a strong loss of HNK1 expression on the Pax7 knockout side of the embryo compared to the control side [Figure 2F], suggesting that loss of Pax7 protein resulted in the failure of neural crest specification and, ultimately, migration. In other embryos, we co-electroporated *CAGG>nls-Cas9-nls* and *U6.3>Pax7.1.gRNAf+e* unilaterally on the right side at stage HH4, and allowed the embryos to develop until stage HH9. Transverse sections through a representative embryo revealed an almost complete loss of Pax7 expression in the dorsal neural tube [Figure 2G-2G'']. Looking more closely at this region, we saw that the number of cells, as assessed by 4,6-diamidino-2-phenylindole (DAPI) staining, appeared unchanged [Figure 2G''']. This suggests that the loss in Pax7 expression was a result of CRISPR-Cas9-mediated modification of the *Pax7* locus, and that the concentration of plasmids electroporated in the embryo did not result in cellular toxicity.

Once we verified efficient reduction in protein levels, we asked whether this effect reflects the presence of fewer transcripts of target genes following CRISPR-Cas9-mediated mutations. To test this, we designed a gRNA targeting the start codon of Sox10 [Figure 3A], a transcription factor expressed in the migrating neural crest [Figure 3C] that plays a critical role in the migratory neural crest gene regulatory network (Betancur et al., 2010; Carney et al., 2006; Ghislain et al., 2003). We began by co-electroporating *CAGG>nls-Cas9-nls*, *U6.3>Sox10.1.gRNAf+e*, and *CAGG>H2B-RFP* bilaterally in stage

HH4 embryos, and genotyping RFP⁺ cells sorted by flow cytometry as described above for the Pax7 locus. Similar to Pax7, we identified several mutations surrounding the Sox10 target sequence [Figure 3B]. We co-electroporated *CAGG>nls-Cas9-nls*, *U6.3>Sox10.1.gRNAf+e*, and a reporter *CAGG>H2B-RFP* on the right side of a stage HH4 embryo. The left side was electroporated with *U6.3>Control.gRNAf+e* and served as an internal control. Embryos were cultured *ex ovo* until stage HH9-10, then processed for *in situ* hybridization.

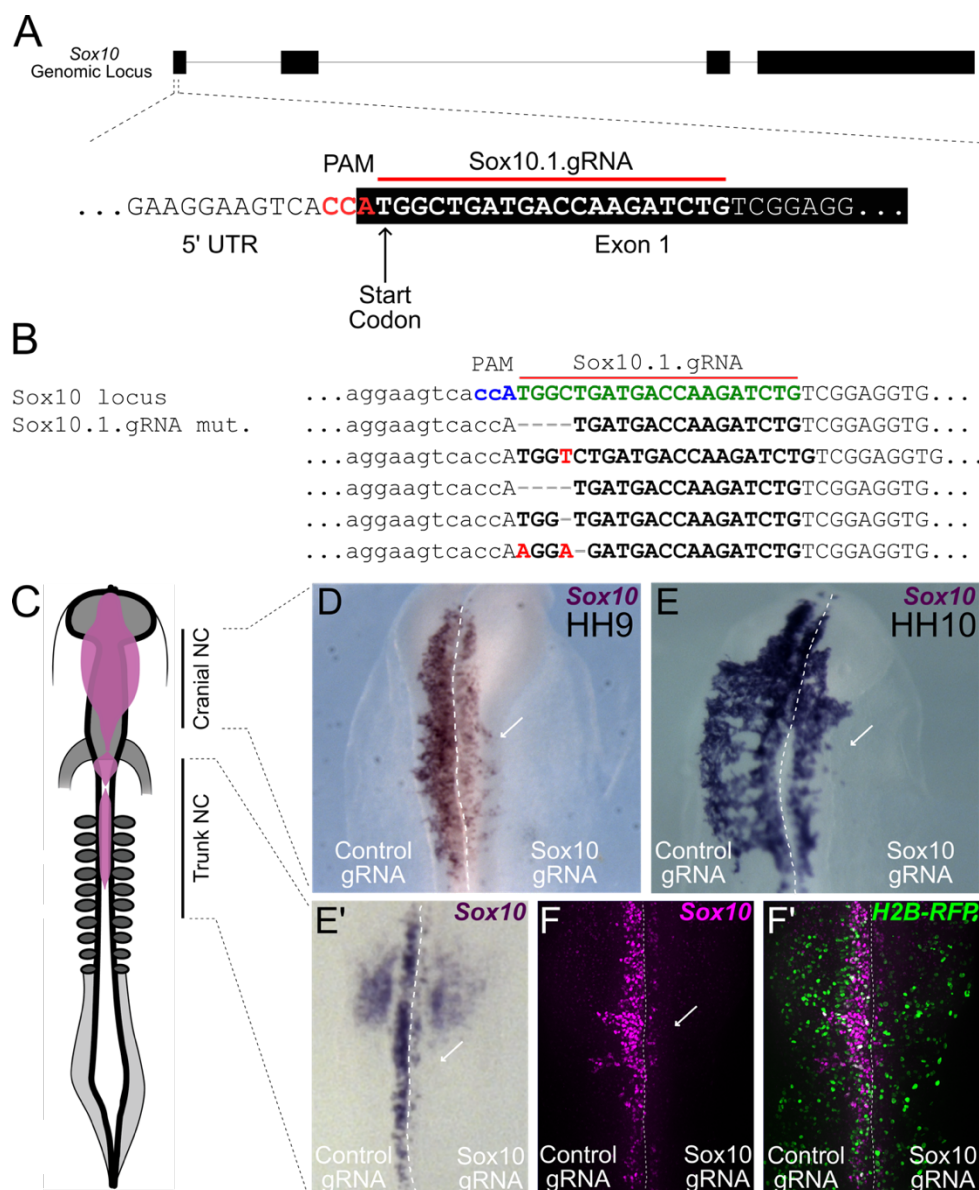


Figure 3. See next page for legend.

Figure 3. CRISPR-Cas9-mediated knockout of Sox10. **A.** (Top) Schematic of the *G. gallus Sox10* gene, which contains 4 exons (black solid boxes). (Bottom) Nucleotide sequence surrounding the Sox10 start codon, with the PAM marked in red, and the *Sox10.1.gRNA* protospacer sequence highlighted with a red bar. **B.** Genotyping of Sox10 knockout cells isolated from HH10 chicken embryos following electroporation of Sox10-targeting CRISPR reagents identified multiple mutations that would result in a splicing error or frameshift in the predicted protein. **C.** A cartoon model of a stage HH10 chicken embryo with the Sox10-expressed migratory cranial and vagal neural crest (highlighted in violet). Stage HH4 embryos were electroporated with *U6.3>Control.gRNAf+e* and *U6.3>Sox10.1.gRNAf+e* on the left and right side, respectively, along with *CAGG>nls-Cas9-nls* and *CAGG>H2B-RFP* on both sides, then cultured *ex ovo* until stage HH9-10, after which they were processed for *in situ* hybridization against Sox10. **D-E.** Reduced Sox10 expression levels were observed at stage HH9 in the emigrating cranial neural crest cells (D) and at stage HH10 in the migratory cranial neural crest cells (E). **E'.** Expression of Sox10 (embryo described in E) was reduced in the vagal neural crest and in the otic placode. Notably, the right side shows a nearly complete loss of Sox10 expression in the neural crest. **F.** Another stage HH4 embryo electroporated with *U6.3>Control.gRNAf+e* and *U6.3>Sox10.1.gRNAf+e* on the left and right side, respectively, along with *CAGG>nls-Cas9-nls* and *CAGG>H2B-RFP* on both sides, was cultured *ex ovo* until stage HH10, and then immunostained for Sox10 and RFP. The right side shows a nearly complete loss of Sox10 protein compared to the left side control (n=9/9), indicating that CRISPR-Cas9-mediated mutations at the Sox10 locus affected both transcript and protein levels. **F'.** Expression of Sox10 is detected in RFP⁺ transfected neural crest cells on the control side, whereas the transfected cells on the right side are Sox10⁻.

The results revealed a substantial decrease in Sox10 transcript levels on the side electroporated with the *Sox10.1* gRNA [Figure 3D, E], both in the neural crest and in the otic placode [Figure 3E'] (Betancur et al., 2011). The loss of transcripts detected by *in situ* hybridization is consistent with the degradation of mutant transcripts by nonsense-mediated decay (Losson and Lacroute, 1979). To confirm that the effect on Sox10 transcripts was reflected at the Sox10 protein level, we immunostained for Sox10 protein in embryos electroporated using the same strategy. We observed a nearly complete loss of Sox10 in the right side of the embryo following *Sox10.1* gRNA electroporation [Figure 3F, F']. Similarly, knockout of Pax7 caused a near complete loss of Pax7 transcripts [Figure 4A]. Taken together, these results show that our CRISPR-Cas9 system is highly robust at causing loss of function of target genes.

4.2.3 Establishing epistatic relationships using CRISPR-Cas9

The ability to knock out genes of interest is particularly important when constructing gene regulatory networks underlying developmental events. To demonstrate that CRISPR-Cas9 can be used to interrogate regulatory relationships between genes, we examined the effects of knocking out Pax7 and Sox10 on other neural crest transcription

factors. To this end, we co-electroporated *CAGG>nls-Cas9-nls*, *CAGG>H2B-RFP*, and control *U6.3>Control.gRNAf+e* on the left side with Pax7-targeting *U6.3>Pax7.1.gRNAf+e* or Sox10-targeting *U6.3>Sox10.1.gRNAf+e* on the right side of gastrulating stage HH4 embryos. The embryos were cultured *ex ovo* until stage HH9-10 and then processed for *in situ* hybridization for *Pax7*, *FoxD3*, *Ets1*, and *Sox10* [Figure 4A]. Pax7 knockout resulted in reduced staining for *Pax7*, *FoxD3*, *Ets1*, and *Sox10*

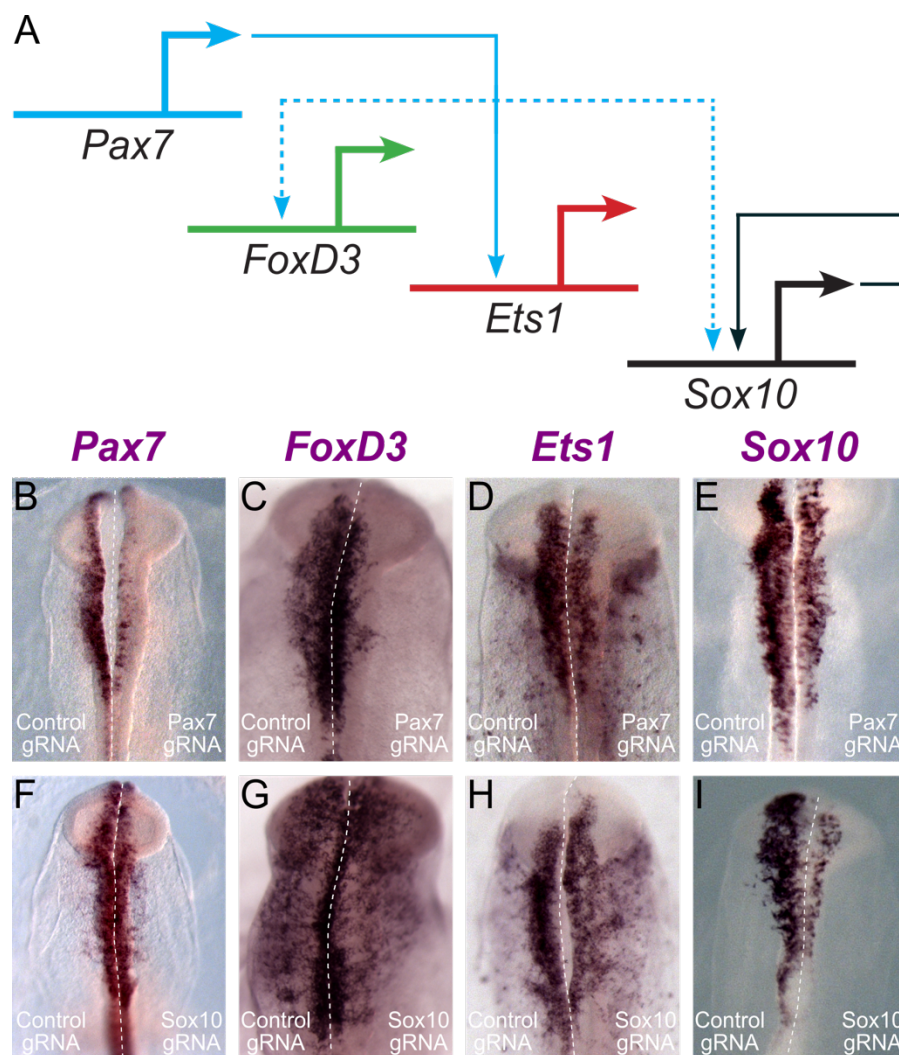


Figure 4. Application of CRISPR-Cas9 to study epistatic relationships. **A.** A gene regulatory network model derived from previous studies shows regulatory interactions between key neural crest transcription factors. **B-I.** Gastrulating embryos were electroporated with *CAGG>nls-Cas9-nls*, *CAGG>H2B-RFP*, *U6.3>Control.gRNAf+e* on the left and either *U6.3>Pax7.1.gRNAf+e* (B-E) or *U6.3>Sox10.1.gRNAf+e* (F-I) on the right side, cultured until stage HH9-10, then processed for *in situ* hybridization for *Pax7* (B, F), *FoxD3* (C, G), *Ets1* (D, H), and *Sox10* (E, I). Pax7 loss resulted in reduced expression of each downstream target in the neural crest (B-E), while Sox10 loss had no effect on the expression of its upstream regulators (F-I).

transcripts in the migratory neural crest [Figure 4B-E]. On the other hand, knockout of *Sox10* caused a loss of its own expression, but as expected had no effect on *Pax7*, *FoxD3* or *Ets1* [Figure 4F-I], all of which are expressed prior to *Sox10* and upstream in the neural crest GRN. Thus, these results recapitulate previously demonstrated gene regulatory interactions (Simões-Costa and Bronner, 2015) and confirm that *Pax7* acts as an upstream regulator of *FoxD3*, *Ets1*, and *Sox10*, whereas *Sox10* expression is downstream of these transcription factors and its subsequent loss does not affect expression of its upstream regulators.

To further test the ability of CRISPR-Cas9 to decipher direct gene regulatory interactions, we examined the effects of *Pax7* loss on one of its direct transcriptional targets, *FoxD3*. We have previously shown that *Pax7* directly regulates activity of *FoxD3* at cranial levels by binding to the NC1 enhancer element upstream of the *FoxD3* coding sequence (Simões-Costa et al., 2012) [Figure 5A]. To confirm this epistatic relationship, we asked if knocking out *Pax7* using CRISPR-Cas9 would reduce exogenous *FoxD3* NC1 enhancer activity. To this end, we co-electroporated *CAGG>nls-Cas9-nls*, *U6.3>Pax7.1.gRNAf+e*, and *FoxD3-NC1.1>eGFP* reporter construct containing a constitutively active version of the *FoxD3-NC1* enhancer on the right side of stage HH4 embryos [Figure 5B]. The left internal control side was co-electroporated with *CAGG>nls-Cas9-nls*, *FoxD3-NC1.1>eGFP*, and *U6.3>Control.gRNAf+e*. After electroporation, embryos were cultured *ex ovo* until stage HH9-9⁺. Consistent with the observed *Pax7* knockout detected by immunostaining [Figure 5C], the level of eGFP expression was reduced on the side of the embryo that was electroporated with *Pax7.1* gRNA compared to the control side [Figure 5D], validating the requirement of *Pax7* for the activation of the *FoxD3-NC1* enhancer. While the exogenous reporter activity through the NC1 enhancer was effectively lost, we further hypothesized that the absence of a transcriptional input from *Pax7* would result in reduced endogenous *FoxD3* protein levels. To test this, we electroporated stage HH4 embryos with *U6.3>Pax7.1.gRNAf+e* and *U6.3>Control.gRNAf+e* on the right and left side respectively, along with *CAGG>nls-*

Cas9-nls and *CAGG>H2B-RFP* on both sides; cultured embryos until stage HH9+; and collected cell lysates for immunoblotting.

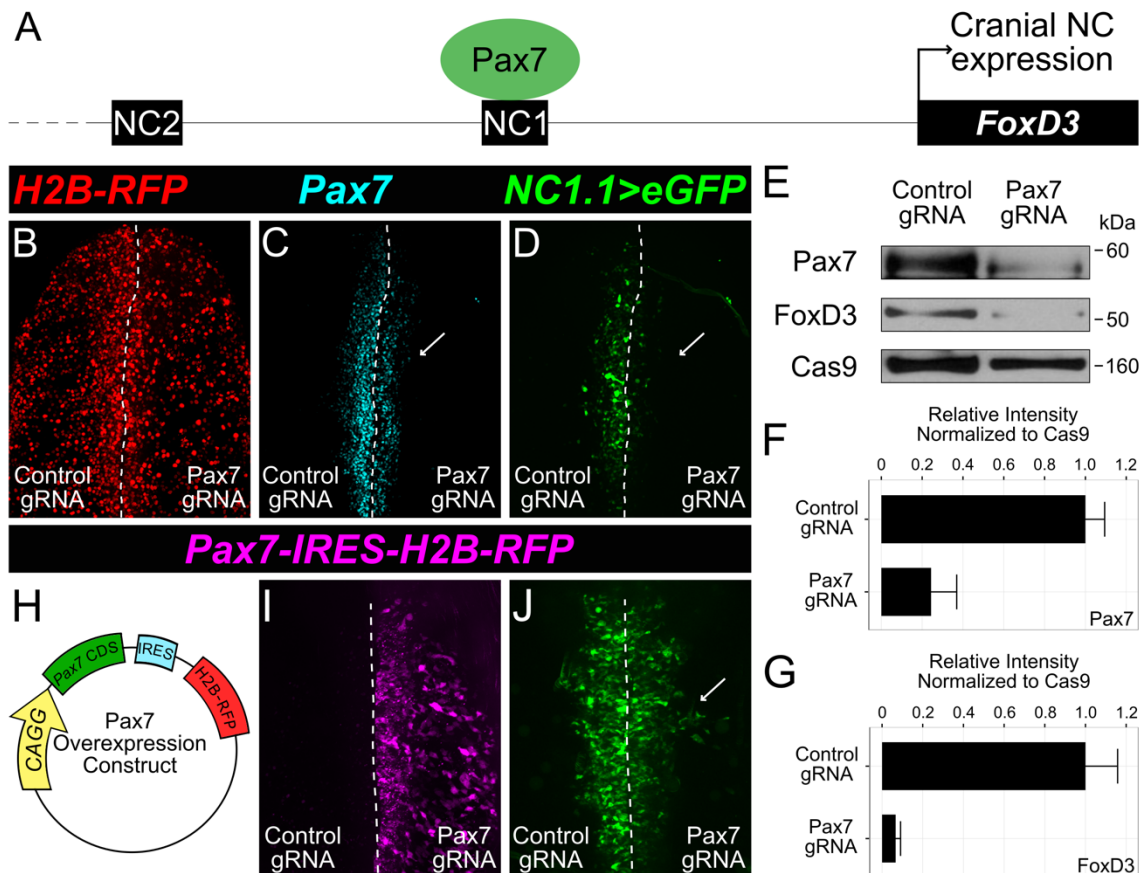


Figure 5. CRISPR-Cas9 allows investigation of direct gene regulatory interactions. **A.** Pax7 regulates the expression of FoxD3 by direct transcriptional input into the NC1 enhancer. The expression pattern in cranial neural crest cells is reproduced by strong expression from the mutated *FoxD3-NC1.1* enhancer. **B-D.** Stage HH4 embryos were co-electroporated with *U6.3>Control.gRNAf+e* and *U6.3>Pax7.1.gRNAf+e* on the left and right side, respectively, along with *CAGG>nls-Cas9-nls*, *FoxD3-NC1.1>GFP*, and *CAGG>H2B-RFP* on both sides. Embryos were cultured *ex ovo* until stage HH9-9+, and reduced Pax7 level was verified using immunostaining (C). The *FoxD3-NC1.1* enhancer driven expression of eGFP was almost completely lost on the side that was electroporated with *U6.3>Pax7.1.gRNAf+e* (D, arrow), recapitulating the previously published epistatic relationship between Pax7 and FoxD3. **E.** Knockout embryos were cultured until stage HH9+ and dissected along the midline. Whole cell lysates were isolated from the two groups, and immunoblots were performed using antibodies against Pax7, FoxD3, and Cas9. **F-G.** Quantitative western blot analysis normalized to Cas9 demonstrates efficient reduction in Pax7 and FoxD3 protein levels following Pax7 knockout when compared to control reagents ($n=3$ technical replicates). **H-J.** We overexpressed Pax7 using *CAGG>Pax7CDS-IRES-H2B-RFP* (H), and co-electroporated this construct with *CAGG>nls-Cas9-nls*, *U6.3>Pax7.1.gRNAf+e*, and *FoxD3-NC1.1>GFP* reporter on the right side of stage HH4 embryos (I-J). The left side was electroporated with control reagents. Overexpression of Pax7 rescued the activity of the *FoxD3-NC1.1* enhancer (J), demonstrating the specificity of Pax7 knockout mediated by our optimized CRISPR-Cas9 system. Error bars represent standard error of the means.

Consistent with our hypothesis, both Pax7 and FoxD3 protein levels were significantly reduced on the side electroporated with the Pax7-targeting gRNA [Figure 5E]. Quantification of these data revealed a 4-fold and 15-fold decrease in the levels of Pax7 and FoxD3 protein, respectively [Figure 5F, G], on the side electroporated with the Pax7-targeting gRNA compared to the control side. Taken together, these results demonstrate the applicability of our optimized CRISPR-Cas9 system for investigating direct epistatic relationships among different genes.

The “gold standard” control for demonstrating specificity in loss-of-function experiments is to perform a rescue that recovers function when the lost protein is exogenously supplied. To extend this to our CRISPR-Cas9 system, we asked if we could restore *FoxD3-NC1.1* enhancer activity after Pax7 knockout by over-expressing Pax7 exogenously. To this end, we electroporated the coding sequence of Pax7 under the control of a basal promoter (*CAGG>Pax7CDS-IRES-H2B-RFP* (Roellig et al., 2017)) [Figure 5H] along with *CAGG>nls-Cas9-nls*, *U6.3>Pax7.1.gRNAf+e*, and *FoxD3-NC1.1>eGFP* on the right side of stage HH4 embryos [Figure 5I]. The left side was electroporated with *U6.3>Control.gRNAf+e* and served as an internal control. The PAM adjacent to the *Pax7.1* gRNA target site lies in the first intron, and hence would be missing from the Pax7 coding sequence. Since identification of the PAM is essential for Cas9 binding, we predicted that our Pax7 overexpression construct would not be recognized by the Cas9-Pax7.1.gRNA complex. Embryos were developed until stage HH9-10, after which they were imaged for *FoxD3-NC1.1* enhancer driven eGFP reporter expression. The activity of the *FoxD3-NC1.1* enhancer appeared similar on both the control and experimental sides of the embryo [Figure 5J], indicating that exogenous Pax7 rescued the CRISPR-Cas9-mediated loss of endogenous Pax7 protein, and consequently, the *FoxD3-NC1.1* reporter activity, thereby demonstrating specificity. Taken together, these results suggest that our optimized CRISPR system is specific in causing functional gene knockouts at target loci in the chicken genome and demonstrate the functionality of this approach in ordering gene regulatory interactions.

4.2.4 Rapid screening of gRNAs using a Cas9-integrated chicken DF-1 fibroblast cell line

Validating individual gRNAs for knocking out genes *in vivo* using CRISPR-Cas9 can be cumbersome and as a result continues to be one of the potential limitations of designing CRISPR-Cas9 experiments in chick embryos. Although we have reported a simple sorting-based protocol to quantify gRNA efficacy *in vivo*, we sought to develop a simpler strategy to overcome the need for cell sorting. To this end, we have modified the chicken DF-1 fibroblast cell line to constitutively express Cas9 that has been integrated in the genome using a Tol2-flanked CAGGS-driven *Cas9-2A-Puro^R* cassette and *T2TP* transposase (Sato et al., 2007) [Figure 6A]. We validated the constitutive nuclear expression of Cas9 by immunostaining using an antibody against Cas9, followed by DAPI counterstaining [Figure 6B-D]. Interestingly, the expression level was variable in different cells, suggesting that the transposase-mediated genomic integration events were distinct. Once we verified the stable integration of Cas9 in DF-1 cells, we used this system to assay the efficacy of gRNAs for *in vivo* application in embryos. To this end, we transfected Cas9-integrated DF-1 cells with gRNAs targeting the genomic loci of genes *Pax7* and *Sox10* using gRNAs described in previous sections (*U6.3>Pax7.1.gRNAf+e* or *U6.3>Sox10.1.gRNAf+e*). As a control for transfection and to calculate the transfection rate, we also transfected a different well of cells with *CAGG>H2B-RFP*. After 48 hours of incubation, we isolated genomic DNA from the *Pax7* and *Sox10*-targeted cells for genotyping. As expected, both gRNAs generated mutations around the gRNA targeting site for the two genes [Figure 6E-F] that would have resulted in a splicing error and/or frameshift in the coding sequence. Importantly, the efficacy rates for the two gRNAs from unsorted DF-1 cells were consistent with the results obtained from sorted chick embryo cells [Figure 2B, 3B]. Taken together, these results demonstrate the utility of our Cas9-DF-1 cell line in simplifying the experimental designs for future CRISPR-Cas9 knockout experiments in chick embryos.

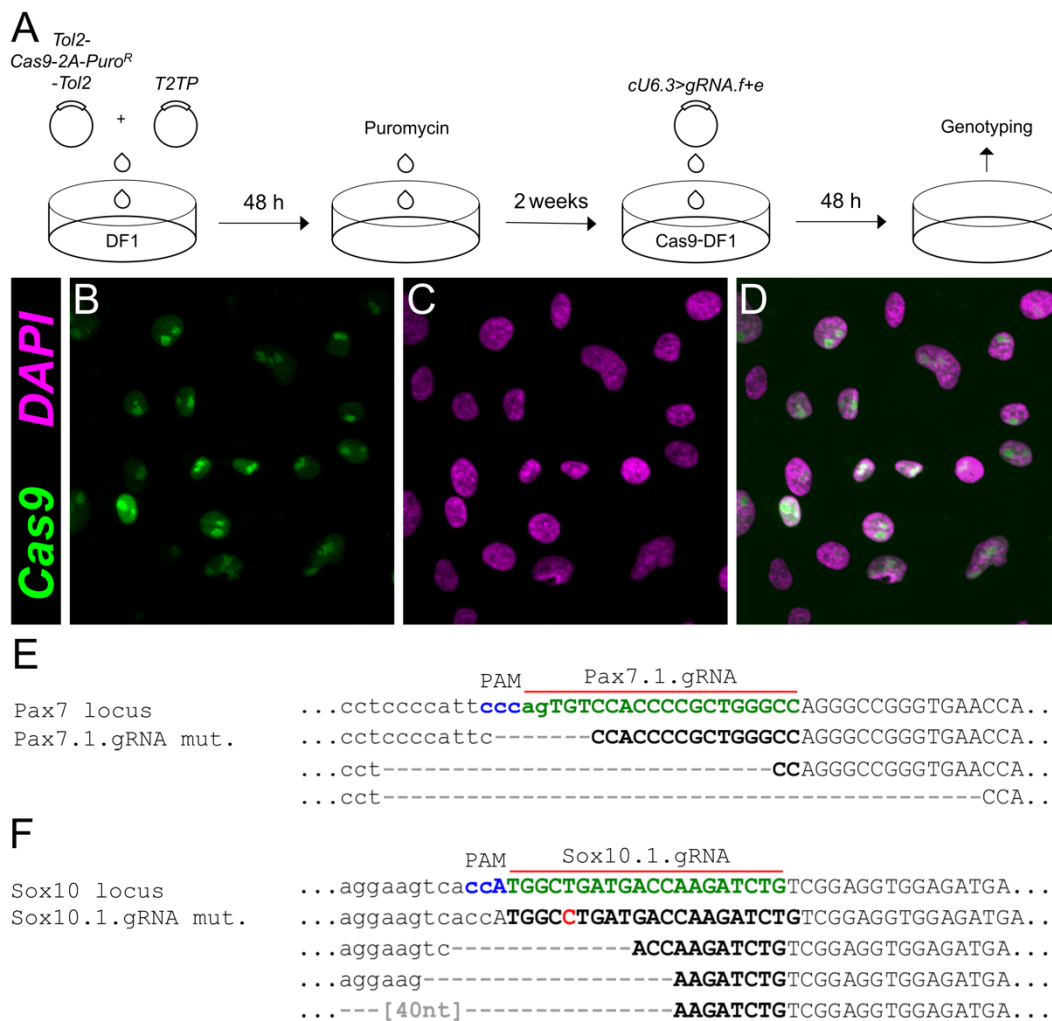


Figure 6. Construction of a Cas9-DF1 fibroblast cell line to validate gRNAs. **A.** The strategy employed to stably integrate a *Cas9-2A-Puro^R* in chicken DF-1 fibroblasts using a T2TP transposase to access gRNA efficacy for *in vivo* applications. Cells were transfected with the two constructs and grown for 48 hours before the first round of selection on puromycin. gRNA plasmids were transfected using a simple lipofectamine-based protocol. **B-D.** After puromycin selection, the cells were immunostained for Cas9 to validate its stable integration and constitutive expression in the cells. Overlay of Cas9 (green) expression with DAPI (magenta) revealed its proper nuclear localization in the cell line. **E-F.** Genotyping of Cas9-DF1 cells following transfection with Pax7 (E) and Sox10 (F) targeting gRNA plasmids identified multiple mutations that would result in a splicing error or frameshift in the predicted protein *in vivo*.

4.3 Conclusions

In summary, here we demonstrate the application of the CRISPR-Cas9 system for effective somatic cell genome editing in chicken embryos. The chick embryo offers many advantages for analysis of gene function in amniotes *in vivo* because of its accessibility,

ease of manipulation, and low cost. Moreover, the ability to perform bilateral electroporations enables an internal control within a single embryo. In the past, loss-of-function studies have relied upon morpholinos, dominant negatives, or RNAi approaches, all of which are transient, and thus useful for relatively short-term analysis. Although morpholinos offer a rapid and efficient method to block translation or splicing, concerns regarding the possibility of toxicity and off-target effects make it important to consider alternative approaches. To this end, we optimized our Cas9 and gRNA expression plasmids by incorporating three modifications: first, by employing two NLS sequences for higher nuclear expression of Cas9 protein (Chen et al., 2013); second, by using a modified gRNA (“F+E”) scaffold to enhance *in vivo* gRNA transcription (Chen et al., 2013; Stolfi et al., 2014); and third, by using a species-specific chicken U6 promoter. In addition, we have generated a Cas9-DF1 cell line that greatly streamlines the process of gRNA design for knockout experiments in chick embryos. The results highlight the robustness and reproducibility of this modified CRISPR-Cas9 system for generating loss-of-function in chick embryos in a manner that can be applied to many developmental processes, including protein functional analysis and the dissection of gene regulatory interactions.

4.4 Acknowledgments

We would like to thank Alberto Stolfi from Lionel Christiaen’s lab (New York University) and Chao-Yuan Yeh from Cheng-Ming Chuong’s lab (University of Southern California) for reagents, Erica Hutchins for technical assistance, Yuwei Li, Meyer Barembaum and the rest of the Bronner lab for valuable discussions on the project, Elena K. Perry for helpful comments on the manuscript, the Caltech Biological Imaging Facility for technical assistance on imaging, and Jamie Tijerina with the Caltech Flow Cytometry Facility for assistance with flow cytometry.

4.5 Author contributions

S.G. and M.E.B. conceived this study. S.G., M.L.P., F.M.V., and M.E.B. designed the experiments. S.G., M.L.P., and F.M.V performed the experiments and analyzed the results. S.G., M.L.P., and M.E.B. wrote the manuscript.

4.6 Funding

This work was partially supported by the National Institutes of Health (NIH) grants R01 DE024157 to M.E.B. and F32 HD088022 to M.L.P., and the Brazilian National Council for Scientific and Technological Development grant PDE 207656/2014-2 to F.M.V.

4.7 Materials and methods

4.7.1 Molecular cloning

The Pax7 and Sox10 genomic loci were obtained from the UCSC genome browser (Karolchik et al., 2003). The initial set of gRNA targets was designed by searching these loci for the motif G-<N20>-GG. Protospacer sequences overlapping with splice junctions were preferred over ones within coding sequences. The *Gallus gallus 5.0* genome assembly available on the UCSC genome browser was used to screen for polymorphisms. Using this approach, we generated the gRNA targets used in this study: Pax7 (GGCCCAGCGGGGTGGACACT), Sox10 (GAGATCTTGGTCATCAGCCA). We also designed a control gRNA with a protospacer sequence not found in the chicken genome (GCACTGCTACGATCTACACC). Previously described design principles (Doench et al., 2014; Gandhi et al., 2017; Moreno-Mateos et al., 2015) were followed when choosing between multiple gRNA targets for the same gene to avoid off-target effects. All protospacers were cloned into a modified gRNA “F+E” backbone, which was a gift from Lionel Christiaen (Addgene plasmid # 59986). The human codon-optimized Cas9 was obtained as a gift from Lionel Christiaen (Addgene plasmid # 59987). *nls-Cas9-nls* was PCR amplified using High-Fidelity Phusion polymerase (NEB) and inserted downstream of the chicken beta-actin promoter (CAGG). Our gRNA and Cas9 vectors can be obtained through Addgene (https://www.addgene.org/Marianne_Bronner/).

For the U6 promoter optimization assay, the “*gRNA.f+e*” backbone was PCR amplified to remove the terminator sequence from the 3’ end of the scaffold. This amplicon was fused to the 5’ end of GFP using overlap PCR, and this entire cassette was then

cloned downstream of the human U6 and chicken U6.3 promoter (gift from Chao-Yuan Yeh at the Cheng-Ming Chuong lab).

For qRT-PCR, following electroporation with the human and chicken U6 promoter constructs, RNA was extracted using the RNAqueous kit (Ambion). cDNA strands were synthesized using SuperScript III Reverse Transcriptase (Invitrogen) using random hexamers, and stored at -20°C. Primers for qRT-PCR against GFP were (for 5'-AAGCTGACCCTGAAGTTCATCTGC-3', rev 5'-CTTGTAGTTGCCGTCGTCCTTGAA-3').

4.7.2 Electroporation

Fertilized chicken embryos were obtained from local farmers, and were electroporated at stage HH4 using previously described techniques (Sauka-Spengler and Barembaum, 2008). For Pax7 and Sox10 knockout experiments, the right side of the embryos were electroporated with $2\mu\text{g}/\mu\text{L}$ *CAGG>nls-Cas9-nls*, $1.5\mu\text{g}/\mu\text{L}$ *U6.3>Pax7/Sox10gRNAf+e*, and $2\mu\text{g}/\mu\text{L}$ *CAGG>H2B-RFP*, while the left side was electroporated with $1.5\mu\text{g}/\mu\text{L}$ *U6.3>Control.gRNAf+e* along with Cas9 and H2B-RFP reporter. For the epistasis experiment, $2\mu\text{g}/\mu\text{L}$ of *FoxD3-NC1.1>eGFP* was electroporated on both sides of the embryo, combined with CRISPR-Cas9 reagents as described above. For overexpression of Pax7, $2\mu\text{g}/\mu\text{L}$ of *CAGG>Pax7CDS-IRES-H2B-RFP* was electroporated on the right side, leaving the other side as control. Electroporated embryos were cultured *ex ovo* in 35mm dishes with 1mL of albumen at 37°C in humidified chambers until the desired Hamburger Hamilton stages were reached (Hamburger and Hamilton, 1992).

4.7.3 Genotyping

Whole embryos were electroporated with *CAGG>nls-Cas9-nls* and *CAGG>H2B-RFP* together with either *U6.3>Pax7.1.gRNAf+e* or *U6.3>Sox10.1.gRNAf+e* at stage HH4, then incubated to stage HH10. Live embryos were dissected in Ringer's solution on ice, washed with sterile PBS, and dissociated with Accumax cell dissociation solution

(EMD Millipore). Dissociation was terminated by addition of Hanks Buffered Saline Solution (HBSS) (Corning) supplemented with 25mM HEPES pH 7.0, 2.5mg/mL BSA Fraction V (Sigma), and 10mM MgCl₂. Cells were then passed through a 40 μ m filter to remove debris, and RFP⁺ cells were then isolated using a Sony Synergy 3200 cell sorter equipped with a 561nm laser (Caltech Flow Cytometry Facility). Cells were pelleted, then genomic DNA was prepared in 20 μ L 1x AccuPrime PCR Buffer II (ThermoFisher). This resuspension was incubated at 95°C for 15 minutes, after which 2.5 μ L of 20 mg/mL Proteinase K was added and the suspension was reincubated at 55°C for 2 hours with frequent pipetting to mix, then heated to 95°C for another 15 minutes. The resulting preparation was used for PCR amplification using AccuPrime High Fidelity Taq Polymerase (ThermoFisher) with Pax7 (for 5'-TAAATCGCGAGGCAATTTCT-3', rev 5'-GTCCCCTCGACCCTACTTTC-3') or Sox10 (for 5'-GGAGATATGTGAGCAGACAGG-3', rev 5'-TTCCATTGACCCGAACAGG-3') locus primers. Amplicons were then PCR purified (QIAGEN) and TA cloned into pGEM T Easy (Promega) for transformation and Sanger sequencing (Laragen).

4.7.4 *In situ* hybridization

Whole mount embryos were fixed in 4% paraformaldehyde for 2 hours at room temperature. Post-fixation, embryos were washed three times in PBS-0.1% Tween, and were serially dehydrated in methanol, after which they were stored at -20°C. *In situ* hybridization for *Sox10* (Betancur et al., 2010), *Pax7* (Basch et al., 2006), *FoxD3* (Kos et al., 2001), and *Ets1* (Barembaum and Bronner, 2013) was performed using a previously described protocol (Acloque et al., 2008). *In situ* hybridization for GFP was performed using a modified protocol which involved incubating the embryos in DNase I (Promega) at 37°C for 1 hour (Arede and Tavares, 2008). The DIG-labeled RNA probe against GFP was a gift from Marcos Simões-Costa.

4.7.5 Immunostaining and Imaging

Whole-mount immunostaining was performed using previously described procedures (Ezin et al., 2009). Briefly, embryos cultured *ex ovo* at 37°C post-

electroporation were fixed in 4% paraformaldehyde in phosphate buffer for 20 minutes at room temperature. Embryos were then washed three times in PBS-0.1% Triton for 5 minutes each, after which they were blocked for 2 hours at room temperature in 5% donkey serum for Pax7 and Sox10 staining, and 5% goat serum for Pax7 and HNK1 co-staining. Embryos were incubated with primary antibody at 4°C for 1 night for Pax7, and 2 nights for Sox10. The concentrations of primary antibodies used were: Pax7 (1:10; Developmental Studies Hybridoma Bank, Iowa city, Iowa), Sox10 (1:250; R&D Systems Cat # AF2864), HNK1 (1:5; Developmental Studies Hybridoma Bank, Iowa city, Iowa), RFP (1:500; MBL Cat # PM005), GFP (1:500; Abcam Cat # Ab290), Cas9 (1:500; Diagenode Cat # C15200216). The signal was detected using secondary antibodies Donkey anti-mouse IgG1 Alexa Fluor 488 and Goat anti-mouse IgG1 Alexa Fluor 488 (for Pax7 and Cas9), Donkey anti-goat IgG1 Alexa Fluor 488 (for Sox10), Goat anti-mouse IgM Alexa Fluor 350 (for HNK1), Donkey anti-rabbit IgG1 Alexa Fluor 594 (for RFP), and Donkey anti-rabbit IgG1 Alexa Fluor 488 (for GFP), respectively, all diluted to 1:500 final concentrations in PBS-0.5% Triton with 5% donkey or goat serum. For DAPI staining, transverse sections were incubated with DAPI (0.1 μ g/mL) for 5 minutes. Whole mount embryos were imaged on a Zeiss Imager M2 with an ApoTome module. Transverse sections were imaged on Zeiss 710 inverted confocal microscope at the Caltech Biological Imaging Facility. All images were processed using FIJI imaging software (Schindelin et al., 2012).

4.7.6 Cryosectioning

Whole mount embryos immunostained for Pax7 and RFP were incubated in 5% sucrose for 2 hours at room temperature, followed by overnight incubation in 15% sucrose. The next day, embryos were incubated in gelatin at 37°C for 6 hours and then mounted in silicone molds before they were frozen in liquid nitrogen and stored at -80°C until sectioning. 12 μ m wide sections were obtained, incubated in PBS for 30 minutes at 37°C to remove gelatin, and processed for imaging.

4.7.7 Western Blots

Stage HH4 gastrulating embryos co-electroporated with *CAGG>nls-Cas9-nls* and *CAGG>H2B-RFP* together with *U6.3>Pax7.1.gRNAf+e* (right) and *U6.3>Control.gRNAf+e* (left) were cultured *ex ovo* until stage HH9+, and the cranial region was dissected in Ringer's. Dissected heads were split at the midline to collect both "Control" and "Treatment" halves, which were homogenized in 8M urea/2.5% Sodium Dodecyl Sulfate (SDS). 10 μ g of total protein from the control and treatment groups was run on a 4-12% polyacrylamide gel (ThermoFisher) and transferred to nitrocellulose for 1h at 100V at 4°C (Amersham Protran Premium 0.2 NC). The membrane was incubated with primary antibodies against Pax7 (1:50), RFP (1:5000), Cas9 (1:5000), and FoxD3 (Santa Cruz; 1:2000) diluted in 5% BSA/TBS-Tween in a sealed bag overnight at 4°C. The membranes were then incubated in secondary antibodies (KPL; α -Mouse 1:15,000; α -Rabbit 1: 30,000) dissolved in 5% milk/TBS-Tween. The Amersham ECL chemiluminescence reagents were used to develop signal, which was then visualized and captured by X-ray autoradiography. Quantification of the films was performed using FIJI (Schindelin et al., 2012).

4.7.8 Cell culture, transfection, and genotyping

Immortalized chicken DF-1 fibroblast cells (ATCC CRL-12203) were cultured at 37°C in 5% CO₂ in DMEM (Corning) supplemented with 10% fetal bovine serum (Gibco) and penicillin/streptomycin (Corning). To generate the Cas9-DF-1 cell line, *Cas9-2A-Puro^R* was cloned into *pT2K-CAGGS* (Sato et al., 2007) using Gibson Assembly (NEB). Cells were transfected in 12-well plates at approximately 80% confluency using Lipofectamine 3000 (Invitrogen). Briefly, each well received 2 μ L of Lipofectamine 3000 reagent, 0.5 μ g of *T2K-CAGG>Cas9-2A-Puro^R*, and 0.5 μ g of *CAGG>T2TP* (Sato et al., 2007), and 2 μ L P3000 reagent following the manufacturer's instructions. Transfected cells were incubated for 48 hours before the media was changed. At this point, the first round of selection was performed by treating the transfected cells with 4 μ g/mL puromycin

(Alfa Aesar) for 6 days, making sure that the media was changed every 48 hours. Selected cells were then passaged twice in 8 days in media containing 4 $\mu\text{g}/\text{mL}$ puromycin to ensure propagation of a pure population of Cas9-integrated DF-1 cells. To test gRNAs, these cells were transfected with 1 μg of *U6.3>Pax7.1.gRNAf+e* or 1 μg of *U6.3>Sox10.1.gRNAf+e* using Lipofectamine 3000 as described above. To validate our transfection protocol, a separate well was transfected with 1 μg of *CAGG>H2B-RFP*. Cells transfected with gRNA plasmids were then reincubated for 48 hours at which point they were washed with sterile PBS, then trypsinized, and genomic DNA was harvested following the QIAGEN DNeasy Blood and Tissue kit instructions. Genotyping was performed as described above.

4.8 References

Ablain, J., Durand, E.M., Yang, S., Zhou, Y., and Zon, L.I. (2015). A CRISPR/Cas9 vector system for tissue-specific gene disruption in zebrafish. *Dev. Cell* 32, 756–764.

Acloque, H., Wilkinson, D.G., and Nieto, M.A. (2008). Chapter 9 In Situ Hybridization Analysis of Chick Embryos in Whole-Mount and Tissue Sections. *Methods Cell Biol.* 87, 169–185.

Alexopoulou, A.N., Couchman, J.R., and Whiteford, J.R. (2008). The CMV early enhancer/chicken beta actin (CAG) promoter can be used to drive transgene expression during the differentiation of murine embryonic stem cells into vascular progenitors. *BMC Cell Biol.* 9, 2.

Arede, N., and Tavares, A.T. (2008). Modified whole-mount in situ hybridization protocol for the detection of transgene expression in electroporated chick embryos. *PLoS One* 3, e2638.

Bai, Y., He, L., Li, P., Xu, K., Shao, S., Ren, C., Liu, Z., Wei, Z., and Zhang, Z. (2016). Efficient genome editing in chicken DF-1 cells using the CRISPR/Cas9 system. *G3 Genes, Genomes, Genet.* 6, 917–923.

Barembaum, M., and Bronner, M.E. (2013). Identification and dissection of a key enhancer mediating cranial neural crest specific expression of transcription factor, *Ets-1*. *Dev. Biol.* *382*, 567–575.

Basch, M.L., Bronner-Fraser, M., and García-Castro, M.I. (2006). Specification of the neural crest occurs during gastrulation and requires *Pax7*. *Nature* *441*, 218–222.

Betancur, P., Bronner-Fraser, M., and Sauka-Spengler, T. (2010). Genomic code for *Sox10* activation reveals a key regulatory enhancer for cranial neural crest. *Proc. Natl Acad. Sci. USA* *107*, 3570–3575.

Betancur, P., Sauka-Spengler, T., and Bronner, M. (2011). A *Sox10* enhancer element common to the otic placode and neural crest is activated by tissue-specific paralogs. *Development* *138*, 3689–3698.

Carney, T.J., Dutton, K.A., Greenhill, E., Delfino-Machín, M., Dufourcq, P., Blader, P., and Kelsh, R.N. (2006). A direct role for *Sox10* in specification of neural crest-derived sensory neurons. *Development* *133*, 4619–4630.

Chen, B., Gilbert, L.A., Cimini, B.A., Schnitzbauer, J., Zhang, W., Li, G.W., Park, J., Blackburn, E.H., Weissman, J.S., Qi, L.S., et al. (2013). Dynamic imaging of genomic loci in living human cells by an optimized CRISPR/Cas system. *Cell* *155*, 1479–1491.

Cho, S.W., Kim, S., Kim, Y., Kweon, J., Kim, H.S., Bae, S., and Kim, J.S. (2014). Analysis of off-target effects of CRISPR/Cas-derived RNA-guided endonucleases and nickases. *Genome Res.* *24*, 132–141.

Cong, L., Ran, F.A., Cox, D., Lin, S., Barretto, R., Habib, N., Hsu, P.D., Wu, X., Jiang, W., Marraffini, L.A., et al. (2013). Multiplex genome engineering using CRISPR/Cas systems. *Science* *339*, 819–823.

Corey, D.R., and Abrams, J.M. (2001). Morpholino antisense oligonucleotides: tools for investigating vertebrate development. *Genome Biol.* *2*, 1015.1-1015.3.

- Darnell, D.K., and Schoenwolf, G.C. (2000). The chick embryo as a model system for analyzing mechanisms of development. *Methods Mol. Biol.* *135*, 25–29.
- Diao, Y., Li, B., Meng, Z., Jung, I., Lee, A.Y., Dixon, J., Maliskova, L., Guan, K.L., Shen, Y., and Ren, B. (2016). A new class of temporarily phenotypic enhancers identified by CRISPR/Cas9-mediated genetic screening. *Genome Res.* *26*, 397–405.
- Dickinson, D.J., Ward, J.D., Reiner, D.J., and Goldstein, B. (2013). Engineering the *Caenorhabditis elegans* genome using Cas9-triggered homologous recombination. *Nat. Methods* *10*, 1028–1034.
- Doench, J.G., Hartenian, E., Graham, D.B., Tothova, Z., Hegde, M., Smith, I., Sullender, M., Ebert, B.L., Xavier, R.J., and Root, D.E. (2014). Rational design of highly active sgRNAs for CRISPR-Cas9-mediated gene inactivation. *Nat. Biotechnol.* *32*, 1262–1267.
- Doench, J.G., Fusi, N., Sullender, M., Hegde, M., Vaimberg, E.W., Donovan, K.F., Smith, I., Tothova, Z., Wilen, C., Orchard, R., et al. (2016). Optimized sgRNA design to maximize activity and minimize off-target effects of CRISPR-Cas9. *Nat. Biotechnol.* *34*, 1–12.
- Le Douarin, N.M., and Kalcheim, C. (1982). *The Neural Crest*.
- Eisen, J.S., and Smith, J.C. (2008). Controlling morpholino experiments: Don't stop making antisense. *Development* *135*, 1735–1743.
- Ezin, A.M., Fraser, S.E., and Bronner-Fraser, M. (2009). Fate map and morphogenesis of presumptive neural crest and dorsal neural tube. *Dev. Biol.* *330*, 221–236.
- Gagnon, J.A., Valen, E., Thyme, S.B., Huang, P., Ahkmetova, L., Pauli, A., Montague, T.G., Zimmerman, S., Richter, C., and Schier, A.F. (2014). Efficient mutagenesis by Cas9 protein-mediated oligonucleotide insertion and large-scale assessment of single-guide RNAs. *PLoS One* *9*, e98186.

Gandhi, S., Haeussler, M., Razy-Krajka, F., Christiaen, L., and Stolfi, A. (2017). Evaluation and rational design of guide RNAs for efficient CRISPR/Cas9-mediated mutagenesis in *Ciona*. *Dev. Biol.* *425*, 8–20.

Gerety, S.S., and Wilkinson, D.G. (2011). Morpholino artifacts provide pitfalls and reveal a novel role for pro-apoptotic genes in hindbrain boundary development. *Dev. Biol.* *350*, 279–289.

Ghislain, J., Desmarquet-Trin-Dinh, C., Gilardi-Hebenstreit, P., Charnay, P., and Frain, M. (2003). Neural crest patterning: autoregulatory and crest-specific elements co-operate for Krox20 transcriptional control. *Development* *130*, 941–953.

Green, S.A., Simões-Costa, M., and Bronner, M.E. (2015). Evolution of vertebrates as viewed from the crest. *Nature* *520*, 474–482.

Hamburger, V., and Hamilton, H.L. (1992). A series of normal stages in the development of the chick embryo. *Dev. Dyn.* *195*, 231–272.

Han, J., Zhang, J., Chen, L., Shen, B., Zhou, J., Hu, B., Du, Y., Tate, P.H., Huang, X., and Zhang, W. (2014). Efficient in vivo deletion of a large imprinted lncRNA by CRISPR/Cas9. *RNA Biol.* *11*, 829–835.

Jinek, M., Chylinski, K., Fonfara, I., Hauer, M., Doudna, J.A., and Charpentier, E. (2012). A programmable dual-RNA-guided DNA endonuclease in adaptive bacterial immunity. *Science* *337*, 816–821.

Jinek, M., East, A., Cheng, A., Lin, S., Ma, E., and Doudna, J. (2013). RNA-programmed genome editing in human cells. *ELife* *2013*, e00471.

Karolchik, D., Baertsch, R., Diekhans, M., Furey, T.S., Hinrichs, A., Lu, Y.T., Roskin, K.M., Schwartz, M., Sugnet, C.W., Thomas, D.J., et al. (2003). The UCSC Genome Browser Database. *Nucleic Acids Res.* *31*, 51–54.

Kok, F.O., Shin, M., Ni, C.W., Gupta, A., Grosse, A.S., VanImpel, A., Kirchmaier, B.C., Peterson-Maduro, J., Kourkoulis, G., Male, I., et al. (2015). Reverse genetic screening reveals poor correlation between morpholino-induced and mutant phenotypes in zebrafish. *Dev. Cell* *32*, 97–108.

Korkmaz, G., Lopes, R., Ugalde, A.P., Nevedomskaya, E., Han, R., Myacheva, K., Zwart, W., Elkon, R., and Agami, R. (2016). Functional genetic screens for enhancer elements in the human genome using CRISPR-Cas9. *Nat. Biotechnol.* *34*, 1–10.

Kos, R., Reedy, M. V., Johnson, R.L., and Erickson, C.A. (2001). The winged-helix transcription factor FoxD3 is important for establishing the neural crest lineage and repressing melanogenesis in avian embryos. *Development* *128*, 1467–1479.

Kudo, T., and Sutou, S. (2005). Usage of putative chicken U6 promoters for vector-based RNA interference. *J. Reprod. Dev.* *51*, 411–417.

Labosky, P.A., and Kaestner, K.H. (1998). The winged helix transcription factor Hfh2 is expressed in neural crest and spinal cord during mouse development. *Mech. Dev.* *76*, 185–190.

Lopes, R., Korkmaz, G., and Agami, R. (2016). Applying CRISPR-Cas9 tools to identify and characterize transcriptional enhancers. *Nat. Rev. Mol. Cell Biol.* *17*, 597–604.

Losson, R., and Lacroute, F. (1979). Interference of nonsense mutations with eukaryotic messenger RNA stability. *Proc. Natl Acad. Sci. USA* *76*, 5134–5137.

Mali, P., Yang, L., Esvelt, K.M., Aach, J., Guell, M., DiCarlo, J.E., Norville, J.E., and Church, G.M. (2013). RNA-guided human genome engineering via Cas9. *Science* *339*, 823–826.

Moreno-Mateos, M.A., Vejnar, C.E., Beaudoin, J.D., Fernandez, J.P., Mis, E.K., Khokha, M.K., and Giraldez, A.J. (2015). CRISPRscan: Designing highly efficient sgRNAs for CRISPR-Cas9 targeting in vivo. *Nat. Methods* *12*, 982–988.

Nishiyama, A., and Fujiwara, S. (2008). RNA interference by expressing short hairpin RNA in the *Ciona intestinalis* embryo. *Dev. Growth Differ.* *50*, 521–529.

Oishi, I., Yoshii, K., Miyahara, D., Kagami, H., and Tagami, T. (2016). Targeted mutagenesis in chicken using CRISPR/Cas9 system. *Sci. Rep.* *6*, 23980.

Orioli, A., Pascali, C., Quartararo, J., Diebel, K.W.K.W.K.W., Praz, V., Romascano, D., Percudani, R., van Dyk, L.F.L.F.L.F., Hernandez, N., Teichmann, M., et al. (2011). Widespread occurrence of non-canonical transcription termination by human RNA polymerase III. *Nucleic Acids Res.* *39*, 5499–5512.

Port, F., Chen, H.-M., Lee, T., and Bullock, S.L. (2014). Optimized CRISPR/Cas tools for efficient germline and somatic genome engineering in *Drosophila*. *Proc. Natl Acad. Sci. USA* *111*, E2967-2976.

Qi, L.S., Larson, M.H., Gilbert, L.A., Doudna, J.A., Weissman, J.S., Arkin, A.P., and Lim, W.A. (2013). Repurposing CRISPR as an RNA-guided platform for sequence-specific control of gene expression. *Cell* *152*, 1173–1183.

Ren, X., Yang, Z., Xu, J., Sun, J., Mao, D., Hu, Y., Yang, S.-J., Qiao, H.-H., Wang, X., Hu, Q., et al. (2014). Enhanced Specificity and Efficiency of the CRISPR/Cas9 System with Optimized sgRNA Parameters in *Drosophila*. *Cell Rep.* *9*, 1151–1162.

Roellig, D., Tan-Cabugao, J., Esaian, S., and Bronner, M.E. (2017). Dynamic transcriptional signature and cell fate analysis reveals plasticity of individual neural plate border cells. *ELife* *6*, e21620.

Sato, Y., Kasai, T., Nakagawa, S., Tanabe, K., Watanabe, T., Kawakami, K., and Takahashi, Y. (2007). Stable integration and conditional expression of electroporated transgenes in chicken embryos. *Dev. Biol.* *305*, 616–624.

Sauka-Spengler, T., and Barembaum, M. (2008). Chapter 12 Gain- and Loss-of-Function Approaches in the Chick Embryo. *Methods Cell Biol.* *87*, 237–256.

Schindelin, J., Arganda-Carreras, I., Frise, E., Kaynig, V., Longair, M., Pietzsch, T., Preibisch, S., Rueden, C., Saalfeld, S., Schmid, B., et al. (2012). Fiji: an open-source platform for biological-image analysis. *Nat. Methods* *9*, 676–682.

Schulte-Merker, S., and Stainier, D.Y.R. (2014). Out with the old, in with the new: reassessing morpholino knockdowns in light of genome editing technology. *Development* *141*, 3103–3104.

Simões-Costa, M., and Bronner, M.E. (2015). Establishing neural crest identity: a gene regulatory recipe. *Development* *142*, 242–257.

Simões-Costa, M., McKeown, S.J., Tan-Cabugao, J., Sauka-Spengler, T., and Bronner, M.E. (2012). Dynamic and differential regulation of stem cell factor FoxD3 in the neural crest is encrypted in the genome. *PLoS Genet.* *8*, e1003142.

Sternberg, S.H., Redding, S., Jinek, M., Greene, E.C., and Doudna, J. a (2014). DNA interrogation by the CRISPR RNA-guided endonuclease Cas9. *Nature* *507*, 62–67.

Stolfi, A., Gandhi, S., Salek, F., and Christiaen, L. (2014). Tissue-specific genome editing in zebrafish embryos by CRISPR/Cas9. *Development* *141*, 4115–4120.

Streit, A., Tambalo, M., Chen, J., Grocott, T., Anwar, M., Sosinsky, A., and Stern, C.D. (2013). Experimental approaches for gene regulatory network construction: the chick as a model system. *Genesis* *51*, 296–310.

Thakore, P.I., M, D'Ippolito, A., Song, L., Safi, A., Shivakumar, N.K., Kabadi, A.M., Reddy, T.E., Crawford, G.E., Gersbach, C.A., D'Ippolito, A.M., et al. (2015). Highly specific epigenome editing by CRISPR-Cas9 repressors for silencing of distal regulatory elements. *Nat Methods* *12*, 1143–1149.

Tsai, S.Q., Zheng, Z., Nguyen, N.T., Liebers, M., Topkar, V. V, Thapar, V., Wyvekens, N., Khayter, C., Iafrate, A.J., Le, L.P., et al. (2015). GUIDE-seq enables genome-wide profiling of off-target cleavage by CRISPR-Cas nucleases. *Nat. Biotechnol.* *33*, 187–197.

Véron, N., Qu, Z., Kipen, P.A.S., Hirst, C.E., and Marcelle, C. (2015). CRISPR mediated somatic cell genome engineering in the chicken. *Dev. Biol.* *407*, 68–74.

Wang, T., Wei, J.J., Sabatini, D.M., and Lander, E.S. (2014). Genetic screens in human cells using the CRISPR-Cas9 system. *Science* *343*, 80–84.

Wise, T.G., Schafer, D.J., Lambeth, L.S., Tyack, S.G., Bruce, M.P., Moore, R.J., and Doran, T.J. (2007). Characterization and comparison of chicken U6 promoters for the expression of short hairpin RNAs. *Anim. Biotechnol.* *18*, 153–162.

Chapter 5

A combinatorial approach for gene editing and lineage tracing

A modified version of this chapter was published as:

Gandhi, S.[#], Li, Y., Tang, W., Christensen, J.B., Urrutia, H.A., Vieceli, F.M., Piacentino, M.L., and Bronner, M.E.[#] (2021). A single-plasmid approach for genome editing coupled with long-term lineage analysis in chick embryos. *Development* 148, dev.193565.

([#] co-corresponding authors)

<https://doi.org/10.1242/dev.193565>

5.1 Introduction

The advent of CRISPR-Cas9 (Clustered Regularly Interspaced Short Palindromic Repeats-CRISPR-associated protein 9) is a highlight of the past decade, having enabled genome editing across multiple species (Chen et al., 2013; Cong et al., 2013; Dickinson et al., 2013; Gagnon et al., 2014; Stolfi et al., 2014). Recently, it has been applied to early gene perturbations at stages ranging from gastrulation to neurulation in the chick embryo (Gandhi et al., 2017; Williams et al., 2018), an important model organism due to its amenability to transplantation, surgical ablation, live imaging, and gene perturbation (Darnell and Schoenwolf, 2000; Li et al., 2019; Streit et al., 2013).

Conventional molecular perturbation studies in chick embryos have relied upon electroporation of dominant negative transgenes, antisense morpholinos, or short-hairpin RNAs (Corey and Abrams, 2001; Sauka-Spengler and Barembaum, 2008), and more recently, Cas9 and guide RNAs (gRNAs) (Gandhi et al., 2017; Williams et al., 2018). A major drawback of the latter approach was that Cas9 and gRNAs were delivered through separate constructs. While only those cells co-transfected with both plasmids were mutants, those could not be distinguished from cells transfected with the fluorescent marker alone. In addition, the transient nature of electroporation resulted in the dilution of transcripts and encoded proteins over time (Andreason and Evans, 1988; Eisen and Smith, 2008; Nakamura and Funahashi, 2001). As a result, knocking out genes expressed at later embryonic stages was challenging, particularly in tissues that are not easily amenable to electroporation. Moreover, the absence of permanent labeling compromised the ability to identify/trace the descendants of individually perturbed cells.

Here, we report several improvements to the CRISPR-Cas9 toolkit for generation of fluorescently-labeled mutant cells in different tissues of the chick embryo. First, we use a self-cleaving-ribozyme-mediated approach to facilitate production of the optimized gRNA^{f+e} scaffold (Chen et al., 2013; Gandhi et al., 2017) through an RNA-polymerase (RNA-pol) II-based promoter. By eliminating the need for a chick U6 promoter to drive gRNA transcription, this strategy allows delivery of Cas9 and gRNA via a single plasmid.

Second, we incorporate this ribozyme gRNA downstream of Cas9 flanked with nuclear localization signal sequences followed by a fluorescent protein (Williams et al., 2018) to enable fluorescent readout of mutant cells. We use this single-plasmid approach to knock out β -catenin *in vitro* in multiple species. Next, we demonstrate the ability to knock out *Sox10* and *Pax7* in the neural crest, and *Pax6* in the optic vesicle and hindbrain of chicken embryos using electroporation, and the ability to analyze the movement of *Sox10*-mutant cells through live imaging. Finally, we enable cisgenic integration of Cas9, Citrine, and gene-specific gRNA in the host genome by constructing Replication-incompetent avian (RIA-CRISPR) retroviruses. We demonstrate that virally-infected identifiable cells can be successfully perturbed, labeled, and their progeny tracked long-term. Taken together, our approach combines the targeted-knockout ability of CRISPR-Cas9 with retroviral delivery to establish a method that enables genetic perturbations of identifiable mutant cells in an otherwise normal microenvironment of both early and late-stage chick embryos, and potentially other species.

5.2 Results and Discussion

5.2.1 Single-plasmid approach to deliver CRISPR components

Our previously reported modifications in designing individual CRISPR-Cas9 constructs substantially improved gene editing in early chick embryos (Gandhi et al., 2017), allowing successful gene knockouts in numerous studies following electroporation in early embryos (Gandhi et al., 2020a; Hutchins and Bronner, 2018; Piacentino and Bronner, 2018; Tani-Matsuhana et al., 2018; Vieceli and Bronner, 2018). However, because Cas9 and guide RNAs were delivered via separate constructs, a complication was that only cells co-transfected with Cas9 and gRNA plasmids were mutants.

To circumvent this limitation and facilitate delivery of all components through a single construct, we explored alternate strategies to transcribe gRNAs that eliminated the requirement for a U6 promoter, thereby enabling Cas9 and gRNA production via the same promoter. We turned to a ribozyme-based approach (Gao and Zhao, 2014; He et al., 2017), flanking the gRNA^{f+e} backbone with the hammerhead (HH) ribozyme on the 5' end,

and the hepatitis delta virus (HDV) ribozyme on the 3' end [Figure 1A]. Once transcribed, the precursor *HH:gRNA^{f+e}:HDV* transcript undergoes self-catalyzed cleavage to release a functional gRNA molecule, allowing Cas9-mediated genome targeting [Figure 1B]. As a marker for successful transfection, we also included Citrine, which was separated from Cas9 by the self-cleaving 2A peptide sequence as described by Williams et al. (2018).

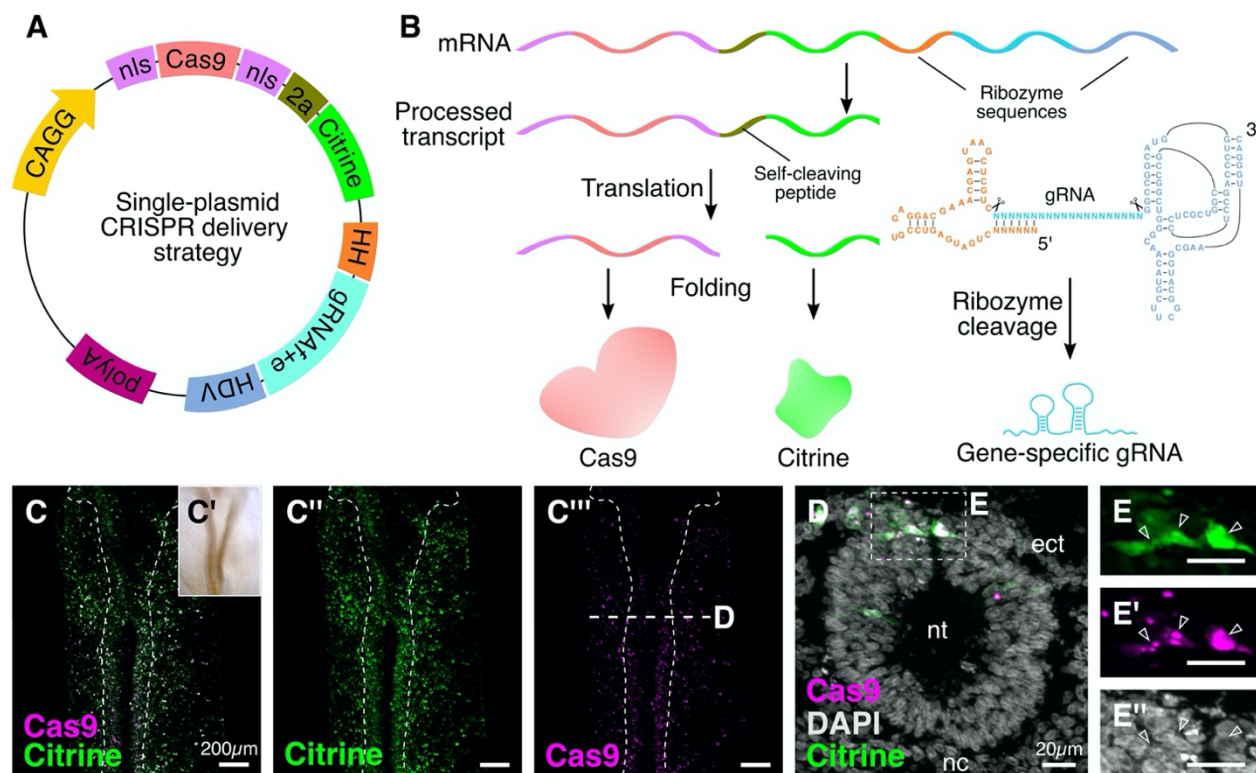


Figure 1. Optimizing delivery of CRISPR components in chick embryos. **A.** A single-plasmid engineered vector for optimal delivery of Cas9, gene-specific gRNA, and Citrine fluorescent protein in transfected cells. **B.** After transfection, the cistronic transcript is cleaved at the HH and HDV ribozyme sites, thereby releasing the gene-specific gRNA. Following translation of the remaining transcript, Cas9 and Citrine will be separated through self-cleavage of the 2A peptide. **C-C'''.** Embryos electroporated with the plasmid depicted in (A) at HH9 (C') and stained with antibodies against Citrine (C'') and Cas9 (C''') to verify cellular localization. **D.** A transverse cross-section through the embryo in (C) with DAPI-stained nuclei. **E-E'''.** Citrine was enriched in the cytoplasm (E, white empty arrowheads), whereas Cas9, in the absence of a gene-specific gRNA, was restricted to the nucleolus (E', white empty arrowheads) within the DAPI-stained nuclei (E''). (nt-neural tube; nc-notochord; ect-ectoderm).

We tested this cistronic system by cloning the *HH:ControlgRNA^{f+e}:HDV* fragment downstream of *Cas9-2A-Citrine* under regulation of the ubiquitous chicken β -actin promoter [Figure 1A]. We electroporated gastrula stage chick embryos with this construct, cultured them *ex ovo* until HH9 [Figure 1C'], and then processed them for immunostaining

against Cas9 and Citrine [Figure 1C]. As expected, Citrine [Figure 1C''] and Cas9 [Figure 1C'''] were expressed in transfected cells throughout the embryo. Transverse sections further validated the respective localizations of individual components [Figure 1D,E], with Citrine expression in the cytoplasm [Figure 1E], and Cas9 [Figure 1E'] expression in the nucleus overlapping with that of DAPI [Figure 1E'']. In fact, Cas9 was retained in the nucleolus, consistent with previous work that demonstrated this phenomenon when Cas9 is not associated with a gene-specific gRNA (Gu et al., 2018). Together, these results indicate that addition of the *HH:gRNA^{f+e}:HDV* precursor does not interfere with the nuclear and cytoplasmic localization of Cas9 and the fluorescent protein, respectively.

5.2.2 Single-plasmid strategy can efficiently perturb function across species

To validate that the *HH:gRNA^{f+e}:HDV* precursor cleaves properly to release a functional gRNA molecule, we turned to an *in vitro* transfection-based approach, targeting the β -catenin (CTNNB1) locus in the human epithelial Osteosarcoma U2OS cells [Figure 2A]. We identified a protospacer in the third exon of the *Ctnnb1* coding sequence and produced the plasmid *CAG>nls-Cas9-nls-2A-Citrine-HH-HsCtnnb1gRNA^{f+e}-HDV* to knock out β -catenin. We transfected U2OS cells with this plasmid, incubated them for 24 hours at 37°C, and then fixed and processed them for immunostaining against β -catenin. Cells in the “control” well were transfected with the *CAG>nls-Cas9-nls-2A-Citrine-HH-CtrlgRNA^{f+e}-HDV* plasmid. Whereas β -catenin was retained at the cellular junctions of control cells [Figure 2B,B'], those successfully electroporated with the *Ctnnb1gRNA*-containing construct, as identified by the expression of Citrine, had reduced levels of β -catenin at cell junctions [Figure 2C,C']. β -catenin fluorescence intensity across cell junctions was quantified by line scan analysis, with transfected cells displaying significant reduction in β -catenin protein production following CTNNB1 knockout compared to those transfected with non-binding control gRNA construct [Figure 2D; $p < 0.001$, Kolmogorov-Smirnov test]. This confirms that *Ctnnb1* gRNA molecules were successfully synthesized in transfected human U2OS cells, and this single plasmid was sufficient to reduce β -catenin protein levels.

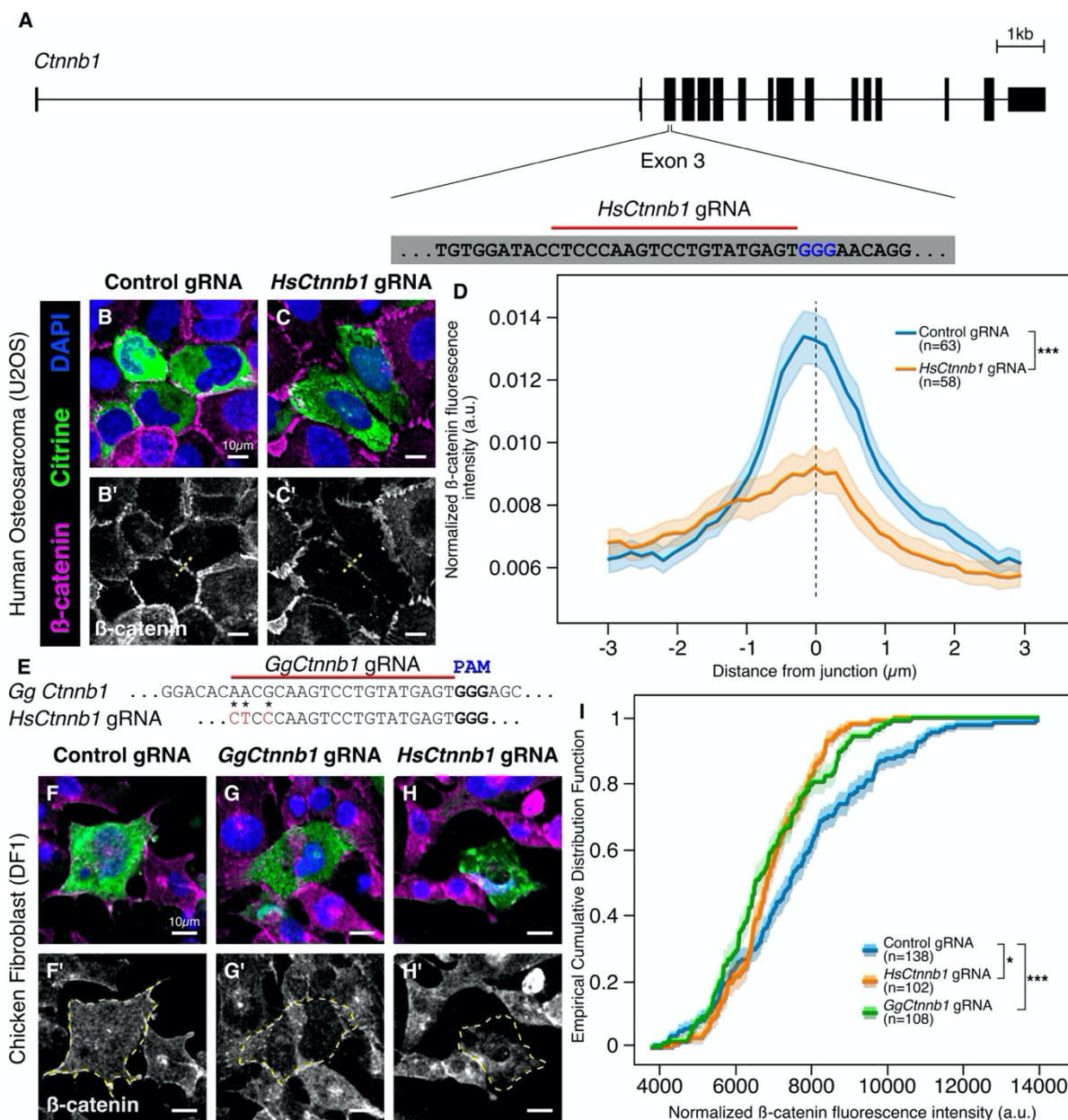


Figure 2. Single CRISPR plasmid efficiently perturbs function across multiple species. A. The genomic locus for *Ctnnb1* in the human genome. A gRNA protospacer targeting the third exon was designed. **B-C.** Representative images from human epithelial cells following transfection with the single CRISPR plasmid harboring control gRNA (B) and human *Ctnnb1*-targeted gRNA (C). **D.** Mean fluorescence intensity from line scan analysis (dashed lines in B ,C') shows that junctions between transfected cells display reduced β -catenin immunoreactivity following *Ctnnb1* knockout (Kolmogorov-Smirnov test, *** $p < 0.001$). **E.** Sequence alignment surrounding the *Ctnnb1* gRNA protospacer between human and chicken. Red characters within the *HsCtnnb1* gRNA protospacer indicate non-conserved nucleotides (asterisks). **F-H.** Representative images from chicken fibroblast cell culture following transfection with the single CRISPR plasmid harboring control gRNA (F), chicken *Ctnnb1*-targeted gRNA (G), and human *Ctnnb1*-targeted gRNA (H). **F'-H'.** Dotted line (yellow) represents cell boundary for representative cells transfected with control gRNA (F'), chicken *Ctnnb1*-targeted gRNA (G'), and human *Ctnnb1*-targeted gRNA (H') that were used to calculate cell fluorescence. **I.** Empirical cumulative distribution frequency analysis indicates that gRNAs targeting human or chicken *Ctnnb1* cause significant reduction of β -catenin immunolabeling within chicken fibroblasts compared to non-binding control gRNA transfections (Kruskal-Wallis test, * $p < 0.05$, ** $p < 0.01$). Error bands reflect standard error.

We next asked if our single-plasmid approach would allow CRISPR-Cas9-mediated gene knockout in multiple species using the same single construct. To do this, we looked for homology between the human and chicken *Ctnnb1* genomic locus and discovered an 85% conservation between these species in the third exon. Importantly, the gRNA protospacer that allowed a robust β -catenin knockdown in human U2OS cells was highly conserved between the two species, with only three nucleotide differences distal to the PAM sequence [Figure 2E; asterisks]. Therefore, we tested the ability of our single-plasmid strategy to knock out *Ctnnb1* in chicken fibroblast cells (DF-1) using both human and chicken gRNA sequences. To this end, we transfected chicken DF-1 fibroblasts with the *CAG>nls-Cas9-nls-2A-Citrine-HH-HsCtnnb1gRNA^{f+e}-HDV* plasmid, while transfecting *CAG>nls-Cas9-nls-2A-Citrine-HH-CtrlgRNA^{f+e}-HDV* or *CAG>nls-Cas9-nls-2A-Citrine-HH-GgCtnnb1gRNA^{f+e}-HDV* plasmids as negative and positive controls, respectively. 24 hours post-transfection, we immunostained these cells against β -catenin. Interestingly, both chicken [Figure 2G,G'] and human [Figure 2H,H'] plasmids were sufficient to reduce the levels of β -catenin compared to the control group [Figure 2F,F']. We quantified this phenotype using cumulative distribution frequency analysis, which revealed significantly diminished β -catenin protein levels in transfected DF-1 cells when supplied with either the chicken or human gRNA constructs, compared with the non-binding control gRNA construct [Figure 2I]. That the same construct produced CRISPR-Cas9-mediated knockouts in both chick and human cells illustrates the versatility of our single-plasmid approach in performing perturbation experiments across species, especially when regions with high homology near the PAM site are targeted.

5.2.3 Early effects of loss of *Sox10* using single-plasmid approach

Using the loss of the gene of interest as a readout for efficient gene knockout, we next used our single-plasmid strategy to target the pan-neural crest marker *Sox10*. An important member of the neural crest gene regulatory network, *Sox10* is critical for proper specification, migration, and differentiation of neural crest cells into mature neurons and glia of the peripheral nervous system (Martik and Bronner, 2017). To test if the modified single-plasmid strategy was sufficient to perturb *Sox10* levels in the neural crest, we

electroporated the right side of gastrula stage embryos with the *CAG>nls-Cas9-nls-2A-Citrine-HH-Sox10gRNA^{f/e}-HDV* plasmid [Figure 3A] encoding a *Sox10* protospacer previously shown to result in its efficient knockdown (Gandhi et al., 2017).

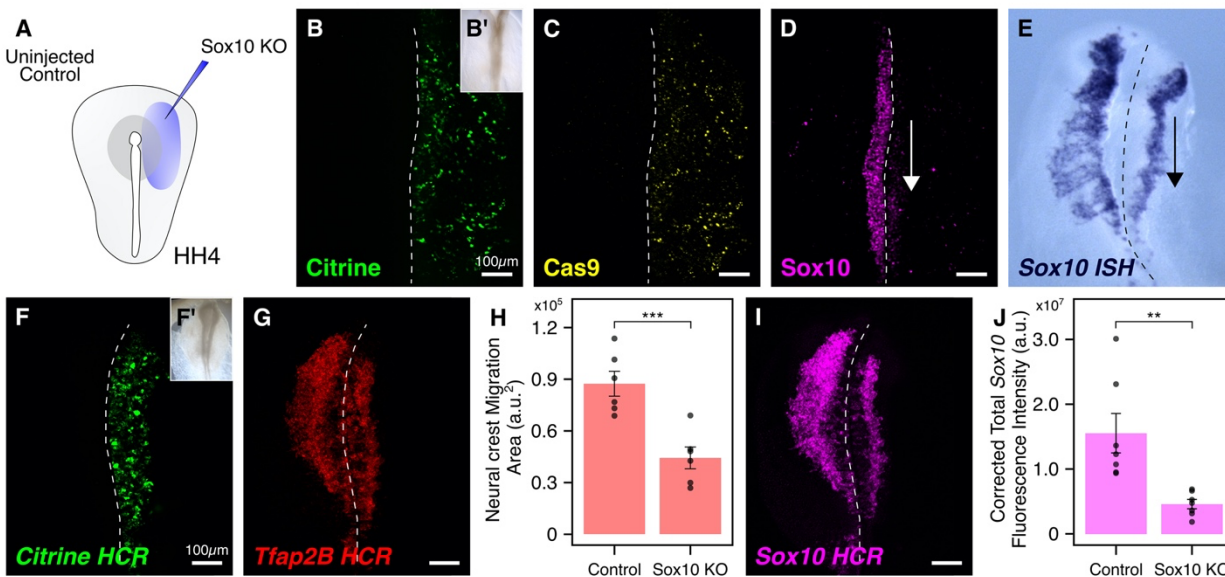


Figure 3. Electroporation-mediated early knockout of *Sox10* using single CRISPR plasmid. **A.** Electroporation strategy to target *Sox10* in the neural crest. The right side of gastrula stage HH4 embryos was electroporated with single CRISPR plasmid containing validated gRNA protospacer. **B-C.** Embryos electroporated with the knockout construct developed to HH9 (B') and immunostained for the expression of Citrine (B) and Cas9 (C). **D.** The single-plasmid approach efficiently reduced *Sox10* protein levels in emigrating cranial neural crest cells at HH9. **E.** Chromogenic *in situ* hybridization revealed a notable reduction in *Sox10* mRNA levels in migrating cranial neural crest cells on the knockout side at HH9+. **F-J.** Knockout embryos (F') were processed for *in situ* HCR against *Citrine* (F), *Tfap2B* (G), and *Sox10* (I). Quantification of migration area (H) and *Sox10* fluorescence intensity (J) showed significant reduction in total area occupied by cranial neural crest cells (H; paired Student's t-test, *** $p < 0.001$), and *Sox10* mRNA levels (J; paired Student's t-test, ** $p < 0.01$) following single-CRISPR-plasmid-mediated *Sox10* knockout. Error bars reflect standard error.

After culturing embryos *ex ovo* until HH9/HH9+ to capture premigratory [Figure 3B'] and migratory [Figure 3F'] neural crest cells, respectively, we processed them for immunohistochemistry and *in situ* hybridization. Antibody staining for Citrine, Cas9, and *Sox10* revealed expression of both Citrine [Figure 3B] and Cas9 [Figure 3C] on the electroporated side, as well as a drastic reduction in *Sox10* protein levels in emigrating neural crest cells [Figure 3D]. Moreover, *in situ* hybridization revealed a significant downregulation in *Sox10* mRNA levels in migrating neural crest cells [Figure 3E]. For quantification, we processed targeted embryos for high resolution *in situ* Hybridization Chain Reaction (HCR). We first labeled nascent Citrine transcripts [Figure 3F] and

observed a strong signal, confirming active transcription through the electroporated single CRISPR plasmid on the transfected side. Next, we labeled the transcripts for the neural crest marker *Tfap2B*, which allowed us to quantify the effect of reduced *Sox10* on neural crest migration. We observed a 50% reduction in the migration area (n=6), with cranial neural crest cells occupying an area of 87336 ± 7203 a.u.² on the control side compared to 44264 ± 6224 a.u.² on the treatment side [Figure 3H; $p < 0.001$, paired Student's t-test]. Finally, consistent with chromogenic *in situ* hybridization, we observed a notable reduction in the levels of *Sox10* mRNA [Figure 3I] on the knockout side. Quantification of the Corrected Total Cell Fluorescence (CTCF) intensity revealed a 70% reduction in *Sox10* intensity (n=7) between the control and knockout sides [Figure 3J; $p < 0.01$, paired Student's t-test]. Together, these results demonstrate that the single-plasmid approach is efficient in perturbing the levels of *Sox10* *in vivo*.

5.2.4 Using single-plasmid approach for live imaging

Next, we explored the possibility of applying live imaging to analyze the effects of CRISPR-Cas9-mediated knockouts, not previously possible in chick cells since components were delivered using separate plasmids. To test this, we electroporated the neural tube of HH10 chick embryos with *FoxD3-NC2>Cerulean*, *CAG>H2B-RFP*, and *CAG>nls-Cas9-nls-2a-Citrine-HH-Sox10gRNA-HDV* on the right side [Figure 4A]. Control embryos were electroporated with *FoxD3-NC2>GFP* at the same concentration. *FoxD3* is a neural crest specifier gene, expressed in premigratory and early migrating neural crest cells along the entire anterior-posterior axis (Stewart et al., 2006; Teng et al., 2008) of developing embryos. Its enhancer, NC2 (Simões-Costa et al., 2012), drives strong reporter expression in post-otic neural crest cells (Gandhi et al., 2020a; Ling and Sauka-Spengler, 2019), including the trunk neural crest (Simões-Costa and Bronner, 2016). H2B-RFP was electroporated in knockout embryos as a nuclear transfection control to complement the cytoplasmic expression of Citrine. The embryos were cultured *in ovo* at 37°C for 24h before harvesting. Using *FoxD3-NC2*-mediated reporter activity as a reference for neural crest expression, slice cultures were prepared spanning 1-2 somites

in length (Li et al., 2020), which were then imaged for 12 hours with a temporal resolution of ten minutes.

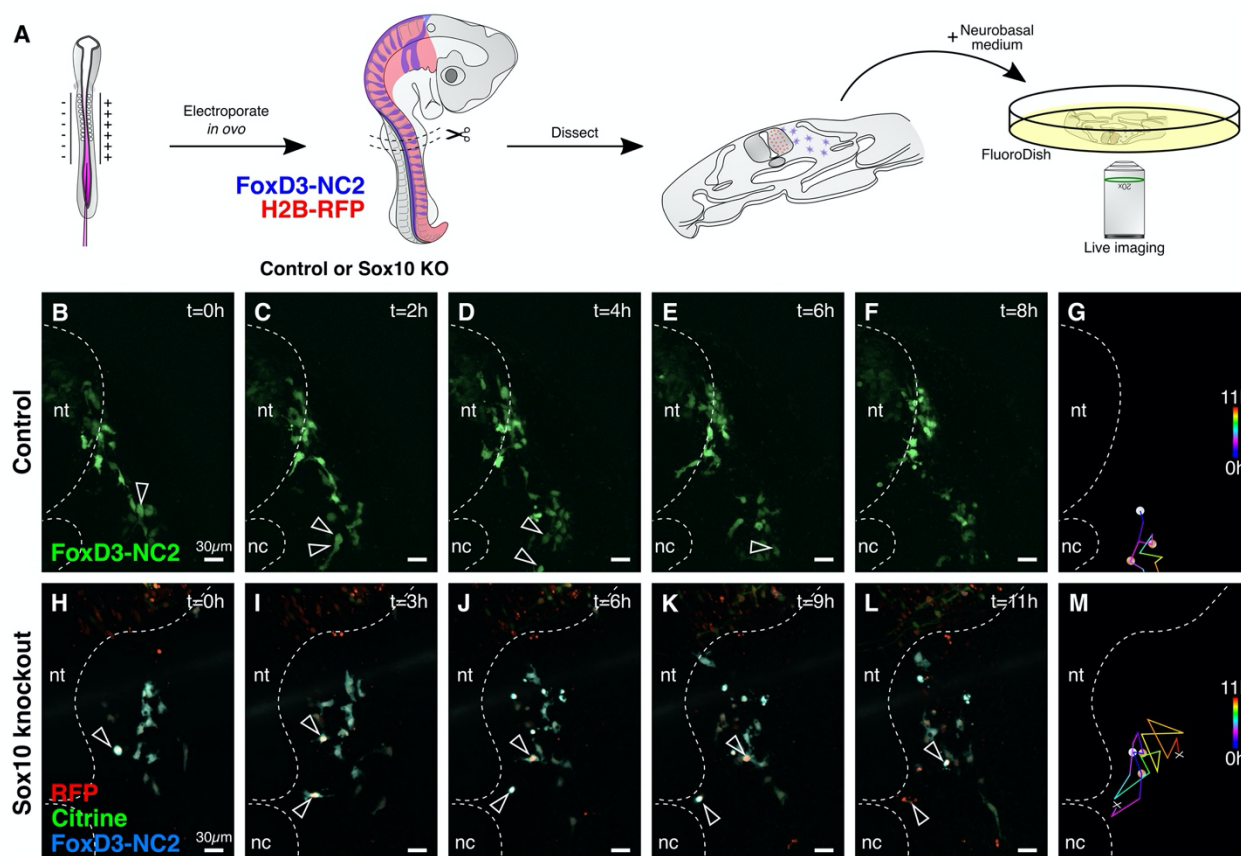


Figure 4. Live imaging application of the single CRISPR plasmid. **A.** Strategy for processing control and mutant embryos for live imaging. Neural crest cells were labeled using the *FoxD3* enhancer NC2; knockout embryos were also electroporated with the single CRISPR plasmid targeting *Sox10* and H2B-RFP as a transfection marker. **B-F.** In control embryos, trunk neural crest cells divide (B,C; empty arrowheads) and migrate properly (D,E,F), with the daughter cells leaving the imaging frame/plane in (E) and (F). **G.** Tracking migration of cells highlighted in (C) reveals proper trunk neural crest migration. **H-L.** When *Sox10* was knocked out before neural crest emigration, mutant cells still divided (H,I; empty arrowheads), but migrated in a circle (J,K) before undergoing apoptosis (L). **M.** Cell tracking of mutant cells shows aberrant migration. Dotted line represents neural tube (nt) and notochord (nc).

To establish the baseline migration pattern of trunk neural crest cells as they migrated ventrally away from the dorsal neural tube toward the sensory and sympathetic ganglia, we visualized labeled control neural crest cells and their progeny [Figure 4B]. Control daughter cells after cell division migrated extensively and typically moved out of the imaging frame and/or plane during the imaging session [Figure 4C-G, supplementary movie 1]. In contrast, labeled cells lacking *Sox10* exhibited aberrant cell migration [Figure 4H-L, supplementary movie 2]. While *Sox10*-mutant cells still underwent mitosis [Figure

4H,I], thus demonstrating that loss of *Sox10* did not inhibit their ability to divide, trajectory analysis revealed abnormal migration of the resultant sister cells before their apoptosis [Figure 4M]. These results are consistent with previous literature, in which loss of *Sox10* in premigratory neural crest resulted in premature apoptosis shortly after delamination (Dutton et al., 2001; Kelsh, 2006). Taken together, these results confirm that loss of *Sox10* prior to delamination of neural crest cells results in aberrant migration and premature apoptosis (Carney et al., 2006; Dutton et al., 2001), whereas its primary effects at later stages of neural crest development appear to be on neuronal and glial differentiation (Britsch et al., 2001). To our knowledge, this is the first instance that combines CRISPR-Cas9-mediated knockouts with live imaging in chick embryos.

5.2.5 Incorporating CRISPR components into RIA retroviruses

While the electroporation strategy works well for gastrula and neurula stage embryos, many other tissues that form in late embryos are inaccessible to electroporation. Therefore, we asked whether using viruses, which allow integration into the genome and ease of delivery, might represent an alternative method of introducing CRISPR-Cas9 components. In the chick embryo, replication-incompetent avian (RIA) retrovirus has served as a versatile tool for long-term lineage tracing (Li et al., 2017, 2019; Tang et al., 2019). Once a susceptible cell is infected with this virus, the viral RNA is reverse transcribed and stably integrated into the host genome. Since the integrated viral DNA lacks the gene for the envelope protein to produce virus, it fails to horizontally transfer its genetic material into neighboring cells (Chen et al., 1999; Witte and Baltimore, 1977). On the other hand, as an intrinsic component of the host genome, the viral DNA can be vertically transferred to daughter cells through mitosis, resulting in permanent labeling of the entire lineage derived from infected progenitors. These combined attributes make RIA a powerful system for exploring lineage relationships within complex tissues (Li et al., 2017; Tang et al., 2019). Recently, this RIA-mediated approach has been extended for clonal analysis, by identifying rare color combinations coupled with intracellular

localization of fluorophores that result from simultaneous infection of more than one virion (Tang et al., 2019).

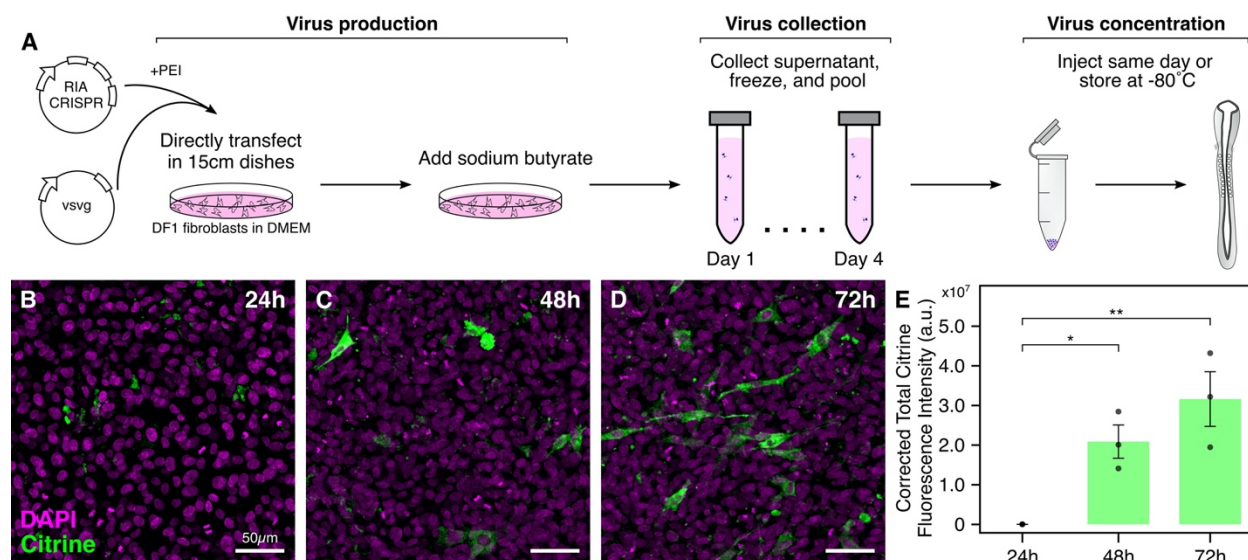


Figure 5. Incorporating single CRISPR plasmid into RIA retroviruses. **A.** Illustration of optimized protocol to synthesize high-titer avian retroviruses that contain large inserts. Viral particles are produced in 15cm plates supplemented with sodium butyrate. Supernatant can be pooled and stored at -80°C for several months, while concentrated virus can be injected the same day or stored at -80°C for a few weeks. **B-E.** Chicken DF1 fibroblasts were infected with RIA-CRISPR retrovirus and collected 24 (B), 48 (C), and 72 hours (D) post-infection. Citrine expression was first observed at the 48 hours timepoint, as validated by the quantification of Citrine fluorescence intensity (E; ANOVA followed by Tukey's HSD, ** p<0.01, * p<0.05). Error bars reflect standard error.

Our initial attempt involved injecting two different viruses in the neural tube: one encoding for nuclear Cas9 and the other encoding a gene-specific gRNA. However, this approach was unsuccessful in knocking out *Sox10* in the trunk neural crest due to the low probability of double infection. As an alternative, we explored the possibility of incorporating our single-plasmid design into the RIA virus for targeting later stages of development. However, given the relatively larger size of the *nls-Cas9-nls-2a-Citrine-HH-gRNA^{f/e}-HDV* fragment, it was necessary to improve the RIA virus preparation protocol to accommodate this large insert. We achieved this by making three modifications to maintain the functionality of the recombinant virus [Figure 5A]. First, we minimized the time duration that secreted virus stayed in the culture medium by transfecting RIA and VSVG expression constructs directly in 15 cm dishes instead of sequentially passaging transfected cells from 6 to 10 to 15 cm dishes (Chen et al., 1999), which often led to the deletion of inserted genes in the viral particles over time. Second,

we used polyethylenimine (PEI), a polymer composed of repeating units of amine group and carbon spacer (Tang et al., 2015), as a less expensive substitute for previously used commercial transfection reagents (Chen et al., 1999), making the transfection process better suited for large-scale production. Finally, we added sodium butyrate, a histone deacetylase inhibitor that has been shown to enhance viral DNA transfection (Sakoda et al., 1999). Together, these modifications allowed us to successfully make high titer retrovirus encoding three large inserts of variable sizes, *nls-Cas9-nls* (4.2kb), *nls-Cas9-nls-eGFP* (4.9kb), and *nls-Cas9-nls-2a-Citrine-HH-gRNA^{f+e}-HDV* (5.1kb), hereby referred to as RIA-Cas9, RIA-Cas9-GFP, and RIA-CRISPR retroviruses, respectively.

To test the time-course of protein expression following infection with the RIA-CRISPR retrovirus, we infected chicken DF-1 fibroblast cells, incubated them at 37°C and 5% CO₂, and collected cells in triplicates at 24 [Figure 5B], 48 [Figure 5C], and 72 hours [Figure 5D] post-infection. Infected cells collected at these three timepoints were then processed for immunostaining against Cas9 and Citrine. Robust Citrine expression was first observed in cells collected at 48 hours [Figure 5C], suggesting a delay between the time of initial infection and formation of readily detectable protein. Quantification of Citrine CTCF intensity confirmed that significant differences existed in Citrine protein levels between the 24 and 48 hours [Figure 5E; p<0.05, ANOVA followed by Tukey's HSD] and 24 and 72 hours timepoints [Figure 5E; p<0.01, ANOVA followed by Tukey's HSD], respectively. These data agree well with our previous findings that detection of robust fluorescent protein *in vivo* in neural crest cells infected with RIA retroviruses is observed after 2 days (Tang et al., 2019). We next sought to test these retroviruses *in ovo* by targeting *Sox10*, *Pax7*, and *Pax6* in the neural crest, segmental plate, and retina, respectively.

5.2.6 Targeting *Sox10* in neural crest derivatives using RIA-CRISPR retroviruses

Sox10 is known to affect differentiation of several neural crest lineages. Therefore, we cloned the cisronic fragment *nls-Cas9-nls-2A-Citrine-HH-Sox10gRNA^{f+e}-HDV* into the RIA viral vector to generate a Sox10-RIA-CRISPR retrovirus [Figure 6A] that was

injected into the lumen of the chick neural tube [Figure 6B] at HH10 (n=20), and we examined subsequent effects on neural crest derivatives at a population level.

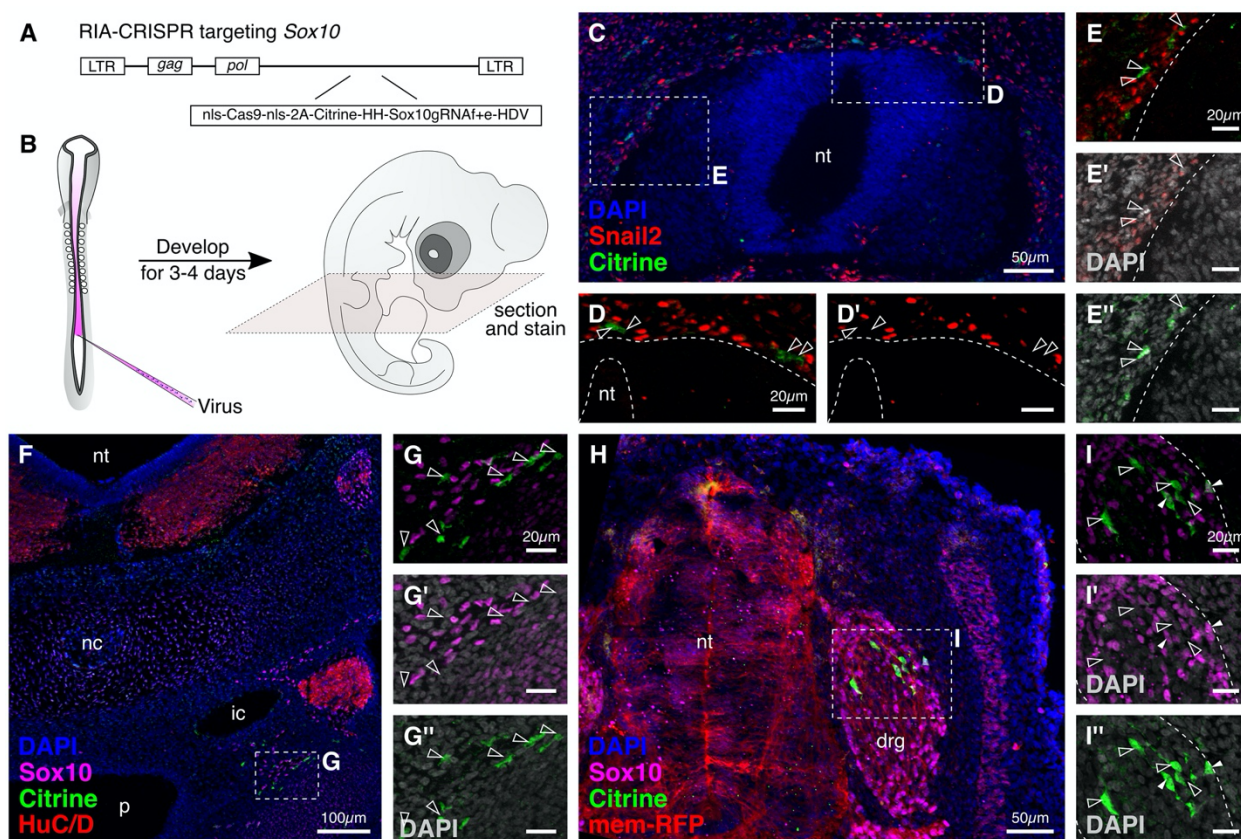


Figure 6. RIA retrovirus-mediated knockout of *Sox10* in neural crest derivatives. **A.** Schematic diagram for cloning *Sox10*-RIA-CRISPR virus plasmid. **B.** *Sox10*-RIA-CRISPR retrovirus was injected into the neural tube lumen of HH10. At HH25, embryos were fixed, cryosectioned, and immunostained. **C.** Knockout of *Sox10* following emigration from the neural tube does not affect survival but rather causes downregulation of *Snail2*, a neural crest specification marker. **D-E.** Early (D) and Late (E) migrating neural crest cells labeled with Citrine fluorescent protein (D',E'') do not express *Snail2* (empty arrowheads). **F-G.** Transverse section through an injected embryo (F) shows labeled migrating trunk neural crest cells mutant for *Sox10* expression close to the sympathetic ganglion (G,G'), with DAPI-labeled nuclei (G''). **H.** Labeled cells were also observed in the dorsal root ganglion. **I.** While most Citrine-positive cells were *Sox10*-negative (I'; empty arrowheads), *Sox10* protein was detected in a couple of labeled cells (I'; solid arrowheads). (nt-neural tube; nc-notochord; p-pharynx; ic-internal carotid; drg-dorsal root ganglion)

High-titer RIA-membrane-RFP retrovirus was co-injected as a readout for infection efficiency. As expected, RIA infection failed to robustly label migratory neural crest cells shortly after delamination due to the time needed to generate proteins after viral integration [Figure 5E]. The proportion of Citrine expressing cells increased with time, reflecting synthesis of Cas9 protein and gRNA molecules that results in *Sox10* knockout at later stages of neural crest migration. Embryos at >2 days of development contained

clusters of Citrine+ cells migrating along the ventromedial neural crest migratory pathway [Figure 6C]. Contrasting with early loss of *Sox10*, neural crest cell death was not observed. Rather, there was loss of the neural crest transcription factor *Snail2* in migratory neural crest cells [Figure 6D-E], and *Sox10* protein was diminished in the Citrine-labeled cells [Figure 6F-G,G',G'']. That these cells did not undergo premature apoptosis and appeared to migrate properly suggested that *Sox10* plays distinct roles in early and later stages of neural crest development, and confirms that our retroviral approach can be used to analyze phenotypes at later stages.

After 4 days, labeled cells were observed in the dorsal root ganglion in transverse sections through the trunk [Figure 6H]. Immunostaining revealed discrete clusters of Citrine-labeled cells, $96\pm 2.7\%$ of which had lost *Sox10* protein [Figure 6I], suggesting a clean knockdown. As expected given potential perdurance of protein generated prior to the knockout and/or incomplete knockout in cells where only a single allele was deleted, a low level of *Sox10* protein was detectable in $4\pm 2.7\%$ of the Citrine-labeled cells [Figure 6I'; white solid arrowheads]. Given the relatively sparse Citrine expression, it is easy to identify a small number of mutant cells in an otherwise normal embryonic background. Taken together, these results suggest that our RIA-CRISPR retroviruses can be used to decouple early function of *Sox10* in maintaining neural crest cell viability from its later role in cell differentiation.

5.2.7 Targeting *Pax6* in the chick retina

In the chick, outgrowth of the optic vesicles in the forebrain marks the first sign of eye development (O'Rahilly and Meyer, 1959). This is followed by formation of layers with the neural retina as the inner layer and outer retinal pigment epithelium. In *Pax6*^{-/-} mice, the optic cup and other ocular tissues fail to develop (Marquardt et al., 2001), suggesting that expression of this paired-box transcription factor plays a critical role in the survival of optic vesicle cells (Canto-Soler and Adler, 2006). After optic vesicle formation, *Pax6* maintains multipotentiality of retinal progenitor cells (Marquardt et al., 2001). Similarly, in *Drosophila* and *Xenopus* embryos, ectopic expression of the *Pax6* coding sequence

results in formation of ectopic eyes (Chow et al., 1999; Halder et al., 1995). While inducible Cre-LoxP has contributed greatly to understanding the role of *Pax6* in murine eye development, the only feasible method for genetic perturbations in the chick retina has been electroporation at different stages (Sebastián-Serrano et al., 2012), which has limitations, including reduced tissue accessibility and lack of permanent labeling of transfected cells. To establish the feasibility of applying our modified RIA-CRISPR retroviruses to the chick retina, we targeted *Pax6* in the optic vesicle. We first sought to identify a functional gRNA that would successfully knock out chick *Pax6*. The genomic locus in the chicken genome spans 16.8kb on chromosome 5 and consists of 14 exons, with the paired-box domain spanning between exons 5 to 8, and the homeodomain spanning between exons 9 to 11 [Figure 7A].

We designed two gRNAs, one targeting the splice acceptor site of exon 5 and another targeting the splice acceptor site of exon 7, and individually tested their efficacy by electroporating the right side of gastrula stage embryos with constructs encoding Cas9, the two individual gRNAs, and nuclear RFP (as a transfection control). Only the gRNA targeting the splice acceptor site of exon 5 was successful in knocking out *Pax6* in electroporated cells within the neural tube [Figure 7B-D], as confirmed by loss of Pax6 protein [Figure 7D]. Next, we incorporated this protospacer into our single-plasmid design to synthesize the *CAG>nls-Cas9-nls-2A-Citrine-HH-Pax6gRNAf+e-HDV* construct, which we electroporated on the right side of gastrula stage embryos that were fixed and processed for cryosectioning and immunostaining at HH9. The quantified Pax6 CTCF intensity (4 sections obtained from two representative embryos) was significantly different in the neural tube of the knockout side compared to the control side [Figure 7E; $p < 0.05$, paired Student's t-test]. Therefore, we selected this gRNA for all our subsequent experiments.

Given the large size of Cas9 and the fluorescent protein insert, we began by confirming that injection of a large-insert virus would sufficiently label cells in the developing chick retina and not interfere with normal retinal development. To this end, we utilized the RIA-Cas9-GFP retrovirus and injected it in the optic vesicle of HH9 chick

embryos, co-injecting RIA-H2B-RFP retrovirus as an infection control. Embryos were harvested after 3 days, and the eyes were dissected, cryosectioned, and immunostained. Imaging of sections revealed distinct clusters of GFP⁺ and RFP⁺ cells in the developing retina and the retinal pigmented epithelium layer [Figure 7F]. The eye developed normally, and cells labeled with the two retroviruses were evenly distributed throughout the presumptive outer and inner nuclear layers [Figure 7F'], confirming lack of interference of the large insert size with normal eye development, efficiency of infection, and subsequent fluorescent protein expression. Accordingly, we incorporated the *nls*-

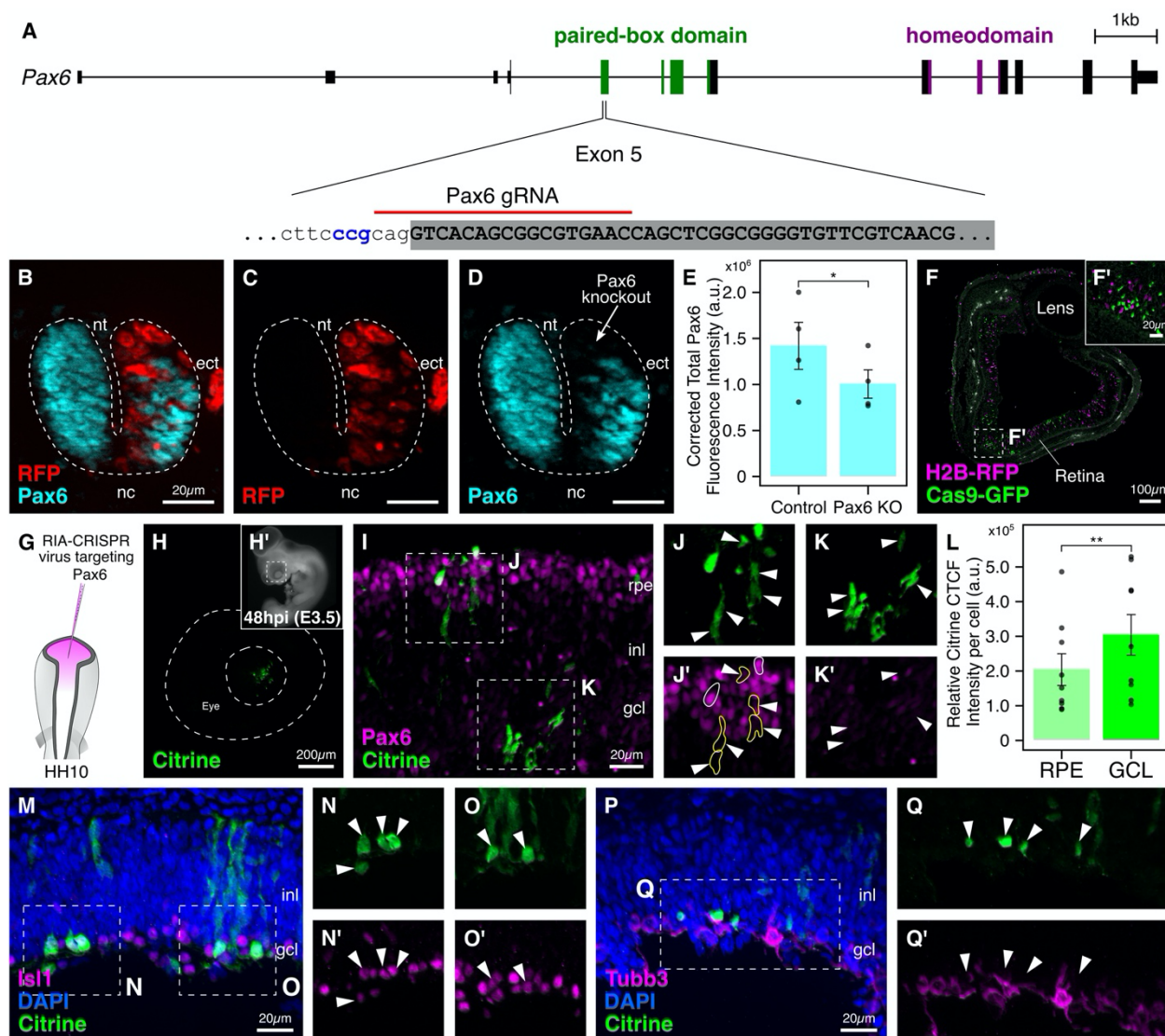


Figure 7. See next page for legend.

Figure 7. Targeting *Pax6* in the developing chick retina using RIA-CRISPR retrovirus. A. The genomic locus for *Pax6* in the chick with paired-box (green) and homeodomain (purple) indicated. Of the tested gRNAs, the one targeting the splice acceptor site of exon 5 was most efficient. **B-E.** The right side of gastrula stage embryos was electroporated with constructs encoding Cas9, RFP, and *Pax6* gRNA. Transfected cells (C) lacked expression of Pax6 (D), as seen in the overlay image (B). Cross-sections through embryos electroporated with single CRISPR plasmid targeting *Pax6* were used to quantify fluorescence intensity of Pax6 in the neural tube; results reveal a significant difference in PAX6 expression between the knockout and control sides (E; * $p < 0.05$, paired Student's t-test). **F-F'.** Section through the eye at embryonic day (F) injected with RIA-Cas9-GFP and RIA-H2B-RFP retroviruses. Labeled cells were evenly distributed (F') through all layers of the developing retina. **G.** The injection strategy for targeting *Pax6* in retinal progenitor cell precursors residing in the optic vesicle. **H-H'.** Citrine expression (H) in the developing eye (H') was first observed 48 hours post-infection. **I-K'.** Citrine-labeled cells (I,J,K) in both the retinal pigmented epithelium and the ganglion cell layers were negative for Pax6 expression (J',K'; solid white arrowheads). Intensity of Citrine expression together with endogenous Pax6 levels allowed identification of two clones in the retinal pigmented epithelium layer (J'): outlined in white – high Citrine, high Pax6; outlined in yellow – low Citrine, no Pax6. **L.** Relative Citrine fluorescence intensity per labeled cell was significantly higher in the ganglion cell layer (GCL) compared to the retinal pigmented epithelium (RPE) (* $p < 0.01$, paired Student's t-test). **M-O'.** 77.08±5.5% of Citrine-labeled cells (M,N,O) were biased towards an amacrine cell fate based on expression of *Islet1* (N',O'; solid white arrowheads). Several migratory cells were observed in the inner nuclear layer. **P-Q'.** 80.24±3.1% of Citrine-labeled cells (P,Q) in the ganglion cell layer failed to turn on TUBB3, a marker for differentiated mature neurons (Q'; solid white arrowheads). nt-neural tube; nc-notochord; ect-ectoderm; rpe-retinal pigmented epithelium; inl-inner nuclear layer, gcl-ganglion cell layer. Error bars reflect standard error.

Cas9-nls-2A-Citrine-HH-Pax6gRNA^{f+e}-HDV fragment into the RIA vector to synthesize Pax6-RIA-CRISPR virus for injection in the optic vesicle of HH9 embryos [Figure 7G]. Following injections, expression of Citrine was first observed in the developing eye 48 hours post-injection [Figure 7H].

Next, we harvested injected embryos following 4-5 days of development (n=25) and obtained transverse sections through the dissected eyes. Given the delay between infection and expression of Citrine, targeting *Pax6* in the optic vesicle allows us to decouple Pax6's early and later roles. Indeed, immunostaining of sections through eyes infected with the Pax6-RIA-CRISPR retrovirus demonstrated several distinct clones distributed along the retinal pigmented epithelium, the ganglion cell layer, and as elongated migratory cells in the inner cell layer [Figure 7I]. Using the intensity of Citrine expression and levels of endogenous Pax6 protein, we were able to identify labelled cells within the retinal pigmented epithelium layer that are likely to be sister cells [Figure 7J']. One such "clone" had high levels of Citrine (outlined in white) and retained Pax6 expression, while the second had low levels of Citrine (outlined in yellow) and diminished Pax6 expression. Labeled cells with high Citrine [Figure 7K] and downregulated Pax6

expression [Figure 7K'] were also scattered within the developing ganglionic cell layer. Interestingly, the signal intensity of Citrine was stronger in the ganglionic cell layer compared to the inner nuclear or the retinal pigmented epithelium layer (n=9), with a statistically significant difference in the Citrine CTCF intensity per unit cell between the two layers [Figure 7L; $p < 0.01$, paired Student's t-test].

Finally, we assessed effects of the Pax6-RIA-CRISPR retrovirus on the fate of retinal progenitor cells by immunostaining cross-sections through the eyes with antibodies against *Islet1*, a marker for amacrine cells, one of the six cell types that are derived from the retinal progenitor cells. In the chick retina, retinal gangliogenesis begins around embryonic day 6, marked by expression of the *Brn3* family of proteins (Doh et al., 2010; Liu et al., 2000). Consistent with previous findings suggesting that temporally-restricted loss of Pax6 is associated with preferential generation of amacrine interneurons (Marquardt et al., 2001), examination of representative sections revealed that $77.08 \pm 5.5\%$ of Citrine+ cells in the ganglionic cell layer expressed Islet1 [Figure 7M-O], supporting the possibility that in the virally-infected cells initiate amacrine differentiation. We tested whether these labeled cells were terminally differentiated neurons by staining sections for β -III tubulin, a marker for post-mitotic mature neurons. Of the representative sections examined, $80.24 \pm 3.1\%$ of Citrine+ cells within the ganglionic cell layer were β -III tubulin negative, suggesting that these were amacrine precursors rather than prematurely differentiated amacrine neurons [Figure 7P-Q]. This was consistent with results in a Pax6^{lacZ} mutant mouse model, where cells failed to turn on Tuj1 in the absence of Pax6 (Oron-Karni et al., 2008). Of note, the RIA approach successfully labeled a subpopulation of retinal cells, suggesting that this sparse labeling approach is well-suited for examination and long-term tracking of mutant cells in an otherwise normal environment. Taken together, our results show that the RIA-CRISPR viruses can be used for later stage knockdown of genes of interest in the chick retina, enabling new lines of investigation previously limited to genetically tractable model systems.

5.2.8 Targeting *Pax7* in the neural crest and presomitic mesoderm

In early chick embryos, neural crest cells are induced shortly after gastrulation at the neural plate border, a region between the neural plate and non-neural ectoderm (Gandhi and Bronner, 2018). Expression of *Pax7* primes neural plate border cells to become neural crest at the expense of other lineages (Gandhi et al., 2020b; Roellig et al., 2017). To test that the single-plasmid strategy reduces *Pax7* levels, we electroporated the right side of gastrula stage embryos with the *CAG>nls-Cas9-nls-2A-Citrine-HH-Pax7gRNA^{f/e}-HDV* plasmid [Figure 8A], which contained a previously validated *Pax7* protospacer (Gandhi et al., 2017). As an internal control, the left side was either not injected, or injected with a control plasmid (*CAG>nls-Cas9-nls-2A-Citrine-HH-CtrlgRNA^{f/e}-HDV*), with similar results in both cases. Embryos were cultured *ex ovo* until HH9+ [Figure 8B], fixed, and stained for PAX7 expression.

Levels of *Pax7* were very notably reduced in cranial neural crest cells [Figure 8C], as quantified by measuring the number of cranial neural crest cells and *Pax7* CTCF intensity on the treated and control sides. Following *Pax7* knockout, we observed a 33% reduction in the number of neural crest cells [Figure 8D; $p < 0.05$, paired Student's t-test] and a 37% reduction in the *Pax7*-CTCF intensity [Figure 8E; $p < 0.05$, paired Student's t-test]. Furthermore, levels of *Pax7* mRNA were also notably downregulated, as demonstrated by *in situ* HCR [Figure 8F]. Next, we focused on the area occupied by neural crest cells on the control and knockout sides. *Pax7* mRNA signal was used to trace the extent of migration on either side of the embryo [Figure 8G]. Indeed, the migration area ($n=9$) was significantly downregulated by 31%, with neural crest cells occupying an area of 125143 ± 17353 a.u.² on the control side compared to 85079 ± 12109 a.u.² on the treatment side [Figure 8H; $p < 0.01$, paired Student's t-test]. Finally, given that *Pax7* acts upstream of the neural crest specifier gene *FoxD3* and directly regulates its activity by binding to a proximal enhancer (Simões-Costa et al., 2012), we processed knockout embryos for *in situ* HCR against *FoxD3* [Figure 8I], and noticed a significant reduction in its CTCF intensity ($n=4$) on the right side of the embryo [Figure 8J; $p < 0.05$, Student's t-test], particularly in the hindbrain [Figure 8I'].

As the embryo develops, *Pax7* is expressed in other tissues, including the dermis and skeletal muscle progenitors that reside in the dorsal dermatome and ventral myotome. The myogenic progenitors delaminate from the myotome, migrate to the developing limb bud, and proliferate (Buckingham et al., 2003). Once these cells are in the limb bud, expression of *MyoD*, a determination factor for the myogenic lineage, results

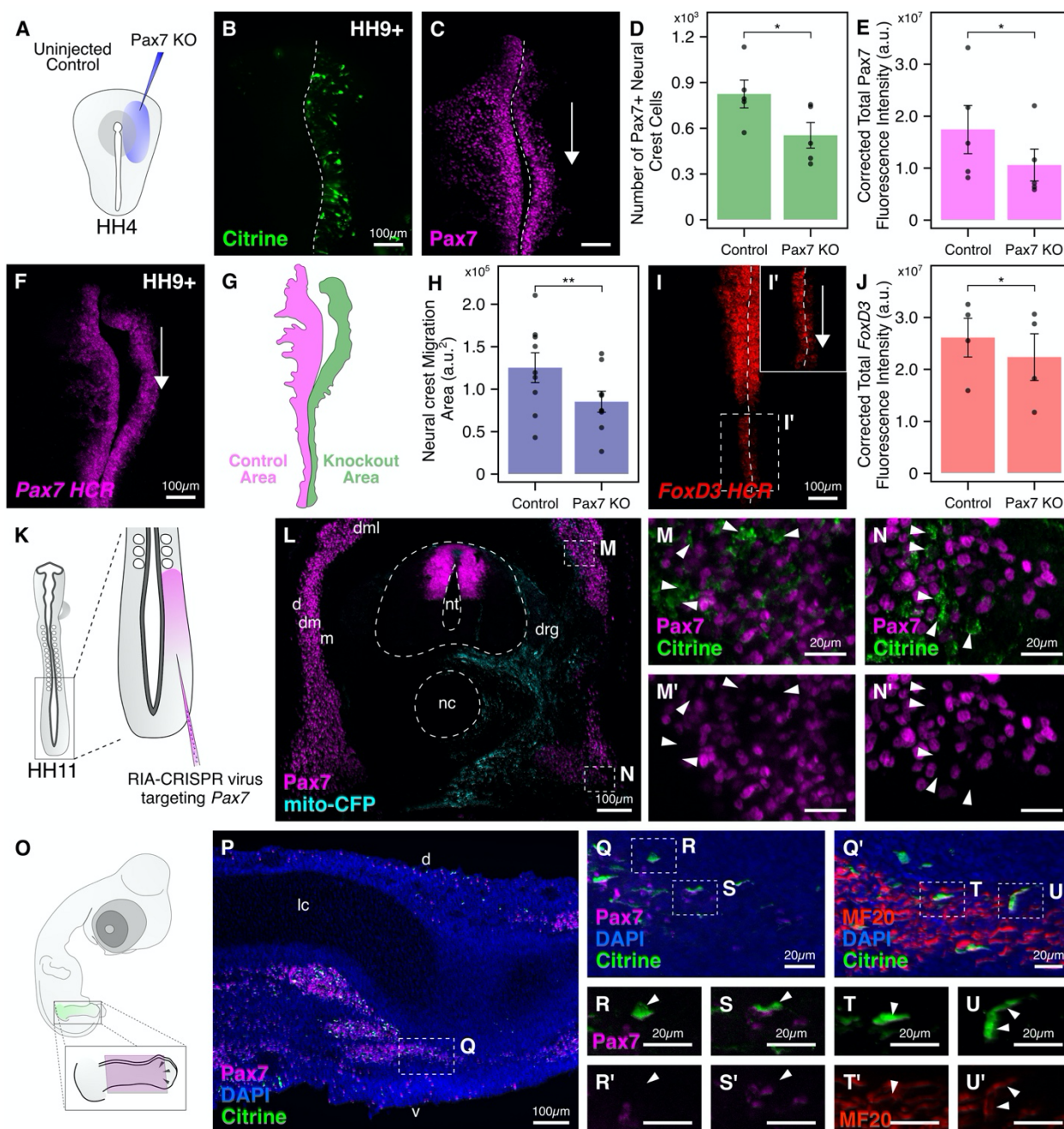


Figure 8. See next page for legend.

Figure 8. Targeting *Pax7* in the dermomyotome and hindlimb using RIA-CRISPR retrovirus. **A.** Electroporation strategy for knocking out *Pax7* in the neural crest. The right side of gastrula stage embryos was electroporated with the single CRISPR plasmid. **B.** Embryos developed to HH9+ displayed robust expression of Citrine fluorescent protein on the right side. **C-E.** The engineered single plasmid efficiently knocked out *Pax7* (C) on the electroporated side. The number of neural crest cells (D; * $p < 0.05$, paired Student's t-test) and *Pax7* fluorescence intensity (E; * $p < 0.05$, paired Student's t-test) were significantly reduced on the knockout compared to control side. **F-H.** *In situ* Hybridization Chain Reaction showed that *Pax7* mRNA levels were also downregulated on the knockout side. The boundary of migration area (G) occupied by cranial neural crest cells in (F) was identified using the position of the lateral-most leader cell for both control (magenta) and knockout (green) sides. Quantification of this difference revealed a significant reduction in neural crest migration on the knockout side (H; ** $p < 0.01$, paired Student's t-test). **I-J.** In the absence of *Pax7*, the expression of the neural crest specifier gene *FoxD3* is severely downregulated (I), especially in the hindbrain, where the effect of the CRISPR plasmid is most penetrant (I'). Quantification of the *FoxD3* fluorescence intensity revealed significant difference between knockout and control sides (J; * $p < 0.05$, paired Student's t-test). **K.** Injection strategy for targeting *Pax7* in the presomitic mesoderm of HH11 embryos using the *Pax7*-RIA-CRISPR retrovirus. **L.** Transverse section through embryos developed to HH25 shows positive labeling with tracer virus (mito-CFP) on the injected side. **M-N'.** Citrine+ cells in the dorsal (M) and ventral (N) aspects of the dermomyotome were *Pax7*-negative (M',N'; solid white arrowheads). **O.** In infected embryos developed to embryonic day 6, the limb was dissected and sectioned along the coronal plane, shown in magenta. **P.** Several Citrine+ mutant cells were observed in the dorsal and ventral muscle mass. **Q-U'.** *Pax7*-mutant cells (Q,S,S') robustly turn on the skeletal muscle marker MF20 (Q',T,T',U,U'). Several Citrine+/MF20- cells that failed to turn on *Pax7* (R,R'; solid white arrowhead) were observed in close to ventral and dorsal muscle masses, perhaps corresponding to muscle satellite cell precursors. Q and Q' are adjacent sections that captured the same cell. dml-dorsomedial lip; d-dermatome; dm-dermomyotome; m-myotome; nt-neural tube; nc-notochord; drg-dorsal root ganglion; d-dorsal; v-ventral; lc-limb cartilage. Error bars reflect standard error.

in their differentiation into skeletal muscle (Rudnicki et al., 1993). Expression of *Pax7* is critical for the proper development of muscle satellite cells, that are also derived from the *Pax7*-expressing precursors residing in the dermomyotome (Von Maltzahn et al., 2013).

To diversify the application of our single-plasmid approach, we sought to target *Pax7* not only in presumptive neural crest, but also later in the muscle progenitor population of the developing dermomyotome. We cloned this transgene into the RIA viral vector and generated RIA-CRISPR virus with the aim of infecting cells that express *Pax7* in the dorsolateral region of the developing somites that gives rise to the dermis and skeletal muscles. While *in ovo* electroporation of the presomitic mesoderm is possible (Itasaki et al., 1999), the technique requires puncturing the egg yolk to insert the positive electrode, which can reduce viability. Instead, we injected the *Pax7* RIA-CRISPR virus directly in the segmental plate of HH11 chick embryos on the right side [Figure 8K] and allowed them to develop for 3-4 days post-infection (n=18). RIA-CFP fluorescent protein tagged with a mitochondrial localization sequence served as an infection control. At

HH25, embryos were harvested, sectioned through the region caudal to the injection site, and immunostained. We found Citrine+ infected cells that lacked Pax7 expression on the injected side [Figure 8L], within the dorsal [Figure 8M,M'] and ventral aspects [Figure 8N,N'] of the dermomyotome. The high proportion of infected cells was likely derived from proliferating progenitors that had successful integration of Cas9, Pax7 gRNA, and Citrine in their genome. The injected embryos had a high survival rate (>90%), suggesting that targeted retroviral injection was less likely than *in ovo* electroporation to affect long-term viability of embryos.

Finally, in a subset of embryos that were injected with the RIA-CRISPR virus targeting *Pax7* (n=6), the hindlimb on the injected side was strongly labeled with Citrine. Therefore, we dissected these hindlimbs [Figure 8O], made coronal sections, and stained them for the myogenic marker MF20. We found several clusters of Citrine+ cells in both the ventral and dorsal muscle mass of the hindlimb [Figure 8P]. To confirm that the cells that successfully differentiated into muscles were indeed mutant for *Pax7* expression, we also stained adjacent sections for Pax7. Consistent with the loss of Pax7 expression in the dermomyotome [Figure 8L], Citrine-positive cells did not express PAX7 [Figure 8Q,S,S'] showing that *Pax7* was successfully knocked out in their progenitors but mutant cells expressed strong levels of MF20 [Figure 8Q',T,T',U,U']. On the other hand, we observed several infected cells that were anatomically adjacent to the muscle cells but were negative for MF20 and Pax7 expression [Figure 8R], which we speculate correspond to muscle satellite cell precursors [Figure 8R'], although further characterization is required to validate their identity. Taken together, these results establish an additional potential application of our engineered RIA-CRISPR retroviruses to a tissue that that was previously difficult to access in chicken embryos.

5.2.9 Coupling RIA-CRISPR retrovirus-mediated perturbation with clonal lineage tracing

Finally, we asked if the RIA-CRISPR retrovirus-mediated gene editing can be used in combination with other RIA viruses for *in vivo* clonal analysis. To establish proof-of-

principle for this application, we chose the developing spinal cord as our tissue of interest, and co-injected RIA-CRISPR retrovirus targeting Pax7 (Citrine+) with an RIA retrovirus encoding only nuclear RFP (H2B-RFP) at a volumetric ratio of 10:1 into the lumen of the neural tube of HH12 embryos [Figure 9A].

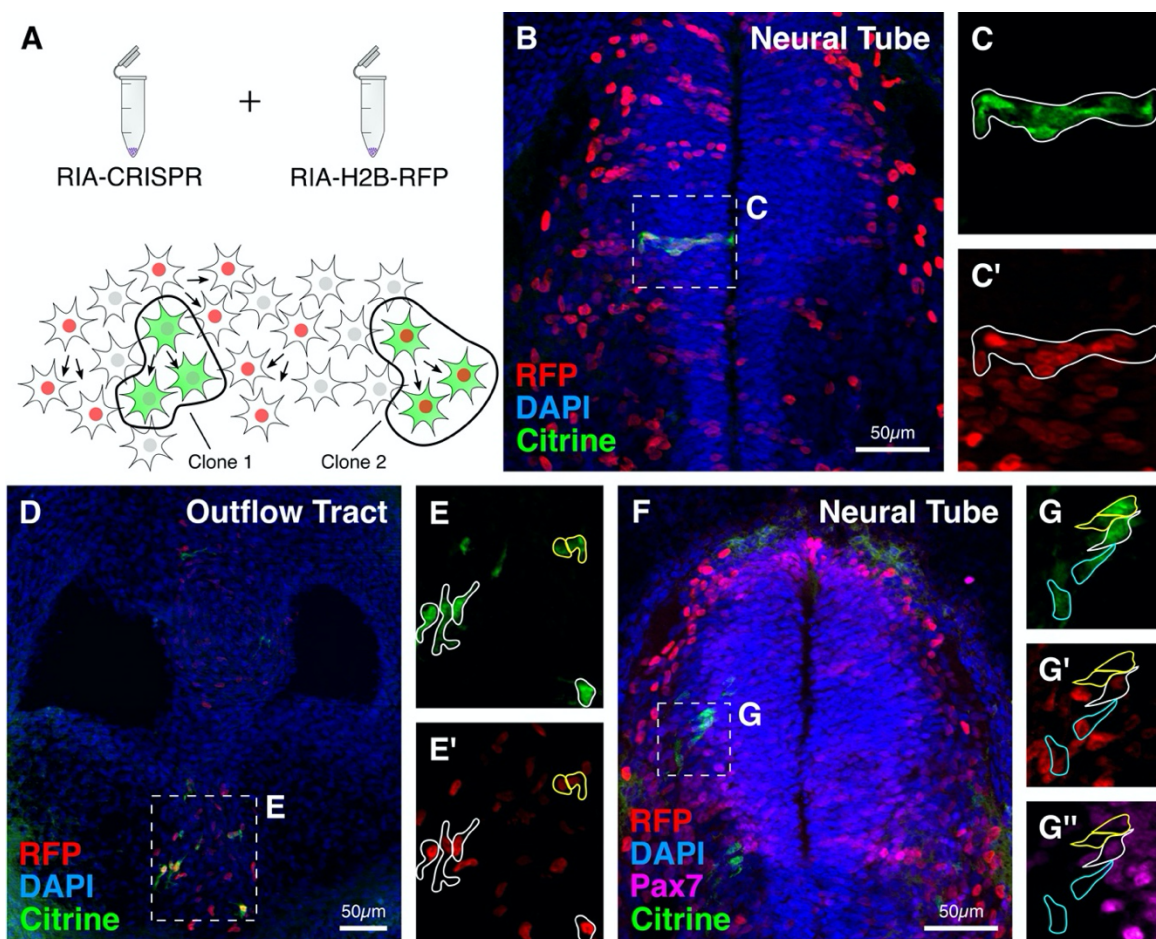


Figure 9. Proof-of-principle experiment to show application of RIA-CRISPR retroviruses for clonal analysis.

A. Experimental design for performing clonal analysis using RIA-CRISPR retroviruses. Clones were identified as single-infected cells with shared fluorescence intensity for Citrine, or double-infected cells with shared fluorescence intensity for Citrine and RFP. **B-E'.** Examples of clonally-related cells observed in the medial neural tube (B) and developing outflow tract (D). In the neural tube, clones were horizontally distributed (C,C'), whereas in the outflow tract, clones were distributed evenly within the aorticopulmonary septum (E,E'). **F.** In a representative embryo, double-labeling with Citrine and RFP, together with intensity of Citrine and RFP and expression levels of Pax7 indicate clonal relationships. **G-G''.** This allowed identification of three distinct clones: outlined in white – high Citrine (G), low RFP (G'), low Pax7 (G''); outlined in cyan – low Citrine (G), high RFP (G'), no Pax7 (G''); outlined in yellow – high Citrine (G), no RFP (G'), no Pax7 (G'').

Following a three-day incubation *in ovo*, embryos were fixed, cryosectioned, and processed for immunostaining, allowing us to identify labeled cells both within the neural tube and in neural crest-derived cells in the periphery. Building upon our previously published work (Tang et al., 2019), we estimated that the probability of infection with the RIA-CRISPR virus alone was 1:10,000, whereas the probability of double infection with the RIA-CRISPR and RIA-H2B-RFP retrovirus was 1:100,000 (detailed in the Materials and methods). Moreover, given that the number and location of integrations varies with each infection event, the progeny of the infected cell share similar levels of fluorescent protein expression, thus facilitating identification of clonally-related cells [Figure 9A]. The labeling in the neural tube was sparse, and we therefore posited that Citrine-positive cells in close proximity and with similar fluorescence intensity, reflecting the integration site, were likely to be clonally related. In rare cases, we also observed cells that were double labeled with RIA-CRISPR and RIA-H2B-RFP retroviruses, and we predicted that these cells also represented a clone. As expected, if *Pax7* was successfully knocked out in a particular cell, the entire clone also lacked *Pax7* expression. If only one allele was targeted, then similar levels of residual *Pax7* expression would be apparent in all clonally related progeny.

Based on these criteria, we identified putative clonally-related cells in both the neural tube [Figure 9B-C] and periphery [Figure 9D-E]. Within the developing spinal cord, immunostaining revealed either no or low levels of *Pax7* expression in Citrine labeled cells [Figure 9G’]. The deletion of only one of the alleles in some cases likely accounts for persistence of *Pax7* expression in some cells. Interestingly, two different double-labeled clones within the neural tube were distinguishable based on their levels of RFP, Citrine, and endogenous *Pax7* protein expression [Figure 9F]. One clone of neural tube cells with high Citrine and low RFP (outlined in white) had low *Pax7* expression [Figure 9G-G’], whereas the other adjacent clone with high RFP but low Citrine (outlined in blue) appeared to lack *Pax7* expression. Together, we identified 18 double-labeled clones across 6 embryos, of which 11 lacked *Pax7* expression. In addition, Citrine+ only clones were identified based on sparse labeling and linear distribution along the coronal plane

within the neural tube (n = 22 Citrine+ only clones), of which 10 lacked Pax7 expression; one such example is outlined in yellow [Figure 9G-G’]. Together, these results demonstrate that long-term lineage analysis can be accomplished with our RIA-CRISPR retroviruses in chick embryos at either the single cell or population level. In principle, our single construct can be incorporated into a number of different viruses, including lentiviral or adenoviral vectors, and can therefore be utilized to assess gene functions in diverse morphogenic events within an otherwise normal embryonic environment in multiple species.

5.3 Conclusions

Cell lineage analysis is an essential tool for following cell fate by marking progenitor cells and determining the cell types into which they differentiate. By combining lineage tracing with perturbation methodologies, one can challenge the cell’s developmental potential and interrogate the role of particular genes in normal developmental processes. Our single plasmid technology enables concomitant delivery of guide RNAs, Cas9 and a fluorescent tag into embryonic cells by electroporation or via replication-incompetent avian retroviral delivery. By targeting genes in the neural tube and neural crest, retina, and segmental plate, we have demonstrated the versatility of our engineered RIA-CRISPR viruses. This single-plasmid approach can also be incorporated in other virus families, including adeno- and lenti-viruses for application in other species. Moreover, we have expanded the application of the CRISPR-Cas9 system to investigations involving live imaging. These modified constructs can be efficiently adapted to several tissues in the developing embryo to study behavior of mutant cells for either short term or long term analysis in their endogenous wildtype environment.

5.4 Acknowledgments

For technical assistance, we thank Andres Collazo and Steven Wilbert with the Caltech Biological Imaging facility of the Beckman Institute. We thank members of the Bronner lab for helpful discussions.

5.5 Author contributions

Conceptualization, S.G. and M.E.B.; Methodology, S.G., Y.L., and M.E.B.; Validation, S.G.; Investigation, S.G., Y.L., J.B.C., H.A.U., W.T., F.M.V., and M.E.B.; Writing – Original Draft, S.G., W.T., H.A.U., and M.E.B.; Writing – Review & Editing, S.G., and M.E.B.; Visualization, S.G. and W.T.; Supervision, M.E.B.; Funding Acquisition, M.E.B.

5.6 Funding

This work is supported by the National Institutes of Health (NIH) grants R01DE027568 to M.E.B. and K99DE029240 to M.L.P., and the American Heart Association (AHA) predoctoral fellowship 18PRE34050063 to S.G.

5.7 Materials and Methods

5.7.1 Chicken embryos

Fertilized chicken embryos (*Gallus gallus*) were commercially obtained from local farms (Sun Valley and AA Laboratory Eggs, Inc) and developed to desired stages as per Hamburger and Hamilton (1951) in humidified incubators set to 37°C. For *ex ovo* experiments, embryos were developed for 18-21h, while for *in ovo* experiments, eggs were incubated for 36-48h to obtain HH10-HH12 embryos. *Ex ovo* electroporations were performed as previously described (Sauka-Spengler and Barembaum, 2008) by passing five 5.2V pulses for 50ms each every 100ms. The electroporated embryos were then cultured in 1mL albumin supplemented with penicillin/streptomycin at 37°C. The next day, the embryos were screened for transfection efficiency (high fluorescence intensity within the neural tube in wholemount embryos), and unhealthy and/or poorly transfected embryos were discarded. All plasmids were injected at a final concentration of 2.5µg/µL. Specific-pathogen-free fertilized chicken eggs were also commercially obtained from Charles River Laboratories and incubated for similar durations as above.

5.7.2 Molecular cloning

The plasmid *CAGG>nls-Cas9-nls-2a-Citrine* (a gift from Tatjana Sauka-Spengler; Addgene plasmid # 92393) was modified by inserting an EcoRI restriction enzyme site downstream of the Citrine sequence. The HH and HDV ribozyme sequences were PCR amplified from the plasmid pUDP044 (a gift from Jean-Marc Daran; Addgene plasmid # 101168), cloned upstream and downstream of the previously published *Pax7* and *Sox10* (Gandhi et al., 2017) or the newly designed *Pax6* protospacer, respectively. This allowed synthesis of the *HH-gRNA^{f/e}-HDV* fragments, which was directionally cloned in the modified *CAGG>nls-Cas9-nls-2a-Citrine* vector [Appendix B]. Finally, the *nls-Cas9-nls-2a-Cit-HH-gRNA-HDV* fragment was digested with *AscI* and *NotI* and cloned in the Replication Incompetent Avian retrovirus backbone (Tang et al., 2019) under the regulation of the RIA promoter.

The following gRNA protospacers were used in this study:

gRNA	Protospacer (5' → 3')
<i>Hs.Cttnb1</i>	CTCCAAGTCCTGTATGAGT
<i>Gg.Cttnb1</i>	AACGCAAGTCCTGTATGAGT
<i>Sox10</i>	gAGATCTTGGTCATCAGCCA
<i>Pax6</i>	GTTACGCCGCTGTGACCTG
<i>Pax7</i>	GGCCAGCGGGGTGGACAct
<i>Control</i>	GCACTGCTACGATCTACACC

5.7.3 Tissue culture transfection experiments

Human osteosarcoma cells (U2OS, ATCC CRL-3455) were cultured in McCoy's 5a Modified Media (ThermoFisher), and chicken fibroblasts (DF-1, ATCC CRL-12203) were cultured in DMEM (Corning), both supplemented with 10% fetal bovine serum (Gibco) and penicillin/ streptomycin (Corning) at 37°C with 5% CO₂. Cells were seeded at a density of 0.04x10⁶ cells per well into ibidi μ -Slide 8-well glass bottom imaging slides (ibidi #80827) and incubated for 48 hours before transfection using Lipofectamine 3000 (Invitrogen). For antibody staining, cells were washed 24 hours post transfection with 1x PBS, then fixed by dropwise addition of ice-cold 100% methanol. Fixed cells were then

washed 2x with TBST+Ca²⁺ (50mM Tris + 150mM NaCl + 1mM CaCl₂ + 0.1% Tween-20), blocked in 10% donkey serum in TBST+Ca²⁺, then incubated in primary antibody solution overnight at 4°C. The following day, cells were washed 3x with TBST+Ca²⁺ then incubated in secondary antibody solution at room temperature for 1h, washed 3x with TBST+Ca²⁺, and imaged using a Zeiss LSM 800 inverted confocal microscope.

5.7.4 Virus preparation and injection

Virus particles were harvested and concentrated using a protocol optimized for large insert size [Appendix C]. Viruses that contained fluorescent reporters were synthesized using previously described protocols. (Li et al., 2019). For the optimizations, chick DF-1 fibroblasts cells were transfected with the RIA-nls-Cas9-nls-2a-Citrine-HH-gRNA-HDV plasmid together with a plasmid encoding VSVG mixed with PEI. The next day after transfection, sodium butyrate was added to the media. 6h later, the media was replaced with fresh DMEM and the cells were given 24h to start producing virus particles. The supernatant was collected every 12 hours for several days and stored at -80°C to enable pooling. Finally, the viruses were concentrated by centrifugation and the pellet dissolved in DMEM on the day of the experiment. 0.5μL of 2% red food dye was added to the virus to enable visualization of the injection solution. *RIA-nls-Cas9-nls-2a-Cit-HH-Sox10.gRNA^{f/e}-HDV* and *RIA-nls-Cas9-nls-2a-Cit-HH-Pax6.gRNA^{f/e}-HDV* viruses were injected *in ovo* into the lumen of the neural tube of HH10 embryos, whereas the *RIA-nls-Cas9-nls-2a-Cit-HH-Pax7.gRNA^{f/e}-HDV* virus was injected in the segmental plate of HH11 embryos. The embryos were developed for 3-5 days following injections, harvested, screened for the expression of Citrine, and processed for cryosectioning and immunostaining.

5.7.5 Clonal analysis in the neural tube with RIA-CRISPR viruses

Pax7-RIA-CRISPR and RIA-H2B-RFP retrovirus were mixed at a volumetric ratio of 10:1 and injected into the lumen of the neural tube in chick embryos at HH12. 72 hours post injection, embryos were fixed with 4% PFA in PB for 30mins at 4 degrees Celsius. To perform clonal analysis, the trunk neural tubes were dissected and imbedded in

gelatin. Transverse cryosections were made across the spinal cord to reveal clonal structures. Subsequently, frozen sections were washed in 1xPBS at 42°C until residual gelatin was removed. Immunohistochemistry was performed using primary antibodies against Citrine, RFP, and Pax7. Slides were counterstained with DAPI to reveal tissue morphology and imaged on a Zeiss Imager M2 with an ApoTome module. All images were processed using Apotome Raw Convert in Zen Blue software. Single infection with the RIA-CRISPR virus and double infection with RIA-CRISPR and RIA-H2B-RFP viruses were both defined as rare clones. Cells distributed horizontally along the neural tube, together with ones that shared similar fluorescence intensity for Citrine, RFP, and/or endogenous Pax7 were identified as clonally-related. Because clones were generally thicker along the anterior-posterior axis than the transverse sections made, cells expressing the same combination of viruses but spanning multiple transverse sections were recorded as a single clone.

5.7.6 Calculating probability of co-infection

The probability of “k” number of infections given a specific multiplicity of infection (MOI) “λ” for each virus can be modeled by a Poisson distribution, such that:

$$P(X = k) = \frac{\lambda^k e^{-\lambda}}{k!}$$

where k = number of infections,

λ = multiplicity of infection.

Typically, the titer of RIA retrovirus prepared using our standard protocol is approximately 10^7 pfu/mL for fluorescent proteins, including the H2B-RFP-encoding retrovirus used in this experiment. Since the RIA-H2B-RFP was diluted at a volumetric ratio of 1:10, the resulting titer of the injected virus was 10^6 pfu/mL. In our previous work where we performed clonal analysis on the trunk neural crest (Tang et al., 2019), we had calculated the volume of virus injected in the embryo to be $0.5\mu\text{L}$, which corresponded to 500 retrovirus particles encoding H2B-RFP. Given that each infection event is

independent, using the Poisson distribution, the probability of a neural tube cell getting infected with the RIA-H2B-RFP retrovirus is calculated to be:

$$P(\text{RIA} - \text{H2B} - \text{RFP}) = \frac{(10^{-1})^1 \cdot 2.7^{-10^{-1}}}{1!} = 0.0911.$$

On the other hand, the increased insert length for the RIA-CRISPR virus results in a titer that is 100-1000 fold lower than that of the RIA-H2B-RFP retrovirus. Therefore, the probability of a neural tube cell getting infected with the RIA-CRISPR retrovirus can be calculated as:

$$P(\text{RIA} - \text{CRISPR}) = \frac{(10^{-4})^1 \cdot 2.7^{-10^{-4}}}{1!} = 0.0001.$$

Finally, the probability of co-infection of a single neural tube cell with both the RIA-H2B-RFP and RIA-CRISPR retroviruses can be calculated as:

$$P(\text{RIA} - \text{H2B} - \text{RFP} \text{ and } \text{RIA} - \text{CRISPR}) = 0.0911 * 0.0001 = 0.00000911.$$

5.7.7 Slice culture and live imaging

Embryos electroporated with *pCAG>nls-Cas9-nls-2a-Cit-HH-Sox10.gRNA^{f+e}-HDV*, *pCAG>H2B-RFP*, and *FoxD3-NC2>Cerulean* plasmids were incubated at 37°C, harvested after 24 hours, and screened for the expression of nuclear RFP that was co-electroporated as a transfection control. Embryos that were poorly transfected were discarded, while the rest were processed as follows: Transverse cuts spanning 2 somites were made through the trunk region using a micro-knife (Fine Science Tools). The slices were washed in ringers and transferred into fluorodish containing prewarmed Neuro-basal media (GIBCO) supplemented with glutamine and PenStrep. The slices were positioned under custom made nylon grids and given 15 minutes to stabilize, after which the whole fluorodish was transferred into the incubation chamber of a Zeiss LSM 800 microscope for time-lapse imaging. Control embryos were processed in the same way as the mutant embryos.

For imaging the tissue slices, one-photon laser excitation was used at wavelengths of 405, 488 and 561nm, respectively. For these experiments, the 20x/0.8 NA M27 objective was used and Z-stacks comprising 25 slices spanning 38.4 μ m were collected every 10 minutes for 11 hours. The images were imported into Imaris to generate movies.

5.7.8 *In situ* hybridization, immunohistochemistry, and hybridization chain reaction

Chromogenic *in situ* hybridization for *Sox10* was performed as previously described (Simões-Costa and Bronner, 2016; Simões-Costa et al., 2015).

For antibody staining of whole-mount embryos, embryos fixed in 4% PFA were washed in 0.1% PBS-Triton, blocked in 10% donkey serum in 0.5% PBS-Triton for 2 hours at room temperature, and incubated in primary antibody solution at 4°C for 2 nights. On the third day, the embryos were washed in 0.5% PBS-Triton (30 minutes per wash, 6 washes) and incubated in secondary antibody solution for 2 nights at 4°C. Stained embryos were then washed in 0.5% PBS-Triton (30 minutes per wash, 6 washes) and processed for imaging and/or cryosectioning.

For antibody staining of cross-sections, slides were degelatinized in 1X PBS for 10 minutes at 42°C, permeabilized in 10% donkey or goat serum in 0.3% PBS-Triton, incubated in primary antibody solution overnight at 4°C, washed the following day in 1X PBS (4 washes, 15 minutes per wash), incubated in secondary antibody solution at room temperature for 1h, washed in 1X PBS twice, soaked in 1x PBS containing 0.1 μ g/mL DAPI for 2 minutes, and washed in 1x PBS followed by distilled water. Fluoromount medium was used to mount coverslips on slides.

Primary antibodies that were used in this study: Mouse anti-Cas9 (diagenode, Cat#C15200216; 1:500), Goat anti-GFP (Rockland, Cat#600-101-215; 1:500), Rabbit anti-GFP (Abcam, Cat#ab290; 1:500), Rabbit anti-Pax6 (Biolegend, Cat#PRB-278P, 1:250), Mouse IgG2b anti-HuC/D (Invitrogen- Cat#A21271; 1:500), Mouse IgG2a anti-Tubb3 (Biolegend, Cat#801201; 1:500), Goat anti-Sox10 (R&D systems, Cat#AF2864,

1:200), Mouse IgG1 anti-Pax7 (Developmental Studies Hybridoma Bank; 1:10), Mouse IgM anti-HNK1 (Developmental Studies Hybridoma Bank; 1:5), Mouse IgG2b anti-Islet1 (Developmental Studies Hybridoma Bank; 1:100), Rabbit anti-Snail2 (Cell Signaling, Cat#95855; 1:200), Mouse IgG2b anti-MF20 (Developmental Studies Hybridoma Bank; 1:100), Mouse IgG1 anti- β -catenin (Abcam, Cat#ab6301; 1:250). Primary antibodies were detected using 1:250 Alexa Fluor 350/488/647-conjugated secondary antibodies (Molecular Probes).

For hybridization chain reaction, the manufacturer's (Molecular Technologies) recommended protocol was used as previously described (Gandhi et al., 2020b).

5.7.9 Cryosectioning and imaging

Whole mount embryos were fixed in 4% paraformaldehyde (PFA) at 4°C for 20 minutes, which was followed by three washes in 1X PBS at room temperature. Fixed embryos were incubated in 5% and 15% sucrose at 4°C for one night each. The following day, embryos were transferred to molten gelatin, incubated at 37°C for one night, embedded in silicone molds, frozen in liquid nitrogen, and stored at -80°C. Embedded embryos were sectioned on a micron HM550 cryostat to obtain 16 μ m or 20 μ m sections. Embryos and sections were imaged on a Zeiss Imager M2 with an ApoTome module. Images were post-processed in FIJI imaging software (Schindelin et al., 2012). For corrected total cell fluorescence (CTCF) calculations, the following formula was used:

$$CTCF = IntegratedDensity - (Selectedarea * Meanbackgroundfluorescence).$$

To count number of Citrine positive cells in individual layers of the chick retina, a median filter was applied to 8-bit images, followed by a Bernsen-based auto local-thresholding method (Bernsen, 1986) and watershed segmentation to identify cell boundaries. To count the number of cells, the "Analyze particles" function was used.

5.7.10 Statistics

For direct comparisons between two conditions, a one-sided pairwise Student's t-test was performed to calculate significance after the conditions for normality were verified. For multiple comparisons, ANOVA followed by Tukey's HSD test correction was employed. Experiments were repeated on different days to ensure uniformity. No data were excluded. Group allocation was random and different batches of fertilized eggs were separately incubated in different incubators and electroporated with fresh DNA solutions.

5.8 References

Andreason, G.L., and Evans, G.A. (1988). Introduction and expression of DNA molecules in eukaryotic cells by electroporation. *Biotechniques* 6, 650–660.

Bernsen, J. (1986). Dynamic Thresholding of Grey-Level Images. In *Proceedings - International Conference on Pattern Recognition*, pp. 1251–1255.

Britsch, S., Goerich, D.E., Riethmacher, D., Peirano, R.I., Rossner, M., Nave, K.A., Birchmeier, C., and Wegner, M. (2001). The transcription factor Sox10 is a key regulator of peripheral glial development. *Genes Dev.* 15, 66–78.

Buckingham, M., Bajard, L., Chang, T., Daubas, P., Hadchouel, J., Meilhac, S., Montarras, D., Rocancourt, D., and Relaix, F. (2003). The formation of skeletal muscle: From somite to limb. *J. Anat.* 202, 59–68.

Canto-Soler, M.V., and Adler, R. (2006). Optic cup and lens development requires Pax6 expression in the early optic vesicle during a narrow time window. *Dev. Biol.* 294, 119–132.

Carney, T.J., Dutton, K.A., Greenhill, E., Delfino-Machín, M., Dufourcq, P., Blader, P., and Kelsh, R.N. (2006). A direct role for Sox10 in specification of neural crest-derived sensory neurons. *Development* 133, 4619–4630.

Chen, B., Gilbert, L.A., Cimini, B.A., Schnitzbauer, J., Zhang, W., Li, G.W., Park, J., Blackburn, E.H., Weissman, J.S., Qi, L.S., et al. (2013). Dynamic imaging of genomic loci in living human cells by an optimized CRISPR/Cas system. *Cell* *155*, 1479–1491.

Chen, C.M.A., Smith, D.M., Peters, M.A., Samson, M.E.S., Zitz, J., Tabin, C.J., and Cepko, C.L. (1999). Production and design of more effective avian replication-incompetent retroviral vectors. *Dev. Biol.* *214*, 370–384.

Chow, R.L., Altmann, C.R., Lang, R.A., and Hemmati-Brivanlou, A. (1999). Pax6 induces ectopic eyes in a vertebrate. *Development* *126*, 4213–4222.

Cong, L., Ran, F.A., Cox, D., Lin, S., Barretto, R., Habib, N., Hsu, P.D., Wu, X., Jiang, W., Marraffini, L.A., et al. (2013). Multiplex genome engineering using CRISPR/Cas systems. *Science* *339*, 819–823.

Corey, D.R., and Abrams, J.M. (2001). Morpholino antisense oligonucleotides: tools for investigating vertebrate development. *Genome Biol.* *2*, 1015.1-1015.3.

Darnell, D.K., and Schoenwolf, G.C. (2000). The chick embryo as a model system for analyzing mechanisms of development. *Methods Mol. Biol.* *135*, 25–29.

Dickinson, D.J., Ward, J.D., Reiner, D.J., and Goldstein, B. (2013). Engineering the *Caenorhabditis elegans* genome using Cas9-triggered homologous recombination. *Nat. Methods* *10*, 1028–1034.

Doh, S.T., Hao, H., Loh, S.C., Patel, T., Tawil, H.Y., Chen, D.K., Pashkova, A., Shen, A., Wang, H., and Cai, L. (2010). Analysis of retinal cell development in chick embryo by immunohistochemistry and in ovo electroporation techniques. *BMC Dev. Biol.* *10*, 8.

Dutton, K.A., Pauliny, A., Lopes, S.S., Elworthy, S., Carney, T.J., Rauch, J., Geisler, R., Haffter, P., and Kelsh, R.N. (2001). Zebrafish colourless encodes *sox10* and specifies non-ectomesenchymal neural crest fates. *Development* *128*, 4113–4125.

Eisen, J.S., and Smith, J.C. (2008). Controlling morpholino experiments: Don't stop making antisense. *Development* *135*, 1735–1743.

Gagnon, J.A., Valen, E., Thyme, S.B., Huang, P., Ahkmetova, L., Pauli, A., Montague, T.G., Zimmerman, S., Richter, C., and Schier, A.F. (2014). Efficient mutagenesis by Cas9 protein-mediated oligonucleotide insertion and large-scale assessment of single-guide RNAs. *PLoS One* *9*, e98186.

Gandhi, S., and Bronner, M.E. (2018). Insights into neural crest development from studies of avian embryos. *Int. J. Dev. Biol.* *62*, 179–190.

Gandhi, S., Piacentino, M.L., Vieceli, F.M., and Bronner, M.E. (2017). Optimization of CRISPR/Cas9 genome editing for loss-of-function in the early chick embryo. *Dev. Biol.* *432*, 86–97.

Gandhi, S., Ezin, M., and Bronner, M.E. (2020a). Reprogramming Axial Level Identity to Rescue Neural-Crest-Related Congenital Heart Defects. *Dev. Cell* *53*, 300-315.e4.

Gandhi, S., Hutchins, E.J., Maruszko, K., Park, J.H., Thomson, M., and Bronner, M.E. (2020b). Bimodal function of chromatin remodeler *hmga1* in neural crest induction and wnt-dependent emigration. *ELife* *9*, e57779.

Gao, Y., and Zhao, Y. (2014). Self-processing of ribozyme-flanked RNAs into guide RNAs in vitro and in vivo for CRISPR-mediated genome editing. *J. Integr. Plant Biol.* *56*, 343–349.

Gu, B., Swigut, T., Spencley, A., Bauer, M.R., Chung, M., Meyer, T., and Wysocka, J. (2018). Transcription-coupled changes in nuclear mobility of mammalian cis-regulatory elements. *Science* *359*, 1050–1055.

Halder, G., Callaerts, P., and Gehring, W. (1995). Induction of ectopic eyes by targeted expression of the *eyeless* gene in *Drosophila*. *Science* *267*, 1788–1792.

Hamburger, V., and Hamilton, H.L. (1951). A series of normal stages in the development of the chick embryo. *J. Morphol.* *88*, 49–92.

He, Y., Zhang, T., Yang, N., Xu, M., Yan, L., Wang, L., Wang, R., and Zhao, Y. (2017). Self-cleaving ribozymes enable the production of guide RNAs from unlimited choices of promoters for CRISPR/Cas9 mediated genome editing. *J. Genet. Genomics* *44*, 469–472.

Hutchins, E.J., and Bronner, M.E. (2018). Draxin acts as a molecular rheostat of canonical Wnt signaling to control cranial neural crest EMT. *J. Cell Biol.* *217*, 3683–3697.

Itasaki, N., Bel-Vialar, S., and Krumlauf, R. (1999). “Shocking” developments in chick embryology: Electroporation and in ovo gene expression. *Nat. Cell Biol.* *1*, E203–E207.

Kelsh, R.N. (2006). Sorting out Sox10 functions in neural crest development. *BioEssays* *28*, 788–798.

Li, Y., Li, A., Junge, J., and Bronner, M. (2017). Planar cell polarity signaling coordinates oriented cell division and cell rearrangement in clonally expanding growth plate cartilage. *ELife* *6*, e23279.

Li, Y., Vieceli, F.M., Gonzalez, W.G., Li, A., Tang, W., Lois, C., and Bronner, M.E. (2019). In Vivo Quantitative Imaging Provides Insights into Trunk Neural Crest Migration. *Cell Rep.* *26*, 1489-1500.e3.

Li, Y., Gonzalez, W.G., Andreev, A., Tang, W., Gandhi, S., Cunha, A., Prober, D., Lois, C., and Bronner, M.E. (2020). Macropinocytosis-mediated membrane recycling drives neural crest migration by delivering F-actin to the lamellipodium. *Proc. Natl Acad. Sci. USA* *117*, 27400–27411.

Ling, I.T.C., and Sauka-Spengler, T. (2019). Early chromatin shaping predetermines multipotent vagal neural crest into neural, neuronal and mesenchymal lineages. *Nat. Cell Biol.* *21*, 1504–1517.

- Liu, W., Khare, S.L., Liang, X., Peters, M.A., Liu, X., Cepko, C.L., and Xiang, M. (2000). All Brn3 genes can promote retinal ganglion cell differentiation in the chick. *Development* *127*, 3237–3247.
- Von Maltzahn, J., Jones, A.E., Parks, R.J., and Rudnicki, M.A. (2013). Pax7 is critical for the normal function of satellite cells in adult skeletal muscle. *Proc. Natl Acad. Sci. USA* *110*, 16474–16479.
- Marquardt, T., Ashery-Padan, R., Andrejewski, N., Scardigli, R., Guillemot, F., and Gruss, P. (2001). Pax6 is required for the multipotent state of retinal progenitor cells. *Cell* *105*, 43–55.
- Martik, M.L., and Bronner, M.E. (2017). Regulatory logic underlying diversification of the neural crest. *Trends Genet.* *33*, 715–727.
- Nakamura, H., and Funahashi, J.I. (2001). Introduction of DNA into chick embryos by in ovo electroporation. *Methods* *24*, 43–48.
- O’Rahilly, R., and Meyer, D.B. (1959). The early development of the eye in the chick *Gallus domesticus* (stages 8 to 25). *Acta Anat. (Basel)*. *36*, 20–58.
- Oron-Karni, V., Farhy, C., Elgart, M., Marquardt, T., Remizova, L., Yaron, O., Xie, Q., Cvekl, A., and Ashery-Padan, R. (2008). Dual requirement for Pax6 in retinal progenitor cells. *Development* *135*, 4037–4047.
- Piacentino, M.L., and Bronner, M.E. (2018). Intracellular attenuation of BMP signaling via CKIP-1/Smurf1 is essential during neural crest induction. *PLoS Biol.* *16*, e2004425.
- Roellig, D., Tan-Cabugao, J., Esaian, S., and Bronner, M.E. (2017). Dynamic transcriptional signature and cell fate analysis reveals plasticity of individual neural plate border cells. *ELife* *6*, e21620.

Rudnicki, M.A., Schlegelsberg, P.N.J., Stead, R.H., Braun, T., Arnold, H.-H., and Jaenisch, R. (1993). MyoD or Myf-5 is required for the formation of skeletal muscle. *Cell* 75, 1351–1359.

Sakoda, T., Kasahara, N., Hamamori, Y., and Kedes, L. (1999). A high-titer lentiviral production system mediates efficient transduction of differentiated cells including beating cardiac myocytes. *J. Mol. Cell. Cardiol.* 31, 2037–2047.

Sauka-Spengler, T., and Barembaum, M. (2008). Chapter 12 Gain- and Loss-of-Function Approaches in the Chick Embryo. *Methods Cell Biol.* 87, 237–256.

Schindelin, J., Arganda-Carreras, I., Frise, E., Kaynig, V., Longair, M., Pietzsch, T., Preibisch, S., Rueden, C., Saalfeld, S., Schmid, B., et al. (2012). Fiji: an open-source platform for biological-image analysis. *Nat. Methods* 9, 676–682.

Sebastián-Serrano, A., Sandonis, A., Cardozo, M., Rodríguez-Tornos, F.M., Bovolenta, P., and Nieto, M. (2012). Pax6 expression in postmitotic neurons mediates the growth of axons in response to SFRP1. *PLoS One* 7, e31590.

Simões-Costa, M., and Bronner, M.E. (2016). Reprogramming of avian neural crest axial identity and cell fate. *Science* 352, 1570–1573.

Simões-Costa, M., McKeown, S.J., Tan-Cabugao, J., Sauka-Spengler, T., and Bronner, M.E. (2012). Dynamic and differential regulation of stem cell factor FoxD3 in the neural crest is encrypted in the genome. *PLoS Genet.* 8, e1003142.

Simões-Costa, M., Stone, M., and Bronner, M.E. (2015). Axud1 Integrates Wnt Signaling and Transcriptional Inputs to Drive Neural Crest Formation. *Dev. Cell* 34, 544–554.

Stewart, R.A., Arduini, B.L., Berghmans, S., George, R.E., Kanki, J.P., Henion, P.D., and Look, A.T. (2006). Zebrafish foxd3 is selectively required for neural crest specification, migration and survival. *Dev. Biol.* 292, 174–188.

- Stolfi, A., Gandhi, S., Salek, F., and Christiaen, L. (2014). Tissue-specific genome editing in zebrafish embryos by CRISPR/Cas9. *Development* *141*, 4115–4120.
- Streit, A., Tambalo, M., Chen, J., Grocott, T., Anwar, M., Sosinsky, A., and Stern, C.D. (2013). Experimental approaches for gene regulatory network construction: the chick as a model system. *Genesis* *51*, 296–310.
- Tang, W., Li, Y., Gandhi, S., and Bronner, M.E. (2019). Multiplex clonal analysis in the chick embryo using retrovirally-mediated combinatorial labeling. *Dev. Biol.* *450*, 1–8.
- Tang, Y., Garson, K., Li, L., and Vanderhyden, B.C. (2015). Optimization of lentiviral vector production using polyethylenimine-mediated transfection. *Oncol. Lett.* *9*, 55–62.
- Tani-Matsuhana, S., Vieceli, F.M., Gandhi, S., Inoue, K., and Bronner, M.E. (2018). Transcriptome profiling of the cardiac neural crest reveals a critical role for MafB. *Dev. Biol.* *444*, S209–S218.
- Teng, L., Mundell, N.A., Frist, A.Y., Wang, Q., and Labosky, P.A. (2008). Requirement for Foxd3 in the maintenance of neural crest progenitors. *Development* *135*, 1615–1624.
- Vieceli, F.M., and Bronner, M.E. (2018). Leukocyte receptor tyrosine kinase interacts with secreted midkine to promote survival of migrating neural crest cells. *Development* *145*.
- Williams, R.M., Senanayake, U., Artibani, M., Taylor, G., Wells, D., Ahmed, A.A., and Sauka-Spengler, T. (2018). Genome and epigenome engineering CRISPR toolkit for in vivo modulation of cis-regulatory interactions and gene expression in the chicken embryo. *Development* *145*, dev160333.
- Witte, O.N., and Baltimore, D. (1977). Mechanism of formation of pseudotypes between vesicular stomatitis virus and murine leukemia virus. *Cell* *11*, 505–511.

Chapter 6

Plasticity at the neural plate border

A modified version of this chapter was published as:

Gandhi, S.#, Hutchins, E.J., Maruszko, K., Park, J.H., Thomson, M., Bronner, M.E.# (2020). Bimodal function of chromatin remodeler *Hmga1* in neural crest induction and Wnt-dependent emigration. *eLife* ; 9:e57779. (# co-corresponding authors)

<https://doi.org/10.7554/eLife.57779>

6.1 Introduction

The neural crest is a vertebrate-specific stem cell population with the capacity to migrate long distances during embryonic development (Bronner and LeDouarin, 2012; Le Douarin, 1980; Simões-Costa and Bronner, 2013). Originating at the neural plate border, these cells occupy the leading edges of the closing neural folds during neurulation. Subsequently, premigratory neural crest cells that initially reside within the dorsal aspect of the developing neural tube undergo an epithelial-to-mesenchymal (EMT) transition in order to delaminate and migrate extensively. Upon reaching their terminal locations within the embryo, neural crest cells differentiate into a plethora of derivatives, including craniofacial cartilage, pigment cells, smooth muscle, and peripheral neurons and glia (reviewed in Gandhi and Bronner, 2018).

A feed-forward gene regulatory network (GRN) underlies the formation of the neural crest, from induction at the neural plate border to final differentiation into a multitude of cell types. This GRN is comprised of transcription factors and signaling pathways, partitioned into developmental modules (Martik and Bronner, 2017; Simões-Costa and Bronner, 2015). Recently, new tools like single-cell RNA sequencing (scRNA-seq) and Assay for Transposase-Accessible Chromatin using sequencing (ATAC-seq) have enabled analysis of the neural crest GRN at a global level, helping to clarify lineage trajectories and elucidate key biological processes therein, ranging from proliferation to differentiation (Williams et al., 2019). These approaches have opened the way to extensive functional analysis of important nodes within the GRN, particularly at early stages of neural crest development, which are less well-studied.

Neural crest formation begins at the gastrula stage, with establishment of the presumptive neural ectoderm bordering the non-neural ectoderm. Quantitative gene expression analysis of gastrula stage chick embryos has revealed a surprisingly high degree of overlap of multiple transcription factors associated with diverse cell types within single cells in the early neural plate border region, ranging from markers characteristic of the neural crest (*Pax7*), to neural (*Sox2*) and placodal (*Six1*) cell types (Roellig et al.,

2017). This is consistent with the possibility that cells in the neural plate border are transcriptionally primed toward multiple cell fates, rather than committed to a particular lineage. What then leads to cell lineage commitment and specification toward neural crest rather than alternative fates, and to their subsequent ability to initiate migration from the neural tube? One possibility is that previously unidentified transcriptional and epigenetic regulators play a critical role in these processes.

In this study, we used scRNA-seq to identify novel transcription factors and chromatin remodelers expressed in neural crest cells of the early chick embryo. We first describe the single-cell transcriptome of early migrating neural crest cells emerging from the hindbrain, with a focus on identifying new transcriptional regulators. One of the genes uncovered in the neural crest cluster was *Hmga1*, a non-histone chromatin remodeler that has known roles in tumor metastasis (Resar et al., 2018), but has been understudied in development. We first characterized the expression and function of *Hmga1* during neural crest development using *in situ* Hybridization Chain Reaction (HCR) and observed *Hmga1* transcripts enriched in the neural crest, with the onset of expression preceding neural crest specification in the neural plate border. To test its functional role in neural crest development, we used plasmid- and protein-based CRISPR-Cas9 strategies to knock out *Hmga1* in neural crest progenitors with temporal precision. The results demonstrate an early role for *Hmga1* in neural crest lineage specification in a *Pax7*-dependent manner, resulting in the downregulation of neural crest specifier genes such as *Snail2*, *FoxD3*, and *Sox10*. Interestingly, loss of *Hmga1* after completion of neural crest specification revealed a distinct set of defects in cranial neural crest emigration and migration. Using *in situ* hybridization and a fluorescent protein-based reporter, we show that this is a consequence of reduced canonical Wnt activity mediated by *Wnt1*, which can be rescued by concomitantly expressing stabilized β -catenin, thus establishing a separate role for *Hmga1* in delaminating neural crest cells as a Wnt pathway activator. Taken together, these results identify a dual role for *Hmga1* in neural crest development with an early effect on neural crest specification and a later effect on initiation of migration

via the canonical Wnt signaling pathway, mechanisms that may be inappropriately redeployed during tumorigenesis.

6.2 Results

6.2.1 Single-cell RNA-seq of early migrating hindbrain neural crest reveals novel transcriptional regulators

Many RNA-seq datasets have sought to examine genes that are enriched in cranial neural crest cells compared with other tissues (Simões-Costa et al., 2014) or axial levels (Martik et al., 2019). However, here we aimed to identify highly expressed transcription factors and chromatin remodelers that may have been missed due to overlapping expression between neural crest cells and surrounding tissues. To this end, gastrula stage Hamburger Hamilton (HH) 4 embryos were electroporated with the neural crest enhancer FoxD3-NC2:eGFP and cultured *ex ovo* until stage HH12 (Hamburger and Hamilton, 1951). The NC2 enhancer labels early migrating neural crest cells (Simões-Costa et al., 2012), thereby facilitating dissection of the region surrounding the rhombomere (r) 6 migratory neural crest stream for dissociation [Figure 1A-A']. To aid downstream analysis and clustering, we introduced an “outgroup” of dissected primary heart tube cells into the single-cell suspension and generated barcoded Gel Bead-In-Emulsions (GEMs) on the 10X Genomics platform. The library was sequenced at a depth of 50,000 median reads/cell to profile a total of 1268 cells, out of which 1241 cells passed the quality control filters [Supplementary Figure 1A-C].

Following mapping and dimensional reduction, the cells split into distinct cellular subtypes [Figure 1B], including five cell types (mesoderm, otic, ectoderm, hindbrain, and neural crest) derived from the dissected tissue, and the spiked-in outgroup (“Heart tube”; *Myf2*⁺, *Tnnt2*⁺). Known genetic markers that were enriched in each population served to distinguish the neural crest subcluster (*Tfap2B*⁺, *ItgB3*⁺) from the surrounding tissues [*i.e.* otic placode (*Cldn3*⁺, *Gbx2*⁺); hindbrain (*Pax6*⁺, *Zic2*⁺); ectoderm (*Epcam*⁺, *Crabp2*⁺); mesoderm (*FoxC2*⁺, *Col1A1*⁺)] [Supplementary Figure 2A-B].

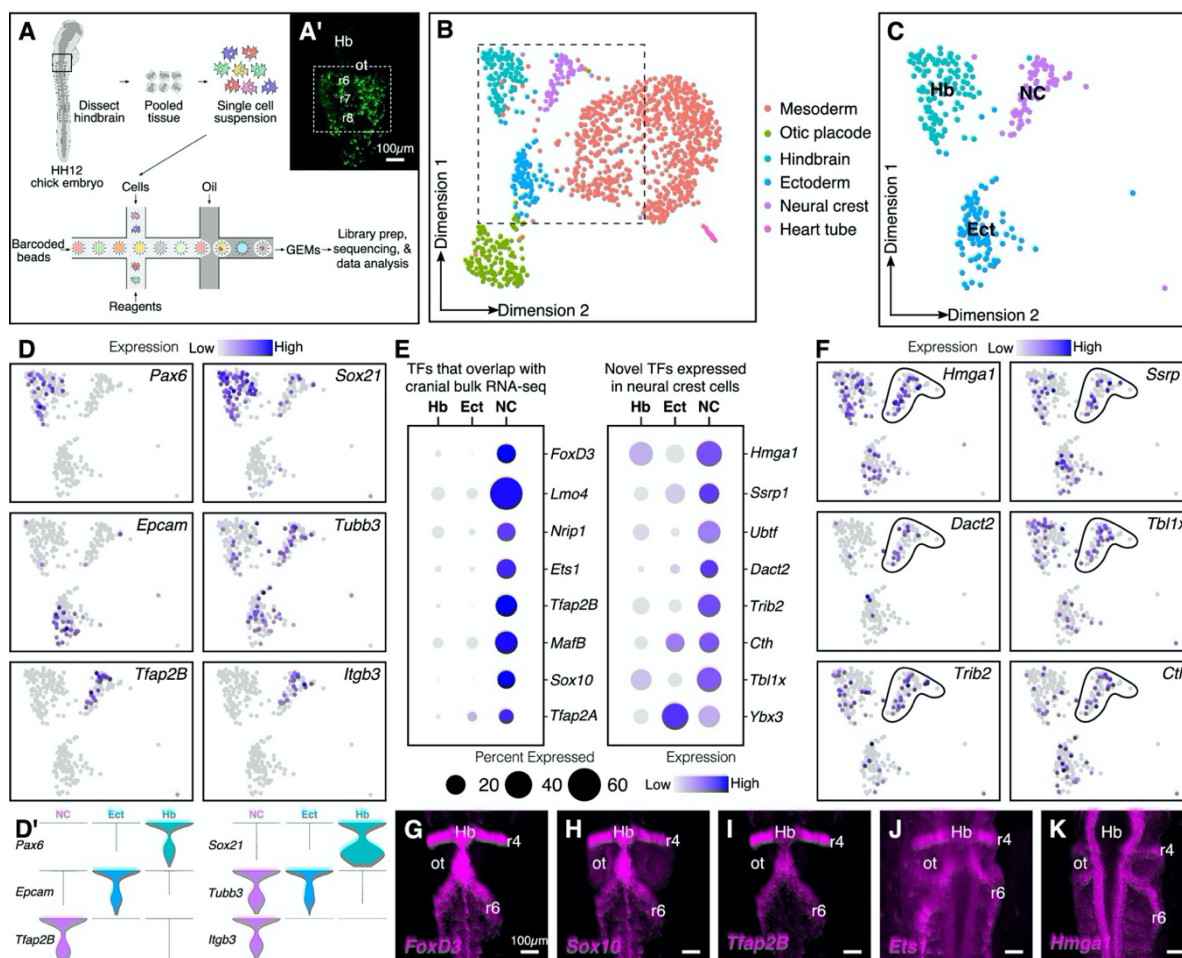


Figure 1: Single-cell (sc) RNA-seq of hindbrain neural crest reveals known and novel transcriptional regulators. **A.** Schematic diagram illustrating the pipeline for performing scRNA-seq on the 10X Genomics platform. Reporter expression mediated by the *FoxD3*-NC2 enhancer (**A'**) was used as reference to dissect the hindbrain of HH12 chick embryos. **B.** Dimensional reduction using UMAP identifies 6 subpopulations (including the spike-in) contained within the dissociated embryonic hindbrain. **C.** Subset of B showing cells from hindbrain (Hb), ectoderm (Ect), and neural crest (NC). **D-D'.** Feature plots used to visualize the expression of known marker genes as a means of identifying subpopulations in (C) in low dimensional space. Single-cell expression distribution for marker genes (D') in each cluster is shown as violin plots. **E.** Genes that were associated with the GO terms "DNA binding," "regulation of transcription," or "transcription factor" were characterized as transcriptional regulators and the relative expression and abundance of a subset of them was visualized as a dot plot. The size of each dot corresponds to the percentage of cells expressing that specific gene in a given cluster, while the color represents the average expression level. **F.** Feature plots showing expression of previously uncharacterized transcription factors or chromatin remodelers expressed in neural crest cells. **G-K.** Hybridization Chain Reaction was used to validate the expression of a few factors that were identified in (E). Dorsal view of the hindbrain of HH12 shows migratory neural crest streams at r4 and r6 surrounding the otic. Hb, hindbrain; ot, otic placode; r, rhombomere; nc, neural crest; ect, ectoderm.

Consistent with the anatomical diversity of the mesoderm, the latter was further subdivided into specific cell types like myocardium (*Hand2⁺*) and paraxial mesoderm (*Prrx1⁺*) [Supplementary Figure 1D-E]. We particularly focused our subsequent analysis on the neural crest cluster in the context of the neighboring tissues of hindbrain and ectoderm [Figure 1C,D,D’]. We sought to determine all transcription factors and chromatin regulators that were expressed in the neural crest-specific subcluster, regardless of their expression in other cell types. To this end, we shortlisted all genes associated with the gene ontology terms “DNA-binding,” “regulation of transcription,” and “transcription factor.” This revealed several chromatin remodelers and transcription factors with high levels of expression in neural crest cells [Figure 1E; Supplementary Figure 2C]. The identified genes fell into two groups, the first of which was comprised of transcription factors enriched in neural crest cells, with little overlap in surrounding cell types. As expected, many of these genes, including *Sox10*, *Ets1*, *MafB*, and *Nrip1*, are known for their expression in the neural crest (Gandhi et al., 2020; Tani-Matsuhana et al., 2018). Importantly, the second group was comprised of chromatin remodelers and/or transcriptional regulators previously overlooked in bulk transcriptomic datasets, including *Hmga1*, *Dact2*, *Ssrp1*, and *Tbx11x*, due to overlapping expression in other tissues. Indeed, their distribution in low dimensional space confirmed that a high proportion of cells in the hindbrain and/or ectoderm also expressed these genes [Figure 1F]. The expression of a subset of the above genes was validated at HH12 [Figure 1G-K] by *in situ* Hybridization Chain Reaction (HCR), which revealed an abundance of transcripts in both r4 and r6 neural crest streams that emerge from the hindbrain. Taken together, the results show that our single-cell gene expression analysis is sufficient to resolve the underlying heterogeneity of the chick hindbrain. We also identified several genes expressed in migrating neural crest cells not highlighted in previous datasets given their broad expression in other tissues.

6.2.2 *Hmga1* is expressed in the neural plate, neural plate border, and neural crest cells

Of the novel transcriptional regulators that were previously overlooked in bulk transcriptomic datasets, we were particularly intrigued by the chromatin remodeler *Hmga1*, due to its extensively studied role in tumorigenesis. A member of the High Motility Group A (HMGA) superfamily, *Hmga1* encodes a small, nonhistone chromatin remodeling protein that binds to the minor groove of DNA, thereby affecting the chromatin landscape and facilitating the binding of other transcription factors in the opposing major groove (Grosschedl et al., 1994). In developing mouse embryos, *Hmga1* has been shown to have widespread expression across several tissues, including the brain, where its loss has been correlated with reduced developmental potential of neural precursor cells (Kishi et al., 2012). While well-studied in cancer (Masciullo et al., 2003; Sarhadi et al., 2006), little was known about its developmental function in neural crest cells. Given the parallels between the mechanisms that regulate delamination, migration, proliferation, and survival of neural crest cells and tumor cells (Ahsan et al., 2017), we sought to characterize the expression of *Hmga1* during neural crest development.

At HH12, *Hmga1* was observed in migrating neural crest streams emanating from rhombomeres 4 and 6 [Figure 1K], and in the cranial mesenchyme, suggesting that its expression is not restricted to the hindbrain neural crest. Therefore, to determine its spatiotemporal pattern at early stages of neural crest development, we performed HCR for *Hmga1* at stages ranging from gastrulation (HH4), when neural crest cells are undergoing induction in the neural plate border [Figure 2B'''], to HH10, when neural crest cells have delaminated from the dorsal neural tube [Figure 2E'''] and are mid-migration in the cranial region [Figure 2F''']. As an early marker for the neural plate border and neural crest (Basch et al., 2006), we co-labeled *Pax7* transcripts at the aforementioned stages.

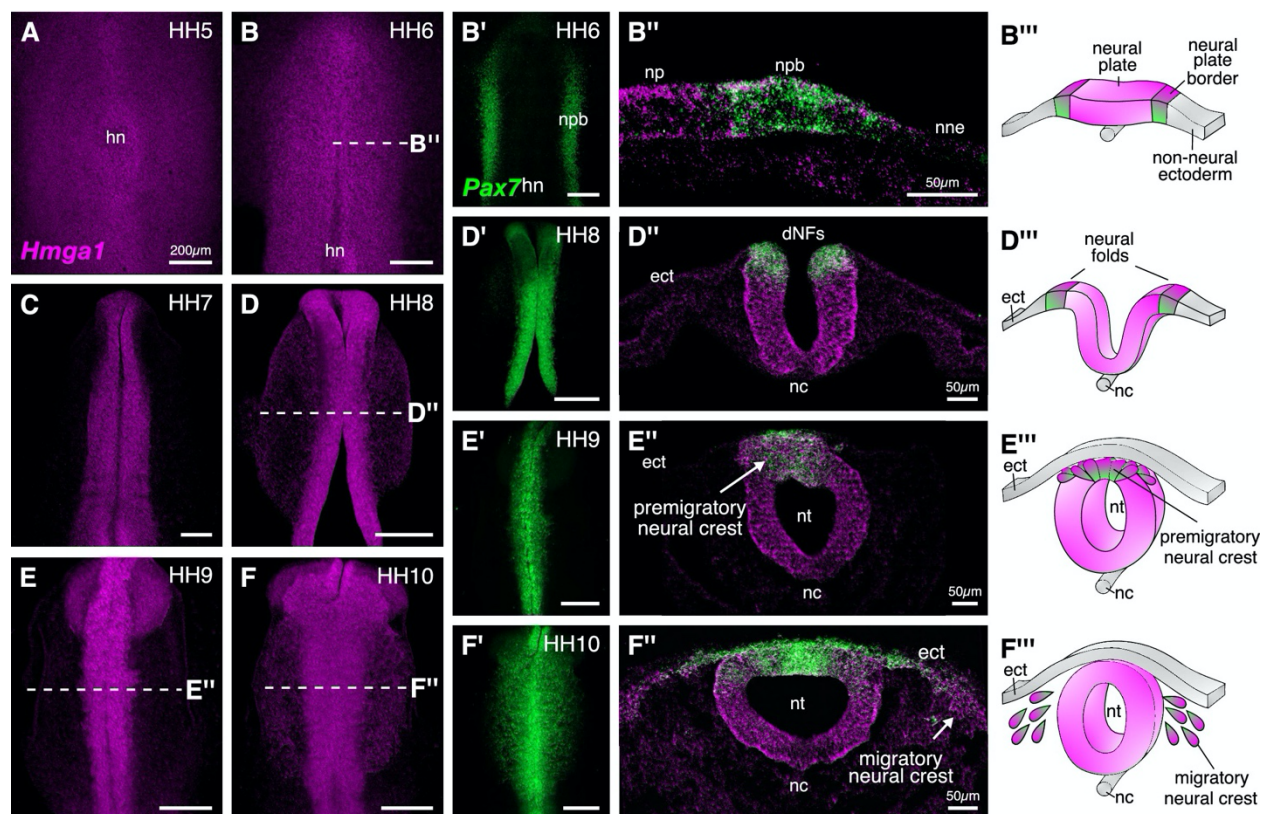


Figure 2: *Hmga1* is expressed in the neural plate, neural plate border, and premigratory and migratory neural crest cells. **A.** HCR against *Hmga1* at HH5 reveals expression in the neural plate and neural plate border. **B-B'**. A wildtype HH6 chick embryo double-labeled with *Hmga1* (B) and *Pax7* (B') probes. *Hmga1* expression overlaps with *Pax7* in the neural plate border. **B''-B'''**. Transverse section through the embryo in (B) shows *Hmga1* and *Pax7* transcripts in the neural plate and neural plate border, respectively, but not the non-neural ectoderm. **C-D'**. As the neural folds elevate, *Hmga1* expression is retained in the dorsal neural tube. **D''-D'''**. Transverse section through the embryo in (D) shows *Hmga1* transcripts in the neural tube. **E-F**. As neural crest cells delaminate (E'') and migrate laterally from the neural tube (F'''), *Hmga1* is expressed in emigrating (E'') and migrating neural crest cells (F''), along with *Pax7* (E' and F'). Arrow points towards delaminating (E'') and migrating (F'') cranial neural crest cells. hn, Hensen's node; npb, neural plate border; np, neural plate; nne, non-neural ectoderm; ect, ectoderm; dNF, dorsal neural folds; nc, notochord; nt, neural tube.

Hmga1 transcripts were first detected in the neural plate and neural plate border, but not in the non-neural ectoderm at HH4+, and preceded the expression of *Pax7* in the neural plate border. *Hmga1* expression remained high at HH5-6 [Figure 2A-B], overlapping in the neural plate border [Supplementary Figure 3A] with *Pax7* transcripts [Figure 2B'], as observed in transverse sections [Figure 2B'', Supplementary Figure 3B-B']. As the neural plate border elevated to form neural folds between HH7 and HH8 [Figure 2D'''], expression of *Hmga1* was retained in the neural tube [Figure 2C-D] and continued to overlap with *Pax7* in the dorsal neural folds [Figure 2D', Supplementary

Figure 3C-D’]. Between stages HH9 and HH10, when neural crest cells delaminated from the dorsal neural tube [Figure 2E’”] and started migrating laterally [Figure 2F’”], *Hmga1* expression was retained in delaminating [Figure 2E,E’,E”, Supplementary Figure 3E-F’] and migrating [Figure 2F,F’,F”, Supplementary Figure 3G-H’] neural crest cells. Interestingly, transverse sections through a representative HH10 embryo revealed that within the migrating neural crest stream, *Hmga1* was expressed in both leader and follower cells, as compared to *Pax7*, which appeared to be downregulated in the leader cells [Figure 2F’”]. Together, these results show that the onset of *Hmga1* in the neural crest occurs in precursors at the neural plate border region prior to their specification, and is retained in premigratory and migrating neural crest cells.

6.2.3 *Hmga1* is necessary for neural crest specification

Given that *Hmga1* transcripts were enriched in the cranial neural crest, we sought to interrogate its possible role therein. To this end, we designed guide RNA plasmids (gRNAs) targeting the coding sequence of *Hmga1* [Supplementary Figure 4A] and electroporated them together with constructs encoding Cas9 and nuclear RFP on the right side of HH4 gastrula stage embryos [Figure 3A]. The left side of the embryo was electroporated with Cas9, nuclear RFP, and a control gRNA, chosen for its lack of binding in chick cells (Gandhi et al., 2017). Embryos were cultured *ex ovo* until stage HH9/9+ [Figure 3B], after which they were processed for immunohistochemistry, *in situ* hybridization, and HCR.

We first validated our knockout approach by probing for the expression of *Hmga1* itself in knockout embryos using HCR. This revealed a significant reduction in the abundance of *Hmga1* transcripts on the knockout side [Figure 3C]. We quantified this phenotype in whole-mount embryos and observed a 25% reduction in *Hmga1* expression [Figure 3D; $p < 0.05$, Wilcoxon rank test]. Notably, the loss of *Hmga1* transcripts in the neural crest was more dramatic than in the neural tube, due to targeted electroporation of knockout reagents to the presumptive neural plate border region.

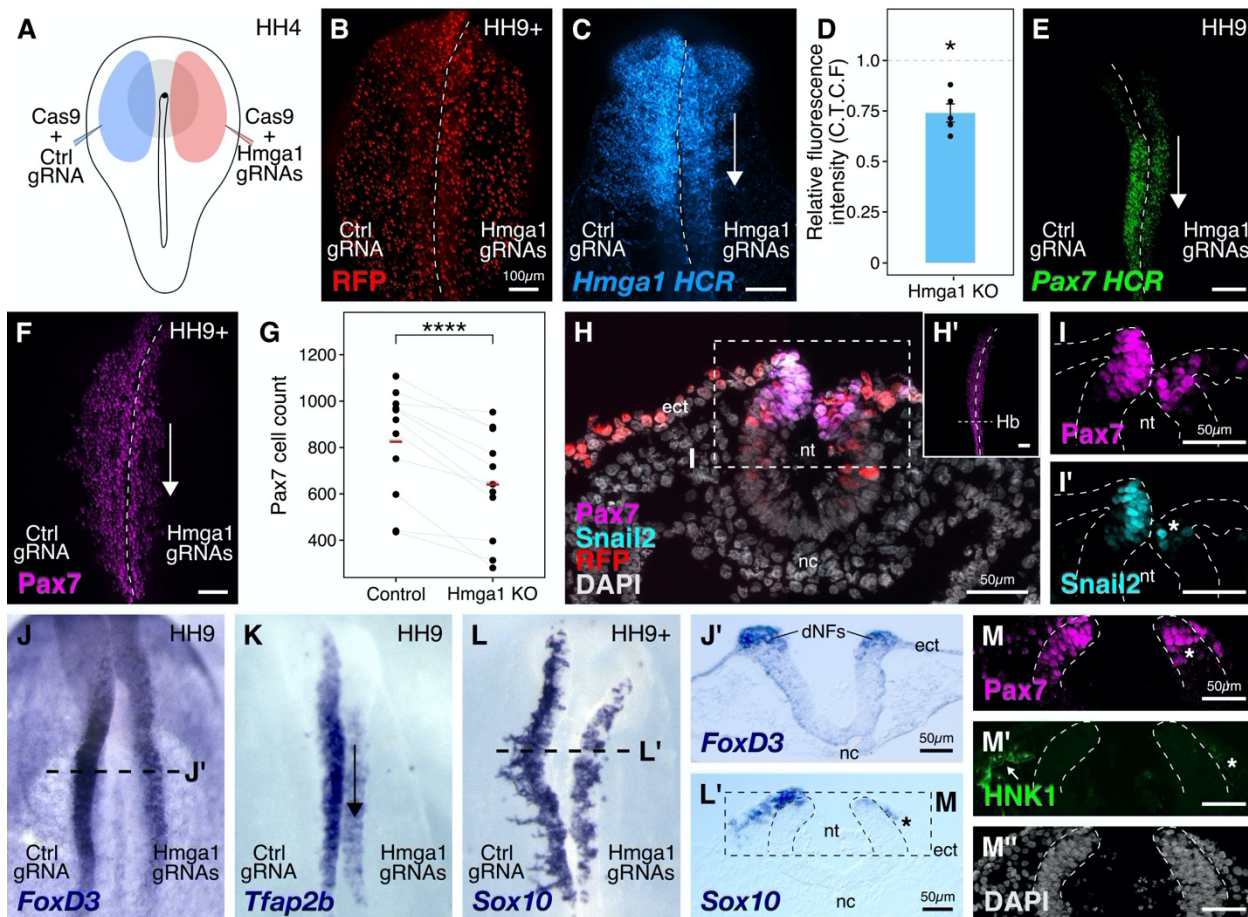


Figure 3: *Hmga1* knockout results in loss of neural crest specification. **A.** The electroporation strategy for knocking out *Hmga1* using CRISPR-Cas9 in gastrula stage chick embryos. **B.** Electroporated embryos were allowed to develop until HH9+ and screened for the expression of H2B-RFP. **C.** Electroporation of Cas9 and *Hmga1* gRNAs on the right side resulted in loss of *Hmga1* transcripts in the neural crest as confirmed using HCR. **D.** *Hmga1* expression in the neural crest quantified as corrected total cell fluorescence (CTCF) intensity in wholemount *Hmga1*-mutant embryos processed for HCR. A significant reduction in expression was observed (p -value <0.05 , Wilcoxon rank test) on the experimental compared to the control side. A ratio of 1 (dotted line) corresponds to similar levels of *Hmga1* expression on both sides. **E-F.** *Hmga1* knockout results in reduced *Pax7* expression in the neural crest, likely resulting from a significant reduction in *Pax7*+ cell count (F) on the knockout compared to the control side (**** p <0.0001 , Student's t-test). **G-H.** Transverse section through the hindbrain of a representative knockout embryo (G') was stained for *Pax7* (H) and the neural crest specifier *Snail2* (H'). **I.** *Hmga1* knockout also resulted in a reduction of *Pax7* transcripts on the knockout side. **J-L.** *Hmga1*-mutant embryos were processed for *in situ* hybridization against neural crest specifier genes *FoxD3* (J, J'), *Tfap2b* (K), and *Sox10* (L, L'). **M.** Transverse section through a representative embryo probed for the expression of *Sox10* showed reduced expression of the migratory neural crest marker, HNK1. The expression of *Pax7* (M') was also reduced, while the thickness of the neural tube remained unchanged (M'').

Next, we investigated the effect of knocking out *Hmga1* on *Pax7* expression in neural crest cells. We examined *Pax7* mRNA expression by HCR in embryos where *Hmga1* was knocked out on the right side, relative to the left side which served as an internal control. Consistent with their hierarchical onset of expression, loss of *Hmga1*

resulted in a notable reduction in *Pax7* mRNA levels [Figure 3E]. Next, we assessed whether the reduction in *Pax7* transcripts would consequently result in a loss of Pax7 protein in the neural crest by immunostaining *Hmga1*-knockout embryos with a Pax7 antibody. As expected, Pax7 protein levels were dramatically reduced in the migratory cranial neural crest [Figure 3F,H'], with further analysis revealing a significant decrease in the number of Pax7+ cells on the knockout side compared to the control side [Figure 3G; $p < 0.0001$, Student's t-test]. Moreover, in the absence of *Hmga1*, cranial neural crest cells failed to migrate properly, as depicted by the expression of the migratory neural crest marker HNK1 [Supplementary Figure 4B]. A transverse section through the hindbrain [Figure 3H] of another representative *Hmga1*-knockout embryo stained for Pax7 [Figure 3H'] revealed a notable reduction in the expression of Pax7 [Figure 3I] as well as the neural crest specifier *Snail2* on the knockout side [Figure 3I']. Furthermore, using *in situ* hybridization, we found that other neural crest specifier genes including *FoxD3* [Figure 3J,J', Supplementary Figure 4D,E',E''], *Tfap2b* [Figure 3K], *Sox10* [Figure 3L,L'], and *c-Myc* [Supplementary Figure 4C] were also downregulated on the knockout side. In transverse sections through *Hmga1*-knockout embryos labeled for *Sox10* expression [Figure 3L], we also detected fewer Pax7+ cells [Figure 3N] and diminished levels of HNK1 expression [Figure 3M]. On the other hand, no notable difference in the thickness of the neural tube was observed [Figure 3H,J',M'', Supplementary Figure 4E], suggesting that the targeted knockout of *Hmga1* in the neural plate border affected the neural folds/dorsal neural tube but not the neural plate itself. Taken together, our results indicate that *Hmga1* is important for proper specification of neural crest cells.

6.2.4 *Hmga1* regulates expression of *Pax7* in neural crest precursors in the neural plate border

As the expression of *Hmga1* precedes that of *Pax7* in the neural plate border, and its loss also causes a reduction of *Pax7* levels in neural crest cells [Figure 3F], we next asked if this regulation occurs in the neural crest precursors that reside in the neural plate border. In the preceding experiments, we characterized the expression of neural crest markers following CRISPR-plasmid-mediated loss of *Hmga1* at stages corresponding to

early stages of neural crest emigration and migration. However, one caveat to our plasmid knockout strategy is that it takes time after electroporation of the CRISPR constructs in gastrula stage embryos for Cas9 to transcribe, translate, and properly fold to form a functional Cas9-gRNA complex. As specification of neural crest cells at the neural plate border is ongoing at HH4, this means that functional Cas9 would not be available until well after initial electroporation. Given that neural crest development occurs in a rostral-to-caudal wave along the body axis (Gandhi and Bronner, 2018), we speculated that effects of plasmid electroporation would be more penetrant in the hindbrain compared to anterior regions of the embryo, such as the midbrain. To test this possibility, we generated transverse sections through the midbrain [Figure 4A] and hindbrain [Figure 4B] of *Hmga1*-knockout embryos and quantified the number of Pax7+ cells as a ratio of cell count on the experimental versus control sides. Accordingly, we noticed that while this ratio was 0.948 ± 0.036 (n=5) at the midbrain level, it was significantly reduced in the dorsal hindbrain, with a mean ratio of 0.69 ± 0.08 (n=5; $p < 0.05$, paired Student's t-test) [Figure 4C]. These results supported our assumption that specification may have already occurred at the midbrain level by the time Cas9 was functionally active.

To circumvent this issue and test the earliest effects of knocking out *Hmga1* concomitant with its onset of expression, we turned to an alternative CRISPR knockout strategy that enabled the loss of *Hmga1* immediately after transfection. To this end, we electroporated recombinant Cas9 protein with *in vitro*-transcribed *Hmga1* or control gRNA as ribonucleoprotein (RNP) complexes on the right and left sides of gastrula stage embryos, respectively [Figure 4D], and cultured embryos *ex ovo* until HH6. First, to validate the Cas9-protein-mediated knockout strategy, we labeled *Hmga1* transcripts in knockout embryos using HCR and observed a very efficient reduction in *Hmga1* expression [Figure 4E], especially in the neural plate border, thereby offering precise temporal control over the loss of this gene's activity.

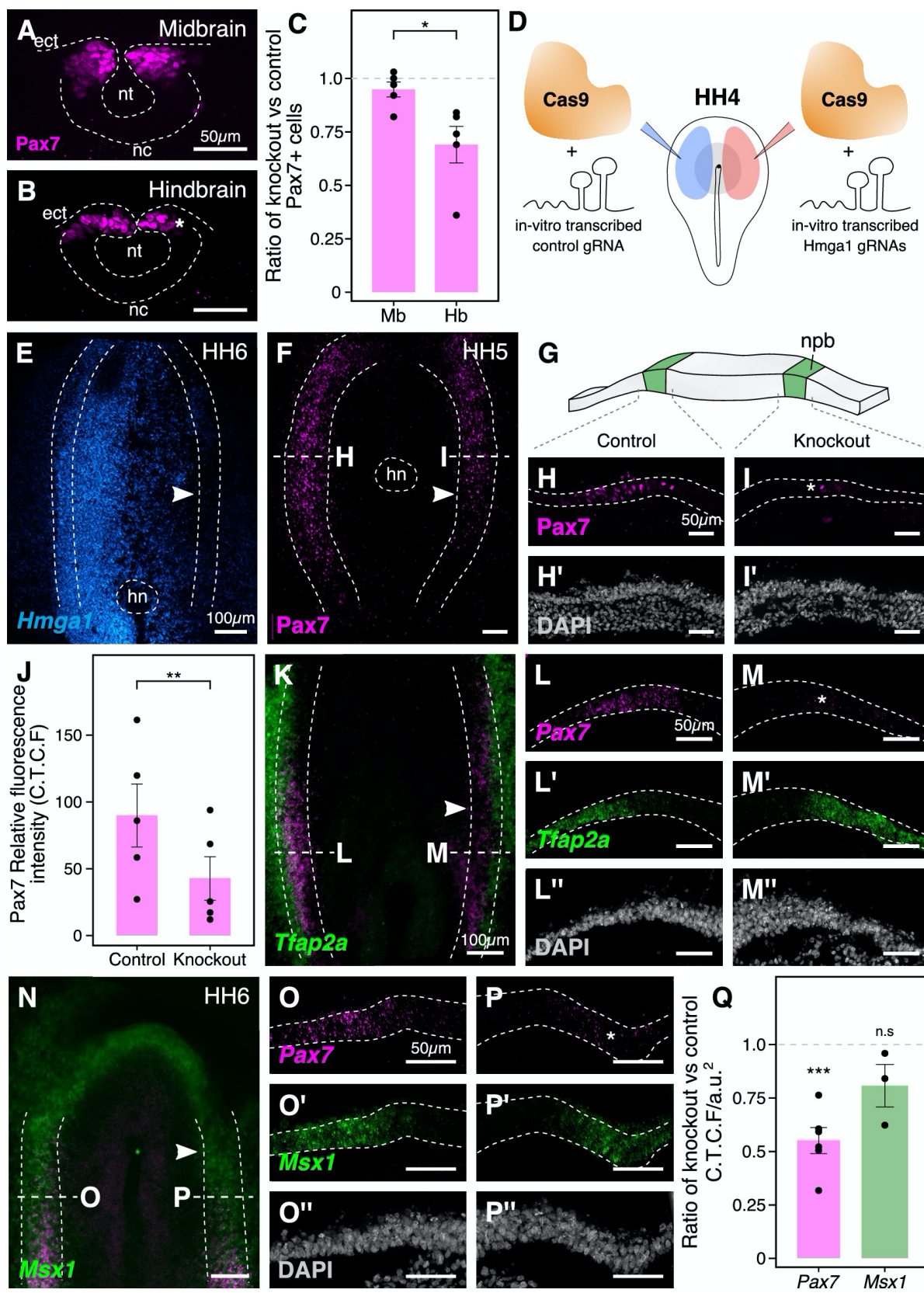


Figure 4. See next page for legend.

Figure 4: The effects of *Hmga1* knockout on neural crest specification are Pax7-dependent. **A-B.** Transverse sections through a representative embryo show a dramatic reduction in the number of Pax7+ cells in the hindbrain (B, asterisk) as compared to the midbrain (A) at HH9/9+. As the hindbrain develops later than the midbrain due to the anterior-posterior progression of neural development, the effect on neural crest specification is more penetrant in the hindbrain (asterisk) due to the time lag between Cas9 plasmid electroporation and its activation in transfected cells. **C.** The ratio of Pax7+ cells between the experimental and control sides quantified at the midbrain and hindbrain levels is significantly different (* $p < 0.05$; Student's t-test). A ratio of 1 (dotted line) corresponds to a similar number of Pax7+ cells on both sides. **D.** Electroporation strategy for knocking out *Hmga1* using Cas9 protein and *in vitro*-transcribed gRNAs. This strategy was used to immediately reduce the levels of *Hmga1* on the knockout side. **E.** HCR against *Hmga1* in mutant embryos shows dramatic transcriptional reduction on the experimental side (arrowhead). **F.** Cas9-protein-mediated loss of *Hmga1* resulted in downregulation of Pax7 expression in the neural plate border on the right side (experimental side; arrowhead). **G.** Illustration of the neural plate border. **H-I'.** Transverse section through embryo shown in F. Electroporation of the control ribonucleoprotein (RNP) complex had no effect on the expression of Pax7 in the neural plate border (H), whereas the knockout side showed an almost complete loss (I, asterisk). No difference in the thickness of the neural plate border was observed between the two sides (H',I'). **J.** Quantification of relative fluorescence intensity for Pax7 signal calculated as corrected total cell fluorescence (C.T.C.F) revealed a statistically significant difference between the control (left) and knockout (right) sides (** $p < 0.01$, paired Student's t-test). **K-P''.** Representative *Hmga1*-mutant embryos that were processed for HCR against neural plate border genes *Tfap2a* (K; experimental side - arrowhead) and *Msx1* (N; experimental side - arrowhead). While *Hmga1* loss resulted in reduction of *Pax7* transcripts on the experimental sides (M,P; asterisk) compared to the control sides (L,O), the expression of *Tfap2a* (L',M') and *Msx1* (O',P') was relatively unchanged. No notable difference was observed in the thickness of the neural plate border (L'',M'',O'',P''). **Q.** Transcriptional response to the loss of *Hmga1* was quantified as the ratio of knockout versus control C.T.C.F per unit area. While *Pax7* expression was significantly reduced (***) $p < 0.001$, paired Student's t-test), no significant difference in *Msx1* expression was observed (n.s. $p > 0.05$, paired Student's t-test). Dotted line represents unperturbed ratio.

Next, we assayed for the expression of Pax7 in the neural plate border by immunostaining *Hmga1*-knockout embryos and found that the levels of Pax7 protein in the neural plate border [Figure 4F, Supplementary Figure 5A] were severely downregulated. Transverse sections through the experimental compared with control sides revealed that neural plate border cells no longer expressed Pax7 after the loss of *Hmga1* [Figure 4H,I], and that this was not a result of premature apoptosis or aberrant cell proliferation [Supplementary Figure 5B-G']. In further support of the latter, the thickness of the neural plate border remained unchanged [Figure 4H',I']. We also quantified the corrected Pax7 total fluorescence intensity (C.T.C.F) in the neural plate border and observed a statistically significant difference between the control and knockout sides ($p < 0.01$, paired Student's t-test), with mean Pax7 intensity on the control side being 89.853 ± 23.388 a.u. (n=5) as compared to 42.763 ± 16.079 a.u. (n=5) on the knockout side [Figure 4J, Supplementary Figure 5H]. Taken together, these results suggest that *Hmga1* is required for the expression of Pax7 in neural crest precursors that are induced in the neural plate border.

6.2.5 *Hmga1* is not required for expression of neural plate border genes *Msx1* or *Tfap2a*

The neural plate border was initially thought to contain discrete domains corresponding to neural, neural crest, placodal, and epidermal precursors. However, recent work has demonstrated that cells in this region co-express genes characteristic of different cell fates and exhibit a broad developmental potential, suggesting they are not restricted to individual cell fates until later in development (Roellig et al., 2017). In chick embryos, *Tfap2a* and *Msx1* are expressed in the neural plate border, with *Tfap2a* transcripts spanning both the neural plate border and the non-neural ectoderm (De Croz e et al., 2011; Luo et al., 2003), whereas *Msx1* transcripts are expressed within a subset of Pax7+ cells in the neural plate border region (Khudyakov and Bronner-Fraser, 2009). Given that loss of *Hmga1* resulted in a reduction in Pax7 protein levels in the neural plate border, we asked if this was a result of a general neural plate border defect versus a selective effect on *Pax7*. To test this, we examined the expression of *Tfap2a* [Figure 4K] and *Msx1* [Figure 4N] transcripts together with *Pax7* using HCR in *Hmga1*-knockout embryos developed to neurula stages. Consistent with the loss of Pax7 protein in the neural plate border, *Hmga1* knockout caused reduced *Pax7* mRNA levels on the experimental [Figure 4M,P] compared to the control [Figure 4L,O] sides. However, the expression of *Tfap2a* [Figure 4L',M'] and *Msx1* [Figure 4O',P'] was retained in the absence of *Hmga1*, together with no noticeable difference in the thickness of the neural plate border [Figure 4L'',M'',O'',P'']. Since *Pax7* and *Msx1* are specifically expressed in the neural plate border, we quantified the corrected total cell fluorescence intensity per unit area associated with their transcripts and calculated the ratio between the experimental and control sides. Under control conditions, this ratio would be close to 1. However, for *Pax7*, the mean calculated ratio was 0.552 ± 0.06 (n=6), with a statistically significant difference between the experimental and control sides ($p < 0.001$, paired Student's t-test). On the other hand, while the mean calculated ratio for *Msx1* was 0.809 ± 0.098 (n=3), the fluorescence intensities were not significantly different between

the two sides [Figure 4Q]. Taken together, these results show that *Hmga1* specifically regulates *Pax7* expression at the neural plate border.

6.2.6 *Hmga1* and *Pax7* rescue the effects of losing *Hmga1* on neural crest specification

Given that loss of *Hmga1* affects neural crest specification, we asked if its overexpression would have the converse effect. To exogenously provide *Hmga1*, we designed a plasmid construct containing the coding sequence of *Hmga1* under the regulation of a ubiquitous enhancer/promoter combination [Figure 5A]. This construct also contained the coding sequence for nuclear RFP downstream of an Internal Ribosome Entry Site (IRES), allowing identification of successfully transfected cells. To test the effect of overexpressing *Hmga1*, we electroporated this construct on the right side of gastrula stage embryos and cultured them *ex ovo* until HH9+. The left side served as an internal control and was electroporated with an equal concentration of a construct encoding nuclear RFP alone [Figure 5B]. The results show that, rather than having the opposite effect to loss of function, overexpression of *Hmga1* also resulted in a notable reduction in *Pax7* expression on the experimental side [Figure 5C]. This suggests that maintaining appropriate levels of *Hmga1* is critical for proper neural crest specification.

The gold standard to demonstrate specificity for loss-of-function experiments is to perform a rescue. We posited that if modulating the levels of *Hmga1* was important for neural crest formation, then exogenous expression of *Hmga1* in an *Hmga1*-knockout background should successfully rescue neural crest cell numbers. Since the Protospacer Adjacent Motifs (PAMs) adjacent to both *Hmga1* gRNAs are located in the introns [Supplementary Figure 4A], the coding sequence on the plasmid would be guarded against the endonuclease activity of Cas9. To test our hypothesis, we knocked out *Hmga1* using CRISPR plasmids as described above, but co-electroporated the “rescue” construct on the right side. The left side was electroporated with an equal concentration of a plasmid encoding nuclear RFP.

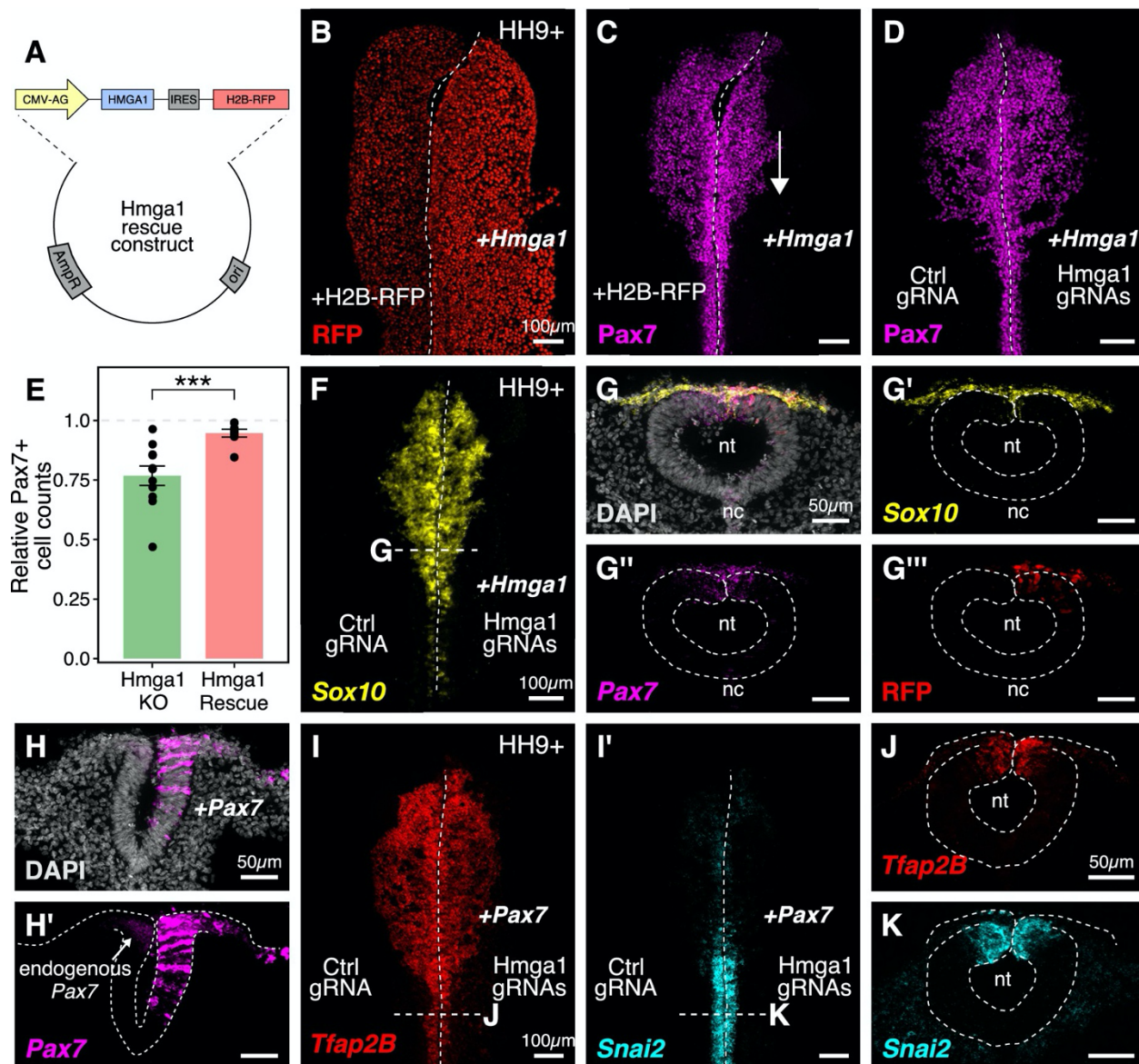


Figure 5: Ectopic expression of Hmga1 or Pax7 rescues cranial neural crest specification. **A.** Plasmid construct used to rescue *Hmga1*. An independent ribosome entry site (IRES) controls translation of nuclear RFP in transfected cells. The electroporation strategy for knocking out *Hmga1* using CRISPR-Cas9 in gastrula stage chick embryos. **B.** Embryos were electroporated with the “rescue” construct on the right side and a control nuclear RFP plasmid on the left side. **C.** Exogenous expression of the *Hmga1* coding sequence under the regulation of a ubiquitous enhancer/promoter combination causes cranial neural crest migration defects. **D-G'''**. Overexpression of the coding sequence (G''') of *Hmga1* compensates for its loss of function, rescuing proper cranial neural crest migration (D), as assayed by number of Pax7-positive neural crest cells (E), and expression of the neural crest specifier gene *Sox10* (F) in migratory cranial neural crest (G,G') and Pax7 in the dorsal neural tube (G''). Electroporated embryos were allowed to develop until HH9+ and screened for the expression of H2B-RFP. **H-H'**. The coding sequence for Pax7 was ectopically expressed in an *Hmga1*-knockout background. Transverse section through a representative embryo shows the comparison between endogenous (left) and overexpressed (right; arrow) Pax7 transcript levels in the dorsal neural tube. **I-K.** Ectopic expression of Pax7 rescued neural crest specification defects caused by the loss of *Hmga1* as assayed by the expression of neural crest specifier genes *Tfp2b* (I) and *Snai2* (I') in transverse cross-sections through the hindbrain (J,K). nt, neural tube; nc, notochord.

Embryos cultured to HH9+ and immunostained for Pax7 revealed that overexpression of *Hmga1* concomitant with knocking out the endogenous gene successfully rescued Pax7 levels in cranial neural crest cells [Figure 5D]. To quantify the extent of rescue, we calculated the ratio of the number of Pax7+ cells on the experimental versus control sides in both wholemount “knockout” [from Figure 3G] and “rescue” embryos [Figure 5D]. In unperturbed embryos, this ratio will be close to 1, reflecting similar numbers of Pax7+ cells on both sides of the embryo. However, in the “knockout” group, we observed a mean ratio of 0.767 ± 0.041 (n=11), which was significantly different from the ratio of 0.946 ± 0.016 (n=8) observed in the “rescue” group ($p < 0.001$, Welch two-sample t-test) [Figure 5E]. Next, we probed for the expression of the neural crest specifier gene *Sox10* to ask if rescuing the expression of *Hmga1* truly restored the process of neural crest specification. To do this, we processed “rescue” embryos for HCR against *Sox10* [Figure 5F] together with *Pax7* [Figure 5G]. Indeed, restoring the levels of *Hmga1* was sufficient to rescue the expression of *Sox10* [Figure 5G'] and *Pax7* [Figure 5G''] in early migrating crest, and *Pax7* in the premigratory crest residing in the dorsal neural tube, as visualized in transverse sections through the embryo. We also confirmed that the expression of the “rescue” construct was restricted to the dorsal neural tube [Figure 5G'''], thereby precluding unintended effects on neural tube development.

Finally, given that the loss of *Hmga1* specifically affected Pax7 expression in neural crest precursors, we asked if exogenous expression of Pax7 would be sufficient to rescue the effects of losing *Hmga1* on neural crest specification. We tested this by overexpressing the coding sequence of Pax7 (Roellig et al., 2017) on the right side of gastrula stage embryos together with CRISPR plasmids targeting *Hmga1* [Figure 5H,H']. Given that the effect of CRISPR-plasmid-mediated loss of *Hmga1* was more penetrant posteriorly, we developed “Pax7-rescue” embryos to HH9+, processed them for HCR against the neural crest specifier genes *Tfap2b* [Figure 5I] and *Snai2* [Figure 5I'], and generated transverse sections through the hindbrain. *Tfap2b* is expressed in delaminating and migrating neural crest cells (Simões-Costa and Bronner, 2016), whereas *Snai2* is expressed in premigratory neural crest and is eventually downregulated as the cells begin

to migrate (Taneyhill et al., 2007). Compared to the *Hmga1*-knockout embryos in which *Tfap2b* mRNA [Figure 3K] and Snail2 protein [Figure 3I'] levels were notably downregulated, restoring the levels of *Pax7* in an *Hmga1* knockout background rescued the expression of both *Tfap2b* [Figure 5J] and *Snai2* [Figure 5K] in the dorsal hindbrain. Together, these results suggest that maintaining the correct levels of *Hmga1* is necessary for proper neural crest specification in a *Pax7*-dependent manner.

6.2.7 *Hmga1* activates Wnt signaling to mediate neural crest emigration

Neural crest induction, specification, and emigration from the neural tube are intricate processes that require an interplay between Wnt, FGF, and BMP signaling pathways (Piacentino and Bronner, 2018; Woda et al., 2003) working reiteratively at different stages of development. For example, at the onset of neural crest emigration, *Wnt1* is prominently expressed in the dorsal neural tube, where premigratory neural crest cells reside (Simões-Costa et al., 2015). As a result, these cells turn on *Snai2*, a critical regulator of EMT (Nieto et al., 1994) known to function downstream of the Wnt signaling pathway. After knocking out *Hmga1* using CRISPR plasmids, we noted not only perturbed emigration but also a dramatic reduction in Snail2 levels, even within the subset of *Pax7*-expressing cells in the dorsal neural folds [Figure 3I']. These results raised the intriguing possibility that this might be due to an effect on Wnt signaling in already-specified premigratory neural crest cells. Accordingly, we hypothesized that *Hmga1* may function as a Wnt activator in these cells. If so, its loss would be predicted to result in reduced Wnt signaling in the dorsal neural tube. To test this possibility, we used a reporter construct expressing nuclear GFP under the regulation of six Tcf/Lef binding sites and a minimal promoter as a readout for canonical Wnt signaling (Ferrer-Vaquer et al., 2010) [Figure 6A]. Plasmids encoding Cas9, gRNAs targeting *Hmga1*, nuclear RFP, and Tcf/Lef:H2B-GFP were electroporated on the right side of gastrula stage embryos, while the left control side was electroporated with plasmids encoding Cas9, control gRNA, nuclear RFP, and Tcf/Lef:H2B-GFP.

As described above, this plasmid-based knockout strategy resulted in the loss of *Hmga1* after neural crest specification in the midbrain but well before their emigration. Embryos were allowed to develop until HH9, by which time neural crest cells have started delaminating from the neural tube at the midbrain level [Figure 6B]. Consistent with our hypothesis, the results show that *Hmga1* knockout caused a notable reduction in canonical Wnt reporter activity on the knockout side compared to the control side [Figure 6C] at the midbrain level.

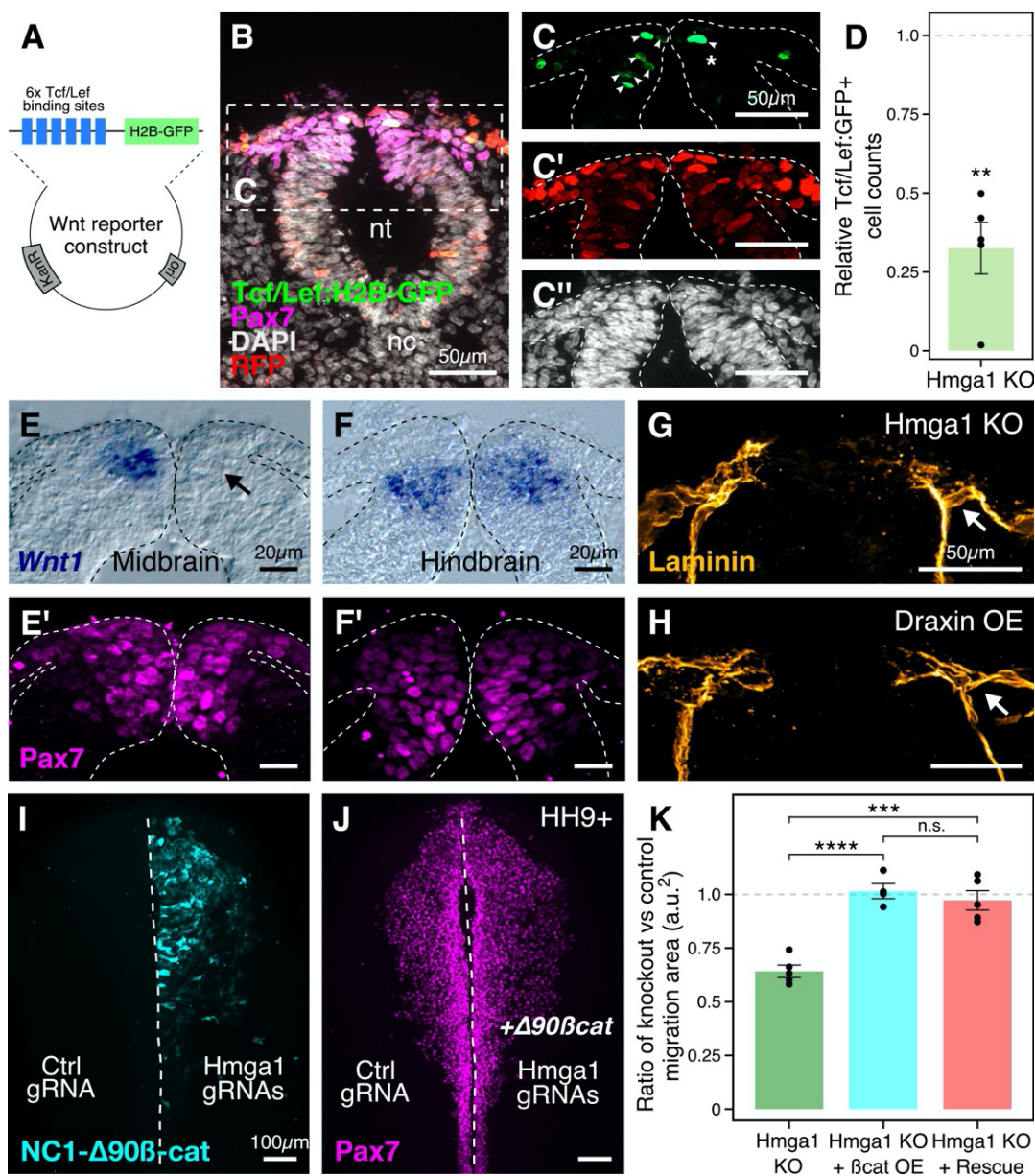


Figure 6. See next page for legend.

Figure 6: Hmga1 activates Wnt signaling pathway in delaminating neural crest cells. **A.** Plasmid construct used as a readout for Wnt activity (after Ferrer-Vaquer et al., 2010). Six TCF/Lef binding sites together with a minimal promoter regulate the expression of nuclear GFP in transfected cells in response to Wnt signaling. **B.** Transverse section through the midbrain of a representative HH9+ embryo immunostained for Pax7, GFP, RFP, and DAPI. **C-C''.** Individual channels of the image in B focused on the dorsal neural tube. In the absence of *Hmga1*, Wnt reporter activity was downregulated, resulting in fewer cells that expressed nuclear GFP (arrowheads) on the right side (C), even though cells were uniformly transfected on both experimental and control sides (C'), and the thickness of the neural tube remained unaffected (C''). **D.** The reduction in Wnt reporter output was quantified as a ratio of number of cells that expressed nuclear GFP, and the number of cells that were successfully transfected and therefore expressed nuclear RFP. The observed difference in GFP+/RFP+ ratio between the knockout and control sides was statistically significant (** $p < 0.01$, Student's t-test). **E-F.** *In situ* hybridization against *Wnt1* in an *Hmga1*-knockout background. Transverse section through the midbrain (E) and hindbrain (F) shows reduced and unchanged levels of *Wnt1* ligand in the dorsal neural tube on the experimental (arrow) versus control neural tubes, respectively. **E'-F'.** The number of Pax7-positive cells in the midbrain appeared unchanged (E'), while a reduction was observed in the hindbrain (F'). **G-H.** Transverse section through a representative embryo where *Hmga1* was knocked out using CRISPR plasmids (G), and an embryo where Draxin was ectopically expressed (H) on the right side, immunostained for Laminin. Similar to Draxin overexpression, *Hmga1* loss caused the laminin channel to remain blocked on the experimental side (arrows). **I-J.** Expression of stabilized β -catenin (NC1- $\Delta 90\beta$ -cat) in delaminating cranial neural crest of *Hmga1*-knockout embryos was sufficient to rescue the migration defect. **K.** Quantification of the area covered by cranial neural crest cells on the experimental versus control sides. In the absence of *Hmga1*, cranial neural crest cells fail to migrate properly, a defect that can be separately rescued in *Hmga1*-knockout background by overexpression (OE) of stabilized β -catenin in delaminating cranial neural crest, or exogenous expression of *Hmga1* coding sequence ectopically (Rescue). nt, neural tube; nc, notochord; KO, knockout; OE, overexpression.

Interestingly, these embryos had a neural crest migration defect [Supplementary Figure 6C-D] but no notable difference in the number of Pax7+ cells between the two sides [Supplementary Figure 6E'], as expected if the *Hmga1* knockout occurred after specification was complete; this is consistent with previous work showing that perturbation of canonical Wnt signaling following specification does not affect the number of Pax7+ cells at cranial EMT stages (Hutchins and Bronner, 2018). Quantitation of this effect revealed a significant reduction in reporter activity following the loss of *Hmga1* [Figure 6D; $p < 0.01$; Student's t-test], as measured by comparing the ratio between the knockout and the control sides of transfected cells (RFP+) that turned on Wnt signaling within the Pax7+ domain, therefore expressing GFP. While this ratio was expected to be 1 for embryos with unperturbed Wnt signaling on both sides, we observed a mean ratio of 0.325 ± 0.082 ($n=5$), suggesting that Wnt activity was disrupted in the absence of *Hmga1*.

Next, to investigate the mechanism by which *Hmga1* regulates Wnt signaling, we turned to a recently published cranial neural crest chromatin accessibility dataset

(Williams et al., 2019) and looked for open chromatin regions surrounding genes that encode for known Wnt ligands. In particular, *Wnt1* expression in the dorsal neural tube is known to be necessary for proper delamination of cranial neural crest cells (Simões-Costa et al., 2015). Interestingly, we discovered a putative enhancer downstream of *Wnt1* [Supplementary Figure 6A] that contained an AT-rich domain consistent with Hmga1 binding motifs [Supplementary Figure 6B] (Reeves and Nissen, 1990). Therefore, we hypothesized that *Hmga1* may modulate Wnt signaling by regulating *Wnt1* expression. To test this, we knocked out *Hmga1* on the right side of gastrula stage embryos using CRISPR plasmids, cultured them *ex ovo* until HH9, and examined *Wnt1* mRNA expression using *in situ* hybridization. Indeed, the dorsal neural tube expression of *Wnt1* was severely downregulated [Figure 6E] in the midbrain. Consistent with the effect of losing *Hmga1* after neural crest specification, the number of Pax7+ cells in the dorsal neural tube appeared unchanged [Figure 6E']. In contrast, no change in *Wnt1* expression was observed at the hindbrain level [Figure 6F], which, being developmentally "younger," instead exhibited a specification defect that resulted in fewer Pax7+ cells in the dorsal neural tube on the experimental side compared to the control side [Figure 6F']. Interestingly, following *Hmga1* knockout, we also observed defects in basement membrane remodeling and laminin channel formation at midbrain levels [Figure 6G], another Wnt-dependent process necessary for neural crest EMT; consistent with Wnt inhibition via Draxin overexpression (Hutchins and Bronner, 2019), loss of *Hmga1* abrogated laminin remodeling and resulted in physical blockage of the channel through which migrating cranial neural crest cells normally transit [Figure 6H]. Together, these data indicate that after neural crest specification, *Hmga1* is necessary for the expression of *Wnt1* and activation of canonical Wnt signaling in the dorsal neural tube, and by extension, Wnt-dependent neural crest delamination/EMT.

Finally, given that Hmga1 functions as a canonical Wnt pathway activator, we asked if the migration defects caused by the loss of *Hmga1* post-specification can be rescued by restoring canonical Wnt signaling in premigratory neural crest cells. To address this, we expressed GFP-tagged, stabilized β -catenin (NC1- Δ 90 β -cat) to

upregulate canonical Wnt signaling output specifically in premigratory neural crest cells, thus circumventing the critical process of neural crest induction at the neural plate border (Hutchins and Bronner, 2018). If loss of *Hmga1* in premigratory neural crest cells resulted in migration defects due to reduced canonical Wnt signaling, expression of a stabilized β -catenin would be predicted to restore those levels, thereby rescuing proper migration. To test this, we knocked out *Hmga1* on the right side of gastrula stage embryos using CRISPR plasmids as previously described, but co-electroporated NC1- Δ 90 β -cat-GFP on the right side. The left side was electroporated with control reagents [Figure 6I]. Embryos were cultured *ex ovo* until HH9+ and processed for immunohistochemistry against Pax7.

Consistent with our hypothesis that *Hmga1* functions as a Wnt activator in neural crest cells, expression of stabilized β -catenin was sufficient to rescue proper cranial neural crest migration from *Hmga1* knockdown [Figure 6J]. We also calculated the ratio of the area occupied by migrating cranial neural crest cells between the experimental and control sides [Figure 6K]. For wildtype embryos, this ratio would be close to 1, reflecting equal neural crest migration on both sides of the embryo. However, after the loss of *Hmga1*, the ratio of areas on experimental versus control sides was 0.642 ± 0.028 ($n=5$). Importantly, co-expression of stabilized β -catenin in premigratory neural crest rescued migration, with an average migration ratio of 1.015 ± 0.035 ($n=4$), which was significantly different from the knockout group ($p < 0.0001$, ANOVA and *post hoc* Tukey HSD). Similarly, ubiquitous expression of the *Hmga1* coding sequence also rescued neural crest migration, with an average migration ratio of 0.972 ± 0.044 ($n=5$), which was also significantly different from the knockout group ($p < 0.001$, ANOVA and *post hoc* Tukey HSD). Taken together, our results suggest that *Hmga1* mediates the process of EMT by activating canonical Wnt signaling in premigratory neural crest cells, thus enabling them to emigrate from the neural tube.

6.3 Discussion

While chromatin modifiers are known to influence gene expression and cell fate decisions at many stages of development (Caia et al., 2014; Laugesen and Helin, 2014;

Miller and Hendrich, 2018; O’Shaughnessy-Kirwan et al., 2015), parsing cell-type-specific functions and targets for these proteins is often challenging due to broad expression across multiple tissues and time points. In this study, we have used scRNA-seq to identify a chromatin-remodeling protein, Hmga1, as highly expressed in neural crest cells. Using high resolution *in situ* HCR and temporally controlled knockdowns, we present evidence for a dual role of Hmga1 in the formation and migration of neural crest cells. At early stages, we find that the neural plate border gene *Pax7* is a downstream target of Hmga1, such that loss of *Hmga1* blocks neural crest specification in a manner that can be rescued by restoring *Pax7* expression. After neural crest specification is complete in the closing neural tube, Hmga1 plays a second role in modulating canonical Wnt signaling via alterations in the levels of *Wnt1* in premigratory neural crest cells. This in turn influences neural crest EMT and delamination from the dorsal neural tube [Figure 7].

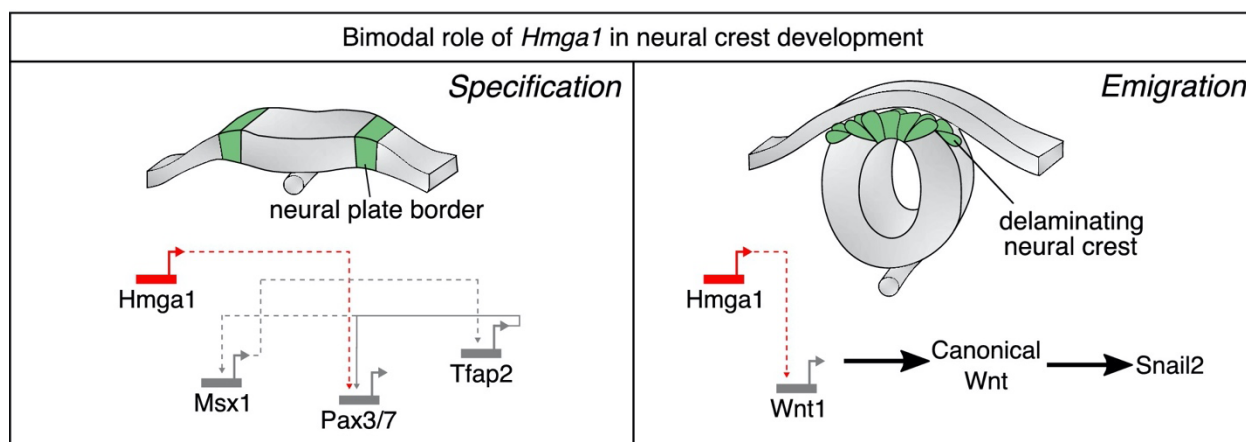


Figure 7: Current model for *Hmga1* function in chick neural crest development. Our data suggest that *Hmga1* plays temporally distinct roles in the neural plate border and dorsal neural tube. At the neural plate border, *Hmga1* acts upstream of *Pax7* and is required for proper neural crest specification. Later, in the dorsal neural tube, *Hmga1* regulates the levels of *Wnt1*, thereby modulating the levels of canonical Wnt signaling to control neural crest delamination and subsequent migration.

The canonical Wnt signaling pathway is a major input in a complex GRN that activates transcriptional circuits and controls neural crest specification and cell lineage decisions (Martik and Bronner, 2017; Simões-Costa and Bronner, 2015; Williams et al., 2019), influencing multiple aspects of neural crest development from induction at the neural plate border to proliferation, onset of migration via EMT, and differentiation (Milet and Monsoro-Burq, 2012; Rabadán et al., 2016; Simões-Costa and Bronner, 2015;

Steventon et al., 2009; Wu et al., 2003; Yanfeng et al., 2003). For example, regulation of the levels of canonical Wnt signaling is critical for progressive basement membrane remodeling during neural tube closure and neural crest delamination. Consequently, perturbation of Wnt signaling output at different stages of basement membrane remodeling or delamination causes severe defects in neural crest EMT (Hutchins and Bronner, 2019; Rabadán et al., 2016). Interestingly, early inhibition of canonical Wnt signaling in gastrula stage chick embryos has been shown to reduce *Pax7* expression (Basch et al., 2006), whereas canonical Wnt inhibition after neural crest specification does not alter *Pax7* expression but has a marked effect on EMT (Hutchins and Bronner, 2018). This suggests that there are separable early versus late effects of canonical Wnt signaling during neural crest development.

Hmga1 has been shown to upregulate canonical Wnt signaling components and downstream targets in the intestinal stem cell niche, thereby amplifying signaling output (Xian et al., 2017) presumably through increased promotor accessibility. Our results are consistent with a similar role for *Hmga1* in the neural crest, where its loss resulted in decreased output from a canonical Wnt reporter [Figure 6] as well as downregulation of the *Wnt1* ligand [Figure 6] and the canonical Wnt target *Snail2* [Figure 3]. However, temporally controlled knockdowns revealed that loss of *Hmga1* reduced *Wnt1* expression following completion of neural crest specification, but not at earlier stages of neural crest induction. Conversely, *Hmga1* knockdown affected *Pax7* expression during neural crest induction but not after specification is complete. One possible explanation is that once open/remodeled, the chromatin landscape surrounding the *Pax7* regulatory regions form topologically-associating domains (TADs) that are stable and resistant to repression. Alternatively, other *Hmga1*-independent *cis*-elements may influence *Pax7* expression following neural crest induction. Given that neural crest cells appear to have highly dynamic chromatin accessibility surrounding spatiotemporally-regulated enhancer elements (Williams et al., 2019), we would predict the latter, though further investigation is needed to distinguish between these possibilities.

An intriguing possibility is that *Hmga1*, in addition to regulating neural crest EMT, is necessary for maintaining the broad developmental potential of neural crest cells. Neural crest cells exhibit stem-cell-like properties, including multipotency and self-renewal. Thus, the early expression of *Hmga1* in neural crest precursors, together with its reported role in maintaining stemness and self-renewal properties in various stem cell and cancer systems (Battista et al., 2003; Schuldenfrei et al., 2011; Shah and Resar, 2012), may indicate a role in maintaining neural crest stemness. In the dorsal neural tube, self-renewal within the premigratory neural crest is driven by the transcription factor *c-Myc* (Kerosuo and Bronner, 2016), which together with its binding partner regulates cell cycle progression. Consistent with this possibility, we found that the mRNA expression of *c-Myc* is downregulated in the dorsal neural tube following *Hmga1* knockout. However, given that canonical Wnt signaling also regulates stem cell self-renewal (Xu et al., 2016), as well as cell cycle progression in neural crest (Burstyn-Cohen et al., 2004), *Hmga1* may have additional Wnt-dependent and/or Wnt-independent roles in the maintenance of the neural crest stem cell pool.

Hmga1 is a member of the high motility group A (HMGA) family of genes that are characterized by their A/T-hook domains and the ability to transform chromatin architecture to regulate transcription of target genes. To date, two members of the HMGA family, *Hmga1* and *Hmga2*, have been identified in mammals (Reeves et al., 2001), each having distinct roles in oncogenesis (Jun et al., 2015; Meyer et al., 2007; Miyazawa et al., 2004). As both genes share several common targets, they may compensate for each other where they overlap. Indeed, *Hmga1/Hmga2* double knockout mice have severe embryonic lethality, compared to less-penetrant effects in individual knockouts (Federico et al., 2014). While both *Hmga1* and *Hmga2* genes are annotated in the chick genome, our scRNA-seq results show that a significant proportion of neural crest cells express *Hmga1* but not *Hmga2*. Consistent with this, loss of *Hmga1* resulted in neural crest-related developmental defects, making it unlikely that there is redundancy and/or compensation by *Hmga2* in chick embryos. Interestingly, only the *hmga2* paralogue is present in *Xenopus laevis* embryos (Macrì et al., 2016), but morpholino-mediated

knockdown of *hmga2* did not affect the expression of neural plate border gene *pax3/7*. This contrasts with our results in chick embryos, where the loss of *Hmga1* affected both *Pax7* transcription and protein levels in the neural plate border. Together with the absence of *Hmga2*⁺ cells in our single-cell data, this raises the possibility that individual HMGA family members play discrete roles in neural crest development, similar to their distinct roles in tumorigenesis.

In addition to *Hmga1*, other chromatin remodeling proteins serve similar functions in neural crest cell fate decisions. For example, both the ATP-dependent chromatin remodeler CHD7 and the histone demethylase Jumonji D2A (KDM4A/Jmjd2A) are necessary for expression of neural crest specifier genes; notably, however, these chromatin modifiers appear to function at later developmental time points than *Hmga1*, as neither knockdown of KDM4A in chick embryos nor CHD7 in *Xenopus* embryos affect *Pax3/7* expression levels (Bajpai et al., 2010; Strobl-Mazzulla et al., 2010). Furthermore, KDM4A influences *Snai2* and *Wnt1* levels, raising the possibility that *Hmga1* may act in concert with KDM4A or other chromatin remodelers to restructure the accessibility of neural crest GRN circuits at different cell fate checkpoints.

In summary, our data reveal a dual role for the chromatin remodeler *Hmga1* during neural crest development. First, during specification at the neural plate border, *Hmga1* regulates the completion of neural crest induction as assayed by readout of *Pax7* expression at the neural plate border. Later, following neural crest specification, *Hmga1* plays a second role in modulating the levels of the canonical Wnt signaling pathway in the closing dorsal neural tube to influence neural crest EMT and delamination at the onset of their migration. Post-embryonically, neural-crest-derived cells are prone to metastasis and give rise to numerous cancers (Maguire et al., 2015). Furthermore, neural crest and cancer cells often employ similar mechanisms to drive EMT; in particular, the hallmarks of metastasis often involve disruption of the basement membrane, which may also be driven by canonical Wnt signaling (Ahsan et al., 2017; Powell et al., 2013). Interestingly, high expression levels of *Hmga1* have been associated with premature EMT and prolonged stemness in several cancers of the pancreas (Abe et al., 2000), breast (Flohr

et al., 2003), lung (Sarhadi et al., 2006), and ovaries (Masciullo et al., 2003). Therefore, it is interesting to note that Hmga1 may play parallel roles in neural crest development and cancer metastasis. Understanding how Hmga1, and chromatin remodeling in general, alters cell fate decisions and EMT through signaling and transcriptional regulation in neural crest cells will undoubtedly have important and broad implications in human development and disease.

6.4 Acknowledgments

For technical assistance, we thank Fan Gao with the Caltech Bioinformatics Resource Center of the Beckman Institute, Giada Spigolon and Andres Collazo with the Caltech Biological Imaging facility of the Beckman Institute, and Sisi Chen and Paul Rivaud with the Single Cell Profiling and Engineering Center (SPEC) of the Beckman Institute. We thank members of the Bronner lab for helpful discussions.

6.5 Author contributions

Conceptualization, S.G. and M.E.B.; Methodology, S.G., J.H.P., and M.T.; Resources, S.G., E.J.H., J.H.P., M.T., Software, S.G.; Validation, S.G. and E.J.H.; Formal Analysis, S.G.; Investigation, S.G., E.J.H., and K.M.; Writing – Original Draft, S.G. and K.M.; Writing – Review & Editing, S.G., M.E.B., E.J.H.; Visualization, S.G., E.J.H., and K.M.; Supervision, S.G. and M.E.B.; Funding Acquisition, M.E.B.

6.6 Funding

This work is supported by the National Institutes of Health (NIH) grants R01DE027568, R01HL14058, and R01DE027538 to M.E.B. and K99DE028592 to E.J.H., and the American Heart Association (AHA) predoctoral fellowship 18PRE34050063 to S.G.

6.7 Materials and methods

6.7.1 Key Resources Table

Reagent type (species) or resource	Designation	Source or reference	Identifiers	Additional information
gene (<i>Gallus gallus</i>)	<i>Hmga1</i>	UCSC genome browser	NM_204369.1	
strain, strain background (<i>Gallus gallus</i>)	<i>G. gallus</i>	Sun State Ranch (Monrovia, CA, USA)		
antibody	Mouse IgG1 anti-Pax7	Developmental Studies Hybridoma Bank	RRID: AB_528428	1:10
antibody	Rabbit anti-Laminin	Sigma-Aldrich	RRID: AB_477163	1:1000 on sections
antibody	Mouse IgM anti-HNK1	Developmental Studies Hybridoma Bank	RRID: AB_2314644	1:5
antibody	Rabbit anti-RFP	MBL	RRID: AB_591279	1:500
antibody	Rabbit anti-Slug (C19G7)	Cell Signaling	RRID: AB_2239535	1:200

antibody	Goat IgG anti-GFP	Rockland	RRID: AB_218182	1:500
antibody	Rabbit anti-cleaved-caspase-3	R&D systems	RRID: AB_2243952	1:500 on sections
antibody	Mouse anti-phospho-histone H3	Abcam	RRID: AB_443110	1:500 on sections
recombinant DNA reagent	pCI-H2B-RFP (plasmid)	Betancur et al., 2010		
recombinant DNA reagent	CAG>nls-Cas9-nls (plasmid)	Gandhi et al., 2017	RRID: Addgene_99138	
recombinant DNA reagent	cU6.3> Ctrl. gRNA.f+e (plasmid)	Gandhi et al., 2017	RRID: Addgene_99140	
recombinant DNA reagent	cU6.3> Hmga1.1. gRNA.f+e (plasmid)	This paper		Detailed in Materials and methods section "CRISPR-Cas9-mediated perturbations"
recombinant DNA reagent	cU6.3> Hmga1.2. gRNA.f+e (plasmid)	This paper		Detailed in Materials and methods section "CRISPR-Cas9-mediated perturbations"
recombinant DNA reagent	FoxD3-NC2:eGFP (plasmid)	Simões-Costa et al., 2012		
recombinant DNA reagent	Tcf/Lef: H2B-GFP (plasmid)	Ferrer-Vaquer et al., 2010	RRID: Addgene_32610	

recombinant DNA reagent	NC1- Δ 90 β -cat (plasmid)	Hutchins and Bronner, 2018		
recombinant DNA reagent	pCI-Pax7-IRES-H2B-RFP (plasmid)	Roellig et al., 2017		
sequence-based reagent	Hmga1.1. gRNA	This paper	PCR primer	5'- gCAGGAAGAAACC GGAGgta
sequence-based reagent	Hmga1.2. gRNA	This paper	PCR primer	5'- GCCAGTCCAAAG GCAGGgt
sequence-based reagent	Ascl-V5-Fwd	This paper	PCR primer	5'- ggcgcgccaccATGGC TGTAAGCCTA
sequence-based reagent	V5-Hmga1-Fwd	This paper	PCR primer	5'- CTCCTCGGTCTCG ATTCTagcgacgccggc gccaagcc
sequence-based reagent	Hmga1OLP-V5-Rev	This paper	PCR primer	5'- ggcttggcgccggcgtcgt AGAATCGAGACCG AGGAG
sequence-based reagent	Hmga1-Clal-Rev	This paper	PCR primer	5'- ttatcgattcactgctcctct cggatg
sequence-based reagent	Hmga1.1 short guide oligo	This paper	PCR primer	5'- GCGTAATACGACT CACTATAGGCAGG AAGAAACCGGAGG TAGTTTTAGAGCTA GAAATAGC

sequence-based reagent	Hmga1.2 short guide oligo	This paper	PCR primer	5'- GCGTAATACGACT CACTATAGGCCAG CTCCAAAGGCAGG GTGTTTTAGAGCTA GAAATAGC
sequence-based reagent	Control short guide oligo	Hutchins and Bronner, 2018	PCR primer	Detailed in Materials and methods section "CRISPR-Cas9-mediated perturbations"
sequence-based reagent	gRNA Primer 1	Hutchins and Bronner, 2018	PCR primer	Detailed in Materials and methods section "CRISPR-Cas9-mediated perturbations"
sequence-based reagent	gRNA Primer 2	Hutchins and Bronner, 2018	PCR primer	Detailed in Materials and methods section "CRISPR-Cas9-mediated perturbations"
sequence-based reagent	Guide-constant oligo	Hutchins and Bronner, 2018	PCR primer	Detailed in Materials and methods section "CRISPR-Cas9-mediated perturbations"
commercial assay or kit	Chromium Single Cell 3' Library & Gel Bead Kit v2	10X Genomics	Cat# PN-120267	
commercial assay or kit	Chromium Single Cell A Chip Kit	10X Genomics	Cat# PN-1000009	
commercial assay or kit	Endofree maxi prep kit	Macharey Nagel	Cat# 740426.50	

commercial assay or kit	Agencourt AMPure XP beads	Beckman Coulter	Cat# A63880	
commercial assay or kit	Dynabeads MyOne SILANE	10X Genomics	Cat# 2000048	
commercial assay or kit	SPRIselect Reagent Kit	Beckman Coulter	Cat# B23318	
commercial assay or kit	High Sensitivity DNA Kit	Agilent	Cat# 5067-4626	
commercial assay or kit	Qubit dsDNA HS Assay Kit	Thermo Fisher Scientific	Cat# Q32854	
software, algorithm	Fiji	Schindelin et al., 2012	RRID: SCR_002285	https://imagej.net/Fiji
software, algorithm	Seurat	Butler et al., 2018	RRID: SCR_007322	https://satijalab.org/seurat/
software, algorithm	Inkscape	Inkscape	RRID: SCR_014479	https://inkscape.org/
software, algorithm	Cellranger	10X Genomics		
software, algorithm	2100 Expert software	Agilent	RRID: SCR_014466	
other	Fluoromount -G	Southern Biotech	Cat# 0100-01	
other	DAPI	Thermo Fisher Scientific	Cat# D1306	1:10000 on sections

6.7.2 Electroporations

Chicken embryos (*Gallus gallus*) were commercially obtained from Sun Valley farms (CA), and developed to the specified Hamburger Hamilton (HH) (Hamburger and Hamilton, 1951) stage in a humidified 37°C incubator. For *ex ovo* electroporations, embryos were dissected from eggs at HH4, injected with specified reagents, then electroporated as described previously (Sauka-Spengler and Barembaum, 2008). Following electroporation, embryos were cultured in fresh albumin/1% penicillin-streptomycin at 37°C and grown to specified HH stages. Once the embryos reached the desired stages, they were screened for transfection efficiency and overall health. Unhealthy and/or poorly transfected embryos were discarded and not included for downstream assays.

6.7.3 Single-cell suspension

HH4 embryos electroporated with FoxD3-NC2:eGFP were cultured until HH12 *ex ovo* at 37°C, following which the hindbrain region spanning rhombomeres 6, 7, and 8 was dissected under a fluorescence microscope. For dissociation, several different conditions were tested (dissociation in a glass dish for 1h in Accumax (EMD Millipore), chemical dissociation on a nutator for 15, 30, and 45 minutes, and chemical dissociation with gentle pipetting for 15, 30, and 45 minutes). The quality of the single cell suspension obtained was tested by a trypan blue-based live-dead staining. Accordingly, we pooled dissected tissue washed in chilled 1X DPBS and incubated it in Accumax cell dissociation solution for 15 minutes at 37°C with gentle mixing every 5 minutes. Dissociation was terminated using Hanks Buffered Saline Solution (HBSS) (Corning) supplemented with BSA Fraction V (Sigma; 0.2% w/v). The suspension was centrifuged at 300g for 4 minutes to collect cells at the bottom, the supernatant was removed, and the pellet was resuspended in 1mL HBSS-BSA. To remove cell debris and clumps, the 1mL suspension was passed through a 20µm filter in a clean hood. This suspension was loaded on a 10X Chromium chip A (v2) to generate GEMs. The library was prepared according to the manufacturer's protocol and sequenced on the Illumina HiSeq platform using the paired end chemistry.

6.7.4 scRNA-seq data analysis

The raw fastq files were aligned to the galgal6 (GRCg6a) genome assembly obtained from the ENSEMBL database using the cellranger pipeline downloaded from the 10X Genomics website. For feature counts, a custom galgal6 GTF file, where all annotated 3' UTRs were extended by 1kb, was used. This was done to compensate for improper gene annotations in the chick genome. The count matrices were then imported in R for analysis using Seurat (Butler et al., 2018). The initial filtering step discarded all cells with fewer than 200 and more than 10000 genes per cell. We also filtered out cells expressing more than 5% mitochondrial or less than 20% ribosomal genes. Next, we removed genes corresponding to small RNAs, micro RNAs, mitochondria, and general housekeeping from the count matrix. Following log normalization and Principal Component Analysis, the cells were clustered using the first 15 dimensions (calculated from the elbow plot). Different resolution parameter values were tested, and a value of 0.45 was used to identify subpopulations within the data. Dimensional reductionality was performed using the UMAP (McInnes et al., 2018) algorithm. All plots were created in R, exported in SVG format, and assembled in Inkscape. All sequencing data has been deposited on NCBI under the accession number PRJNA624258.

6.7.5 Hybridization Chain Reaction

HCR v3 was performed using the protocol suggested by Molecular Technologies (Choi et al., 2018) with minor modifications. Briefly, the embryos were fixed in 4% paraformaldehyde (PFA) overnight at 4°C or 2h at room temperature, washed in 0.1% PBS-Tween, dehydrated in a series of 25%, 50%, 75%, and 100% methanol washes, and incubated overnight at -20°C in 100% methanol. The next day, the embryos were rehydrated, treated with proteinase-K for 2-2.5 minutes, and incubated with 10pmol of probes dissolved in hybridization buffer overnight at 37°C. The next day, following several washes in “probe wash buffer,” embryos were incubated in 30pmol of hairpins H1 and H2 diluted in Amplification buffer at room temperature overnight. The next morning, embryos

were washed in 0.1% 5x-SSC-Tween and imaged. All probes were designed and ordered through Molecular Technologies.

6.7.6 Molecular cloning

The coding sequence of *Hmga1* was obtained from the UCSC genome browser (Karolchik et al., 2003). A V5 tag was cloned in-frame at the N-terminus using overlap PCR (Accuprime). The fusion product was cloned downstream of the CAGG promoter, upstream of the IRES-H2B-RFP segment of pCI-H2B-RFP (Betancur et al., 2010) to clone the final plasmid (CAGG>V5-HMGA1-IRES-H2B-RFP). The Cas9 and gRNA constructs (Gandhi et al., 2017), neural crest enhancer FoxD3-NC2:eGFP (Simões-Costa et al., 2012), canonical Wnt reporter TCF/Lef:H2B-GFP (Ferrer-Vaquer et al., 2010), and neural crest-specific stabilized β -catenin NC1- Δ 90 β -cat (Hutchins and Bronner, 2018) have all been previously described and validated.

6.7.7 CRISPR-Cas9-mediated perturbations

The genomic locus for *Hmga1* was obtained from the UCSC genome browser (Karolchik et al., 2003). Two gRNAs targeting the coding sequence, the first targeting exon 3 (5'-CCAGGAAGAAACCGGAGgta-3'), and the second targeting exon 4 (5'-GCCAGCTCCAAAGGCAGGgt-3'), were designed using CHOPCHOP (Labun et al., 2019). The protospacers were cloned downstream of the chick U6.3 promoter as described in Gandhi et al., 2017. For control electroporations, the control gRNA described in (Gandhi et al., 2017) was used. *CAGG>nls-Cas9-nls* and *CAGG>H2B-RFP* were electroporated at a concentration of $2\mu\text{g}/\mu\text{l}$, together with either $0.75\mu\text{g}/\mu\text{l}$ per *Hmga1* gRNA on the right side or $1.5\mu\text{g}/\mu\text{l}$ of control gRNA on the left side.

For *Cas9/in vitro*-transcribed gRNA RNP experiments, we generated single-guide RNAs (sgRNAs) as described previously (Hutchins and Bronner, 2018).

$2.6\mu\text{l}$ of recombinant Cas9 (M0646; New England Biolabs) was mixed with equal volumes of control gRNA or $1.3\mu\text{l}$ each of the two *Hmga1* gRNAs, and heated to 37°C for

15 minutes. The solution was then incubated at room temperature for 15 minutes, mixed with $2\mu\text{g}/\mu\text{l}$ H2B-RFP and $1\mu\text{l}$ of sterilized 2% food dye, and injected in embryos for electroporation.

6.7.8 In situ hybridization and immunohistochemistry

Chromogenic *in situ* hybridization was performed as described previously for *FoxD3*, *Sox10*, and *Tfap2b*, *c-Myc*, and *Wnt1* (Kerosuo and Bronner, 2016; Simões-Costa and Bronner, 2016; Simões-Costa et al., 2015).

Immunohistochemistry was performed as described previously (Gandhi et al., 2017). Briefly, embryos were fixed for 20 minutes at room temperature, blocked in 10% goat or donkey serum in 0.5% PBS-Triton overnight at 4°C, incubated overnight at 4°C in primary antibodies diluted in blocking solution, washed at room temperature in 0.5% PBS-Triton, incubated overnight at 4°C in secondary antibodies diluted in blocking solution, washed at room temperature in 0.5% PBS-Triton, and processed for imaging and/or cryosectioning. The following primary antibodies and concentrations were used: Mouse IgM HNK1 (1:5; Developmental Studies Hybridoma Bank (3H5)); Mouse IgG1 Pax7 (1:10; Developmental Studies Hybridoma Bank (RRID:AB_528428)); Goat GFP (1:500; Rockland Cat# 600-101-215); Rabbit RFP (1:500; MBL Cat# PM005); Rabbit Snail2 (1:200; Cell Signaling Technology (9585)); Rabbit Laminin (1:1000; Sigma-Aldrich (L9393)); Rabbit cleaved-Caspase 3 (1:500; R&D Systems Cat# AF835); Mouse phospho-histone H3 (1:500; Abcam Cat# Ab14955). The following species-specific secondary antibodies labeled with Alexa Fluor dyes (Invitrogen) were used: Goat/Donkey anti-mouse Alexa Fluor 647 (for Pax7 and pH3; 1:250), Goat/Donkey anti-mouse IgM Alexa Fluor 350/488 (for HNK1; 1:250), Goat/Donkey anti-rabbit Alexa Fluor 488 (for Snail2, cleaved-Caspase3, and Laminin; 1:250), Donkey anti-goat Alexa Fluor 488 (for Citrine; 1:500), and Goat/Donkey anti-rabbit Alexa Fluor 568 (for RFP; 1:500).

6.7.9 Cryosectioning

Following whole mount imaging, embryos were washed in 5% and 15% sucrose overnight at 4°C. The next day, embryos were transferred to molten gelatin for 3-5h at 37°C, embedded in molds at room temperature, frozen in liquid nitrogen, and stored at -80°C overnight. Embedded embryos were sectioned on a micron cryostat to obtain 16µm sections through immunostained embryos and 20µm sections through *in situ* hybridized embryos. The sections were degelatinized at 42°C in 1x PBS for 5 minutes, washed in 1x PBS, soaked in 1x PBS containing 0.1µg/mL DAPI for 2 minutes, washed in 1x PBS and distilled water. Fluoromount mounting medium was used to mount coverslips on slides.

6.7.10 Microscope image acquisition, analysis, and statistical tests

Whole mount embryos and sections on slides were imaged on a Zeiss Imager M2 with an ApoTome module and/or Zeiss LSM 880 confocal microscope at the Caltech Biological Imaging Facility. Images were post-processed using Fiji imaging software (Schindelin et al., 2012). To calculate corrected total cell fluorescence (CTCF), the following formula was used:

$$CTCF = \text{Integrated Density} - (\text{Selected area} * \text{Mean background fluorescence}).$$

For cell counts, a median filter was applied to 8-bit images. A Bernsen-based auto local-thresholding method (Bernsen, 1986) followed by watershed segmentation was used to identify cell boundaries. The “Analyze particles” function was used to count the number of cells. All statistical analyses were performed in R. The Wilcoxon rank test was used on datasets that were not normally distributed. In cases where the underlying distribution was normal, Student’s t-test was used to calculate significance. In cases where multiple samples were compared, Analysis of Variance (ANOVA) test combined with Tukey HSD test was used. *Post hoc* power analysis was used to validate sample size and confirm sufficient statistical power (>0.8).

6.8 References

- Abe, N., Watanabe, T., Masaki, T., Mori, T., Sugiyama, M., Uchimura, H., Fujioka, Y., Chiappetta, G., Fusco, A., and Atomi, Y. (2000). Pancreatic duct cell carcinomas express high levels of high mobility group I(Y) proteins. *Cancer Res.* *60*, 3117–3122.
- Ahsan, K., Treffy, R.W., Nacke, L.M., Green-Saxena, A., and Rocha, M. (2017). Neural crest and cancer: Divergent travelers on similar paths. *Mech. Dev.* *148*, 89–99.
- Bajpai, R., Chen, D.A., Rada-Iglesias, A., Zhang, J., Xiong, Y., Helms, J., Chang, C.P., Zhao, Y., Swigut, T., and Wysocka, J. (2010). CHD7 cooperates with PBAF to control multipotent neural crest formation. *Nature* *463*, 958–962.
- Basch, M.L., Bronner-Fraser, M., and García-Castro, M.I. (2006). Specification of the neural crest occurs during gastrulation and requires Pax7. *Nature* *441*, 218–222.
- Battista, S., Pentimalli, F., Baldassarre, G., Fedele, M., Fidanza, V., Croce, C.M., and Fusco, A. (2003). Loss of Hmga1 gene function affects embryonic stem cell lymphohematopoietic differentiation. *FASEB J.* *17*, 1496–1498.
- Bernsen, J. (1986). Dynamic Thresholding of Grey-Level Images. In *Proceedings - International Conference on Pattern Recognition*, pp. 1251–1255.
- Betancur, P., Bronner-Fraser, M., and Sauka-Spengler, T. (2010). Genomic code for Sox10 activation reveals a key regulatory enhancer for cranial neural crest. *Proc. Natl Acad. Sci. USA* *107*, 3570–3575.
- Bronner, M.E., and LeDouarin, N.M. (2012). Development and evolution of the neural crest: An overview. *Dev. Biol.* *366*, 2–9.
- Burstyn-Cohen, T., Stanleigh, J., Sela-Donenfeld, D., and Kalcheim, C. (2004). Canonical Wnt activity regulates trunk neural crest delamination linking BMP/noggin signaling with G1/S transition. *Development* *131*, 5327–5339.

Butler, A., Hoffman, P., Smibert, P., Papalexi, E., and Satija, R. (2018). Integrating single-cell transcriptomic data across different conditions, technologies, and species. *Nat. Biotechnol.* *36*, 411–420.

Caia, Y., Baka, R.O., and Mikkelsen, J.G. (2014). Targeted genome editing by lentiviral protein transduction of zinc-finger and TAL-effector nucleases. *ELife* e01911.

Choi, H.M.T., Schwarzkopf, M., Fornace, M.E., Acharya, A., Artavanis, G., Stegmaier, J., Cunha, A., and Pierce, N.A. (2018). Third-generation in situ hybridization chain reaction: Multiplexed, quantitative, sensitive, versatile, robust. *Development* *145*, dev165753.

De Croz e, N., Maczkowiak, F., and Monsoro-Burq, A.H. (2011). Reiterative AP2a activity controls sequential steps in the neural crest gene regulatory network. *Proc. Natl Acad. Sci. USA* *108*, 155–160.

Le Douarin, N.M. (1980). The ontogeny of the neural crest in avian embryo chimaeras. *Nature* *286*, 663–669.

Federico, A., Forzati, F., Esposito, F., Arra, C., Palma, G., Barbieri, A., Palmieri, D., Fedele, M., Pierantoni, G.M., De Martino, I., et al. (2014). Hmga1/Hmga2 double knock-out mice display a “superpygmy” phenotype. *Biol. Open* *3*, 372–378.

Ferrer-Vaquer, A., Piliszek, A., Tian, G., Aho, R.J., Dufort, D., and Hadjantonakis, A.K. (2010). A sensitive and bright single-cell resolution live imaging reporter of Wnt/catenin signaling in the mouse. *BMC Dev. Biol.* *10*, 121.

Flohr, A.M., Rogalla, P., Bonk, U., Puettmann, B., Buerger, H., Gohla, G., Packeisen, J., Wosniok, W., Loeschke, S., and Bullerdiek, J. (2003). High mobility group protein HMGA1 expression in breast cancer reveals a positive correlation with tumour grade. *Histol. Histopathol.* *18*, 999–1004.

Gandhi, S., and Bronner, M.E. (2018). Insights into neural crest development from studies of avian embryos. *Int. J. Dev. Biol.* *62*, 179–190.

- Gandhi, S., Piacentino, M.L., Vieceli, F.M., and Bronner, M.E. (2017). Optimization of CRISPR/Cas9 genome editing for loss-of-function in the early chick embryo. *Dev. Biol.* *432*, 86–97.
- Gandhi, S., Ezin, M., and Bronner, M.E. (2020). Reprogramming Axial Level Identity to Rescue Neural-Crest-Related Congenital Heart Defects. *Dev. Cell* *53*, 300-315.e4.
- Grosschedl, R., Giese, K., and Pagel, J. (1994). HMG domain proteins: architectural elements in the assembly of nucleoprotein structures. *Trends Genet.* *10*, 94–100.
- Hamburger, V., and Hamilton, H.L. (1951). A series of normal stages in the development of the chick embryo. *J. Morphol.* *88*, 49–92.
- Hutchins, E.J., and Bronner, M.E. (2018). Draxin acts as a molecular rheostat of canonical Wnt signaling to control cranial neural crest EMT. *J. Cell Biol.* *217*, 3683–3697.
- Hutchins, E.J., and Bronner, M.E. (2019). Draxin alters laminin organization during basement membrane remodeling to control cranial neural crest EMT. *Dev. Biol.* *446*, 151–158.
- Jun, K.H., Jung, J.H., Choi, H.J., Shin, E.Y., and Chin, H.M. (2015). HMGA1/HMGA2 protein expression and prognostic implications in gastric cancer. *Int. J. Surg.* *24*, 39–44.
- Karolchik, D., Baertsch, R., Diekhans, M., Furey, T.S., Hinrichs, A., Lu, Y.T., Roskin, K.M., Schwartz, M., Sugnet, C.W., Thomas, D.J., et al. (2003). The UCSC Genome Browser Database. *Nucleic Acids Res.* *31*, 51–54.
- Kerosuo, L., and Bronner, M.E. (2016). cMyc Regulates the Size of the Premigratory Neural Crest Stem Cell Pool. *Cell Rep.* *17*, 2648–2659.
- Khudyakov, J., and Bronner-Fraser, M. (2009). Comprehensive spatiotemporal analysis of early chick neural crest network genes. *Dev. Dyn.* *238*, 716–723.

- Kishi, Y., Fujii, Y., Hirabayashi, Y., and Gotoh, Y. (2012). HMGA regulates the global chromatin state and neurogenic potential in neocortical precursor cells. *Nat. Neurosci.* *15*, 1127–1133.
- Labun, K., Montague, T.G., Krause, M., Torres Cleuren, Y.N., Tjeldnes, H., and Valen, E. (2019). CHOPCHOP v3: expanding the CRISPR web toolbox beyond genome editing. *Nucleic Acids Res.* *47*, W171–W174.
- Laugesen, A., and Helin, K. (2014). Chromatin repressive complexes in stem cells, development, and cancer. *Cell Stem Cell* *14*, 735–751.
- Luo, T., Lee, Y.H., Saint-Jeannet, J.P., and Sargent, T.D. (2003). Induction of neural crest in *Xenopus* by transcription factor AP2 α . *Proc. Natl Acad. Sci. USA* *100*, 532–537.
- Macrì, S., Simula, L., Pellarin, I., Pegoraro, S., Onorati, M., Sgarra, R., Manfioletti, G., and Vignali, R. (2016). *Hmga2* is required for neural crest cell specification in *Xenopus laevis*. *Dev. Biol.* *411*, 25–37.
- Maguire, L.H., Thomas, A.R., and Goldstein, A.M. (2015). Tumors of the neural crest: Common themes in development and cancer. *Dev. Dyn.* *244*, 311–322.
- Martik, M.L., and Bronner, M.E. (2017). Regulatory logic underlying diversification of the neural crest. *Trends Genet.* *33*, 715–727.
- Martik, M.L., Gandhi, S., Uy, B.R., Gillis, J.A., Green, S.A., Simões-Costa, M., and Bronner, M.E. (2019). Evolution of the new head by gradual acquisition of neural crest regulatory circuits. *Nature* *574*, 675–678.
- Masciullo, V., Baldassarre, G., Pentimalli, F., Berlingieri, M.T., Boccia, A., Chiappetta, G., Palazzo, J., Manfioletti, G., Giancotti, V., Viglietto, G., et al. (2003). HMGA1 protein overexpression is a frequent feature of epithelial ovarian carcinomas. *Carcinogenesis* *24*, 1191–1198.

McInnes, L., Healy, J., and Melville, J. (2018). UMAP: Uniform manifold approximation and projection for dimension reduction. ArXiv EPrints 1802.03426.

Meyer, B., Loeschke, S., Schultze, A., Weigel, T., Sandkamp, M., Goldmann, T., Vollmer, E., and Bullerdiek, J. (2007). HMGA2 overexpression in non-small cell lung cancer. *Mol. Carcinog.* 46, 503–511.

Milet, C., and Monsoro-Burq, A.H. (2012). Neural crest induction at the neural plate border in vertebrates. *Dev. Biol.* 366, 22–33.

Miller, A., and Hendrich, B. (2018). Chromatin Remodelling Proteins and Cell Fate Decisions in Mammalian Preimplantation Development. *Adv. Anat. Embryol. Cell Biol.* 229, 3–14.

Miyazawa, J., Mitoro, A., Kawashiri, S., Chada, K.K., and Imai, K. (2004). Expression of Mesenchyme-Specific Gene HMGA2 in Squamous Cell Carcinomas of the Oral Cavity. *Cancer Res.* 64, 2024–2029.

Nieto, M.A., Sargent, M.G., Wilkinson, D.G., and Cooke, J. (1994). Control of cell behavior during vertebrate development by Slug, a zinc finger gene. *Science* 264, 835–839.

O’Shaughnessy-Kirwan, A., Signolet, J., Costello, I., Gharbi, S., and Hendrich, B. (2015). Constraint of gene expression by the chromatin remodelling protein CHD4 facilitates lineage specification. *Development* 142, 2586–2597.

Piacentino, M.L., and Bronner, M.E. (2018). Intracellular attenuation of BMP signaling via CKIP-1/Smurf1 is essential during neural crest induction. *PLoS Biol.* 16, e2004425.

Powell, D.R., Blasky, A.J., Britt, S.G., and Artinger, K.B. (2013). Riding the crest of the wave: Parallels between the neural crest and cancer in epithelial-to-mesenchymal transition and migration. *Wiley Interdiscip. Rev. Syst. Biol. Med.* 5, 511–522.

Rabadán, M.A., Herrera, A., Fanlo, L., Usieto, S., Carmona-Fontaine, C., Barriga, E.H., Mayor, R., Pons, S., and Martí, E. (2016). Delamination of neural crest cells requires transient and reversible Wnt inhibition mediated by Dact1/2. *Development* *143*, 2194–2205.

Reeves, R., and Nissen, M.S. (1990). The A·T-DNA-binding domain of mammalian high mobility group I chromosomal proteins. A novel peptide motif for recognizing DNA structure. *J. Biol. Chem.* *265*, 8573–8582.

Reeves, R., Edberg, D.D., and Li, Y. (2001). Architectural Transcription Factor HMGI(Y) Promotes Tumor Progression and Mesenchymal Transition of Human Epithelial Cells. *Mol. Cell. Biol.* *21*, 575–594.

Resar, L., Chia, L., and Xian, L. (2018). Lessons from the crypt: HMGA1 — amping up wnt for stem cells and tumor progression. *Cancer Res.* *78*, 1890–1897.

Roellig, D., Tan-Cabugao, J., Esaian, S., and Bronner, M.E. (2017). Dynamic transcriptional signature and cell fate analysis reveals plasticity of individual neural plate border cells. *ELife* *6*, e21620.

Sarhadi, V.K., Wikman, H., Salmenkivi, K., Kuosma, E., Sioris, T., Salo, J., Karjalainen, A., Knuutila, S., and Anttila, S. (2006). Increased expression of high mobility group A proteins in lung cancer. *J. Pathol.* *209*, 206–212.

Sauka-Spengler, T., and Barembaum, M. (2008). Chapter 12 Gain- and Loss-of-Function Approaches in the Chick Embryo. *Methods Cell Biol.* *87*, 237–256.

Schindelin, J., Arganda-Carreras, I., Frise, E., Kaynig, V., Longair, M., Pietzsch, T., Preibisch, S., Rueden, C., Saalfeld, S., Schmid, B., et al. (2012). Fiji: an open-source platform for biological-image analysis. *Nat. Methods* *9*, 676–682.

Schuldenfrei, A., Belton, A., Kowalski, J., Talbot, C.C., Di Cello, F., Poh, W., Tsai, H.L., Shah, S.N., Huso, T.H., Huso, D.L., et al. (2011). HMGA1 drives stem cell, inflammatory pathway, and cell cycle progression genes during lymphoid tumorigenesis. *BMC Genomics* *12*, 549.

Shah, S.N., and Resar, L.M.S. (2012). High mobility Group A1 and cancer: Potential biomarker and therapeutic target. *Histol. Histopathol.* *27*, 567–579.

Simões-Costa, M., and Bronner, M.E. (2013). Insights into neural crest development and evolution from genomic analysis. *Genome Res.* *23*, 1069–1080.

Simões-Costa, M., and Bronner, M.E. (2015). Establishing neural crest identity: a gene regulatory recipe. *Development* *142*, 242–257.

Simões-Costa, M., and Bronner, M.E. (2016). Reprogramming of avian neural crest axial identity and cell fate. *Science* *352*, 1570–1573.

Simões-Costa, M., McKeown, S.J., Tan-Cabugao, J., Sauka-Spengler, T., and Bronner, M.E. (2012). Dynamic and differential regulation of stem cell factor FoxD3 in the neural crest is encrypted in the genome. *PLoS Genet.* *8*, e1003142.

Simões-Costa, M., Tan-Cabugao, J., Antoshechkin, I., Sauka-Spengler, T., and Bronner, M.E. (2014). Transcriptome analysis reveals novel players in the cranial neural crest gene regulatory network. *Genome Res.* *24*, 281–290.

Simões-Costa, M., Stone, M., and Bronner, M.E. (2015). Axud1 Integrates Wnt Signaling and Transcriptional Inputs to Drive Neural Crest Formation. *Dev. Cell* *34*, 544–554.

Steventon, B., Araya, C., Linker, C., Kuriyama, S., and Mayor, R. (2009). Differential requirements of BMP and Wnt signalling during gastrulation and neurulation define two steps in neural crest induction. *Development* *136*, 771–779.

Strobl-Mazzulla, P.H., Sauka-Spengler, T., and Bronner-Fraser, M. (2010). Histone demethylase Jmjd2A regulates neural crest specification. *Dev. Cell* *19*, 460–468.

Taneyhill, L.A., Coles, E.G., and Bronner-Fraser, M. (2007). Snail2 directly represses cadherin6B during epithelial-to-mesenchymal transitions of the neural crest. *Development* *134*, 1481–1490.

Tani-Matsuhana, S., Vieceli, F.M., Gandhi, S., Inoue, K., and Bronner, M.E. (2018). Transcriptome profiling of the cardiac neural crest reveals a critical role for MafB. *Dev. Biol.* *444*, S209–S218.

Williams, R.M., Candido-Ferreira, I., Repapi, E., Gavriouchkina, D., Senanayake, U., Ling, I.T.C., Telenius, J., Taylor, S., Hughes, J., and Sauka-Spengler, T. (2019). Reconstruction of the Global Neural Crest Gene Regulatory Network In Vivo. *Dev. Cell* *51*, 255-276 e7.

Woda, J.M., Pastagia, J., Mercola, M., and Artinger, K.B. (2003). Dlx proteins position the neural plate border and determine adjacent cell fates. *Development* *130*, 331–342.

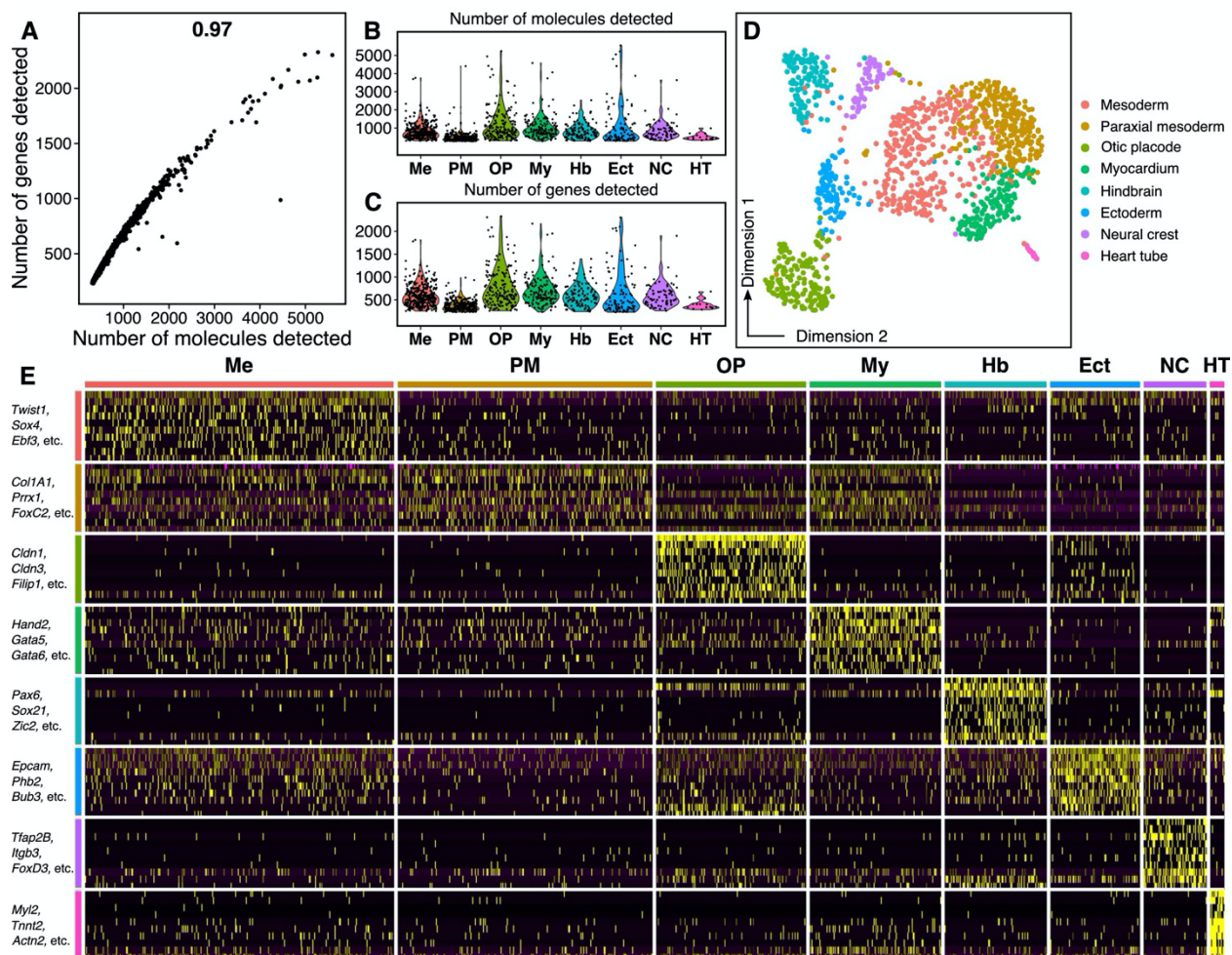
Wu, J., Saint-Jeannet, J.P., and Klein, P.S. (2003). Wnt-frizzled signaling in neural crest formation. *Trends Neurosci* *26*, 40–45.

Xian, L., Georgess, D., Huso, T., Cope, L., Belton, A., Chang, Y.-T., Kuang, W., Gu, Q., Zhang, X., Senger, S., et al. (2017). HMGA1 amplifies Wnt signalling and expands the intestinal stem cell compartment and Paneth cell niche. *Nat. Commun.* *8*, 15008.

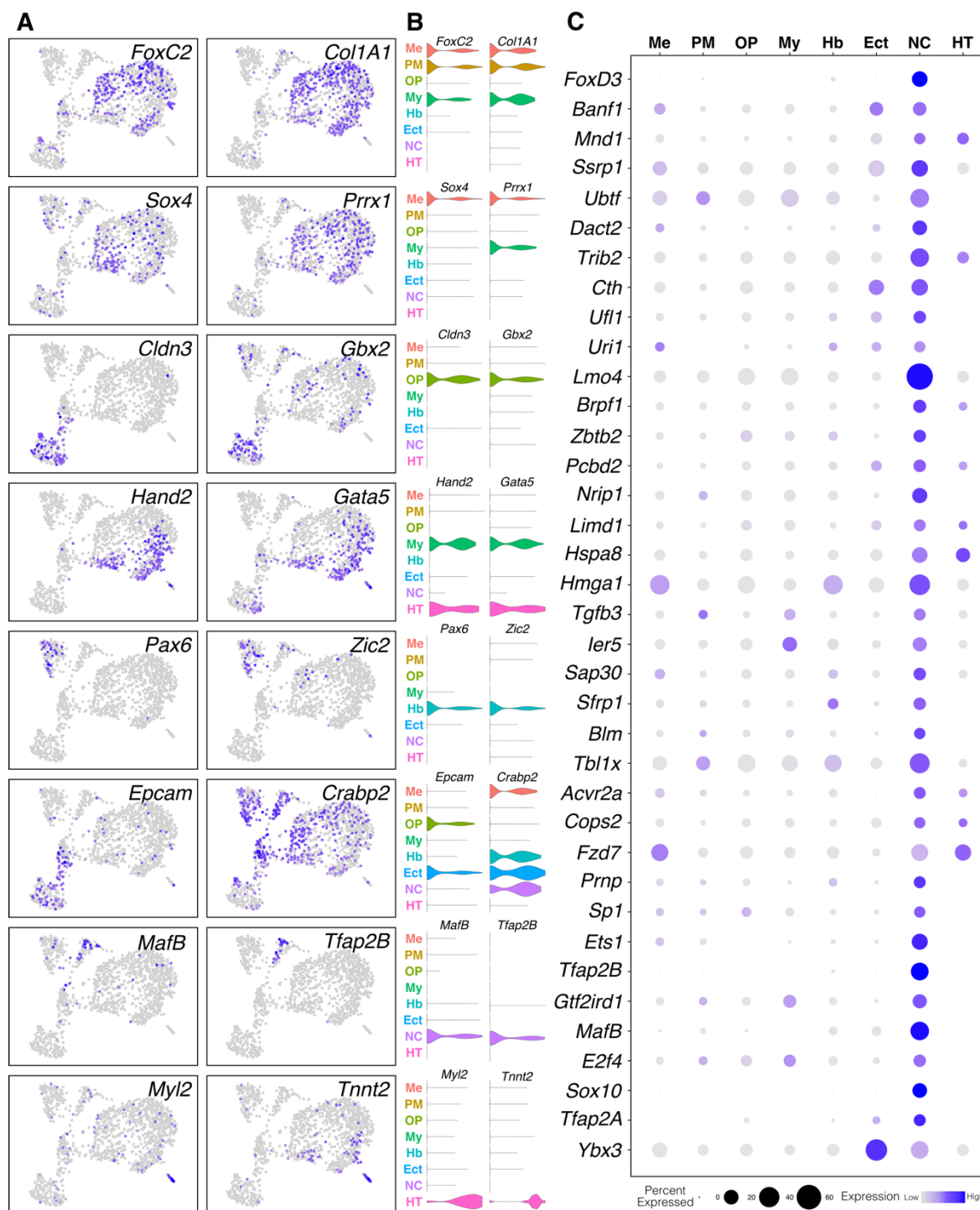
Xu, Z., Robitaille, A.M., Berndt, J.D., Davidson, K.C., Fischer, K.A., Mathieu, J., Potter, J.C., Ruohola-Baker, H., and Moon, R.T. (2016). Wnt/ β -catenin signaling promotes self-renewal and inhibits the primed state transition in naïve human embryonic stem cells. *Proc. Natl Acad. Sci. USA* *113*, E6382–E6390.

Yanfeng, W., Saint-Jeannet, J.P., and Klein, P.S. (2003). Wnt-frizzled signaling in the induction and differentiation of the neural crest. *BioEssays* *25*, 317–325.

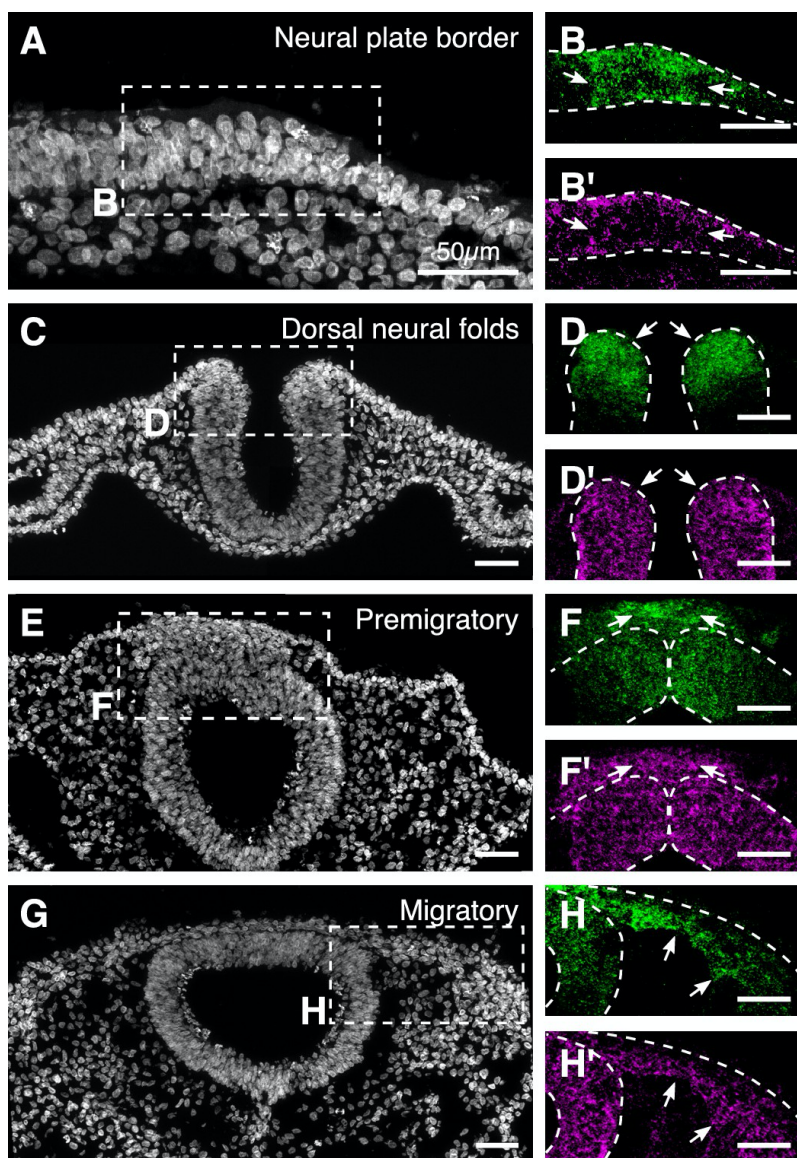
6.9 Supplementary Figures



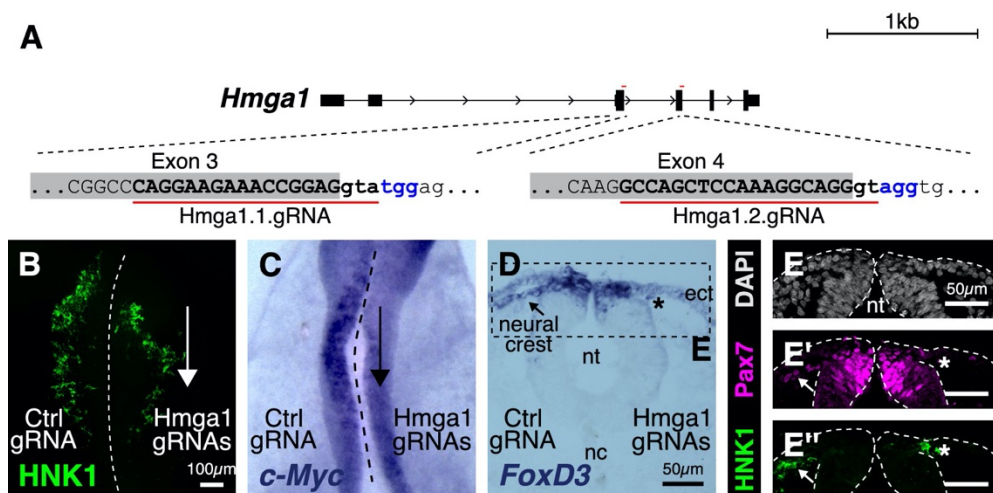
Supplementary Figure 1. Quality of single-cell RNA-seq dataset. **A.** Scatter plot shows high correlation between the number of unique genes and the total number of molecules detected in each cell. **B-C.** The distribution of total number of molecules (B) and number of unique genes (C) detected per cell across the 8 cell types identified within the chick hindbrain. **D.** Increasing the resolution parameter in the single-cell analysis pipeline to calculate a cell's "nearest neighbor" allowed identification of three subpopulations within the 'mesoderm' cluster displayed in Figure 1B. Based on marker gene expression, these subpopulations were identified as mesoderm (*Twist1*⁺), paraxial mesoderm (*Prrx1*⁺), and myocardium (*Hand2*⁺). **E.** The expression of the top 10 most abundant genes from each subcluster was used to plot a heatmap, which also grouped into 8 distinct categories, similar to (D). A subset of these abundant genes are labeled along the y-axis.



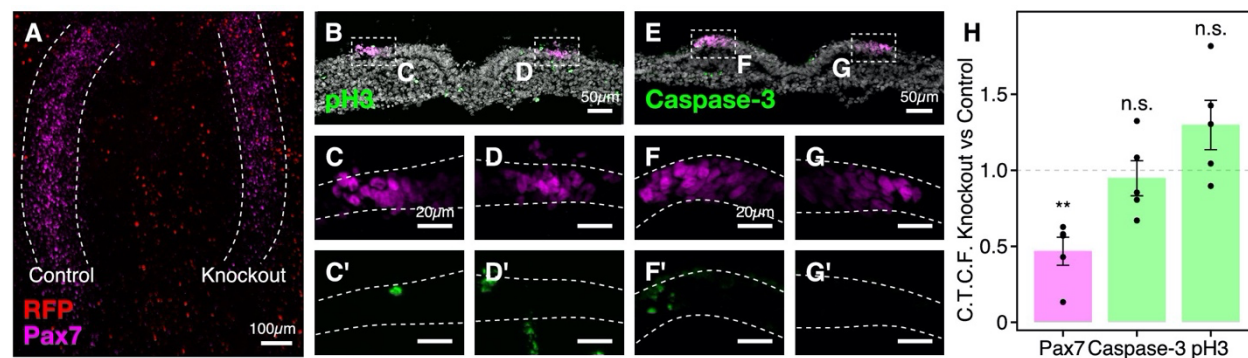
Supplementary Figure 2. Identification of novel genes expressed in the neural crest. A. Feature plots showing expression of marker genes in low-dimensional space used to identify all 8 sub-clusters within the chick hindbrain. **B.** Violin plots showing the distribution of expression of these marker genes (A) in surrounding cell types. **C.** Relative expression of all genes expressed in the neural crest cluster that share the GO terms “DNA binding,” “transcription factor,” and “regulation of transcription.” Several of these genes are transcriptional regulators and/or chromatin remodelers that are also expressed in surrounding tissues. The radius of each point reflects the proportion of cells within individual clusters that express a specific gene, whereas the relative expression is reflected by the color of the point (grey – low/negative expression, blue – high expression). A subset of these genes are highlighted in Figure 1E.



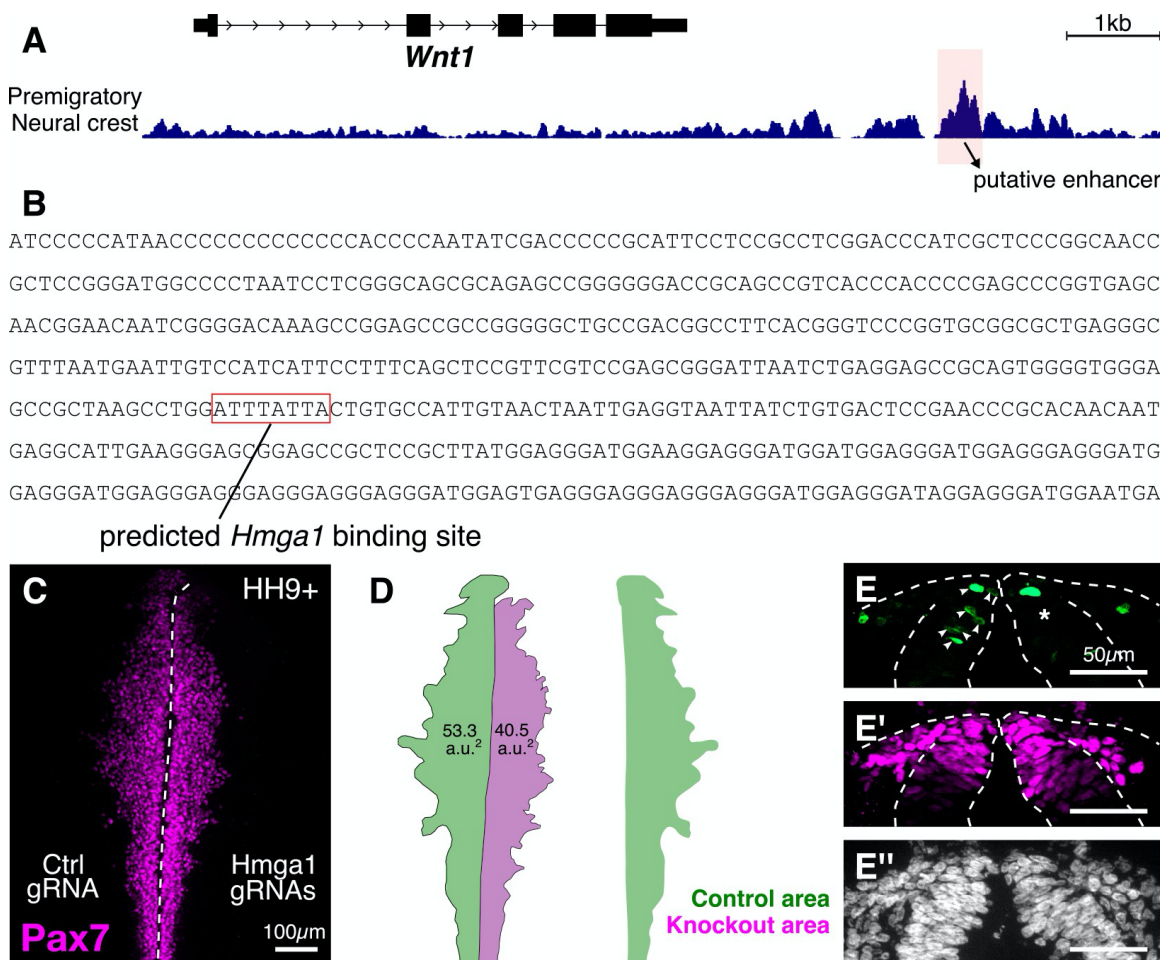
Supplementary Figure 3. Overlapping expression of *Hmga1* and *Pax7* in the neural crest visualized in individual channels. A-H. Transverse sections shown in Figure 2 stained with DAPI (A,C,E,G). The expression of *Hmga1* and *Pax7* overlapped in the neural plate border (B,B'; arrows), dorsal neural folds (D,D'; arrows), premigratory (F,F'; arrows), and migratory neural crest cells (H,H'; arrows).



Supplementary Figure 4. Knocking out *Hmga1* in gastrula stage embryos. **A.** The genomic locus of *Hmga1* in the chick genome. Two gRNAs, one targeting the splice donor site of exon 3 and another one targeting the splice donor site of exon 4 were designed to knock it out using CRISPR-Cas9. The protospacer adjacent motifs for both gRNAs lie in the intronic regions (highlighted in blue). **B.** Electroporated embryos were allowed to develop until HH9+ and immunostained for the migratory neural crest marker HNK1. In the absence of *Hmga1*, neural crest cells failed to migrate properly on the experimental side. **C.** *Hmga1* knockout results in reduced *c-Myc* expression in premigratory neural crest. **D-E''.** Transverse section through a representative *Hmga1*-knockout embryo with *FoxD3* mRNA labeled using *in situ* hybridization. Neural crest cells migrated normally on the control (arrow) compared to the knockout side (asterisk). While the thickness of the neural tube (E) was unaffected on the knockout side, the expression of Pax7 (E') and HNK1 (E'') was also reduced.



Supplementary Figure 5. *Hmga1* knockout does not affect neural crest cell proliferation and apoptosis. **A.** Whole mount embryo shown in Figure 4F. Nuclear RFP was electroporated as a transfection control. **B-G'.** Adjacent transverse sections through embryo in **A** immunostained with antibodies against phospho-histone H3 (**B,C',D'**) and cleaved-caspase-3 (**E,F',G'**) as a readout for cell proliferation and apoptosis, respectively. While the levels of Pax7 protein (**C,D,F,G**) were downregulated in the absence of *Hmga1*, no notable difference was observed in the rate of proliferation or cell death between the experimental (right; **D',G'**) and control (left; **C',F'**) sides. **H.** The relative fluorescence intensity for Pax7, cleaved-caspase-3, and phospho-histone H3 was measured as the ratio of corrected total cell fluorescence (C.T.C.F.) between the knockout versus the control side. The Pax7 fluorescence intensity was significantly reduced (** $p < 0.01$, paired Student's t-test) on the knockout side, whereas the difference between cleaved-caspase-3 and phospho-histone H3 relative intensities was not significant (n.s. $p > 0.05$, paired Student's t-test). Dotted line represents unperturbed ratio.



Supplementary Figure 6. *Hmga1* regulates *Wnt1* expression in premigratory cranial neural crest cells. A. Genomic locus of *Wnt1* obtained from the UCSC genome browser (Karolchik et al., 2003). ATAC-seq profile of premigratory cranial neural crest cells (from Williams et al., 2019) shows a putative *Wnt1* enhancer upstream of the gene (highlighted in red). **B.** Genomic sequence of the putative enhancer identified in (A) contains a predicted AT-rich *Hmga1* binding motif (red box). **C.** A representative *Hmga1*-knockout embryo immunostained for Pax7 shows a migration defect on the experimental side (right) compared to the control side (left). **D.** The area covered by migratory cranial neural crest cells, marked by the position of the lateral-most leader cell, is reduced following *Hmga1* knockout (green – control; 53.3 a.u.², magenta – knockout; 40.5 a.u.²). An overlay of the two areas highlights this reduction. **E.** Transverse section through the embryo shown in (C). The number of dorsal neural tube cells positive for canonical Wnt activity, as indicated by the nuclear GFP reporter expression (E), was significantly decreased following the loss of *Hmga1* (shown in Figure 6C). However, the number of Pax7+ cells (E') on either side of the dorsal neural tube were relatively similar, despite the observed migration defect in (C). No difference in the thickness of the neural tube (E'') was observed (shown in Figure 6C'').

Chapter 7

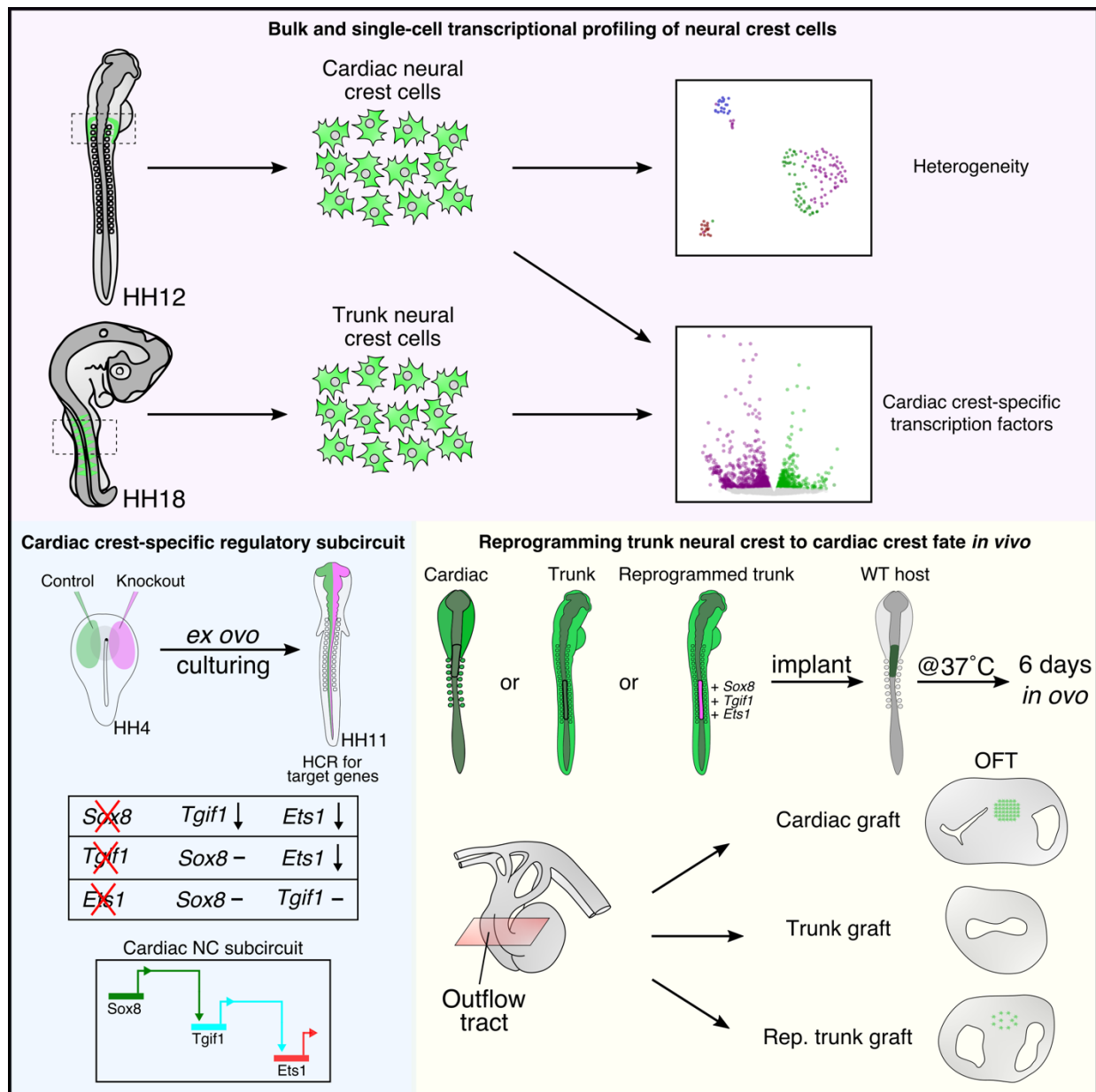
Cardiac neural crest plasticity in heart development

A modified version of this chapter was published as:

Gandhi, S., Ezin, M., and Bronner, M.E. (2020). Reprogramming axial level identity to rescue neural-crest-related congenital heart defects. *Dev. Cell* 53, 300-315.e4.

<https://doi.org/10.1016/j.devcel.2020.04.005>

7.1 Graphical abstract



7.2 Introduction

The vertebrate heart arises from cells in the lateral plate mesoderm that converge at the embryonic midline and fuse into a heart tube. In amniotes, cells from the second heart field are added after the heart tube loops, causing remodeling of the tube to form four heart chambers—two atria and two ventricles. The looped heart connects to the forming lungs by means of the truncus arteriosus, which initially is a single vessel destined to form the outflow tract of the heart. Cardiac neural crest cells make a critical contribution to the heart by septating the truncus arteriosus into the pulmonary trunk, through which deoxygenated blood flows to the lungs, and the aortic trunk, through which oxygenated blood is pumped throughout the body. In fact, abnormal cardiac crest development results in some of the most common human congenital heart defects (Grossfeld et al., 2004; Loffredo, 2000; Neeb et al., 2013), including Persistent Truncus Arteriosus (PTA), in which the aorticopulmonary septum fails to close, resulting in mixing of oxygenated and deoxygenated blood.

Premigratory cardiac neural crest cells initially reside within the developing caudal hindbrain, from which they migrate to the forming pharyngeal arches 3, 4, and 6 (Phillips et al., 1987). While some cells remain in the arches, contributing to the carotid and other arteries (Waldo and Kirby, 1993), others invade the heart to form the aorticopulmonary septum, cardiac cushions, part of the interventricular septum, and cardiac ganglia (Kirby and Stewart, 1983). A small number of neural crest cells also move through arches 1 and 2 to the right ventricle, where they adopt coronary smooth muscle fates (Arima et al., 2012).

Loss of genes important for cardiac neural crest development, such *Pax3* or *Edn1* (endothelin-1), results in cardiac abnormalities (Franz, 1989; Kurihara et al., 1999). Moreover, surgical ablation of the cardiac crest in chick (Kirby and Waldo, 1990; Kirby et al., 1985) phenocopies human PTA (Besson et al., 1986; Kirby and Waldo, 1995; Nishibatake et al., 1987). Importantly, grafting cranial or trunk neural crest in place of ablated cardiac crest cannot rescue the deficit (Kirby, 1989), suggesting that inherent

differences exist along the body axis in the neural crest's ability to form cardiovascular derivatives. However, the mechanisms underlying the cardiac crest's unique developmental potential remain unknown.

Here, we tackle the molecular and cellular basis of cardiac crest-related birth defects by combining classical embryology with state-of-the-art genomics approaches. First, we reproduce and extend classical chick embryological experiments done over 30 years ago and report laterality differences in cardiovascular defects resulting from unilateral cardiac neural fold ablations. Second, we identify new genes enriched in the cardiac neural crest by bulk and single-cell RNA-seq and demonstrate that migrating cardiac crest cells represent a heterogeneous population. Third, we establish regulatory relationships of cardiac neural crest genes and explore their role in heart development. Accordingly, we find that one of these genes, *Tgif1*, functions in a cardiac neural crest subcircuit important for specification and proper outflow tract septation. Finally, we show that ectopic expression of a cardiac crest-specific subcircuit, comprised of *Sox8*, *Tgif1*, and *Ets1*, is sufficient to reprogram trunk neural crest cells, enabling them to migrate to the heart and rescue the effects of a cardiac crest ablation, which they cannot normally do. Taken together, our results help elucidate the unique genetic properties of the cardiac neural crest in formation and function of the heart. Our results uncover potential target genes involved in cardiovascular birth defects and provide a molecular recipe for generating ectomesenchymal derivatives of the cardiac crest for the purposes of regenerative medicine.

7.3 Results

7.3.1 Ablation of the chick cardiac neural crest results in cardiovascular defects

The cardiac neural crest was described by Kirby and colleagues (Besson et al.,1986; Bookman et al.,1987; Harrison et al.,1995; Kirby et al.,1985; Nishibatake et al.,1987) as arising in the caudal hindbrain [Figure 1A,B]. Moreover, bilateral ablation of this region in chick embryos at a time corresponding to when the cardiac crest cell fate is specified (Ezin et al., 2009) resulted in improper cardiovascular development.

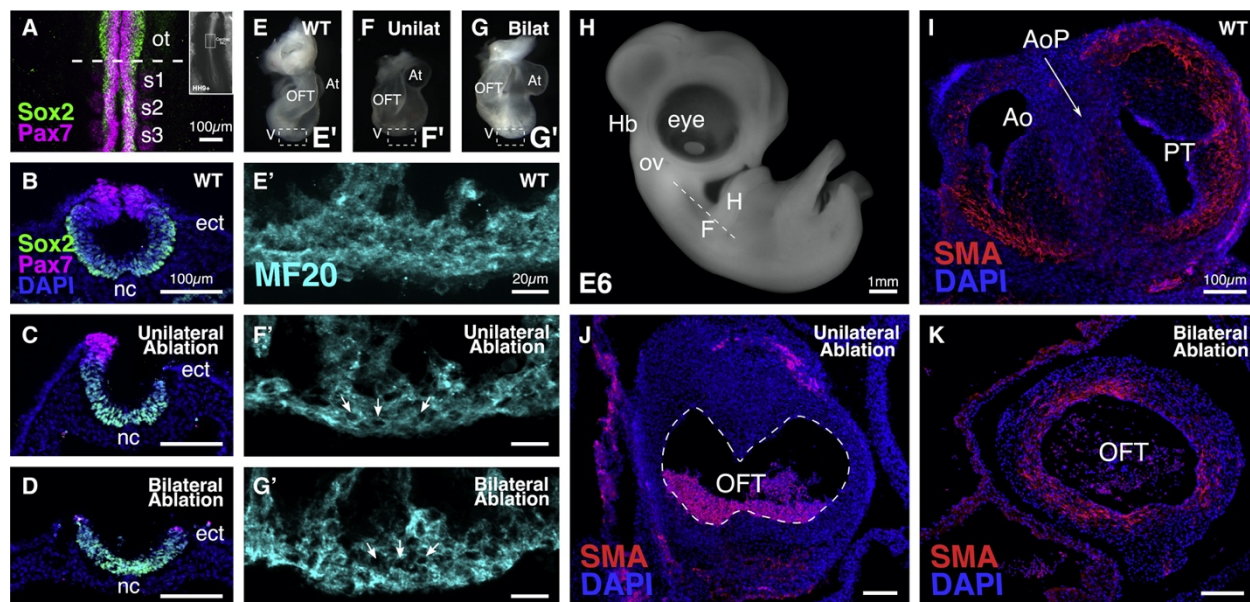


Figure 1. Chick cardiac neural crest ablation results in cardiovascular abnormalities. **A.** Dorsal view of a whole-mount stage HH9+ embryo (inset). Cardiac domain stained with neural crest marker Pax7 (Magenta) and neural tube marker Sox2 (Green). Dotted line indicates level of sections in B-D. **B.** Transverse section through A shows cardiac neural crest residing in the dorsal neural tube in wild type embryo. **C-D.** Transverse section through embryos after unilateral (C) and bilateral (D) dorsal neural fold ablation. **E-G.** Ventral view of E3 control (E), unilaterally ablated (F), and bilaterally ablated (G) primary heart tubes. **E'-G'.** Transverse sections through E-G stained with the muscle marker MF20 show uniform MF20 labeling in wild type (E') heart but patchy expression (arrows) in ablated embryos (F'-G'). **H.** Whole-mount image of an E6 chick embryo. Dotted line shows angle of sectioning in I-K. **I.** Cross-section through the outflow tract of a wild type E6 embryo shows complete septation, with the aorticopulmonary septum (AoP) separating the aorta (Ao) from pulmonary trunk (PT). **J-K.** Unilateral (J) and bilateral (K) cardiac crest ablation results in the failure of outflow tract septation, resulting in a single vessel emerging from the heart. (SMA; red, DAPI; blue) ot-otic placode, s-somites, At-atrium, V-ventricle, OFT-outflow tract, ect-ectoderm, nc-notochord, Hb-hindbrain, ov-otic vesicle, H-heart, F-forelimb. See also Supplementary Figure S1.

To reproduce and extend cardiac neural crest ablation experiments, we ablated the chick dorsal neural tube adjacent to the caudal hindbrain [Figure 1C-D] at Hamburger Hamilton stage (HH) 9-10 (Hamburger and Hamilton, 1951) and allowed embryos to develop until embryonic day (E) 3 or E6. In normal embryos, the primary heart tube exhibited proper elongation and looping dynamics at E3 [Figure 1E; Supplementary Figure 1A]. Staining sections of the heart tube for the myosin heavy chain marker MF20 revealed uniform filamentous staining throughout the myocardial sleeve [Figure 1E'] of the distal outflow limb. At E6, the aorticopulmonary septum of control embryos developed normally [Figure 1I] with the aorta connected to the left ventricle and pulmonary trunk

connected to the right. In contrast, bilaterally ablated embryos had an uneven distribution of MF20 in the distal outflow limb at E3 [Figure 1G'] and a complete lack of septation of the outflow tract at E6, characteristic of severe PTA [Figure 1K].

Next, we unilaterally ablated either the right (n=9) or left (n=8) dorsal neural tube, leaving the contralateral side intact [Figure 1C,D]. At E3, the primary heart tube appeared “bulbous” with a shortened and straighter outflow tract compared to the control group [Figure 1F,G]; no differences were noted between right or left cardiac neural fold ablations. At E6, removal of the cardiac neural folds from the right side caused PTA (n=4/9 embryos) [Figure 1J], albeit not as severe as the phenotype observed following bilateral ablation. Notably, all embryos with an outflow tract septation defect following unilateral ablation had outflow tract cushions that failed to fuse in the middle, suggesting that a critical cardiac neural crest cell number is necessary to form the aorticopulmonary septum. In three cases, we observed Double Outlet Right Ventricle (DORV), another phenotype commonly associated with cardiac crest perturbations. In contrast to right side unilateral ablation, removal of the left dorsal neural tube resulted in DORV as the predominant phenotype (n=6/8) [Supplemental Figure 1B], with one embryo having PTA. These results raise the intriguing possibility that differences exist in the cardiovascular contributions of cardiac crest cells from different sides of the neural tube. Together, our results suggest that a bilateral cardiac neural crest contribution is necessary for proper outflow tract septation, and that unilateral extirpation of the caudal hindbrain is sufficient to cause cardiovascular anomalies.

7.3.2 Population level transcriptome analysis reveals genes enriched in the cardiac neural crest

To identify molecular mechanisms underlying the cardiac crest's unique developmental potential to contribute to the cardiovascular system, we turned to a comparative transcriptomics approach to identify transcription factors enriched in the cardiac relative to trunk crest populations. To this end, we used the FoxD3-NC2 (Simões-Costa et al., 2012) enhancer that drives reporter expression in cardiac crest at HH12

[Figure 2A] and later in the trunk neural crest [Figure 2B]. Dissecting embryos at different axial levels and developmental time points enabled isolation of pure migrating cardiac and trunk neural crest populations by Fluorescence-Activated Cell Sorting (FACS). Following library preparation, sequencing, and data analysis, we identified 474 genes upregulated in cardiac compared to trunk neural crest population [Figure 2C]. Quality control on the sequenced libraries showed that the data were good quality [Supplementary Figures S1C,D].

Next, we focused on transcription factors that were significantly upregulated in cardiac versus trunk crest [Figure 2C']. We identified some transcription factors that were previously known to be expressed and/or functionally relevant in cardiac crest development, including V-Ets Avian Erythroblastosis Virus E26 Oncogene Homolog 1 (*Ets1*) (Gao et al., 2010), MAF BZIP Transcription Factor B (*MafB*), and Transcription Factor AP-2 Beta (*Tfap2b*) (Tani-Matsuhana et al., 2018) [Figure 2D-F]. Others, such as TGFB-Induced Factor Homeobox 1 (*Tgif1*), SRY Box Transcription Factor 8 (*Sox8*), NACC family member 2 (*Nacc2*), and MAF BZIP Transcription Factor K (*MafK*), were transcription factors not previously ascribed to the cardiac neural crest. Their expression in the migrating cardiac crest was validated using *in situ* hybridization [Figure 2G-I]. Next, we compared genes enriched in cardiac crest to those previously shown to be enriched in cranial crest (Simões-Costa and Bronner, 2016). While some genes were shared with the cranial (e.g. *Ets1*, *Sox8*, *Tfap2b*), other genes were unique to the cardiac crest stream (e.g. *Tgif1*, *MafK*, *Nacc2*), thus identifying previously uncharacterized cardiac axial level-selective transcription factors.

7.3.3 Single-cell RNA-seq reveals heterogeneity in migrating cardiac crest

Next, we turned to single-cell RNA-seq (scRNA-seq) to deeply profile individual cardiac neural crest cells. To this end, we labeled cardiac crest cells as described above and isolated 156 single cells using FACS. The libraries containing each barcoded cell were multiplexed and sequenced to obtain over 100,000 reads per cell.

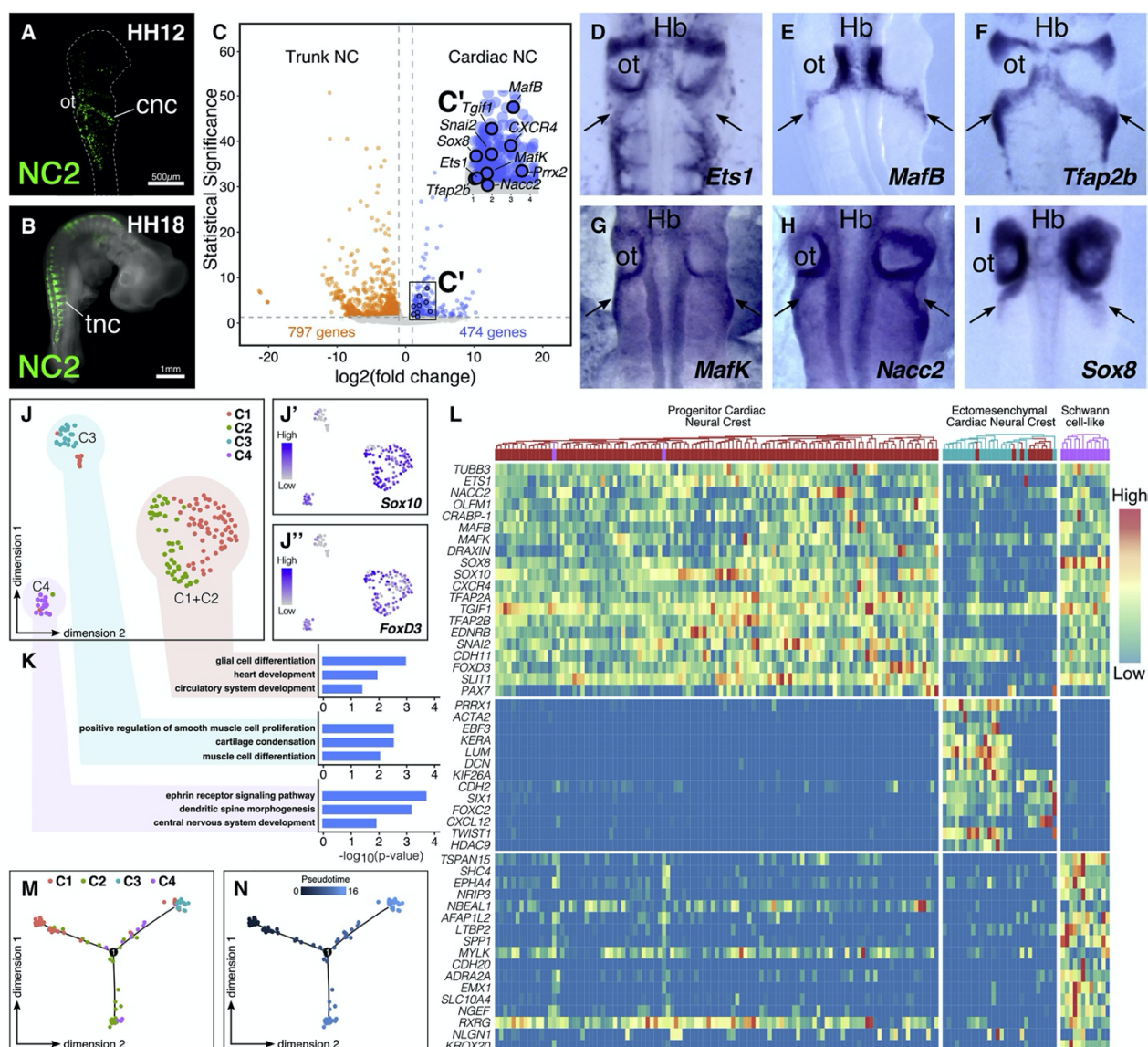


Figure 2. Bulk and single cell transcriptional profiling of cardiac neural crest. **A-B.** Pure populations of cardiac or trunk neural crest cells labeled with the FoxD3-NC2 enhancer were isolated using FACS at HH12 (**A**) and HH18 (**B**), respectively. **C-C'.** Volcano plot showing fold change and significance of genes enriched in cardiac and trunk neural crest ($\log_2(\text{fold change}) > 1$). Transcription factors examined for expression in migrating cardiac crest are highlighted in (**C'**). **D-I.** *In situ* hybridization of HH12 embryos shows expression of selected transcription factors in migratory cardiac crest (dorsal view; arrows). **J.** UMAP plot depicting clustering of 156 single cardiac neural crest cells that were profiled using smart-seq v2. **J'-J''.** Cluster C1 and C2 exhibit high expression of neural crest markers Sox10 (**J'**) and FoxD3 (**J''**) and differed subtly in the expression of proliferation genes. **K.** GO term analysis on differentially upregulated genes in each cluster confirmed the identity of each subpopulation within the migrating cardiac crest (Fisher's exact test, adjusted- $p < 0.05$). **L.** Heatmap illustrating hierarchical clustering of single cells that passed filtering parameters and expression levels of selected neural crest, ectomesenchymal, and neuronal genes. A few cells from the cardiac crest progenitor clusters C1 and C2 grouped together with cells from the ectomesenchymal cluster C3. **M-N.** Pseudotime analysis (**M**) on migratory cardiac crest cells. Cells are labeled according to their pseudotime values (**N**). ot-otic vesicle, cnc-cardiac neural crest, tnc-trunk neural crest, Hb-hindbrain. See also Supplementary Figure S1.

Following alignment, filtering, and normalization, we recovered high quality data for 149 single cells [Supplementary Figure S1E-G]. Principal Component Analysis (PCA) followed by Uniform Manifold Approximation and Projection (UMAP) revealed the presence of 4 distinct clusters (C1, C2, C3, and C4) within the migrating cardiac crest population, suggesting heterogeneity between clusters [Figure 2J]. Bona fide migratory crest markers *Sox10* and *FoxD3* were less abundant in C3 compared to C1, C2, and C4 [Figure 2J'-J''], suggesting that a subset of migrating cardiac crest cells may already be down-regulating an early neural crest program, perhaps indicating fate restriction.

To further explore these differences, we performed GO term enrichment analysis of genes that were differentially upregulated in each cluster [Figure 2K] and found that biological processes such as heart development and circulatory system development were primarily associated with C1 and C2 ($p < 0.05$; Fisher's exact test). C3 was associated with positive regulation of smooth muscle cell proliferation and muscle cell differentiation, consistent with reduced expression of bona fide neural crest markers. Similarly, C4 was associated with ephrin receptor signaling and central nervous system development, supporting a neuronal identity. C1 and C2 were transcriptionally similar to each other [Figure 2L] apart from a subtle increase in expression of cell proliferation genes such as *Kpna2* and *Cdc20* in C2.

In contrast, we found a significant enrichment of ectomesenchymal cell state markers such as *Twist1*, *Prrx1*, and *Acta2* in C3, suggesting that cells in this cluster have acquired a restricted ectomesenchymal cell state at the expense of a multipotent neural crest identity. Furthermore, C4 had increased expression of Schwann cell markers such as *Epha4*, *Krox20*, and *Nrip3*, along with bona fide crest markers such as *Sox10*, *Ets1*, and *FoxD3*. Based on marker genes, we ascribed the following identities to the single cell subclusters: progenitor cardiac crest (C1, C2), ectomesenchymal cardiac crest (C3) and Schwann cell-like (C4). Interestingly, hierarchical clustering with labeled UMAP cluster identity showed that a subset of progenitor cardiac crest cells was affiliated with the ectomesenchymal group, suggesting that we captured single cells that were transitioning from a neural crest progenitor to an ectomesenchymal-like state. We further explored the

potential relationships between subpopulations using Monocle [Figure 2M-N]. Unsupervised clustering along the pseudotime trajectory demonstrated a gradual transition from cells in cluster C1 (progenitor) to proliferating (C2), Schwann cell-like (C4), and ectomesenchymal (C3) cardiac crest [Figure 2M]. Taken together, these results suggest cellular heterogeneity within early migrating cardiac crest populations.

To test whether our single-cell data, pooled together, recapitulated the cardiac neural crest transcriptomic profile obtained from bulk RNA sequencing, we compared the relative abundance of transcripts as measured by fragments per kilobase of exon per million fragments mapped (FPKM). The genes enriched in the two datasets were positively correlated, with a Pearson's correlation coefficient of 0.85 [Supplementary Figure S1H]. Using markers identified and validated at the population level, we looked for their distribution of expression in the scRNA-seq data [Supplementary Figure S1I]. As expected, the expression of cardiac crest markers *Ets1*, *MafB*, *Tfap2b*, *MafK*, *Nacc2*, *Sox8*, and *Tgif1* was uniformly distributed across C1, C2, and C4, with the latter four also similarly expressed in C3. Together, these results demonstrate that the four subclusters reflected the profile observed in the bulk cardiac crest dataset.

7.3.4 Transcription factor *Tgif1* is required for cardiac neural crest specification

With an eye toward finding transcription factor(s) expressed at the onset of cardiac crest specification, we analyzed spatiotemporal expression patterns and were particularly intrigued by *Tgif1* due to its selective expression in the delaminating cardiac crest at HH10 [Figure 3A,B,E], the time at which cardiac crest fate is determined (Ezin et al., 2009). *Tgif1* expression was first observed at stage HH9+ [Figure 3A] in the dorsal neural tube between the otic vesicle and the third somite, overlapping with the cardiac neural crest territory. After delamination at HH10 [Figure 3B,E], *Tgif1* expression was retained in migrating cardiac crest cells co-expressing neural crest marker HNK-1 (Basch et al., 2006) at HH12 [Figure 3C,D,F,F'].

We next examined the role of *Tgif1* in cardiac crest development. To this end, we used a CRISPR-Cas9-mediated strategy (Gandhi et al., 2017) to knock out *Tgif1* in early

chick embryos. We designed two gRNAs, one targeting the splice acceptor site of the second exon, and the second one targeting the third exon [Supplementary Figure S2A].

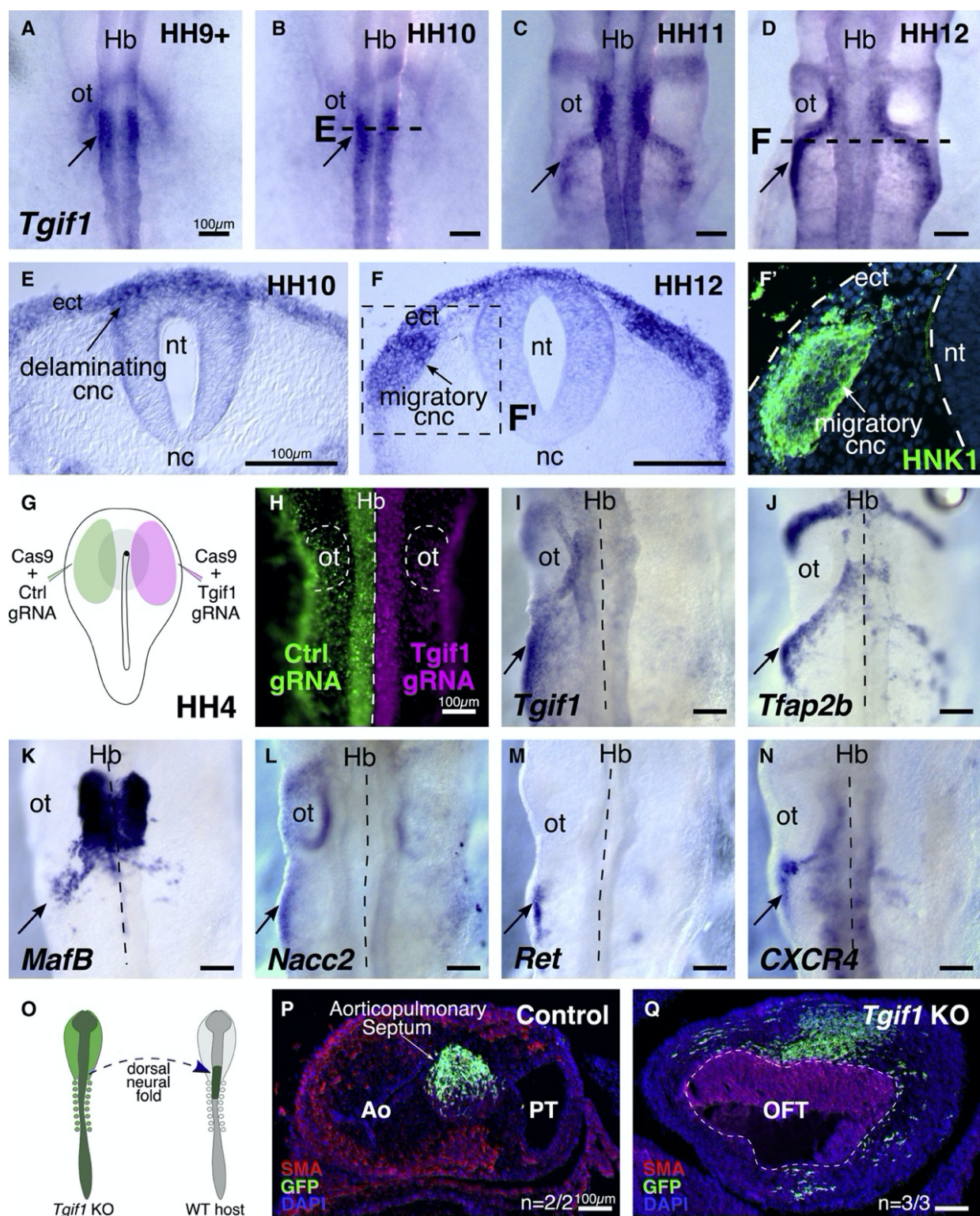


Figure 3. See next page for legend.

Figure 3. *Tgif1* is critical for cardiac neural crest specification and outflow tract septation. **A-D.** Spatiotemporal expression pattern of *Tgif1* in cardiac neural crest between stages HH9+ and HH12 (dorsal view). **E.** Transverse section through (B) shows *Tgif1* expression in delaminating cardiac crest cells in the dorsal neural tube. **F-F'.** Transverse section through (D) shows *Tgif1* expression in migrating cardiac crest which overlaps with the expression of the neural crest marker HNK1 (F'). **G.** Diagram depicting *ex ovo* electroporation strategy for *Tgif1* knockout in gastrula stage embryos. **H.** An embryo transfected with gRNAs targeting *Tgif1* (magenta) and control gRNA (green) (dorsal view). **I-N.** Following CRISPR-Cas9-mediated knockout of *Tgif1*, expression of the indicated transcription factors was significantly reduced (dorsal view). Arrows indicate normal gene expression on control side. **O.** Experimental strategy to investigate the role of *Tgif1* in outflow tract septation. Cardiac neural folds from a transgenic embryo where *Tgif1* was bilaterally knocked out at the gastrula stage were grafted in place of the ablated cardiac crest in a stage-matched HH9 wildtype host. **P.** Cardiac crest cells from control gRNA-electroporated transgenic graft are observed within the condensed mesenchyme of the properly septated outflow tract. **Q.** The OFT of embryos grafted with the *Tgif1* knockout cardiac neural fold failed to septate. Hb-hindbrain, ot-otic placode, ect-ectoderm, nt-neural tube, nc-notochord, cnc-cardiac neural crest, Ao-aorta, PT-pulmonary trunk, OFT-outflow tract. See also Supplementary Figure S2.

To test if gRNAs targeting *Tgif1* were sufficient to knock out its expression, we electroporated the right side of gastrula stage embryos with expression constructs for Cas9, *Tgif1* gRNAs, and H2B-RFP, and the left side with control reagents and GFP [Figure 3G,H]. Embryos were cultured *ex ovo* until HH12 and assayed for expression of *Tgif1* by *in situ* hybridization. As expected, these embryos exhibited nearly complete loss of *Tgif1* [Figure 3I] on the experimental side, validating our approach. Furthermore, knockout of *Tgif1* resulted in a notable reduction in expression of other cardiac crest markers like *Tfap2B*, *MafB*, *Nacc2*, *Ret*, and *CXCR4* [Figure 3J-N]. Interestingly, while expression of the pan-neural crest markers *Sox10* and *FoxD3* was reduced on the *Tgif1* knockout side, the number of cells migrating away from the neural tube was similar, albeit in disorganized migration streams [Supplementary Figure 2B,C]. These data suggest that *Tgif1* plays a pivotal role in the cardiac crest gene regulatory network.

7.3.5 *Tgif1* is necessary for proper outflow tract septation

Given its importance in early cardiac crest development, we asked if *Tgif1* is necessary for proper outflow tract septation using a grafting approach where the dorsal neural tube adjacent to the hindbrain of GFP⁺ control or *Tgif1* knockout embryos was either unilaterally or bilaterally grafted into wild type embryos [Figure 3O]. As right unilateral cardiac neural fold ablation produces PTA [Figure 1H], we first asked whether unilateral knockout of *Tgif1* was sufficient to cause septation defects. To this end, we

electroporated Cas9, *Tgif1* gRNAs, and H2B-RFP on the right side of gastrula stage transgenic embryos and cultured them *ex ovo* until HH9+; control embryos were electroporated with expression constructs for Cas9, control gRNA, and H2B-RFP. Chimeras were developed until E6, the stage by which outflow tract septation in chick embryos is complete. Transverse sections through control chimeras confirmed that the outflow tract was properly septated, with GFP⁺ cardiac crest cells condensed in the septum [Figure 3P; n=2/2], replicating previous results of quail-chick chimeras (Kirby, 1989; Kirby et al., 1985). Next, we repeated this experiment with unilateral grafting of the cardiac neural fold from a *Tgif1* knockout transgenic embryo. The results show that this also results in a fully septated outflow tract, albeit with a significantly reduced number of GFP⁺ cells in the septum [Supplementary Figure S2D; n=4/4]. Thus, the presence of the contralateral host cardiac crest together with a reduced number of transgenic cells appears to be sufficient to compensate for the unilateral loss of *Tgif1*.

As its unilateral loss was not sufficient to cause abnormalities, we tested the effects of bilateral *Tgif1* loss of function using bilateral neural fold grafts from *Tgif1* knockout transgenics. Remarkably, in E6 embryos, the outflow tract failed to septate, resulting in a single outflow vessel emerging from the heart [Figure 3Q; n=3/3], despite the migration of transgenic cells into the outflow tract. GFP⁺ cells were observed in other known derivatives of the cardiac crest, such as the left and right internal and external carotid arteries, demonstrating that outflow tract defects did not result from improper graft incorporation [Supplementary Figure S2E]. Taken together, the results show that *Tgif1* expression in cardiac neural crest cells is necessary for proper outflow tract septation. We confirmed that *Tgif1* was not expressed in trunk neural crest by using Hybridization Chain Reaction (HCR) against *Sox10*, *FoxD3*, and *Tgif1* in a HH15 chick embryo [Supplementary Figure S2F]. While *Sox10*, *FoxD3*, and *Tgif1* expression overlapped in cardiac crest cells invading the circumpharyngeal ridge, *Tgif1* transcripts were absent from migrating trunk neural crest cells [Supplementary Figure S2G-H]. We next asked if *Tgif1* was sufficient to confer “cardiac-like” characteristics onto other axial levels, but found that ectopic expression of *Tgif1* alone failed to activate the Sox10E2 cranial/cardiac

neural crest enhancer (Betancur et al., 2010) in the trunk neural crest, used here as a readout for cardiac identity [Supplementary Figure S2I-K]. This suggested that other factors may work synergistically with *Tgif1* for acquisition of cardiac crest fate. As we previously reported that minimum of three transcription factors was required to reprogram trunk neural crest to a cranial crest identity (Simões-Costa and Bronner, 2016), we broadened our search to identify other putative cardiac neural crest subcircuit genes that might work in concert with *Tgif1*.

7.3.6 HCR and scRNA-seq reveal coexpression of *Tgif1* with *Ets1* and *Sox8*

We were able to eliminate several candidate genes that were not yet expressed in delaminating/early migrating cardiac crest cells [Supplementary Figure S3A]. However, *Ets1* caught our attention as its loss causes ventricular septal defects, commonly associated with defects in cardiac crest development (Gao et al., 2010; Ye et al., 2009). In addition, SoxE transcription factors *Sox8/9/10* are necessary for initiation of neural crest formation at all axial levels (O'Donnell et al., 2006). Amongst the family of SoxE factors, *Sox8* was significantly enriched in cardiac relative to trunk neural crest. We first performed HCR using probes for *Sox8*, *Tgif1*, and *Ets1* on HH12 chick embryos to test their coexpression [Figure 4A]. The results reveal overlapping expression of *Ets1*, *Sox8* and *Tgif1* in migrating cardiac crest cells [Figure 4B-B'] at single-cell resolution, with the three genes overlapping in the post-otic stream of migrating neural crest cells [Supplementary Figure S3B-E]. To further explore their co-expression at the single-cell level, we probed individual cells from our scRNA-seq dataset. Among the four subpopulations, subclusters C1 and C2 had signatures characteristic of progenitor cardiac crest cells. By visualizing the expression of the three genes on a UMAP plot [Figure 4C-E; Supplementary Figure S3F-K], we found overlapping expression of *Tgif1*, *Sox8*, and *Ets1* in 93% of the cells in the two cardiac neural crest progenitor clusters [Figure 4F], suggesting that they could function as a cardiac crest-specific subcircuit. Of note, downstream cardiac crest transcription factors *Tfap2B*, *MafB*, *Nacc2*, and *Ret* were also co-expressed with *Tgif1*, *Sox8*, and *Ets1*.

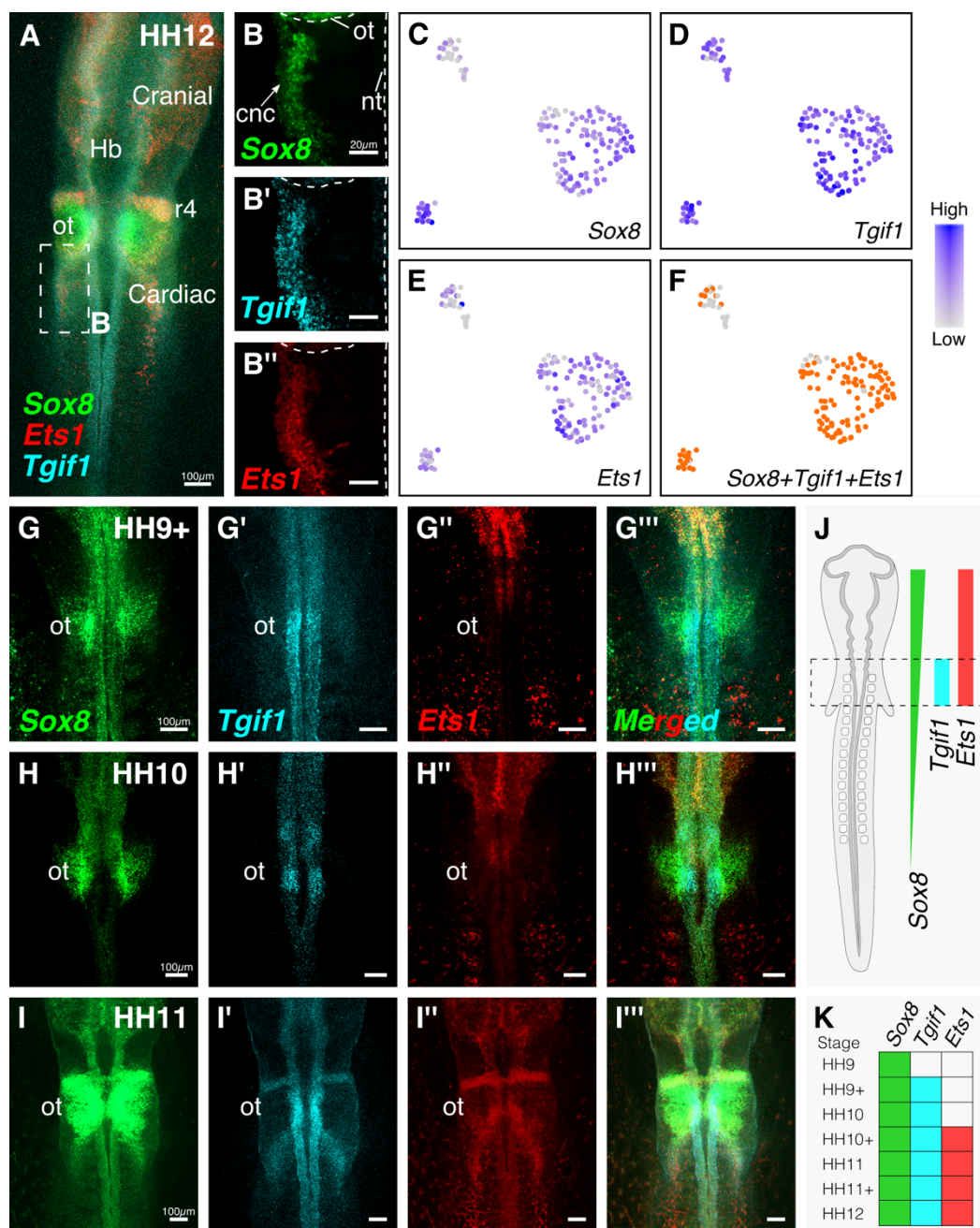


Figure 4. *Tgif1* is coexpressed with *Sox8* and *Ets1* in migrating cardiac neural crest. A-B''. HCR against *Sox8* (B), *Tgif1* (B'), and *Ets1* (B'') shows their overlapping expression in the migrating cardiac crest cells. **C-F.** Expression levels of *Sox8* (C), *Tgif1* (D), and *Ets1* (E) in individual cardiac crest cells following deep single-cell profiling. In progenitor cardiac crest clusters, the three genes had overlapping expression (orange) in 93% of the cells (F). **G-I.** Spatiotemporal expression pattern of *Sox8* (G-G'''), *Tgif1* (H-H'''), and *Ets1* (I-I''') in the cardiac crest region between stages HH9+ and HH12 (dorsal view). **J.** Schematic diagram of HH12 embryo shows overlapping expression domains of *Tgif1*, *Ets1*, and *Sox8* in the cardiac neural crest. **K.** The hierarchy of temporal expression dynamics of cardiac crest subcircuit genes from HH9 to 12. Ot-otic vesicle, Hb-hindbrain, nt-neural tube, cnc-cardiac neural crest, r4-rhombomere 4 migrating crest stream. See also Supplementary Figures S2 and S3.

7.3.7 *Sox8*, *Tgif1* and *Ets1* comprise a transcriptional cascade important for cardiac neural crest identity

To explore regulatory relationships between *Sox8*, *Tgif1*, and *Ets1*, we first performed HCR [Fig.4G-I] to establish their temporal order of expression in the cardiac crest. The results show that *Sox8* turns on first at HH9, followed by *Tgif1* at HH9+ and *Ets1* at HH10+ [Fig.4J-K]. Given this putative hierarchy, we examined their functional relationships within a subcircuit by individually knocking out *Sox8*, *Tgif1*, or *Ets1* using CRISPR-Cas9. To this end, we performed *ex ovo* electroporation of expression constructs for Cas9, gRNAs targeting *Sox8*, *Tgif1* or *Ets1* [Supplementary Figure S2A], and H2B-RFP on the right side of gastrula stage embryos; the left side was transfected with control reagents. Embryos were cultured *ex ovo* until HH11, then assayed for expression of the three factors using HCR.

Sox8 knockout resulted in loss of both *Tgif1* and *Ets1* [Figure 5A,E,J], suggesting that *Sox8* forms the uppermost node of this transcriptional subcircuit. On the other hand, knockout of *Tgif1* resulted in reduction of *Ets1* expression [Figure 5K] but no noticeable effect on *Sox8* [Figure 5B]. Finally, loss of *Ets1* had no effect on either *Sox8* [Figure 5C] or *Tgif1* [Figure 5G] in the premigratory neural crest, albeit *Sox8* levels were reduced in the otic vesicle, suggesting that *Ets1* might be a functional input into *Sox8* in the ear but not cardiac crest. To further explore the epistatic nature of these regulatory relationships, we asked if *Ets1* expression could be rescued after *Sox8* knockout by exogenously expressing *Tgif1*. To test this, we removed *Sox8* on the right side of gastrula stage embryos using CRISPR-Cas9 as described above, and concomitantly ectopically expressed *Tgif1*. Overexpression of *Tgif1* was sufficient to partially rescue the levels of *Ets1*, even though the level of *Sox8* was notably diminished [Figure 5D-D']. Next, we asked if these regulatory linkages might result from direct interactions. To this end, we searched for putative transcription factor binding sites in enhancers that mediated expression of *Tgif1* and *Ets1* in cardiac crest.

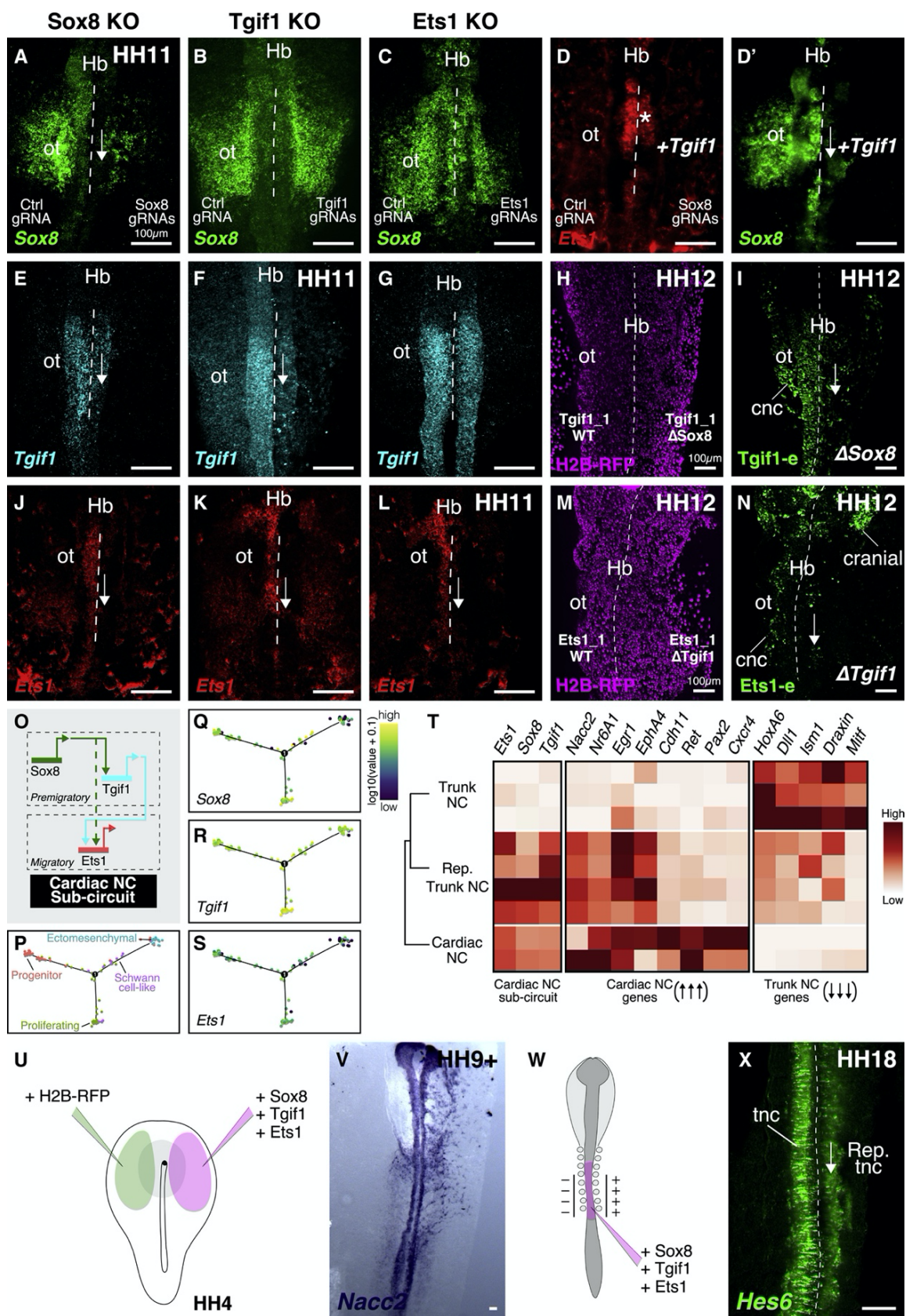


Figure 5. See next page for legend.

Figure 5. *Sox8*, *Tgif1* and *Ets1* comprise a transcriptional cascade important for cardiac crest identity. A-N. Dorsal view of HH11 embryos where *Sox8* (A, E, J), *Tgif1* (B, F, K), or *Ets1* (C, G, L) was knocked out on the right side at gastrula stage. *Sox8* knockout resulted in loss of *Tgif1* (E) and *Ets1* (J), *Tgif1* knockout resulted in reduced *Ets1* (K), but no noticeable change in *Sox8* (B); *Ets1* knockout had no effect on either *Sox8* (C) or *Tgif1* (G). Expression of *Tgif1* on the right side in *Sox8* knockout embryos (D') was sufficient to partially rescue *Ets1* expression (D). Mutation of *Sox8* binding sites in a *Tgif1* enhancer resulted in reduced enhancer activity on the right side (I). H2B-RFP (H, M) was used as a transfection control on both sides. Mutation of *Tgif1* binding site in an *Ets1* enhancer resulted in reduced enhancer activity in cardiac but not cranial neural crest (N). **O.** Functional relationships between *Sox8*, *Tgif1*, and *Ets1* in a transcriptional subcircuit based on the results in A-N. **P-S.** Pseudotime lineage trajectory with each subcluster labeled (P) according to scRNA-seq analysis. Expression of cardiac neural crest subcircuit genes *Sox8*, *Tgif1*, and *Ets1* was overlaid on the trajectory. **T.** Heatmap showing changes in gene expression profiles of reprogrammed trunk neural crest compared to wildtype cardiac and trunk crest. **U-V.** Dorsal view of an HH9+ embryo where *Tgif1*, *Ets1*, and *Sox8* were overexpressed at gastrula stage on the right side (U). *Ex ovo* culturing of the embryos resulted in ectopic expression of cardiac crest gene *Nacc2* in cranial neural crest (V) and surrounding naïve ectoderm. **W-X.** Dorsal view of the trunk neural crest of an HH18 embryo where cardiac crest subcircuit genes were transfected on the right side of the neural tube *in ovo* (W). Expression of trunk neural crest marker *Hes6* was reduced in resident trunk neural crest cells (X). Ot-otic vesicle, Hb-hindbrain, tnc-trunk neural crest, rep-reprogrammed. See also Supplementary Figure S4.

For *Ets1*, we used a previously published enhancer that recapitulates *Ets1* expression in the cranial and cardiac neural crest (Barenbaum and Bronner, 2013). For *Tgif1*, we identified an enhancer that was evolutionary conserved across several vertebrate species [Supplementary Figure S4A-C] and drove reporter expression in a manner that recapitulated that of *Tgif1*. We then identified and mutated putative binding sites for *Sox8* in the *Tgif1* enhancer (*Tgif1*- Δ *Sox8*) and for *Tgif1* in the *Ets1* enhancer (*Ets1*- Δ *Tgif1*). Mutant and wild type enhancers driving GFP were electroporated on the right or left side of gastrula stage embryos, respectively. H2B-RFP was electroporated on both sides as an electroporation control [Figure 5H,M].

The results show that loss of *Sox8* and *Tgif1* binding sites was sufficient to reduce *Tgif1* and *Ets1* enhancer activity in the cardiac crest, respectively [Figure 5I,N]. Interestingly, the *Ets1*- Δ *Tgif1* mutant enhancer retained activity in cranial neural crest [Figure 5N], suggesting its differential regulation in cranial versus cardiac crest. Taken together, our results suggest a regulatory cascade consistent with the sequential expression pattern of *Sox8*, *Tgif1* and *Ets1*, with the former two working together in the premigratory cardiac crest, and regulating the activity of *Ets1* in the migratory neural crest [Figure 5O]. Using the pseudotime lineage trajectory defined earlier [Figure 5P], we plotted the relative expression pattern of our cardiac crest subcircuit genes on the

trajectory map [Figure 5Q-S]. While expression of all three genes was high in both progenitor and proliferative cardiac crest cells, both *Sox8* [Figure 5Q] and *Ets1* [Figure 5S] were down-regulated as the cells transitioned into an ectomesenchymal state. The expression of *Tgif1* [Figure 5R] was relatively unchanged, strengthening our hypothesis that *Tgif1* is important for the formation of ectomesenchymal derivatives of cardiac crest.

Based on these results, we hypothesized that these three genes may comprise a “cardiac neural crest subcircuit” that might confer cardiac-like identity onto other neural crest populations. To examine downstream genes associated with a “cardiac-like” crest identity, we ectopically expressed *Sox8*, *Tgif1*, and *Ets1* along with the *Sox10E2* reporter construct as “reprogramming readout” into the trunk neural crest of HH10 embryos [Supplementary Figure S4D-E]. After RNA-seq of enhancer-expressing sorted cells, we identified genes upregulated in the reprogrammed neural crest cells compared to unelectroporated trunk crest [Supplementary Figure S4F]. Examples of upregulated genes included “cardiac crest markers” like *Nacc2*, *Ret*, and *Cdh11*, that were otherwise absent from trunk crest cells. On the other hand, key trunk neural crest genes including *HoxA6*, *Dll1*, and *Mitf* were down-regulated in the reprogrammed population [Figure 5T].

To validate the observed gene expression differences between reprogrammed and wild type trunk neural crest cells, we electroporated the right side of gastrula stage embryos with expression constructs for *Sox8*, *Tgif1*, and *Ets1*, and the left side with an equal concentration of H2B-RFP [Figure 5U]. As expected, expression of the cardiac crest subcircuit elicited ectopic expression of *Nacc2* [Figure 5V] in both cranial neural crest and the naïve ectoderm. In contrast, overexpression of the three transcription factors in the trunk neural tube of HH10 [Figure 5W] led to reduction of the trunk neural crest gene *Hes6* by HH18 on the experimental (right) compared with control side (left) [Figure 5X], suggesting that neural crest identity was altered to be cardiac-like at the expense of the original trunk-like signature. Taken together, these results suggest that the combination of *Tgif1*, *Ets1*, and *Sox8* was sufficient to alter the character of neural crest cells from other axial levels, imbuing transfected cells with cardiac crest-like identity.

7.3.8 Reprogrammed trunk neural crest cells exhibit cardiac-crest-like migratory behavior

Cardiac neural crest cells emerge in three distinct streams from the dorsal neural tube adjacent to rhombomeres 6, 7, and 8 and exhibit chain migration similar to cranial crest cells. The rostral-most stream of the cardiac crest follows a dorsolateral pathway of migration, forming a distinctive arc-like pattern, as shown by *FoxD3-NC2* enhancer-driven GFP expression at HH12 [Figure 2A]. These cells eventually migrate into the circumpharyngeal ridge, where they pause while the branchial arches form. Once developed, the cardiac crest cells continue their migration and populate branchial arches III, IV, and VI, with some contributing to the satellite cells that surround neurons of the nodose and jugular ganglion of the vagus nerve after 2 days.

Given that overexpression of the cardiac crest subcircuit resulted in altered neural crest molecular identity, we next examined the long-term effects of expressing this cardiac crest subcircuit in the trunk neural crest. To this end, we electroporated expression constructs for *Sox8*, *Tgif1*, and *Ets1* into the trunk neural tube of HH10 transgenic GFP⁺ embryos *in ovo*. The *Sox8* construct contains a cis-Internal Ribosome Entry Site (IRES) allowing the expression of the nuclear fluorescent protein H2B-RFP, used as a marker for electroporation efficiency. These “donors” were incubated at 37°C for 12 hours, after which the dorsal neural tube caudal to somite 10 was surgically removed and grafted in place of the cardiac neural fold unilaterally in wild type HH9⁺ host embryos. As a control, unperturbed cardiac neural fold or trunk neural fold was grafted instead [Figure 6A]. To confirm that the homochronic, homotopic graft extracted from the donor embryo was successfully incorporated in the host embryo, we implanted the dorsal neural tube from the trunk of a GFP embryo electroporated with expression constructs for the cardiac crest subcircuit genes [Figure 6B]. Chimeras were given ten minutes to recover following surgery and incubated for 1h at 37°C prior to fixation and sectioning. Transverse cross-sections through the hindbrain [Figure 6B'-B'''] confirmed that the graft healed efficiently and was properly incorporated in the host.

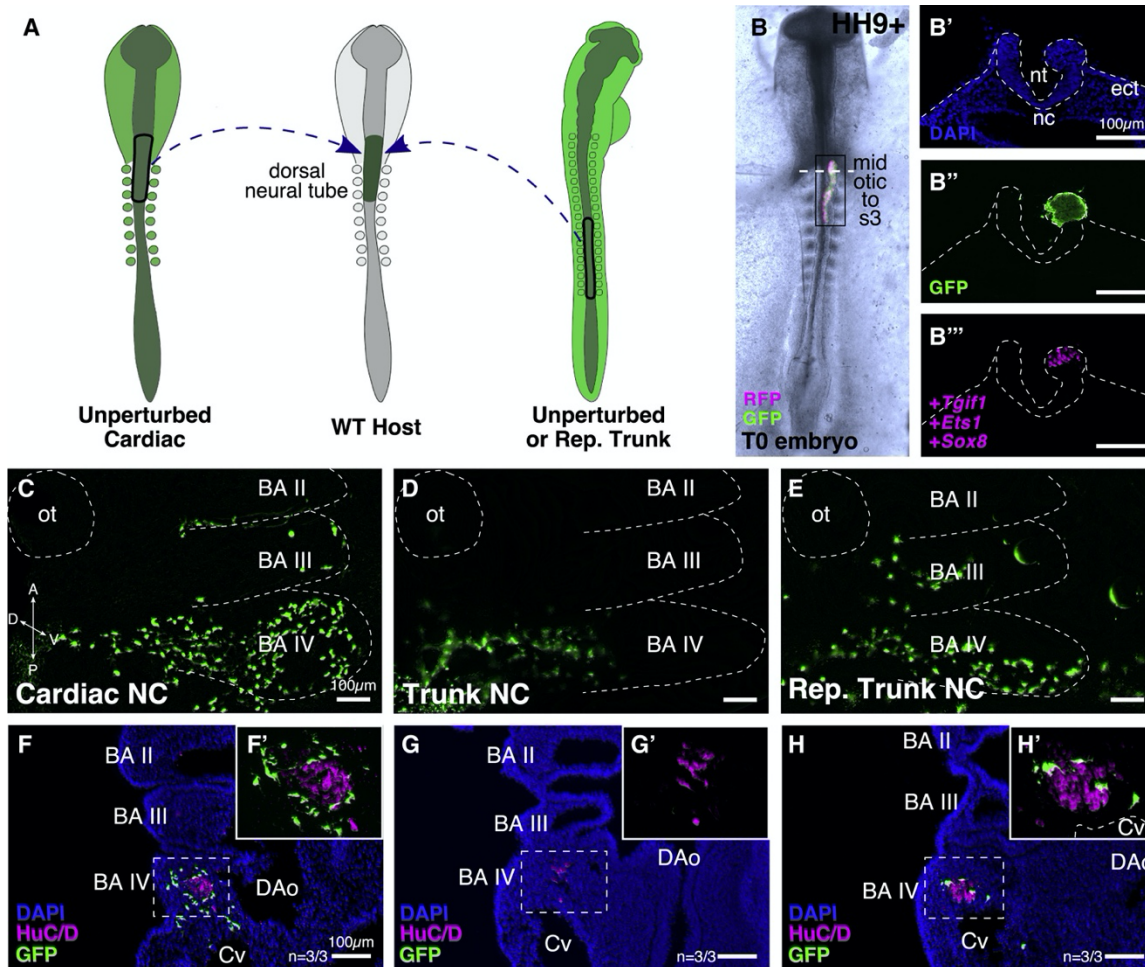


Figure 6. Reprogrammed trunk neural crest cells exhibit cardiac-crest-like migratory behavior. **A.** Grafting strategy to test behavior of transplanted cells. Stage-matched cardiac neural fold, unperturbed trunk neural fold, or trunk neural fold reprogrammed by the ectopic expression of *Sox8*, *Tgif1*, and *Ets1* was grafted in place of ablated cardiac neural folds in a wildtype host at HH9+. **B.** Embryo with a unilateral transgenic implant spanning the cardiac crest domain immediately after grafting (dorsal view). **B'-B'''**. Transverse section through the hindbrain of a chimera showing successful incorporation of the GFP⁺ implant (B''). The graft was electroporated with expression constructs for cardiac neural crest subcircuit genes *Sox8*, *Tgif1*, and *Ets1* (B'''). **C-H.** Whole-mount and cross-section images of chimeric embryos grafted with dorsal cardiac neural folds (C,F,F'), non-transfected dorsal trunk neural folds (D,G,G'), and "reprogrammed" dorsal trunk neural folds (E,H,H') harvested 2 days post grafting. Transgenic cells from the cardiac neural fold graft migrated into branchial arches III-IV, whereas cells from the trunk neural fold graft exhibited restricted migration. Ectopic expression of the cardiac crest subcircuit was sufficient to change the migration behavior of these cells, with transgenic cells populating branchial arches III and IV. Hb-hindbrain, ot-otic placode, Cv-cardinal vein, DAo-dorsal aorta, BA-branchial arch.

To assess effects on cell migration, we allowed chimeras to develop for 2 days. We first analyzed the "control" group grafted with unperturbed GFP⁺ cardiac neural folds in whole mount and transverse section. Consistent with results from quail-chick chimeras, GFP⁺ cardiac crest cells that emerged adjacent to somite 1 and 2 migrated into branchial arch IV (Miyagawa-Tomita et al., 1991) [Figure 6C; n=3/3] and formed satellite cells of

the nodose vagal ganglia [Figure 6F,F’]. However, when unperturbed GFP⁺ trunk neural fold was grafted in place of the cardiac neural fold of wild type hosts, the grafted cells delaminated from the neural tube but exhibited restricted migration [Figure 6D; n=3/3], resulting in failure to invade branchial arch IV [Figure 6G,G’]. Moreover, the neurons of the nodose ganglion, otherwise derived from the post-otic placodal ectoderm (Narayanan and Narayanan, 1980), were malformed compared to those of control embryos, consistent with a previously reported cardiac crest ablation phenotype (Kuratani et al., 1991). Thus, trunk neural crest cells failed to substitute for ablated cardiac neural folds as previously published (Harrison et al., 1995; Kirby, 1989).

Importantly, unilaterally grafted “reprogrammed” trunk neural folds, electroporated with constructs encoding our cardiac subcircuit genes *Sox8*, *Tgif1*, and *Ets1*, exhibited cardiac-crest-like behavior. These cells migrated into branchial arch IV [Figure 6E; n=3/3] to form satellite cells of the jugular ganglion of the vagus nerve [Figure 6H,H’], similar to normal cardiac crest cells at the 2 day time point. The placodally-derived neurons were also evenly distributed. Taken together, these results show that the combined expression of *Tgif1*, *Ets1*, and *Sox8* was sufficient to reprogram trunk neural crest cells to exhibit migration patterns and morphogenesis similar to cardiac crest cells.

7.3.9 Reprogrammed trunk neural crest acquires cardiac ectomesenchymal potential

Once cardiac crest cells have migrated into the caudal pharynx, a subset condense around the pharyngeal arch arteries, contributing to the smooth muscle tunica media surrounding these vessels (Bergwerff et al., 1998). While the endothelial cells lining these arteries are mesoderm-derived and hence not dependent on cardiac crest for initial development, the cardiac crest plays a vital role in the remodeling of the pharyngeal arch arteries (Bookman et al., 1987), resulting in the formation of the aortic arch, brachiocephalic artery, the carotid arteries and the subclavian arteries (Hiruma and Nakajima, 2002). Ultimately, cardiac crest cells migrate into the outflow tract cushions,

where they will condense to form the aortopulmonary septum. Some of these cells also contribute to the proximal segment of the interventricular septum.

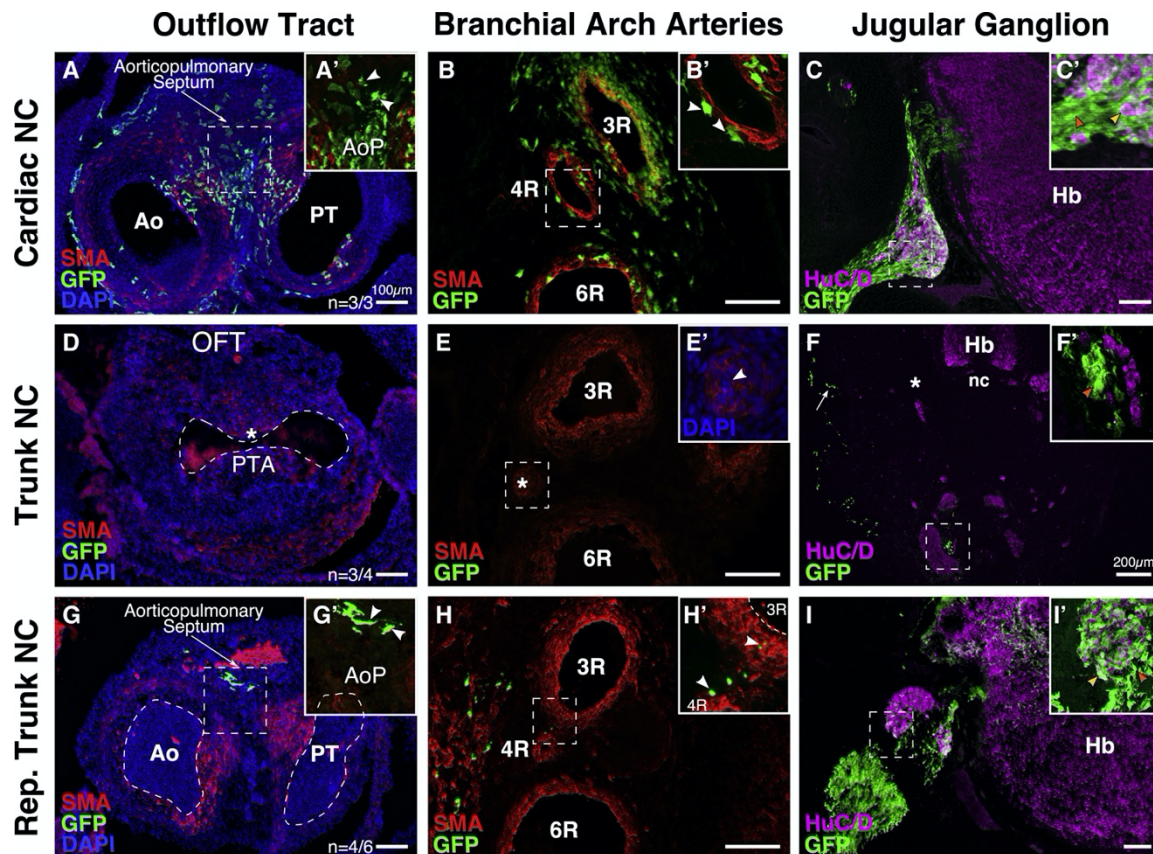


Figure 7. Reprogrammed trunk neural crest acquires cardiac ectomesenchymal potential. **A-C.** Transverse sections through embryos grafted with GFP⁺ cardiac neural folds show cardiac crest-derived cells in the aortopulmonary septum (A, arrowheads in A'), tunica media surrounding the branchial arch arteries (B, arrowheads in B'), and neurons and satellite cells of the jugular ganglion of the vagus nerve (C,C'; orange arrowhead—satellite cells, yellow arrowhead—neurons). **D-F.** Embryos grafted with non-transfected trunk neural fold cells exhibit PTA (D, asterisk), abnormally constricted right-fourth branchial arch artery (E, asterisk; arrowhead in E'), and improper gangliogenesis (F, asterisk). Transplanted cells were found associated with ectopic cervical nerves (F', orange arrowheads). **G-I.** GFP⁺ cells from the reprogrammed trunk implant migrate into the outflow tract and contribute to the aortopulmonary septum (G, arrowheads G'). GFP⁺ cells were found surrounding vessels (H, arrowheads H'), and in neurons and satellite cells of the jugular ganglion (I, I'; orange arrowhead—satellite cells, yellow arrowhead—neurons). Ao—arteria, PT—pulmonary trunk, AoP—arterio-pulmonary septum, OFT—outflow tract, Hb—hindbrain, nc—notochord.

To test whether reprogrammed trunk neural crest cells acquired a developmental potential normally confined to cardiac crest, we analyzed their ability to differentiate into ectomesenchymal derivatives such as the condensed mesenchyme of the aortopulmonary septum, tunica media of the branchial arch arteries, and the nodose

ganglia (Kirby, 1989; Kirby and Stewart, 1983) [Figure 7A-C,7A'-C'], in comparison to wild type cardiac and trunk neural fold grafts. First, to validate the contribution of cardiac crest to these different tissues, we grafted unperturbed GFP⁺ neural folds spanning the entire cardiac crest region from a transgenic embryo into a wildtype host and allowed the embryos to develop to E6. Consistent with results obtained with quail-chick chimeras, cardiac crest cells were found in the aorticopulmonary septum [Figure 7A,A'], the tunica media surrounding the branchial arch arteries [Figure 7B,B'], and neurons and glial cells of the jugular ganglion of the vagus nerve [Figure 7C,C'].

In contrast to GFP⁺ cardiac implants, when unperturbed GFP⁺ transgenic trunk neural folds were grafted into the cardiac crest region, the host embryos exhibited cardiovascular defects at E6, most notably septation defects of the outflow tract (Kirby, 1989; Nishibatake et al., 1987) [n=4/5; Figure 7D]. Interestingly, the phenotype looked similar to what we observed after unilateral ablations, where the outflow tract cushions had developed but failed to fuse, resulting in PTA [Figure 1H]. This suggests that the endogenous cardiac crest from the contralateral side failed to compensate for complete unilateral loss of cardiac neural folds. One embryo exhibited DORV, another similarity observed to that occurring after unilateral cardiac crest ablation. We also noticed defects in remodeling of the pharyngeal arch arteries (Hiruma and Nakajima, 2002), as demonstrated by an abnormally constricted fourth arch artery [Figure 7E, E'], and lack of proper gangliogenesis [Fig.7F] in the hindbrain. To confirm that the phenotypes we observed were not artifacts of improper graft incorporation, we looked for known derivatives of resident trunk neural crest cells in the chimeras. As expected, some GFP⁺ melanocytes (Serbedzija et al., 1994) were identified [white arrow, Figure 7F], suggesting that trunk crest cells retained their developmental potential to contribute to melanocyte precursors. Surprisingly, we found ectopic cervical nerves in proximity to the trachea in these chimeras, with GFP⁺ satellite cells surrounding the ganglionic neurons [Figure 7F']. Taken together, these results confirmed that trunk neural crest was unable to rescue the loss of cardiac crest cells (Kirby, 1989).

However, when we grafted trunk neural tube that was “reprogrammed” by ectopic expression of *Sox8*, *Tgif1*, and *Ets1*, the chimeras exhibited proper septation of the outflow tract [Figure 7G,G’; n=4/6], with GFP⁺ cells present in the aorticopulmonary septum. Moreover, these embryos showed signs of proper remodeling of the pharyngeal arch arteries, as demonstrated by the presence of unconstricted arteries III, IV, and VI leading to the outflow tract, as well as a developed jugular ganglion of the vagus nerve. We found reprogrammed cells in the tunica media of these vessels [Figure 7H,H’], and neurons and glia of the jugular ganglia [Figure 7I,I’]. Taken together, our results show that expression of a transcriptional program comprised of *Tgif1*, *Ets1*, and *Sox8* can confer cardiac ectomesenchymal differentiation potential onto trunk neural crest cells, essentially altering their developmental potential such that they are interchangeable with the cardiac crest.

7.4 Discussion

The neural crest is a versatile cell population with great promise in regenerative medicine due to its ability to form diverse progeny ranging from neurons to facial cartilage and portions of the heart (Gandhi and Bronner, 2018). However, different neural crest subpopulations with distinct developmental potential exist along the body axis. Over 30 years ago, Kirby et al. (1985) defined the “cardiac neural crest” based on quail-chick chimeras as the region arising from the caudal hindbrain with the potential to form ectomesenchymal derivatives of the heart. The heart of amniotes is divided into separate systemic and pulmonary circulations such that deoxygenated blood flows from the heart to the lungs and oxygenated blood returns to the heart to be pumped through the rest of the body. The cardiac crest is critical in separating the aortic and pulmonary arteries by dividing the outflow tract via formation of the aorticopulmonary septum. Importantly, ablation of this cell population in chick embryos resulted in developmental defects of the outflow tract highly reminiscent of the human congenital birth defect PTA (Hutson and Kirby, 2003), highlighting the critical role of the cardiac crest. The cardiac crest is unique amongst neural crest subpopulations, since those from other axial levels are unable to rescue cardiac neural fold ablation (Kirby, 1989). In the present study, we revisit these

classical studies from a modern genomics perspective to identify molecular mechanisms that define the ectomesenchymal differentiation potential of the cardiac neural crest.

Our results suggest that there is left-right asymmetry with respect to contributions of the cardiac crest to the heart. While both left and right cardiac crest ablations resulted in heart defects, they differed in type and severity. Whereas removal of the left neural folds predominantly caused Double Outlet Right Ventricle (DORV) defects (n = 6/8), ablation of the right side caused PTA (n=4/9) and DORV (n=3/9). These differences likely reflect left-right asymmetry in the heart itself, which undergoes dextral looping. Crest ablation also affects heart tube looping and elongation, as ablated hearts appeared bulbous with shortened and straighter outflow tract compared to controls. Remodeling of aortic arches is also asymmetric (Snider et al., 2007; Waldo et al., 1998), with selective regression of the left 4th artery in birds and unequal contribution of the left-right cardiac crest to the vagus nerve's heart innervation (Verberne et al., 2000).

Our results uncover a transcriptional program necessary for normal cardiac crest development that is sufficient to reprogram trunk neural crest cells to take on a cardiac-crest-like fate. We identify *Tgif1* as a critical factor for normal development of the cardiac crest. *Tgif1* encodes a transcriptional repressor that limits TGF β signaling by interacting with SMADs and/or binding directly to DNA and also regulates processes like proliferation, specification, and differentiation (Bartholin et al., 2008; Hamid and Brandt, 2009). In cancer, *Tgif1* promotes the migration and growth of non-small cell lung cancer cells (Xiang et al., 2015), consistent with our findings where loss of *Tgif1* in chick caused impaired cardiac neural crest migration and reduced activity of several cardiac crest-specific genes.

While *Tgif1* mutant mice have severe holoprosencephaly (Taniguchi et al., 2012), no apparent heart defects have been reported, possibly due to the presence of its functionally redundant paralog *Tgif2* in the murine heart (Imoto et al., 2000; Jin et al., 2005). However, *Tgif2* was not differentially enriched in migrating chick cardiac crest. The finding that *Tgif1* is important for proper outflow tract septation expands its proposed role

from central nervous system to cardiovascular development. In sea urchin embryos, *tgif* has been associated with epithelial to mesenchymal transition (EMT) (Saunders and McClay, 2014), an important process in neural crest development. However, in the cardiac crest, *Tgif1* appears to function in specification rather than EMT.

Our data show that *Sox8* functions upstream of *Tgif1*, which in turn regulates activity of *Ets1* in the migratory cardiac neural crest. We postulated that these three factors work together in a cardiac crest specific regulatory subcircuit. To test this, we “reprogrammed” trunk neural crest by ectopically expressing subcircuit genes and found that this is sufficient to alter their character to behave in a cardiac-crest-like manner. Transcriptional profiling of reprogrammed trunk neural crest cells confirmed that they became more cardiac crest-like. Furthermore, grafting reprogrammed trunk neural crest cells in place of the cardiac neural folds changed their migratory and differentiative behavior such that they not only migrated into the heart but also restored septation of the outflow tract. Thus, these data show that the combination of these three factors was sufficient to imbue the transfected cells with cardiac crest-like identity.

Of note, a relatively small number of reprogrammed trunk neural crest cells in the outflow tract appears sufficient for its septation. As crest-derived cells are relatively short lived in the outflow tract, undergoing apoptosis at later stages, one possibility is that an early interaction between cardiac crest cells and neighboring cells, likely derived from the second heart field, is sufficient for proper septation without the need for a large neural crest contribution to the septum itself. On the other hand, perhaps only small numbers of neural crest cells are required, as is true in other contexts; e.g. Barlow et al. (2008) showed that a small number of enteric neural crest cells is sufficient to populate the entire digestive tract. In mice, reprogramming a small contingent of smooth muscle cells into melanocytes results in patent ductus arteriosus (Yajima et al., 2013).

The cardiac neural crest is specified just prior to emigration from the hindbrain. Our findings raise the intriguing possibility that these cells may be biased very early toward contributing to cardiovascular structures. Expression of genes such as *Acta2*, *Prrx1*, and

Twist1 in a single cardiac crest cluster suggests these cells may have already acquired ectomesenchymal characteristics, as these genes are associated with the cardiac crest's ability to form the smooth muscle lining of the pulmonary arteries and the outflow tract septum. Thus, cardiac neural crest cells may acquire an ectomesenchymal identity well before they migrate into the branchial arches. Given that cells from the trunk neural crest graft delaminated from the neural tube but failed to migrate any further, it is likely that the transcriptional state of cardiac crest cells governs their ability to migrate into the corresponding branchial arches.

Together with a previously described cranial crest-specific subcircuit important for the formation of craniofacial cartilage (Simões-Costa and Bronner, 2016), our results suggest that small transcriptional changes can alter neural crest identity and resultant differentiative behavior along the body axis. It is interesting to note that two of the three transcription factors (*Sox8* and *Ets1*) are shared between the cardiac and cranial crest subcircuits, though *Tgif1* is unique to the cardiac region. Moreover, mutation of the *Tgif1* binding site in the *Ets1* enhancer had drastic effects on the activity of the enhancer in the cardiac but not cranial crest. This suggests that a small shift in regulatory subcircuitry can have profound effects in conferring axial level identity, since grafting of the cranial neural folds in place of cardiac neural folds also resulted in PTA (Kirby, 1989). Our results not only validate the reproducibility of experiments done by Kirby and colleagues over 30 years ago (Besson et al., 1986; Kirby and Stewart, 1983; Kirby and Waldo, 1995; Kirby et al., 1985; Nishibatake et al., 1987; Phillips et al., 1987; Waldo and Kirby, 1993), but also shed light on the underlying molecular mechanisms that distinguish the cardiac neural crest from other axial levels. We posit that identification of axial-level-specific transcription factors and subcircuits holds the promise of identifying potentially important genes involved in proper formation of the cardiovascular system and may provide targets for identification of human genetic mutations in coding or regulatory regions. Moreover, elucidation of the gene regulatory subcircuits that underlie axial level identity will be useful for producing the full range of neural crest derivatives for the purposes of regenerative medicine.

7.5 Acknowledgments

We thank Drs. Tatjana Sauka-Spengler and Megan Martik for helpful discussions. For technical assistance, we thank Jamie Tijerina and Rochelle Diamond with the Beckman Institute (BI) Flow Cytometry Facility, Igor Antoshechkin with the Jacobs Genetics and Genomics Laboratory, Giada Spigolon and Andres Collazo with the BI Biological Imaging Facility, and Fan Gao with the BI Bioinformatics Resource Center. We thank Neil Ashley and Ivan Candido Ferreira at the Weatherall Institute (University of Oxford) for help with scRNA-seq library preparation and sequencing.

7.6 Author contributions

Conceptualization, S.G. and M.E.B.; Methodology, S.G. and M.E.; Software, S.G.; Validation, S.G.; Formal Analysis, S.G.; Investigation, S.G. and M.E.; Writing – Original Draft, S.G., M.E., and M.E.B.; Writing – Review & Editing, S.G. and M.E.B.; Visualization, S.G.; Supervision, M.E.B.; Funding Acquisition, M.E.B.

7.7 Funding

This work was supported by the National Institutes of Health (NIH) grants R01DE027568 and R01HL14058 to M.E.B., and AHA predoctoral fellowship 18PRE34050063 and Company of Biologists traveling fellowship DEVTF18119 to S.G.

7.8 Materials and methods

7.8.1 Key Resource Table

REAGENT or RESOURCE	SOURCE	IDENTIFIER
Antibodies		
Mouse IgG1 anti-Pax7	Developmental Studies Hybridoma Bank at University of Iowa	RRID: AB_528428
Rabbit anti-Sox2	Abcam	Cat#ab97959; RRID: AB_2341193
Mouse IgG2b anti-MF20	Developmental Studies Hybridoma Bank at University of Iowa	RRID: AB_2147781
Mouse IgM anti-HNK1	Developmental Studies Hybridoma Bank at University of Iowa	RRID: AB_2314644
Mouse IgG2a anti-SMA	Sigma	Cat#3879S; RRID: AB_2255011
Mouse IgG2b anti-HuC/D	Invitrogen	Cat# A21271; RRID: AB_221448
Goat IgG anti-GFP	Rockland	Cat# 600-101-215; RRID: AB_218182
Mouse IgG2a anti-V5	Invitrogen	Cat#R960-25; RRID: AB_2556564
Rabbit anti-RFP	MBL	Cat#PM005; RRID: AB_591279
Critical Commercial Assays		
RNAqueous Micro Total RNA isolation kit	Ambion	Cat#AM1931

SmartSeq2 V4 kit	Takara Clontech	Cat#634889
Nextera XT DNA library preparation kit	Illumina	Cat#FC-131-1024
Qubit High sensitivity DNA kit	ThermoFisher Scientific	Cat#Q32854
NEB Next High-Fidelity 2X PCR Master Mix	New England Biolabs	Cat#M0543S
NextSeq 500/550 High Output Kit v2 (75 cycles)	Illumina	Cat#FC-404-2005
Endofree maxi prep kit	Macharey Nagel	Cat#740426.50
Agencourt AMPure XP beads	Beckman Coulter	Cat#A63880
illustra MicroSpin G-50 Columns	GE Healthcare Life Sciences	Cat#27533001
Hybridization Chain Reaction	Molecular Technologies	NA
Deposited Data		
Raw and analyzed data	This paper	BioProject ID PRJNA515142
Software and Algorithms		
Fiji/ImageJ	(Schindelin et al., 2012)	https://imagej.nih.gov/ij/
Bowtie2	(Langmead and Salzberg, 2012)	http://bowtie-bio.sourceforge.net/bowtie2/index.shtml
Samtools		http://samtools.sourceforge.net/
HTSeq-count		https://htseq.readthedocs.io/en/release_0.11.1/count.html
Seurat	(Butler et al., 2018)	https://satijalab.org/seurat/
Oligonucleotides		
GCAGGTGTAGTTGCAATATC	This paper	Tgif1.1.gRNA
GTTGGTCCCCCGCCGTGAGA	This paper	Tgif1.2.gRNA
GGGTCATGTTGAGCATTGG	This paper	Sox8.1.gRNA
GTCCACCTTAGCGCCAGCG	This paper	Sox8.2.gRNA
GACGCGACGCCATCCTCAA	This paper	Sox8.3.gRNA

GGCCTCAACCATGAAGGCGG	This paper	Ets1.1.gRNA
GACCTTCAGTGGCTTCGCAA	This paper	Ets1.2.gRNA
GAGAGACGCACGTGCGGGAC	This paper	Ets1.3.gRNA
GAAAGTCAGGCGCTAGCTCC	This paper	Ets1.4.gRNA

7.8.2 Experimental model

Fertilized chicken eggs were purchased from Sun State Valley farm (CA) and incubated at 37°C for 33-36h to get HH9+ embryos for ablation and reprogramming experiments. All experiments were performed on chick embryos younger than E10 and were therefore not subjected to IACUC regulations.

7.8.3 Cardiac neural crest ablation

Windows were made in the eggs and 2% blue food dye solution was injected under the embryo to provide contrast. Unilateral and bilateral ablations were performed using glass needles by surgically removing the dorsal neural tube the level of the mid-otic vesicle to the caudal edge of somite 3 as previously described (Kirby, 1989). The embryos were sealed with surgical tape and incubated at 37°C *in ovo* for 3 or 6-6.5 days.

7.8.4 Embryo electroporation

Ex ovo electroporations were performed as previously described (Sauka-Spengler and Barembaum, 2008) by passing 5 electric pulses every 50ms at an interval of 100ms at 5.2V. The electroporated embryos were cultured in sterile petri dishes in 1mL albumin supplemented with penicillin/streptomycin at 37°C until HH9+ or HH12. *pCAG>H2B-RFP* was electroporated as a marker for transfection efficiency and was used to discard embryos with poor transfection. For *in ovo* electroporations, fertilized eggs were incubated for 33-36h to get HH9 embryos. The DNA solution was injected into the lumen of the neural tube and the right side transfected by passing 5 electric pulses every 30ms at an interval of 100ms at 18V. The egg shell was sealed with surgical tape and the eggs were incubated at 37°C until they reached the desired stage. Fluorescence was checked

under a Leica epifluorescence scope and embryos with improper morphology and/or poor transfection were discarded.

7.8.5 Cell sorting and library preparation

To sort cardiac and trunk neural crest cells, HH4 and HH9 embryos were electroporated with FoxD3-NC2>mCherry (Simões-Costa et al., 2012) *ex ovo* and *in ovo*, respectively. To sort reprogrammed trunk neural crest cells, HH9 embryos were electroporated with expression constructs for Sox8, Tgif1, and Ets1 along with Sox10e2>GFP. The embryos were cultured until HH12 to isolate cardiac neural crest and HH18 to isolate wild-type and reprogrammed trunk neural crest. The embryos were dissected between the otic vesicle and somite 3 and between somite 18 and 25 for cardiac and trunk neural crest, respectively. For cell dissociation, the dissected tissue was collected in chilled 1X DPBS, washed thrice, and incubated in Accumax cell dissociation solution (EMD Millipore) for 15 minutes at 37°C, with gentle pipetting every 5 minutes. Once the tissue appeared dissociated, Hanks Buffered Saline Solution (HBSS) (Corning) supplemented with 25mM HEPES (pH 7), BSA Fraction V (Sigma; 0.2% w/v), and 10mM MgCl₂ was used to terminate dissociation. Cells were collected at the bottom by spinning the solution at 300g for 4 minutes and resuspended in 1mL HANKS-MgCl₂. The cells were then passed through a 40µm filter to remove debris and undissociated clumps. mCherry⁺ cells were sorted on a Sony Synergy 3200 cell sorter equipped with a 561nm laser at the Caltech Flow Cytometry Facility. Sytox Blue staining was used to label dead cells during the sorting run.

For bulk RNA-seq, the SMART-Seq v4 Ultra Low Input RNA Kit for sequencing was used by following the manufacturer's protocol (Takara Bio). Briefly, the sorted cells were washed thrice in chilled sterile 1x PBS. cDNA was synthesized using the 3' SMART-Seq CDS Primer II A (followed by template switching with the SMART-Seq v4 Oligonucleotide primer) and amplified using the following program: 95°C for 1min, 15 cycles of 98°C for 10s, 65°C for 30s, and 68°C for 3min, and a final extension at 72°C for 10min. The amplified cDNA was purified using AMPure beads (Agencourt) and the quality was

confirmed on the Agilent 2100 Bioanalyzer using a high sensitivity DNA chip. The library was prepared by Igor Antoshechkin at the Caltech Genomics Facility and sequenced on a HiSeq 2500 to obtain 50 million single end reads.

For single-cell RNA-seq, individual neural crest cells were collected in 96-well plates by FACS. Sequencing libraries were prepared as previously described (Picelli et al., 2014). Libraries were sequenced on the Illumina NextSeq500 platform using single end 75bp sequencing chemistry.

7.8.6 Molecular cloning and in situ hybridization

Overexpression constructs for *Ets1* and *Sox8* were generously provided by Marcos Simões-Costa and Meyer Barembaum, respectively. The coding sequence for *Tgif1* was obtained from the UCSC genome browser (Karolchik et al., 2003) and amplified using Accuprime polymerase (ThermoFisher). A V5 epitope tag was fused to the N-terminus to allow for construct validation using immunohistochemistry. This fusion gene was then cloned under the regulation of the CAGG promoter. *Tgif1* and *Ets1* enhancers were amplified from genomic DNA using Accuprime polymerase (ThermoFisher).

RNA was extracted from HH12 embryos using an optimized TRIzol-chloroform extraction protocol. SuperScript III Reverse Transcriptase was used to synthesize cDNA using oligo dT primers and PCR program recommended by the manufacturer. Cardiac crest genes were amplified from this cDNA and cloned in *pBluescript* plasmid. All RNA probes were synthesized using Digoxigenin-labeled UTPs and diluted in Hybridization buffer containing 50% formamide, 5mM EDTA, 1.3x SSC, 200 μ g/mL tRNA, 0.2% Tween-20, 0.5% CHAPS, and 100 μ g/mL heparin. All probes were used at a final concentration ranging between 2-5ng/ μ L. *In situ* hybridization was performed using a previously described protocol (Acloque et al., 2008).

7.8.7 Hybridization Chain Reaction

HCR v3 was performed using the protocol suggested by Molecular Technologies (Choi et al., 2018). Briefly, the embryos were cultured to desired stages and fixed in 4% paraformaldehyde overnight at 4°C. On day 2, the fixed embryos were washed in 0.1% PBS-Tween and dehydrated using a series of 25%, 50%, 75%, and 100% methanol. Following an overnight incubation at -20°C in 100% methanol, the embryos were rehydrated, treated with proteinase-K for 2.5 minutes, and incubated with 5-10pmol of probe mixture overnight at 37°C. On day 3, excess probe was washed off and the embryos were incubated with 30pmol of both hairpins H1 and H2 at room temperature overnight. On day 4, the embryos were washed in 0.1% 5x-SSC-Tween and imaged on a Zeiss Imager M2 with an ApoTome module and/or Zeiss LSM 880 confocal microscope at the Caltech Biological Imaging Facility.

7.8.8 CRISPR-Cas9-mediated knockouts

The genomic loci for *Tgif1*, *Sox8*, and *Ets1* were obtained from the UCSC genome browser (Karolchik et al., 2003). Two gRNA targets were generated to knockout *Tgif1*: *Tgif1.1* (5'- GCAGGTGTAGTTGCAATATC -3') and *Tgif1.2* (5'- GTTGGTCCCCCGCCGTGAGA -3'), three gRNA targets were generated to knockout *Sox8*: *Sox8.1* (5' - GGGTCATGTTGAGCATTTGG -3'), *Sox8.2* (5'- gTCCACCTTAGCGCCCAGCG -3'), and *Sox8.3* (5'- GACGCGACGCCCATCCTCAA -3'), and four gRNA targets were generated to knock out *Ets1*: *Ets1.1* (5'- GGCCTCAACCATGAAGGCGG -3'), *Ets1.2* (5'- GACCTTCAGTGGCTTCGCAA -3'), *Ets1.3* (5'- GAGAGACGCACGTGCGGGAC -3'), and *Ets1.4* (5'- GAAAGTCAGGCGCTAGCTCC -3') using CHOPCHOP (Labun et al., 2019). For contralateral control electroporations, we used the control gRNA described in (Gandhi et al., 2017). Gastrula HH4 embryos were bilaterally electroporated with *CAGG>nls-Cas9-nls* (2µg/µl) and *CAGG>H2B-RFP* (2µg/µl) together with either *U6.3>Tgif1.1.gRNAf+e* and *U6.3>Tgif1.2.gRNAf+e* (0.75µg/µl each) on the right side or *U6.3>control.gRNAf+e* (1.5µg/µl) on the left side. The embryos were then cultured ex

ovo until HH12, assayed for good transfection efficiency and morphology, and processed for whole mount *in situ* hybridization and HCR.

7.8.9 Reprogramming resident trunk and cranial neural crest cells

Enhancer element governing the expression of Sox10 (e2) (Betancur et al., 2010) was cloned under the regulation of a constitutive HSV thymidine kinase promoter driving GFP expression. To test whether *Tgif1* alone can reprogram trunk neural crest cells, HH9+ embryos were unilaterally co-electroporated with overexpression constructs *CAGG>V5-Tgif1* (2.5µg/µl each) and the enhancer construct *pTK-Sox10e2>GFP* (2µg/µl) *in ovo* as described above. The eggs were sealed and incubated at 37°C until HH14 to look for enhancer activity. The embryos were screened for the expression of *H2B-RFP* and fixed for antibody staining against GFP. To test the effect of reprogramming on resident trunk neural crest cells, HH9+ embryos were electroporated with *CAGG>V5-Tgif1*, *CAGG>Ets1*, and *CAGG>Sox8-IRES-H2B-RFP* (2µg/µl each) on the right side *in ovo*. The embryos were developed to until HH18 and fixed for HCR. To test the effect of reprogramming on resident cranial neural crest cells, HH4 embryos were electroporated with the three expression constructs (2µg/µl each) on the right side. The left side was electroporated with *CAGG>H2B-RFP* (2.5µg/µl) and served as our internal control. The embryos were cultured *ex ovo* until HH9+, after which they were fixed for *in situ* hybridization against the cardiac neural crest marker *Nacc2*.

7.8.10 Grafting experiments

Wild-type chicken embryos served as hosts in our transplants and were incubated at 37°C until HH9+/HH10 (8-10 somite stage). Donor transgenic Roslin Green GFP eggs, in which CAGGS (CMV enhancer/beta actin promoter/first intron) drives eGFP expression (McGrew et al., 2008) were obtained from Clemson University through Dr. Susan Chapman and incubated to HH14 or to the same stage as their wild-type counterparts. Precautions taken to ensure a high survival rate post-surgery consisted of maintaining high humidity levels (80-100%) in an environment free of fungal contamination. All eggs were individually cleaned with 70% ethanol before incubation; incubators, plastic egg

trays and water tanks were treated with methylene blue to avoid any fungal infection. Host embryos were prepared by removing, unilaterally, the dorsal neural tube of wild-type stage 9+/10 host embryos from the level of the mid-otic vesicle to the caudal edge of somite 3. For positive controls (cardiac to cardiac), a similar microsurgical procedure was carried out on a stage-matched donor transgenic embryo. A homochronic, homotopic graft was completed, with the transgenic dorsal neural tube used as donor tissue to replace the section of dorsal neural tube removed from the wild-type host. Negative controls embryos (trunk to cardiac) were generated similarly, with the difference that the donor tissue originated from the trunk level of a stage 14 donor transgenic embryo, specifically from somite 18 to approximately somite 24. In our experimental group (reprogrammed trunk to cardiac), the reprogrammed transgenic dorsal neural tube originated from a stage 14 transgenic donor, previously electroporated with the regulatory subcircuit (*Tgif1*, *Ets1* and *Sox8*) at HH9. The reprogrammed dorsal neural tube was inserted in place of the host dorsal neural tube. Post-surgery, the host eggs were sealed with surgical tape and incubated until HH18-20 (E4) and stage 31-34 (E6).

7.8.11 Sectioning and histology

E4 and E6 chimeric embryos were washed in 5% (room temperature, 30min) and 15% sucrose (4°C, overnight) and incubated overnight in gelatin at 37°C. The next day, they were embedded in plastic molds, frozen in liquid nitrogen, and stored at -80°C for at least 4 hours. The embedded embryos were then sectioned on a micron cryostat to obtain 16 μ m sections. Immunohistochemistry on sections was performed using a previously described protocol (Ezin et al., 2009). Briefly, the sections were degelatinized at 42°C in 1x PBS for 5 minutes and blocked in PBS-0.3%Triton supplemented with 10% goat or donkey serum. The sections were incubated in primary antibodies overnight at 4°C. The next day, slides were washed thrice in 1x PBS, and the sections were incubated in secondary antibodies for 1h at room temperature. Following 2 washes in 1x PBS, the slides were soaked in 1x PBS containing 0.1 μ g/mL DAPI for 5 minutes. The slides were then washed once each in 1x PBS and distilled water. Transverse sections were imaged on a Zeiss Imager M2 with an ApoTome module and Zeiss LSM 880 confocal microscope

at the Caltech Biological Imaging Facility. All post-processing was done using FIJI imaging software (Schindelin et al., 2012). Early stage embryos (HH10-12) were sectioned using the same protocol as described but with a 6h instead of overnight incubation in gelatin at 37°C.

The following primary antibodies were used: Mouse IgG1 anti-Pax7 (DSHB; 1:10), Rabbit anti-Sox2 (Abcam ab97959; 1:500), Mouse IgG2b anti-MF20 (DSHB; 1:100), Mouse IgM anti-HNK1 (DSHB; 1:5), Mouse IgG2a anti-SMA (Sigma Cat# A5228; 1:500), Mouse IgG2b anti-HuC/D (Invitrogen – Cat# A21271; 1:500), Goat anti-GFP (Rockland Cat# 600-101-215; 1:500), Mouse IgG2a anti-V5 (Invitrogen Cat# R96025; 1:200), and Rabbit anti-RFP (MBL Cat# PM005; 1:500). The signal was detected using the following secondary antibodies: Goat anti-mouse Alexa Fluor 647 (for Pax7; 1:250), Goat anti-mouse IgM Alexa Fluor 350 (for HNK1; 1:250), Goat anti-rabbit Alexa Fluor 488 (for Sox2; 1:500), Donkey anti-goat Alexa Fluor 488 (for GFP; 1:500), Goat anti-mouse IgG2a Alexa Fluor 568 (for SMA and V5; 1:500), Goat anti-mouse IgG2b Alexa Fluor 633 (for HuC/D and MF20: 1:250), and Goat anti-rabbit IgG1 Alexa Fluor 568 (for RFP; 1:500).

7.8.12 Differential gene expression analysis for bulk RNA-seq data

The reads obtained from the HiSeq run were demultiplexed and filtered using custom scripts. The filtered reads were checked for quality using *fastqc* (Andrews and Babraham Bioinformatics, 2010). Based on the traces, the reads were trimmed by 10bp at the 3' end and overrepresented sequences (adapter and poly A tail) were removed using *cutadapt* (Martin, 2011). These 40bp reads were then mapped to the chicken genome (galgal6.0 assembly) obtained from Ensembl using *Bowtie2* (Langmead and Salzberg, 2012). Transcript counts were calculated using *HTseq-count* (Anders et al., 2015), and differential gene expression analysis was performed using *DESeq2* (Love et al., 2014). For our analysis, cardiac neural crest genes were directly compared with trunk neural crest genes. Genes with fold change ≥ 2 and adjusted p-value ≤ 0.05 were considered “enriched and significant” and were included in subsequent analysis. For reprogrammed trunk neural crest comparison, we generated a normalized transcript count matrix as

described in (Martik et al., 2019) and plotted relative values for top genes that have previously been shown to be required for neural crest development at cardiac and trunk axial levels as a heatmap.

7.8.13 Bioinformatics analysis for SMART-Seq data

The raw fastq data of 75-bp single-end sequencing reads were aligned to the chicken galgal6 reference genome using STAR-2.7.0 software (Dobin et al., 2013). The mapped reads were further processed by Cufflinks 2.2 (Trapnell et al., 2012) using the chick gene annotation file obtained from Ensembl to estimate transcript abundance. Relative abundance of transcripts was measured by fragments per kilobase of exon per million fragments mapped (FPKM). For each library, we computed total number of sequencing reads, number of uniquely mapped reads, mapping rate and number of genes detected. We selected cells with more than 100K total reads for downstream analysis. The data was filtered, normalized, and scaled using Seurat v3 (Butler et al., 2018), and all plots were generated using the in-built functions. For GO term analysis, the Bioconductor package topGO (Alexa and Rahnenführer, 2019) was used using default parameters. Adjusted p-values were calculated using Fisher's exact test. The heatmap showing relative expression values for different genes was generated using a normalized matrix as described above. Representative genes for each population (progenitor, proliferative, ectomesenchymal, and Schwann cell-like) were selected for the heatmap. Pseudotime trajectories were generated using Monocle v2 (Trapnell et al., 2014) by following standard instructions from the authors.

7.9 References

Acloque, H., Wilkinson, D.G., and Nieto, M.A. (2008). Chapter 9 In Situ Hybridization Analysis of Chick Embryos in Whole-Mount and Tissue Sections. *Methods Cell Biol.* 87, 169–185.

Alexa, A., and Rahnenführer, J. (2019). Gene set enrichment analysis with topGO.

Anders, S., Pyl, P.T., and Huber, W. (2015). HTSeq—a Python framework to work with high-throughput sequencing data. *Bioinformatics* 31, 166–169.

Andrews, S., and Babraham Bioinformatics (2010). FastQC: A quality control tool for high throughput sequence data.

Arima, Y., Miyagawa-Tomita, S., Maeda, K., Asai, R., Seya, D., Minoux, M., Rijli, F.M., Nishiyama, K., Kim, K.S., Uchijima, Y., et al. (2012). Preotic neural crest cells contribute to coronary artery smooth muscle involving endothelin signalling. *Nat. Commun.* 3.

Barenbaum, M., and Bronner, M.E. (2013). Identification and dissection of a key enhancer mediating cranial neural crest specific expression of transcription factor, *Ets-1*. *Dev. Biol.* 382, 567–575.

Barlow, A.J., Wallace, A.S., Thapar, N., and Burns, A.J. (2008). Critical numbers of neural crest cells are required in the pathways from the neural tube to the foregut to ensure complete enteric nervous system formation. *Development* 135, 1681–1691.

Bartholin, L., Melhuish, T.A., Powers, S.E., Goddard-Léon, S., Treilleux, I., Sutherland, A.E., and Wotton, D. (2008). Maternal *Tgif* is required for vascularization of the embryonic placenta. *Dev. Biol.* 319, 285–297.

Basch, M.L., Bronner-Fraser, M., and García-Castro, M.I. (2006). Specification of the neural crest occurs during gastrulation and requires *Pax7*. *Nature* 441, 218–222.

Bergwerff, M., Verberne, M.E., DeRuiter, M.C., Poelmann, R.E., and Gittenberger-de Groot, A.C. (1998). Neural crest cell contribution to the developing circulatory system implications for vascular morphology? *Circ. Res.* 82, 221–231.

Besson, W.T., Kirby, M.L., Van Mierop, L.H.S., and Teabeaut, J.R. (1986). Effects of the size of lesions of the cardiac neural crest at various embryonic ages on incidence and type of cardiac defects. *Circulation* 73, 360–364.

Betancur, P., Bronner-Fraser, M., and Sauka-Spengler, T. (2010). Genomic code for Sox10 activation reveals a key regulatory enhancer for cranial neural crest. *Proc. Natl Acad. Sci. USA* *107*, 3570–3575.

Bockman, D.E., Redmond, M.E., Waldo, K., Davis, H., and Kirby, M.L. (1987). Effect of neural crest ablation on development of the heart and arch arteries in the chick. *Am. J. Anat.* *180*, 332–341.

Butler, A., Hoffman, P., Smibert, P., Papalex, E., and Satija, R. (2018). Integrating single-cell transcriptomic data across different conditions, technologies, and species. *Nat. Biotechnol.* *36*, 411–420.

Choi, H.M.T., Schwarzkopf, M., Fornace, M.E., Acharya, A., Artavanis, G., Stegmaier, J., Cunha, A., and Pierce, N.A. (2018). Third-generation in situ hybridization chain reaction: Multiplexed, quantitative, sensitive, versatile, robust. *Development* *145*, dev165753.

Dobin, A., Davis, C.A., Schlesinger, F., Drenkow, J., Zaleski, C., Jha, S., Batut, P., Chaisson, M., and Gingeras, T.R. (2013). STAR: Ultrafast universal RNA-seq aligner. *Bioinformatics* *29*, 15–21.

Ezin, A.M., Fraser, S.E., and Bronner-Fraser, M. (2009). Fate map and morphogenesis of presumptive neural crest and dorsal neural tube. *Dev. Biol.* *330*, 221–236.

Franz, T. (1989). Persistent truncus arteriosus in the *Spotch* mutant mouse. *Anat. Embryol. (Berl.)* *180*, 457–464.

Gandhi, S., and Bronner, M.E. (2018). Insights into neural crest development from studies of avian embryos. *Int. J. Dev. Biol.* *62*, 179–190.

Gandhi, S., Piacentino, M.L., Vieceli, F.M., and Bronner, M.E. (2017). Optimization of CRISPR/Cas9 genome editing for loss-of-function in the early chick embryo. *Dev. Biol.* *432*, 86–97.

Gao, Z., Kim, G.H., Mackinnon, A.C., Flagg, A.E., Bassett, B., Earley, J.U., and Svensson, E.C. (2010). *Ets1* is required for proper migration and differentiation of the cardiac neural crest. *Development* 137, 1543–1551.

Grossfeld, P.D., Mattina, T., Lai, Z., Favier, R., Lyons Jones, K., Cotter, F., and Jones, C. (2004). The 11q Terminal Deletion Disorder: A Prospective Study of 110 Cases. *Am. J. Med. Genet.* 129, 51–61.

Hamburger, V., and Hamilton, H.L. (1951). A series of normal stages in the development of the chick embryo. *J. Morphol.* 88, 49–92.

Hamid, R., and Brandt, S.J. (2009). Transforming growth-interacting factor (TGIF) regulates proliferation and differentiation of human myeloid leukemia cells. *Mol. Oncol.* 3, 451–463.

Harrison, T.A., Stadt, H.A., Kumiski, D., and Kirby, M.L. (1995). Compensatory responses and development of the nodose ganglion following ablation of placodal precursors in the embryonic chick (*Gallus domesticus*). *Cell Tissue Res.* 281, 379–385.

Hiruma, T., and Nakajima, Y. (2002). Development of pharyngeal arch arteries in early mouse embryo. *J. Anat.* 201, 15–29.

Hutson, M.R., and Kirby, M.L. (2003). Neural crest and cardiovascular development: A 20-year perspective. *Birth Defects Res. Part C - Embryo Today Rev.* 69, 2–13.

Imoto, I., Pimkhaokham, A., Watanabe, T., Saito-Ohara, F., Soeda, E., and Inazawa, J. (2000). Amplification and overexpression of TGIF2, a novel homeobox gene of the TALE superclass, in ovarian cancer cell lines. *Biochem. Biophys. Res. Commun.* 276, 264–270.

Jin, L., Zhou, Y., Kuang, C., Lin, L., and Chen, Y. (2005). Expression pattern of TG-interacting factor 2 during mouse development. *Gene Expr. Patterns* 5, 457–462.

Karolchik, D., Baertsch, R., Diekhans, M., Furey, T.S., Hinrichs, A., Lu, Y.T., Roskin, K.M., Schwartz, M., Sugnet, C.W., Thomas, D.J., et al. (2003). The UCSC Genome Browser Database. *Nucleic Acids Res.* *31*, 51–54.

Kirby, M.L. (1989). Plasticity and predetermination of mesencephalic and trunk neural crest transplanted into the region of the cardiac neural crest. *Dev. Biol.* *134*, 402–412.

Kirby, M.L., and Stewart, D.E. (1983). Neural crest origin of cardiac ganglion cells in the chick embryo: Identification and extirpation. *Dev. Biol.* *97*, 433–443.

Kirby, M.L., and Waldo, K.L. (1990). Role of neural crest in congenital heart disease. *Circulation* *82*, 332–340.

Kirby, M.L., and Waldo, K.L. (1995). Neural crest and cardiovascular patterning. *Circ. Res.* *77*, 211–215.

Kirby, M.L., Turnage, K.L., and Hays, B.M. (1985). Characterization of conotruncal malformations following ablation of “cardiac” neural crest. *Anat. Rec.* *213*, 87–93.

Kuratani, S.C., Miyagawa-Tomita, S., and Kirby, M.L. (1991). Development of cranial nerves in the chick embryo with special reference to the alterations of cardiac branches after ablation of the cardiac neural crest. *Anat. Embryol. (Berl.)* *183*, 501–514.

Kurihara, H., Kurihara, Y., Nagai, R., and Yazaki, Y. (1999). Endothelin and neural crest development. *Cell. Mol. Biol. (Noisy-Le-Grand)* *45*, 639–651.

Labun, K., Montague, T.G., Krause, M., Torres Cleuren, Y.N., Tjeldnes, H., and Valen, E. (2019). CHOPCHOP v3: expanding the CRISPR web toolbox beyond genome editing. *Nucleic Acids Res.* *47*, W171–W174.

Langmead, B., and Salzberg, S.L. (2012). Fast gapped-read alignment with Bowtie 2. *Nat. Methods* *9*, 357–359.

Loffredo, C.A. (2000). Epidemiology of cardiovascular malformations: prevalence and risk factors. *Am. J. Med. Genet.* 97, 319–325.

Love, M.I., Huber, W., and Anders, S. (2014). Moderated estimation of fold change and dispersion for RNA-seq data with DESeq2. *Genome Biol.* 15.

Martik, M.L., Gandhi, S., Uy, B.R., Gillis, J.A., Green, S.A., Simões-Costa, M., and Bronner, M.E. (2019). Evolution of the new head by gradual acquisition of neural crest regulatory circuits. *Nature* 574, 675–678.

Martin, M. (2011). Cutadapt removes adapter sequences from high-throughput sequencing reads. *EMBnet.Journal* 17, 10.

McGrew, M.J., Sherman, A., Lillico, S.G., Ellard, F.M., Radcliffe, P.A., Gilhooley, H.J., Mitrophanous, K.A., Cambray, N., Wilson, V., and Sang, H. (2008). Localised axial progenitor cell populations in the avian tail bud are not committed to a posterior Hox identity. *Development* 135, 2289–2299.

Miyagawa-Tomita, S., Waldo, K., Tomita, H., and Kirby, M.L. (1991). Temporospatial study of the migration and distribution of cardiac neural crest in quail-chick chimeras. *Am. J. Anat.* 192, 79–88.

Narayanan, C.H., and Narayanan, Y. (1980). Neural crest and placodal contributions in the development of the glossopharyngeal-vagal complex in the chick. *Anat. Rec.* 196, 71–82.

Neeb, Z., Lajiness, J.D., Bolanis, E., and Conway, S.J. (2013). Cardiac outflow tract anomalies. *Wiley Interdiscip. Rev. Dev. Biol.* 2, 499–530.

Nishibatake, M., Kirby, M.L., and Van Mierop, L.H.S. (1987). Pathogenesis of persistent truncus arteriosus and dextroposed aorta in the chick embryo after neural crest ablation. *Circulation* 75, 255–264.

- O'Donnell, M., Hong, C.-S., Huang, X., Delnicki, R.J., and Saint-Jeannet, J.-P. (2006). Functional analysis of Sox8 during neural crest development in *Xenopus*. *Development* *133*, 3817–3826.
- Phillips, M.T., Kirby, M.L., and Forbes, G. (1987). Analysis of cranial neural crest distribution in the developing heart using quail-chick chimeras. *Circ. Res.* *60*, 27–30.
- Picelli, S., Faridani, O.R., Björklund, Å.K., Winberg, G., Sagasser, S., and Sandberg, R. (2014). Full-length RNA-seq from single cells using Smart-seq2. *Nat. Protoc.* *9*, 171–181.
- Sauka-Spengler, T., and Barembaum, M. (2008). Chapter 12 Gain- and Loss-of-Function Approaches in the Chick Embryo. *Methods Cell Biol.* *87*, 237–256.
- Saunders, L.R., and McClay, D.R. (2014). Sub-circuits of a gene regulatory network control a developmental epithelial-mesenchymal transition. *Development* *141*, 1503–1513.
- Schindelin, J., Arganda-Carreras, I., Frise, E., Kaynig, V., Longair, M., Pietzsch, T., Preibisch, S., Rueden, C., Saalfeld, S., Schmid, B., et al. (2012). Fiji: an open-source platform for biological-image analysis. *Nat. Methods* *9*, 676–682.
- Serbedzija, G.N., Bronner-Fraser, M., and Fraser, S.E. (1994). Developmental potential of trunk neural crest cells in the mouse. *Development* *120*, 1709–1718.
- Simões-Costa, M., and Bronner, M.E. (2016). Reprogramming of avian neural crest axial identity and cell fate. *Science* *352*, 1570–1573.
- Simões-Costa, M., McKeown, S.J., Tan-Cabugao, J., Sauka-Spengler, T., and Bronner, M.E. (2012). Dynamic and differential regulation of stem cell factor FoxD3 in the neural crest is encrypted in the genome. *PLoS Genet.* *8*, e1003142.
- Snider, P., Olaopa, M., Firulli, A.B., and Conway, S.J. (2007). Cardiovascular Development and the Colonizing Cardiac Neural Crest Lineage. *Sci. World J.* *7*, 1090–1113.

Tani-Matsuhana, S., Vieceli, F.M., Gandhi, S., Inoue, K., and Bronner, M.E. (2018). Transcriptome profiling of the cardiac neural crest reveals a critical role for MafB. *Dev. Biol.* *444*, S209–S218.

Taniguchi, K., Anderson, A.E., Sutherland, A.E., and Wotton, D. (2012). Loss of tgif function causes holoprosencephaly by disrupting the Shh signaling pathway. *PLoS Genet.* *8*, e1002524.

Trapnell, C., Roberts, A., Goff, L., Pertea, G., Kim, D., Kelley, D.R., Pimentel, H., Salzberg, S.L., Rinn, J.L., and Pachter, L. (2012). Differential gene and transcript expression analysis of RNA-seq experiments with TopHat and Cufflinks. *Nat. Protoc.* *7*, 562–578.

Trapnell, C., Cacchiarelli, D., Grimsby, J., Pokharel, P., Li, S., Morse, M., Lennon, N.J., Livak, K.J., Mikkelsen, T.S., and Rinn, J.L. (2014). The dynamics and regulators of cell fate decisions are revealed by pseudotemporal ordering of single cells. *Nat. Biotechnol.* *32*, 381–386.

Verberne, M.E., Gittenberger-de Groot, A.C., Van Iperen, L., and Poelmann, R.E. (2000). Distribution of different regions of cardiac neural crest in the extrinsic and the intrinsic cardiac nervous system. *Dev. Dyn.* *217*, 191–204.

Waldo, K.L., and Kirby, M.L. (1993). Cardiac neural crest contribution to the pulmonary artery and sixth aortic arch artery complex in chick embryos aged 6 to 18 days. *Anat. Rec.* *237*, 385–399.

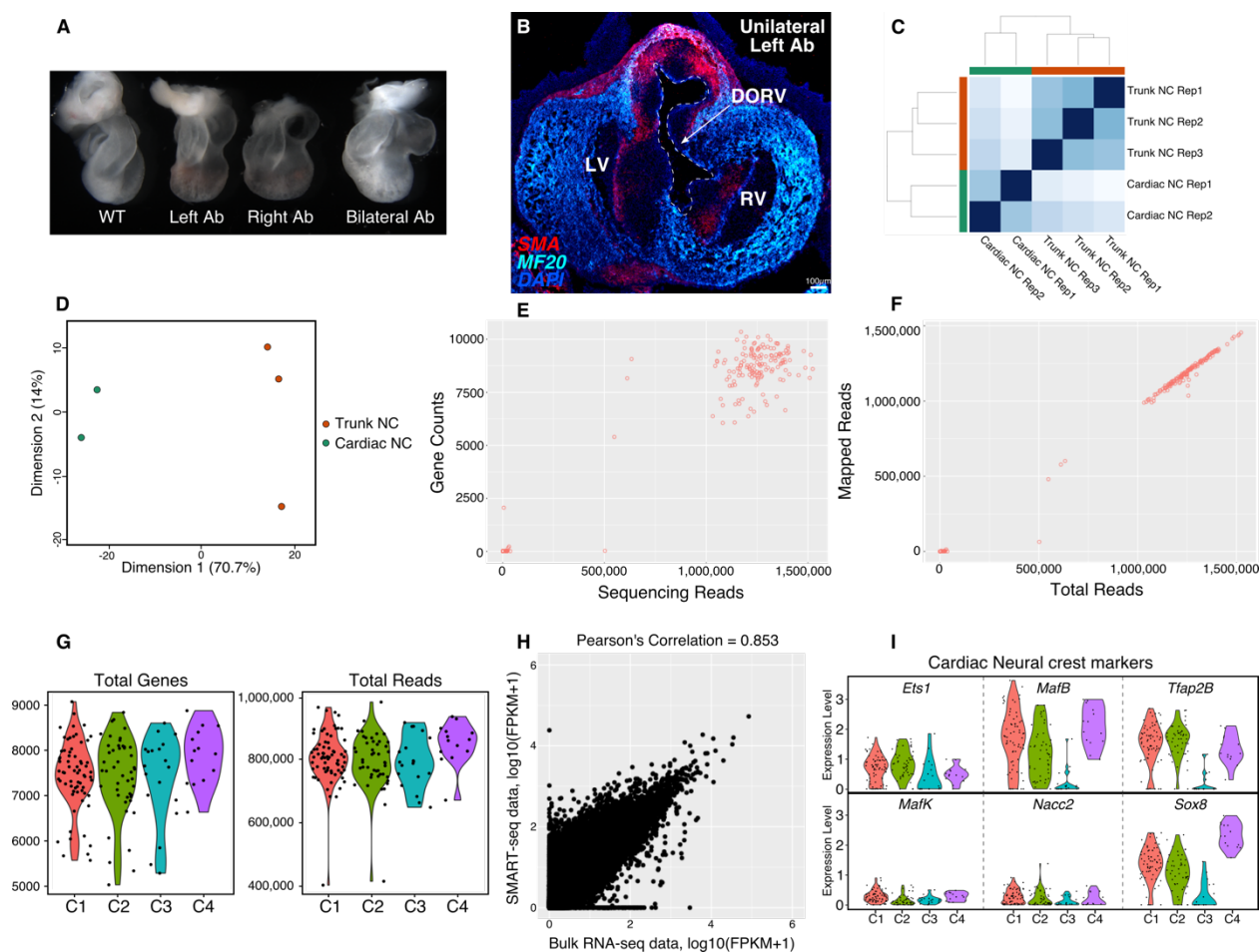
Waldo, K., Miyagawa-Tomita, S., Kumiski, D., and Kirby, M.L. (1998). Cardiac neural crest cells provide new insight into septation of the cardiac outflow tract: Aortic sac to ventricular septal closure. *Dev. Biol.* *196*, 129–144.

Xiang, G., Yi, Y., Weiwei, H., and Weiming, W. (2015). TGIF1 promoted the growth and migration of cancer cells in nonsmall cell lung cancer. *Tumor Biol.* *36*, 9303–9310.

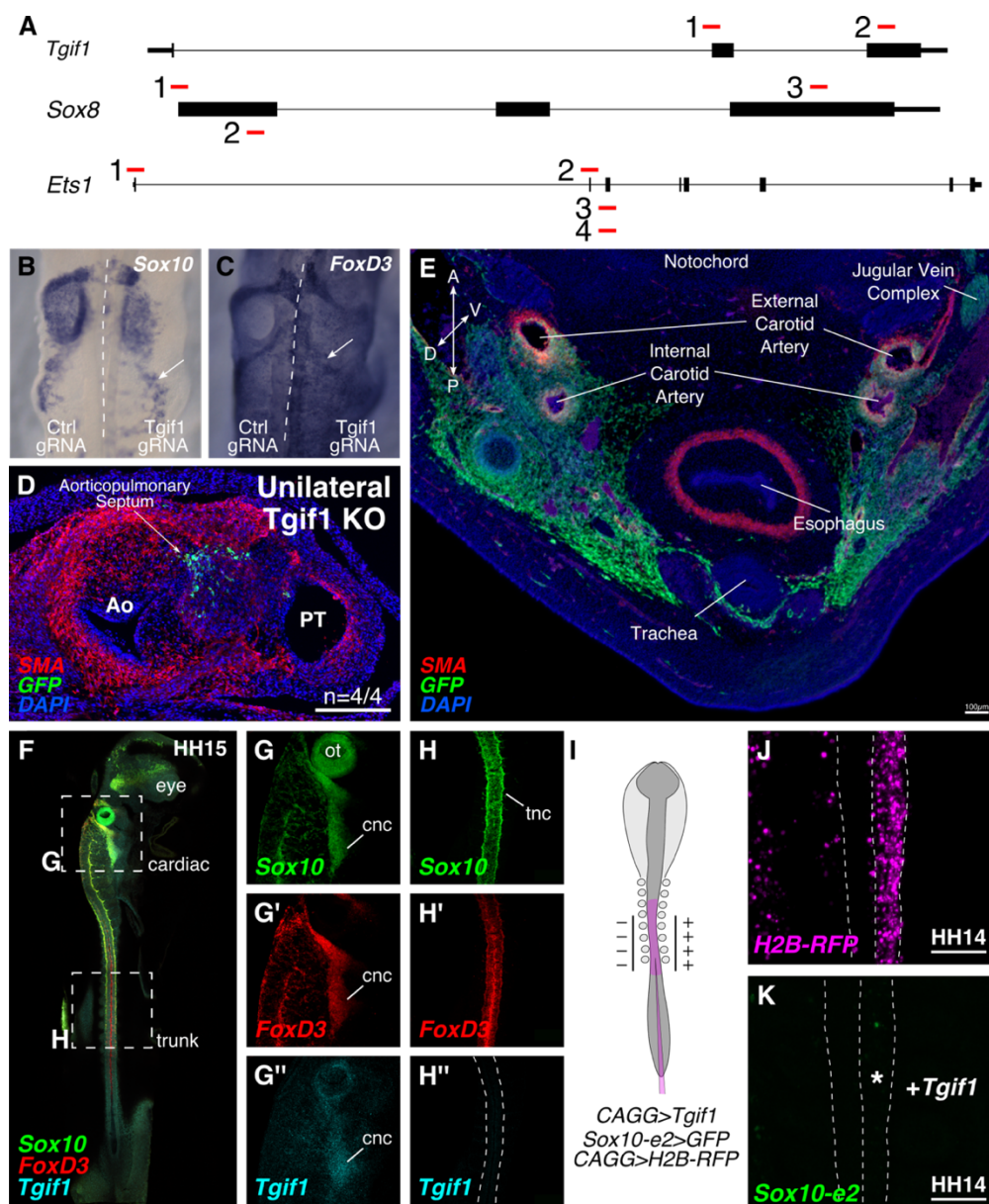
Yajima, I., Colombo, S., Puig, I., Champeval, D., Kumasaka, M., Belloir, E., Bonaventure, J., Mark, M., Yamamoto, H., Taketo, M.M., et al. (2013). A Subpopulation of Smooth Muscle Cells, Derived from Melanocyte-Competent Precursors, Prevents Patent Ductus Arteriosus. *PLoS One* 8, e53183.

Ye, M., Coldren, C., Liang, X., Mattina, T., Goldmuntz, E., Benson, D.W., Ivy, D., Perryman, M.B., Garrett-Sinha, L.A., and Grossfeld, P. (2009). Deletion of ETS-1, a gene in the Jacobsen syndrome critical region, causes ventricular septal defects and abnormal ventricular morphology in mice. *Hum. Mol. Genet.* 19, 648–656.

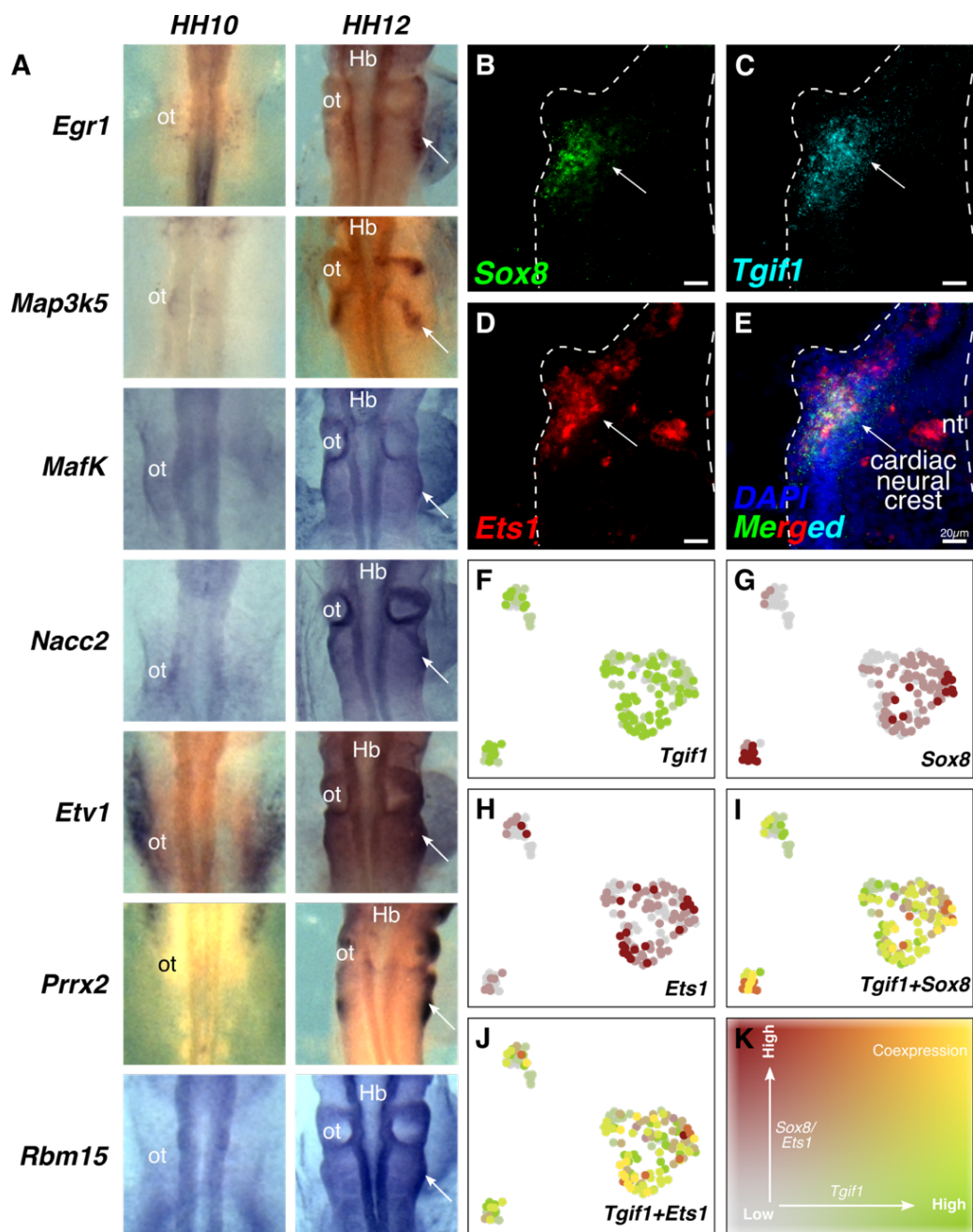
7.10 Supplementary Figures



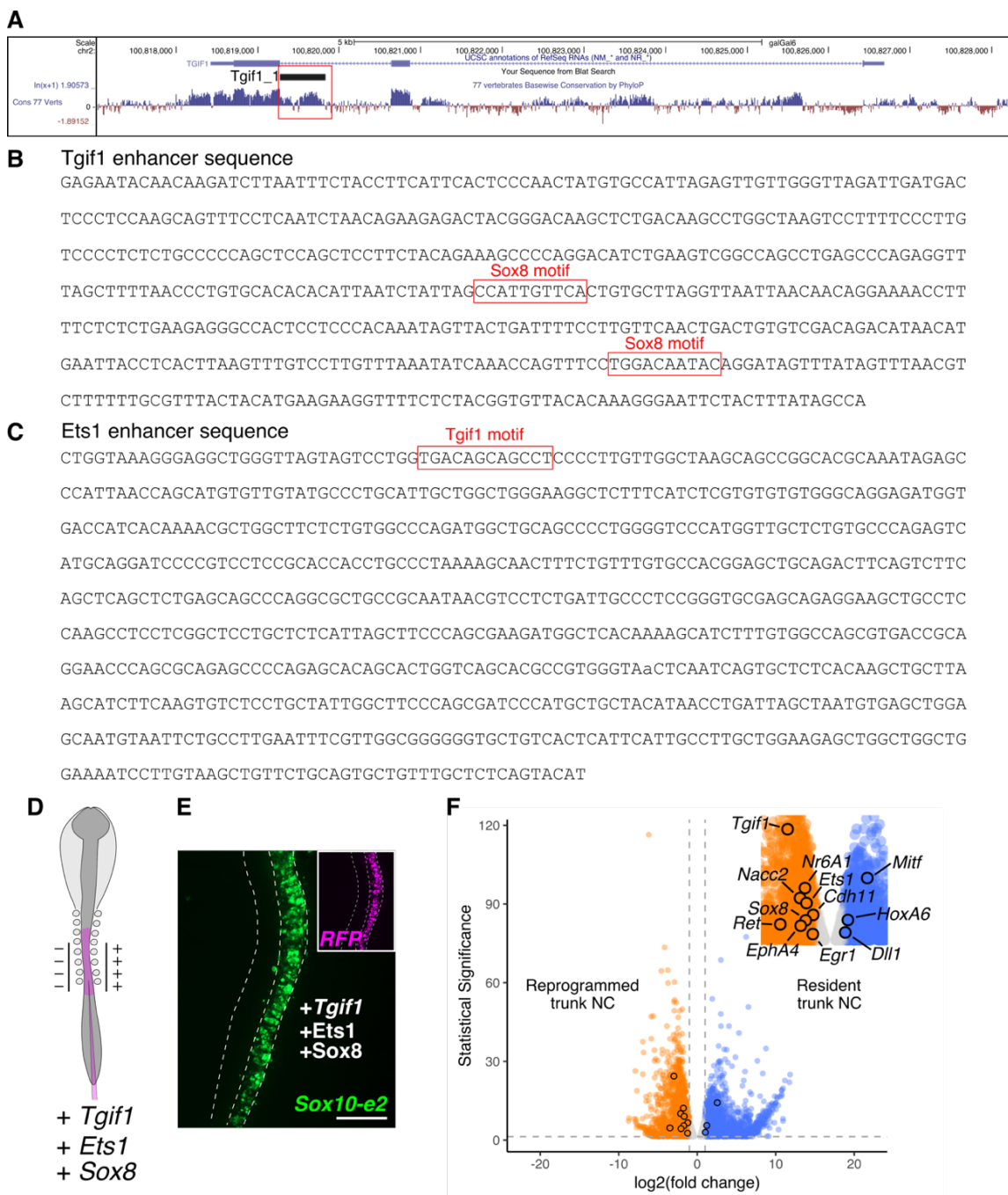
Supplementary Figure S1 (related to figure 1, 2). Effect of ablations on cardiovascular development, and quality control on bulk and single cell RNA-seq data. A. (left to right) Primary heart tubes of E3 embryos where the cardiac neural folds were left intact, unilaterally ablated on the left, unilaterally ablated on the right, and bilaterally ablated. No difference was observed on the effect of left and right unilateral ablation on primary heart tube looping and elongation. **B.** Transverse cross-section through an E6 outflow tract of an embryo where the cardiac neural crest was unilaterally ablated on the left side exhibits Double Outlet Right Ventricle (DORV). **C-D.** Hierarchical clustering (C) and Principal Component Analysis (D) done on the two cardiac and three trunk neural crest libraries prepared for population-level transcriptional profiling shows high correlation between replicates. **E-G.** Quality control on SMART-seq sequencing data showing the number of genes identified per cell (E, G) and high correlation between mapped and sequencing reads (F). **H.** Scatter plot comparing genes enriched in the bulk and single cell RNA-seq datasets. **I.** Genes validated in main figure 2 using in situ hybridization were highly expressed across C1, C2, and C4, with lower expression levels in the ectomesenchymal C3.



Supplementary Figure S2 (related to figure 3, 4). Role of *Tgif1* in cardiac neural crest. **A.** Loci for *Tgif1*, *Sox8*, and *Ets1* with gRNA target sites highlighted in red. 2 gRNAs for *Tgif1*, 3 gRNAs for *Sox8*, and 4 gRNAs for *Ets1* were designed. **B-C.** Loss of *Tgif1* resulted in reduced expression of pan-neural crest markers *Sox10* (B) and *FoxD3* (C), but little difference was observed in the number of cells. **D.** The outflow tract of embryos that were unilaterally grafted with a *Tgif1* knockout dorsal cardiac neural fold septated properly. **E.** Cross-section through the neck of a chimera where *Tgif1* knockout dorsal cardiac neural folds were bilaterally grafted in the embryo. Cardiac neural crest cells surrounded in the internal and external carotid artery, but failed to form the outflow tract septum. **F-H.** Hybridization Chain Reaction in a HH15 embryo shows expression of *Sox10* (G,H) and *FoxD3* (G',H') in both cardiac and trunk neural crest cells. *Tgif1* was expressed in the cardiac region (G''), but absent from the trunk neural crest (H''). **I-K.** Electroporation strategy (I) to check the effect of ectopic expression of *Tgif1* on resident trunk neural crest cells. DNA solutions containing expression constructs for *Tgif1*, *Sox10-e2>GFP*, and H2B-RFP were injected in the lumen of the neural tube of an HH9+ embryo. The electroporation efficiency was checked using H2B-RFP expression (J). Overexpression of *Tgif1* failed to turn on the *Sox10-e2* enhancer in the trunk neural crest (K).



Supplementary Figure S3 (related to figure 5). Identification of cardiac neural crest subcircuit genes. A. *in situ* hybridization against genes enriched in the cardiac compared to trunk neural crest that are expressed in migratory (HH12) but not premigratory (HH10) cardiac neural crest. **B-E.** Transverse cross-sections through a HH12 embryo where *Tgif1*, *Sox8*, and *Ets1* transcripts were labeled using Hybridization Chain Reaction. Cardiac neural crest cells from the post-otic r6 stream showed overlapping expression of the three genes. **F-K.** Coexpression analysis of *Tgif1* with *Sox8* and *Ets1* using the SMART-seq data. Both genes were abundant in a high proportion of cardiac neural crest cells profiled using single cell RNA-seq.



Supplementary Figure S4. Investigation of functional relationships between cardiac neural crest subcircuit genes and identification of downstream targets (related to figure 5). **A.** UCSC genome browser track shows an evolutionary conserved region in the second intron of *Tgif1*. **B-C.** The *Tgif1* (B) and *Ets1* (C) enhancer sequence that recapitulated expression of the respective genes in the cardiac neural crest at HH12. *Sox8* binding sites in the *Tgif1* enhancer and *Tgif1* binding site in the *Ets1* enhancer are labeled. **D.** Electroporation strategy for isolating reprogrammed trunk neural crest cells for transcriptional profiling. **E.** Dorsal view of trunk neural crest from a representative HH14 embryo transfected with expression constructs for *Sox8*, *Tgif1*, and *Ets1* together with *Sox10-e2* enhancer-mediated GFP expression (Scale bar = 100 μ m). **F.** Volcano plot showing genes differentially expressed in resident trunk (blue) and reprogrammed trunk (orange) neural crest cells. Inset – genes included in the heatmap in figure 5T are labeled.

Chapter 8

Concluding remarks

A modified version of this chapter is currently *in press* as:

Gandhi, S., Bronner, M.E. (2021). Seq your destiny: Neural crest fate determination in the genomic era. *Annu. Rev. Genet.* 55

8.1 Introduction

During early embryonic development, multipotent precursors, capable of giving rise to most cell types found in the adult organism, are gradually committed to discrete lineages. Classically, this restriction was thought to be a binary fate choice, with onset of expression of a “master” regulator (Davidson, 1991) biasing a bipotent cell towards one fate or the other (Huang et al., 2007; Laslo et al., 2006). Recently, the application of single-cell technologies has greatly enhanced our understanding of how cells become committed to different fates. Surprisingly, current data suggest that multipotent progenitor cells express several lineage markers concomitantly and can exist in an uncommitted state just prior to their differentiation (Brunskill et al., 2014; Gouti et al., 2014; Hanchate et al., 2015; Treutlein et al., 2014). Thus, rather than being influenced by a single factor, it seems more likely that modulating the relative levels of lineage determinants may lead to a cell’s decision to adopt a particular cell fate.

The neural crest (Le Douarin, 1982) is an important example of a cell population in vertebrate embryos that serves as an excellent model system for addressing how cell fate decisions are made (Dupin et al., 2006; Powell et al., 2013; Smith, 1990; Tucker, 2004). Arising from the junction of the neural plate (future central nervous system) and non-neural ectoderm (future epidermis), presumptive neural crest cell progenitors first arise at the neural plate border (Streit and Stern, 1999) [Figure 1A-C], which elevates during neurulation to become the closing neural folds [Figure 1D-F] that will then transform into the dorsal neural tube (Gammill and Bronner-Fraser, 2003). After neural tube closure in most species, these cells undergo an epithelial-to-mesenchymal transition, losing their cell-cell adhesion and transforming into a migratory and mesenchymal state (Sauka-Spengler and Bronner-Fraser, 2008) [Figure 1G-I]. Motile neural crest cells then migrate throughout the embryo to form a wide range of derivatives, including craniofacial bone and cartilage, ganglia of the peripheral nervous system, and pigment cells of the epidermis (reviewed in (Gandhi and Bronner, 2018; Martik and Bronner, 2017; Simões-Costa and Bronner, 2015)).

In my graduate studies, I have addressed questions pertaining to neural crest plasticity and cell fate determination in avian embryos. I particularly focused on the cranial neural crest, which contributes to craniofacial structures including the facial skeleton, and the cardiac neural crest, which emerges from the caudal hindbrain and has the unique developmental potential to contribute to the heart.

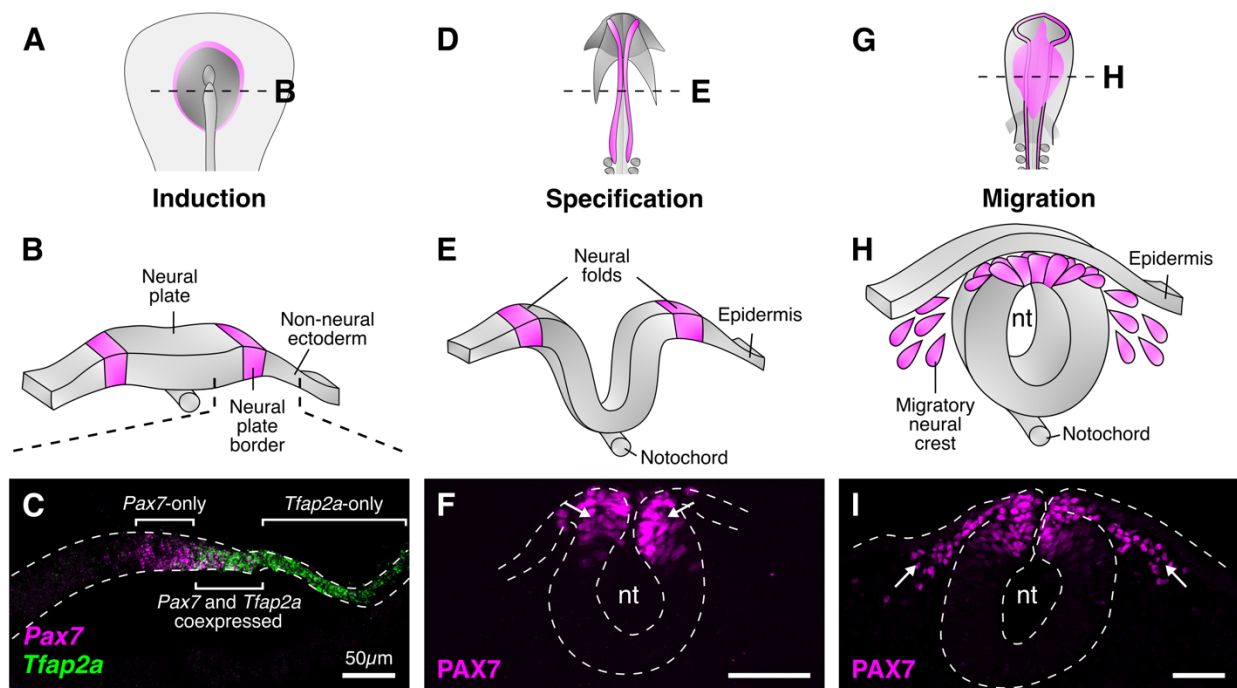


Figure 1. Early stages of neural crest development. **A-C.** Neural crest cells are induced at the neural plate border (A), a strip of ectoderm that lies at the juxtaposition of the neural plate and the non-neural ectoderm (B). Lineage-specific markers are expressed in neural plate border precursors as the embryo develops. *Pax7* transcripts label the presumptive neural crest, whereas *Tfp2a* transcripts label the developing ectoderm. However, a subset of the neural plate border cells express both *Pax7* and *Tfp2a*, supporting the hypothesis that the neural plate border represents a heterogeneous mixture of multipotent progenitors with the capacity to contribute cells to the neural, neural crest, ectoderm, and the placodal lineages. **D-F.** During neurulation, the neural plate border elevates to form neural folds (D,E), and a battery of transcription factors known as the neural crest specifier genes are expressed in the dorsal aspect of the developing neural tube. Eventually, as the neural folds fuse to form the neural tube, premigratory neural crest cells in the dorsal midline of the neural tube undergo an epithelial to mesenchymal transition, losing expression of cell junction proteins and gaining mesenchymal characteristics. *Pax7* protein continues to be expressed in emigrating neural crest cells (F). **G-I.** Following their emigration (G), neural crest cells migrate extensively throughout the embryo (H) to give rise to diverse array of cell types, including neurons, glia, smooth muscle, cartilage and bone, melanocytes, etc. *Pax7* expression is retained in migratory cranial neural crest cells (I).

8.2 The neural crest

The neural crest is a uniquely vertebrate cell type (Bronner and LeDouarin, 2012). On this basis, Gans and Northcutt (Gans and Northcutt, 1983), in their seminal paper from 1983, proposed that the advent of the neural crest at the base of vertebrates played a critical role in vertebrate evolution. By giving rise to bone and cartilage of the lower jaw as well as contributing to sensory structures of the head, they proposed that innovation of this new cell type facilitated a behavioral shift in vertebrates towards active predation (Glenn Northcutt, 2005). Moreover, despite their ectodermal origin, the fact that neural crest cells were capable of giving rise to critical mesenchymal derivatives challenged existing hypotheses regarding germ layer contributions (Green et al., 2015; Hall, 2000).

In Chapter 2, I discussed the early principles of neural crest development and provided a summary of research that addressed a long-standing question of whether individual premigratory neural crest cells that reside within the dorsal neural tube are multipotent or a mixture of predetermined progenitors each with the ability to give rise to a particular cell type. Through a combination of *in vitro* and *in vivo* techniques, the multipotency of the neural crest has been established. The experimental techniques used to address the question of multipotency have been recently reviewed in detail (Tang and Bronner, 2020). I also discussed how neural crest cells move in a highly patterned fashion through neighboring tissues and how their patterns of migration and types of derivatives formed depend upon their axial level of origin (Le Douarin, 1982; Noden, 1975). Four distinct axial levels were noted, designated as cranial, vagal, trunk and lumbosacral neural crest [Figure 2]. While neural crest cells at all axial levels contribute to some common derivatives such as skin melanocytes, glia and Schwann cells (Le Douarin, 1982), there are also neural crest-derived cell types that are unique to particular axial levels (Le Douarin and Teillet, 1974). Cranial and vagal neural crest cells, that originate in the rostral half of the embryo, follow different patterns of migration compared to the trunk and sacral neural crest and differentiate into some unique cell types. For example, neural crest cells originating in the midbrain migrate primarily as a broad, unsegmented sheet under the ectoderm; they contribute to derivatives ranging from the perocular

skeleton to the ciliary and trigeminal ganglia (D'amico-Martel and Noden, 1983; Le Douarin and Kalcheim, 1982). Neural crest cells originating in the rostral hindbrain enter the branchial arches and form many of the cartilaginous elements of the facial skeleton, including the quadrate, Meckel's cartilage and surrounding membrane bones, and the basihyoid cartilage in the tongue (Couly et al., 1992, 1993; Noden, 1978).

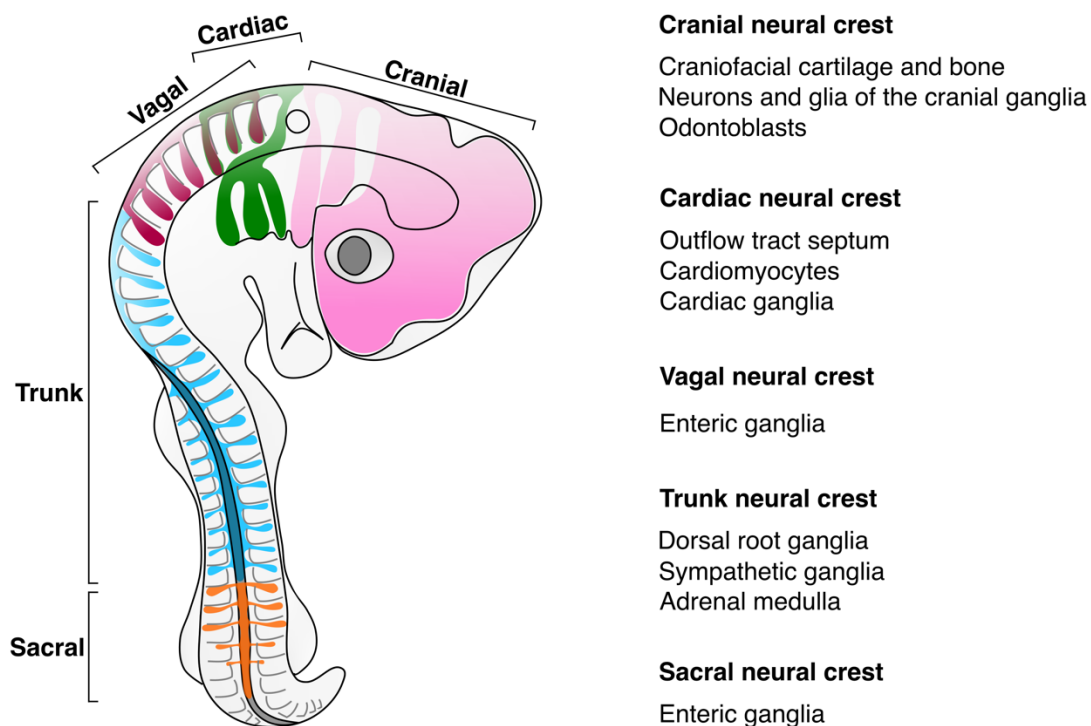


Figure 2. Rostrocaudal arrangement of neural crest populations. Neural crest derivatives are segregated based on their axial levels of origin. Cranial neural crest cells have the unique ability to contribute bone and cartilage of the craniofacial skeleton and odontoblasts to the developing dental pulp. The cardiac neural crest, which is considered a subset of the vagal neural crest, is also the only neural crest subpopulation that can contribute smooth muscle cells to the developing heart. Embryos in which the cardiac neural crest was surgically ablated suffer from persistent truncus arteriosus, a condition where the outflow tract fails to septate, resulting in a single vessel emerging from the heart that carries both oxygenated and deoxygenated blood. Recent work has highlighted the contribution of the cardiac neural crest to the ventricular myocardium (Tang et al., 2019b). The rest of the vagal neural crest gives rise to the enteric ganglia. Trunk neural crest is the largest neural crest population in the early embryo. While lacking the ability to form specialized ectomesenchymal derivatives such as cartilage and smooth muscle, these cells give rise to the dorsal root ganglia, the adrenal medulla, sympathetic ganglia, and melanocytes. Finally, the sacral neural crest contributes to the developing enteric nervous system, complementing the contribution of the vagal neural crest.

Another neural crest population, developmentally unique from the cranial neural crest, originates in the caudal hindbrain and is called the “cardiac” neural crest, originally

designated by Le Douarin and colleagues as a subset of the vagal neural crest (Le Douarin and Teillet, 1973). These cells arise adjacent to the mid-otic to somite 3 level and are the only neural crest subpopulation that contributes to the cardiovascular system (Kirby et al., 1983). Following delamination from the dorsal hindbrain, they migrate into the pharyngeal arches 3, 4, and 6, from which a subset of cardiac crest cells migrates into the cardiac outflow tract, within which they condense to form the aorticopulmonary septum (Hutson and Kirby, 2007; Kirby et al., 1983; Neeb et al., 2013; Snider et al., 2007; Stoller and Epstein, 2005). Some cells migrate still further into the ventricles and form cardiomyocytes (Tang et al., 2019b). Other vagal neural crest cells enter the foregut and contribute to the neurons and glia of the enteric nervous system (Epstein et al., 1994), which also receives a contribution from the sacral neural crest (Burns et al., 2000). The largest neural crest population is the “trunk” neural crest which arises at spinal cord levels [Sidebar 3] and forms sympathetic and sensory ganglia of the peripheral nervous system as well as to the adrenal medulla (Bronner-Fraser, 1986; Kuo and Erickson, 2010; Osorio et al., 2009; Rickmann et al., 1985; Vega-Lopez et al., 2017).

In Chapter 3, we investigated the evolutionary origin of the neural crest population in vertebrates (Martik et al., 2019) by comparing cranial and trunk neural crest gene expression from the sea lamprey, which are parasitic, eel-shaped fish without jaws, with those of jawed vertebrates embryos at different positions on the vertebrate tree of life (skate, zebrafish, chick). While the chick possess a cranial neural crest subcircuit that is transcriptionally unique from its trunk neural crest, lamprey cranial neural crest lacks this subcircuit and more closely resembles chick trunk neural crest. Interestingly, cranial crest subcircuit genes appear to have been progressively added as the vertebrates continued to evolve. Based on these results, we proposed that ancestral neural crest of jawless vertebrates exists in a primitive “trunk-like” state, and that progressive addition of new genes during the course of vertebrate evolution gradually conferred onto neural crest the ability to form bone and cartilage of the lower jaw.

In Chapters 4 and 5, I described our work on developing molecular tools for genetic perturbations in both early (Gandhi et al., 2017) and late (Gandhi et al., 2021) avian

embryos. My graduate thesis work has helped expand the experimental toolkit available to understand the development of the neural crest and other embryonic cell types, making this an opportune time to delve deeply into the molecular mechanisms underlying specification, migration and differentiation of this cell population.

8.3 Plasticity at the neural plate border

All neural crest subpopulations are induced at the neural plate border (Streit and Stern, 1999), a broad stripe of ectoderm immediately adjacent to the future neural plate. Neural crest induction precedes the onset of expression of early neural marker genes such as *Otx2*, *Sox3*, and *ERNI* (Rex et al., 1997; Streit et al., 2000) in the presumptive neural plate of a pre-gastrula stage embryo. Expression of these markers relies on activating FGF signaling and inhibiting Wnt and BMP signaling to establish the neural lineage from the underlying ectoderm (Albazerchi and Stern, 2007; Rogers et al., 2011; Stern and Downs, 2012; Streit et al., 2000). On the other hand, in the lateral edges of the embryo, the absence of antagonistic Wnt and BMP signals triggers the expression of genes that mark the non-neural ectoderm, such as those belonging to the transcription factor families *Tfap2*, *Dlx*, *Foxi*, and *Msx* (reviewed in Thawani and Groves, 2020). While the neural and non-neural lineages are segregating, a battery of genes belonging to the neural crest gene regulatory network, termed neural plate border specifiers (Simões-Costa and Bronner, 2015), are transcribed in the early gastrula, including *Pax3/7*, *Zic1*, and *Msx1*, thereby establishing the boundaries of the neural plate border. The expression of these genes is maintained in the neural plate border through a series of positive-feedback cross-regulatory interactions (Martik and Bronner, 2017).

The classical view of the neural plate border region was that it was comprised of separate zones containing cells with different prospective fates, with placodal precursors found more laterally and neural crest precursors more medially (Ahrens and Schlosser, 2005; Pieper et al., 2012). In contrast, Roellig et al. (2017) proposed that neural plate border cells initially may be naïve and capable of giving rise to several possible derivatives. Through careful characterization of protein expression in individual cells

located within the neural plate border, they showed that neural plate border cells are heterogeneous based on their protein expression profiles and often co-express two or three markers characteristic of neural (*Sox2*) (Fernández-Garre et al., 2002), neural crest (*Pax7*) (Basch et al., 2006), ectodermal (*Tfap2a*) (Knight et al., 2005), or placodal (*Six1*) (Ahrens and Schlosser, 2005) lineages. They further demonstrated that expression of the neural plate marker *Sox2* extends throughout the whole neural plate border when compared to *Msx1/2* and *Pax7*, which suggests that numerous cells at the neural plate border simultaneously express a subset of markers of definitive neural, neural crest, placodal and epidermal progenitors. Consistent with these observations, modulation of *Sox2* and *Pax7* expression level was sufficient to shift the balance between neural and neural crest fates. Moreover, when small groups of neural plate border (Schoenwolf and Sheard, 1990) or presumptive placodal precursors (Streit, 2002) were labeled using focal Dil injections in the neural plate border region of gastrula-stage chick embryos, Dil-labeled cells were found in the epidermis, neural tube, neural crest and placodal tissues, also supporting the idea of shared lineages.

While Roellig et al. (2017) characterized the molecular switch that controls the fate switch between neural and neural crest lineages, the role of epigenetic modifiers in regulating these cell fate decisions was previously unclear. In Chapter 6, I delved deeper into this question (Gandhi et al., 2020a) by profiling the chick embryonic hindbrain at a single-cell resolution using scRNA-seq, looking for genes that were expressed in neural (hindbrain), neural crest (cardiac neural crest), and epidermis (non-neural ectoderm), three lineages derived from the neural plate border. This allowed us to identify the chromatin remodeler gene *Hmga1* (Fedele et al., 2006; Xian et al., 2017) as broadly expressed across the three cell populations. Extensively studied for its role in several types of cancers (Resar et al., 2018; Shah and Resar, 2012), *Hmga1* increases the accessibility for transcriptional complexes to bind in proximity and regulate the expression of target genes (Reeves and Beckerbauer, 2001). However, little was known about its role in early neural crest development. In avian embryos, Hybridization Chain Reaction revealed that *Hmga1* transcripts were first observed in gastrula stage embryos in the

neural plate and the presumptive neural plate border (Gandhi et al., 2020a). Its expression preceded that of *Pax7* in neural plate border precursors, such that CRISPR-Cas9-mediated knockout of *Hmga1* resulted in a specific loss of *Pax7* in the neural plate border without affecting the expression of other neural plate border specifier genes, such as *Msx1* and *Tfap2a*. These experiments established *Hmga1* as an upstream regulator of *Pax7*-dependent neural crest specification at the neural plate border. Following the loss of *Hmga1* in neural crest precursors, the expression of *Sox2* was elevated at the expense of *Pax7*, suggesting that cells acquired a neural fate at the expense of neural crest fate. My work further illuminates the importance of proper nucleosomal remodeling as an additional regulatory mechanism for governing cell fate choices at the neural plate border.

8.4 Specification of the cardiac neural crest in the dorsal hindbrain

One of the neural crest populations along the body axis about which the least is known is the cardiac neural crest (Hutson and Kirby, 2003). The axial level of origin for the cardiac neural crest was identified as the hindbrain over 30 years ago by Margaret Kirby and colleagues, using ablation experiments and quail-chick chimeric grafts (Kirby et al., 1985). They showed that bilateral ablation of the dorsal neural tube adjacent to mid-otic vesicle to somite 3 caused a broad range of defects, including persistent truncus arteriosus (PTA), double outlet right ventricle (DORV), abnormal myocardium function, and misalignment of the arch arteries (Bockman et al., 1987). Conversely, quail-chick grafts showed that hindbrain neural crest cells contribute to the cardiac outflow tract, pharyngeal arch arteries and some valves of the heart (Kirby and Stewart, 1983; Waldo and Kirby, 1993; Waldo et al., 1998). More recently, retroviral lineage tracing (Tang et al., 2019b) has confirmed these cardiac crest derivatives and additionally revealed a contribution of the cardiac neural crest to cardiomyocytes in the ventricles in both birds and mice similar to that previously noted in zebrafish (zebrafish contribution reviewed in George et al., 2020). Moreover, after resection of the adult heart of zebrafish, a neural crest gene regulatory program is redeployed and heart regeneration fails upon ablation of the neural crest population (Tang et al., 2019b).

The specification of cardiac neural crest cells is similar to but temporally follows that of the cranial neural crest. Expression of neural plate border specifier genes is swiftly followed by the expression of a set of transcription factors known as neural crest specifiers (Rothstein et al., 2018; Simões-Costa and Bronner, 2015; Simões-Costa et al., 2014). The onset of specification is a Wnt signaling dependent process, where the neural plate border specifier genes *Pax7* and *Msx1* interact with the Wnt effector *Axud1* to directly regulate the levels of *FoxD3* in specified neural crest cells (Simões-Costa et al., 2015). *Tfap2a*, which is expressed in the neural plate border and non-neural ectoderm lineages, is also essential for proper specification of neural crest cells (De Crozé et al., 2011; Knight et al., 2003; Luo et al., 2003; Rothstein and Simões-Costa, 2020), and acts in a manner independent of its role in the non-neural ectoderm.

Upon completion of specification, neural crest specifier genes appear in the cardiac neural crest population that are similar to those expressed in cranial neural crest, including *Sox10* (Betancur et al., 2010a), *Tfap2b* (Rothstein and Simões-Costa, 2020), *Snai2* (Nieto et al., 1994), *FoxD3* (Barenbaum and Bronner-Fraser, 2005), *Ets1* (Théveneau et al., 2007) and *cMyc* (Kerosuo and Bronner, 2016). However, unlike midbrain level neural crest cells which lack *Hox* gene expression, a number of different *Hox* genes are expressed in the cardiac neural crest including *Hoxa1*, *Hoxb1*, and *Hoxb5* (Gandhi et al., 2020b; Tani-Matsuhana et al., 2018). As is the case with neural plate border specifier genes, the expression of neural crest specifier genes is maintained in premigratory and migratory neural crest cells through a series of positive feedback/feed-forward loops. For example, *Ets1* is necessary for maintaining the expression of *FoxD3* (Simões-Costa et al., 2012).

A cardiac neural crest specific program appears to be superimposed upon a more general neural crest specification program. In Chapter 7, I showed that the cardiac crest subcircuit includes the transcription factor *Tgif1* (Gandhi et al., 2020b), which is specifically expressed in premigratory and migrating cardiac neural crest cells. When *Tgif1* was knocked out from the cardiac neural crest using CRISPR-Cas9, the expression of cardiac neural crest markers such as *Cxcr4*, *Ret*, and *MafB* (Tani-Matsuhana et al.,

2018) was downregulated, without affecting the levels of other pan-neural crest specifier genes such as *FoxD3*. Moreover, *Tgif1* acted downstream of the transcription factor *Sox8*, which is required for induction of neural crest cells (O'Donnell et al., 2006), and upstream of *Ets1*, which has been implicated in their proper specification and delamination (Gao et al., 2010). The expression of *Ets1* is also regulated by the neural plate border specifier genes *Pax7* and *Msx1* in specified neural crest cells (gene circuitry reviewed in Martik and Bronner, 2017; Simões-Costa and Bronner, 2015), suggesting that members of the neural plate border specifier gene circuits continue to play a crucial role in the establishment of neural crest identity.

Following specification, the cardiac crest migrates to the body wall and settles in the circumpharyngeal area of forming pharyngeal arches 3, 4, and 6, known as the circumpharyngeal ridge. From there, some of these cells will continue migration into the cardiac outflow tract where they condense and form the outflow tract septum, which septates the outflow tract into the aorta and the pulmonary trunk (Creazzo et al., 1998). Other cardiac neural crest cells remain in these arches and contribute to the aortic arch arteries (precursors to the brachiocephalic arteries, medial common carotid artery, aorta and ductus arteriosus), as well as the thymus, thyroid, and parathyroid glands (Hutson and Kirby, 2007; Jiang et al., 2000). These cells also play a critical role in remodeling of the aortic arch arteries. Cardiac neural crest cells also populate the cardiac cushions (future semilunar valves), interventricular septum, and form the nerves of the cardiac parasympathetic nervous system including the cardiac ganglia. My graduate work has raised important outstanding questions, including whether individual cardiac neural crest cells contribute to all derivatives of the heart, or whether precursors are set aside that are already committed to particular lineages.

8.5 Molecular recipe for neural crest cell fate

Within the last decade, genome sequences of a broad spectrum of species (e.g. chick (Hillier et al., 2004), opossum (Mikkelsen et al., 2007), armadillo (Lindblad-Toh et al., 2011), and lizard (Alföldi et al., 2011)) have enabled evolutionary comparisons across

vertebrates, considerably increasing the fidelity with which conserved regions across species can be predicted. Detailed cis-regulatory analysis, through a combination of phylogenomics and high-throughput sequencing-based approaches, has enabled the identification and dissection of active tissue-specific enhancers. Using genomic alignment between multiple vertebrate species, conserved non-coding regions at the loci of neural crest specifier genes *Sox10* (Betancur et al., 2011), *FoxD3* (Simões-Costa et al., 2012), and *Ets1* (Barenbaum and Bronner, 2013) have been identified. Not only have these enhancers provided the means of establishing positive and negative links between downstream factors and their direct transcriptional inputs, but in genetically intractable systems such as the chick, they have allowed the isolation of pure populations of neural crest cells. In Chapters 6 and 7, I demonstrated how these cis-regulatory elements can be applied to elaborate our understanding of the regulatory differences between different neural crest populations originating at distinct axial levels.

8.5.1 Cranial neural crest

Following induction of the neural crest at the neural plate border, the cranial neural crest is the first population that undergoes delamination from the dorsal neural tube. These cells will give rise to diverse cell types in the developing head, including much of the craniofacial cartilage and bone, and neurons and glia of the cranial ganglia (Le Douarin, 1982). Their ability to form cartilage is unique amongst neural crest populations, such that the trunk neural crest lacks the ability to form ectomesenchymal derivatives (Nakamura and Ayer-Le Lievre, 1982). This raised the possibility that inherent transcriptional differences exist between cranial and trunk neural crest cells.

Simões-Costa and Bronner took advantage of cranial versus trunk neural crest specific enhancers to isolate pure neural crest populations for transcriptional profiling (Simões-Costa and Bronner, 2016). Accordingly, they identified transcription factors enriched in the cranial neural crest compared to the trunk neural crest: *Brn3c*, *Lhx5*, *Dmbx1*, *Ets1*, *Sox8*, and *Tfap2b*.

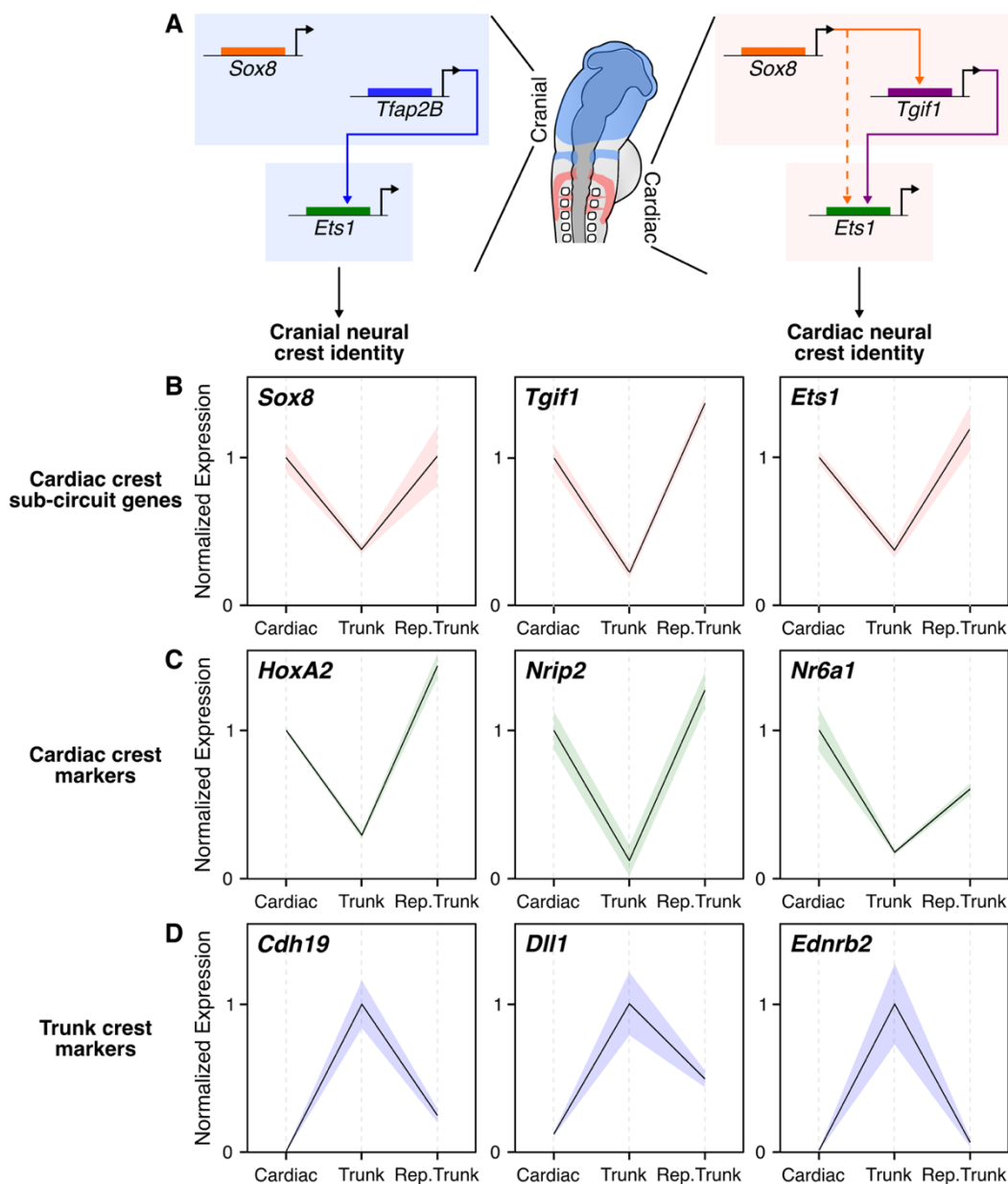


Figure 3. Transcriptional subcircuits and neural crest identity. **A.** Slight changes in transcriptional circuitry can alter neural crest identity. The ectopic expression of a cranial “subcircuit” comprising of the transcription factors *Sox8*, *Tfap2b*, and *Ets1* can confer onto trunk neural crest cells the ability to form cartilage. However, the ectopic expression of a cardiac “subcircuit” where *Sox8* and *Ets1* work with *Tgif1* instead of *Tfap2b* imbues cardiac-like migration and differentiation ability onto trunk neural crest cells. **B-D.** Normalized expression for the cardiac subcircuit genes *Sox8*, *Tgif1*, and *Ets1* (B), genes enriched in wildtype cardiac neural crest cells *HoxA2*, *Nrip2*, and *Nr6a1* (C), and genes enriched in wildtype trunk neural crest cells (D) following expression of the cardiac subcircuit in the trunk neural crest. The expression of cardiac markers was upregulated in “reprogrammed” trunk neural crest, while the expression of the trunk neural crest markers was downregulated. Data from Gandhi et al. (2020). Shaded area in B, C, and D represents standard error of the mean.

These factors comprised a “cranial-specific” subcircuit, with *Brn3c*, *Lhx5*, and *Dmbx1* expressed in the neural plate border and *Sox8*, *Tfap2b*, and *Ets1* expressed in the premigratory and emigrating cranial neural crest [Figure 3A]. Through a series of loss-of-function and promoter-ChIP experiments, they established regulatory linkages between these factors. Importantly, ectopic expression of the downstream factors *Ets1*, *Sox8*, and *Tfap2b* in the trunk neural crest resulted in upregulation of genes associated with the chondrogenic potential of cranial neural crest cells, such as *Alx1* and *Runx2*, and concomitant downregulation of trunk neural crest genes, such as *Dbx2* and *Hes6*. When “reprogrammed” trunk neural crest tissue was transplanted into the cranial region, the cells gave rise to ectopic cartilage nodules, as identified by the expression of COL9A. This was the first direct demonstration of how neural crest cells from other axial levels can be successfully reprogrammed into a cranial-like fate (Simões-Costa and Bronner, 2016).

8.5.2 Cardiac neural crest

Like cranial neural crest, the cardiac neural crest also has a unique developmental potential—the ability to form the ectomesenchymal derivatives of the developing heart, most notably the aorticopulmonary septum that septates the outflow tract into the pulmonary and aortic trunks (Kirby et al., 1983). When trunk neural crest from a quail embryo was grafted in place of the cardiac neural crest in a chick embryo, the neural crest cells failed to migrate into the heart, resulting in cardiovascular anomalies consistent similar to cardiac neural crest ablation (Kirby, 1989).

In Chapter 7, I used specific neural crest enhancers to isolate pure neural crest populations for bulk RNA-seq to identify transcription factors that were enriched in the cardiac neural crest compared to the trunk neural crest (Gandhi et al., 2020b). While many of the enriched transcription factors were shared with the cranial neural crest (Simões-Costa et al., 2014), one transcription factor, *Tgif1*, was specifically expressed in the delaminating cardiac neural crest in the dorsal hindbrain. This was particularly interesting since it correlates with the time at which the neural crest cells from this axial

level become restricted to a cardiac fate (Ezin et al., 2011). Loss of *Tgif1* resulted in a downregulation of cardiac neural crest markers, without affecting the expression of pan neural crest genes. We posited that *Tgif1* may cooperate with other transcription factors, and found that it worked together with *Sox8* and *Ets1* in a cardiac-crest-specific subcircuit. *Sox8* is a member of the SoxE family of genes and *Ets1*, a member of the ETS-domain transcription factor family, has been implicated in Jacobsen syndrome (11q-), a disease often associated with ventricular septal defects (Grossfeld et al., 2004; Ye et al., 2009). In addition, *Sox10* expression is lost in *Ets1*^{-/-} mutant mice, and embryos suffer from large membranous interventricular septal defects in the absence of other structural heart defects (Ye et al., 2016).

CRISPR-Cas9-mediated knockouts of *Sox8*, *Ets1*, and *Tgif1* allowed us to assemble the cardiac crest gene regulatory subcircuit where *Sox8* and *Tgif1* were expressed in premigratory cardiac neural crest cells, and regulated the expression of *Ets1* in migratory cardiac neural crest cells [Figure 3A]. Through transcription factor motif mutational analysis, we found that the interactions between *Sox8* and *Tgif1*, and between *Tgif1* and *Ets1*, were direct. Ectopic expression of this circuit [Figure 3B] in the trunk resulted in “reprogramming” of the trunk neural crest as assayed by upregulation of cardiac neural crest genes [Figure 3C] and downregulation of endogenous trunk neural crest markers [Figure 3D]. Transplantation of these reprogrammed trunk neural crest cells in place of ablated cardiac neural crest, resulted in neural crest cells following cardiac-like migration pathways and populated branchial arches 3 and 4. Moreover, when the grafted embryos developed to stages of normal outflow tract septation, the reprogrammed trunk neural crest cells populated the aorticopulmonary septum. This shows that expression of the cardiac subcircuit imbued a “cardiac-like” identity onto the trunk neural crest (Gandhi et al., 2020b).

8.5.3 Vagal neural crest

Vagal neural crest, of which cardiac neural crest is a subset, originates in the dorsal neural tube adjacent to somites 1-7 and gives rise to a diverse array of cell types (Le

Douarin and Teillet, 1973; Epstein et al., 1994) [Figure 2]. Errors in their development can lead to severe birth defects, including Hirschsprung disease, which presents with a lack of enteric neurons in the distal portion of the gut (Iwashita et al., 2003). In spite of its importance for proper human gut development, the genetic circuitry underlying vagal neural crest fate specification was not well known previously. Ling and Sauka-Spengler performed a comprehensive genome-wide study to identify the genetic and epigenetic mechanisms that orchestrate the diversification of vagal neural crest cells into enteric derivatives (Ling and Sauka-Spengler, 2019). By profiling the vagal population at a single-cell resolution using scRNA-seq, they uncovered three distinct lineages derived from these precursors: neural, neuronal, and mesenchymal. Each of these lineages expressed distinct set of molecular markers, including *Sox10* and *FoxD3* for neural, *Sox3* and *Elavl4* for neuronal, and *Prrx1* and *Twist1* for mesenchymal. The chromatin accessibility data collected across different time points revealed that the Tfp2, Sox, Hbox, and bHLH families of transcription factors were involved in diversification of vagal crest derivatives. These results, together with their single-cell data, provided a unique perspective on vagal neural crest colonization of the gut, with a migrating heterogeneous population of vagal neural crest cells epigenetically predetermined to form enteric glia, neurons, and a previously overlooked mesenchymal population within the gut. Ling and Sauka-Spengler's proposed model that vagal neural crest cells, regardless of their axial level of origin, are predestined to form derivatives of the gut, runs contrary to the results observed by Barlow et al., (2008), who found that while cells adjacent to somite 3 are capable of giving rise to enteric neurons, cells adjacent to somite 1 primarily migrate into the heart.

8.6 To go with your heart or your gut?

While cardiac neural crest cells migrate into the developing heart where they assume a mesodermal-like identity, vagal neural crest cells migrate into the developing enteric nervous system where they give rise to the sympathetic, parasympathetic, and enteric neurons. The mechanisms of these cell fate choices have long been debated. While some groups have proposed that cardiac neural crest cells are bipotent precursors with the ability of giving rise to derivatives in both the heart and the gut, others have

proposed that heart-specific and gut-specific precursors are intermingled within the vagal neural crest domain (Espinosa-Medina et al., 2017; Kuo and Erickson, 2011).

Tang et al. (2021) approached this question using replication incompetent avian retroviruses that have been established as a versatile tool for lineage tracing (Tang et al., 2019a), gene editing, and clonal analysis in chick embryos. Using a combination of different retroviruses encoding unique combinations of fluorescent proteins and subcellular localization signals, they demonstrated that cardiac neural crest cells are indeed multipotent, with individual cardiac neural crest cells having a broad developmental potential to give rise to smooth muscle cells, neurons and glia. To address the possibility that premigratory neural crest cells residing in the caudal hindbrain are multipotent and able to migrate to both the heart and the gut, they performed single-cell photoconversion of sparsely labeled premigratory cardiac neural crest cells. Following photoconversion, daughter cells migrated extensively towards both the pharyngeal pouches and the developing gut. Not only were clonally-related cells found within the dorsal neural tube, glossopharyngeal nerve complex, pharyngeal arch arteries, and the outflow tract, tissues that are derived from the cardiac neural crest, but several clonally derived cells were also found in the developing gut. The neural tube adjacent to somites 4-7 was not found to be retrovirally labeled, suggesting that the clones found in the gut originated within the cardiac axial level. Slice culture-based live imaging of virally-labeled cardiac neural crest cells revealed that following delamination from the dorsal neural tube, neural crest cells intermixed in the circumpharyngeal ridge. Interestingly, a subset of the cells migrating into the sixth pharyngeal pouch instead migrated caudally to colonize the gut. Tang et al. further characterized the molecular cues that controls migration into the heart versus the gut. When they expressed a dominant negative form of the receptor CXCR4, cardiac neural crest cells failed to migrate into the outflow tract. However, the proportion of cells that migrated into the gut remained unchanged, suggesting that CXCR4-SDF1-based chemoattraction is necessary to bias a cardiac crest precursor towards the heart. On the other hand, when a dominant negative form of Ret was expressed in premigratory cardiac neural crest cells, cells migrated to the developing

outflow tract, but failed to colonize the gut. Overall, these results are complementary to phenotypes observed in mice that lack proper CXCR4-SDF1 (Escot et al., 2013) or RET-GDNF (Bogni et al., 2008) signaling. The former resulted in DiGeorge Syndrome-like malformations, whereas the latter resulted in a significant reduction in the number of enteric neurons.

While Tang et al. uncovered the signaling cues that attract cardiac neural crest cells in the heart or the gut, their work did not explore possible intrinsic parameters that might control this fate switch. Vincentz et al. (2013) employed *Wnt1^{Cre}* mice to target the bHLH transcription factor *Twist1* from cardiac neural crest cells, in an effort to dissect the principles that drive a mesodermal identity in cardiac neural crest derivatives as compared to an ectodermal identity in the vagal neural crest. Conditional deletion of *Twist1* in premigratory cardiac neural crest cells resulted in the formation of unusual cell aggregates within the outflow tract at the expense of the aorticopulmonary septum, resulting in completely penetrant persistent truncus arteriosus. These aggregates were cardiac-neural-crest-derived and expressed *Sox10* and the pan-neuronal marker *Tubb3*, as well as bona fide sympathetic ganglion neuronal markers such as *Phox2a*, *Phox2b*, and *Ascl1*. These data demonstrated that in the absence of *Twist1*, cardiac neural crest cells in the outflow tract turned on a neuronal at the expense of a smooth muscle program. Vincentz et al. then inactivated *Twist1* using the *Hand1^{Cre}* knock in allele. While the *Wnt1^{Cre}* driver line ablated *Twist1* in premigratory cardiac neural crest cells, the *Hand1^{Cre}* driver line deleted *Twist1* in post-migratory cardiac crest cells. In contrast to the highly penetrant OFT defect in the *Twist1*;*Wnt1^{Cre}* conditional knockouts, the *Twist1*;*Hand1^{Cre}* conditional knockouts were less penetrant, even though neuronal aggregates still formed in the outflow tract. Further investigation into the mechanism revealed that the ectopic neurogenesis in the outflow tract in a *Twist1* conditional knockout background was dependent on the paired-like homeobox gene *Phox2b*. In *Phox2b* null homozygotes mice, vagal neural crest cells migrate into the gut but fail to turn on neuronal markers, eventually undergoing premature apoptosis (Pattyn et al., 1999). When *Phox2b* gene was deleted in a *Twist1* knockout background, ectopic neurons in the outflow tract failed to develop,

suggesting that in cardiac neural crest cells, *Twist1* represses the activity of *Phox2b* to bias cardiac neural crest cells towards a smooth muscle fate. Consistent with this, Soldatov et al. (2019) examined the transcriptional profile of neural crest cells in the mouse embryo at a single cell resolution and found that *Twist1* was an important determinant of mesenchymal identity. Accordingly, *Twist1* overexpression in the trunk neural crest altered cell fate from neuronal to mesenchymal.

8.7 Epigenomic regulation of neural crest cell fate

Over the last decade, there has been interest in deciphering the gene regulatory network underlying neural crest development (Betancur et al., 2010b; Gammill and Bronner-Fraser, 2002; Martik and Bronner, 2017; Sauka-Spengler and Bronner-Fraser, 2008; Simões-Costa and Bronner, 2015). In addition to transcriptional circuitry, neural crest formation also relies on an ever changing epigenetic landscape that culminates in alterations in gene expression. This is achieved by chromatin remodeling complexes and chromatin-modifying enzymes such as DNA and histone methylases, demethylases, and acetylases, which orchestrate changes in gene expression (reviewed in (Hu et al., 2014)). Histone methylation has been associated with both transcriptional activation and repression. Whereas methylation of H3 lysines 4 and 36 (H3K4me2/me3 and H3K36me2/3) are enriched in transcriptionally active euchromatic regions, H3 lysines 9 and 27 (H3K9me3 and H3K27me3) are located in repressed sites as well as associated with heterochromatin. Chromatin remodeler proteins, such as CHD7 and HMGA1, are critical for proper neural crest development. CHD7, an ATP-dependent helicase, has been shown to activate the expression of neural crest specifier genes like *Sox9* and *Twist1* through direct regulation of their enhancers (Bajpai et al., 2010). Mutations in the CHD7 locus have been associated with CHARGE syndrome, a rare congenital disorder that causes defects in neural crest development. As I discussed in Chapter 6, HMGA1, which acts upstream of *Pax7* and regulates a neural versus neural crest fate switch in neural plate border precursors, functions as a Wnt-activator in the dorsal neural tube (Gandhi et al., 2020a). Maintaining appropriate levels of Wnt-signaling is critical for proper

emigration of neural crest cells from the neuroepithelium (Burstyn-Cohen et al., 2004; Rabadán et al., 2016).

8.7.1 Non-coding RNAs

The post-transcriptional circuitry that governs neural crest fate determination has remained poorly understood. Recent evidence suggests potential roles for non-coding RNAs and, in particular, microRNAs (miRNAs), small non-coding RNA molecules that post-transcriptionally regulate gene expression by binding to the 3' UTR and/or the coding sequence of their target genes. Neural crest-specific knockout of Dicer in mice results in craniofacial (Nie et al., 2011) and cardiovascular defects (Huang et al., 2010), including ventricular septal defects. Interestingly, there are distinct effects of losing Dicer on neural crest cells originating from different axial levels; loss of Dicer caused premature cell death in cranial neural crest cells, whereas its loss in the cardiac neural crest altered their migration and patterning of the aortic arch arteries and the outflow tract.

To examine the possible role of miRNAs in establishing the neural crest formation, Xi et al. (2017) took advantage of an *in vitro* embryonic stem cell model to characterize the function of miRNAs in the fate switch between neural and neural crest. They discovered that the miRNA-29b was upregulated in differentiated neural tube cells compared to differentiated neural crest cells. Using a miRNA sponge strategy to reduce miRNA-29b-mediated repression of its target genes, they demonstrated its necessity for neural tube differentiation. The expression of neural tube markers such as *Pax6*, *Nestin*, and *Tubb3* were downregulated, with no change in the levels of pluripotency marker genes such as *Oct4* and *Nanog*. Conversely, overexpression of miRNA-29b resulted in an increased proportion of neural tube cells derived from mESCs at the expense of the neural crest lineage. It was previously known that miRNA-29b targeted the DNMT family members *Dnmt3a* and *Dnmt3b*. Consequently, they assayed for DNMT3A/3B protein levels in miRNA-29b sponge and overexpression backgrounds and observed that DNMT3A but not DNMT3B protein was increased and reduced, respectively. Indeed, knocking down the levels of *Dnmt3a* in a miRNA-29b-sponge background rescued neural

tube differentiation whereas overexpression rescued neural crest differentiation. The transcription factor POU3F1, which has been previously shown to activate neural lineage genes resulting in fate commitment towards the neural lineage (Zhu et al., 2014), was found to act upstream of miRNA-29b in both mouse and human cells.

While the results of this study were entirely *in vitro*, they are consistent with previous *in vivo* literature. For example, in avian embryos, Dnmt3a has been shown to be important for the cell fate decision between neural versus neural crest lineages, where it actively represses the levels of *Sox2* and *Sox3*, priming the cells towards a neural crest fate (Hu et al., 2012). Loss of DICER prior to neural crest specification also results in a fate switch of neural crest precursors into neural plate cells (Copeland and Simões-Costa, 2021), likely due to an accumulation of SOX2 protein. These results suggest post-transcriptional regulators function synergistically with the molecular circuitry to control bifurcation of the neural and neural crest lineages from neural plate border precursors.

8.7.2 RNA-binding proteins

In addition to chromatin modifiers, RNA binding protein partners of non-coding RNAs play central regulatory roles in modulating transcriptional and post-transcriptional gene expression. Hutchins et al. recently demonstrated that the RNA-binding protein HuR is required for proper neural crest specification (Hutchins et al., 2020). Loss of HuR resulted in a downregulation of *FoxD3*, its activator *Axud1* (Simões-Costa et al., 2015), and the secreted molecule Draxin (Hutchins and Bronner, 2018, 2019), without affecting the relative proportions of neural crest precursors in the neural plate border. The authors suggest that HuR associates with and stabilizes *Draxin* mRNA, as evidenced by the enrichment of *Draxin* transcripts bound to the HuR ribonucleoprotein complex. Moreover, overexpression of *Draxin* in a HuR knockdown background rescued neural crest specification, suggesting a direct mechanism by which RNA-binding proteins can regulate key processes during early neural crest development.

8.8 Genomics and neural crest cell fate

The advent of sequencing technologies that permit characterization of the transcriptional (RNA-seq) and epigenetic (ATAC-seq) landscape at the single-cell level has opened up the possibility to glean a near complete transcriptional program of individual cells at unprecedented resolution. Moreover, computational approaches that enable comparison of cell profiles over time provide a window into understanding cell trajectories as they move from an undifferentiated to a differentiated state. In this manner, genomic approaches can help understand cell fate choices. In this section, we discuss how the advent of new sequencing technologies has facilitated our understanding of how multipotent neural crest precursors may acquire a unique ectomesenchymal identity, and also revealed heterogeneity that may be inherent within the population.

8.8.1 Acquisition of neural crest identity

Historically, gene regulatory interactions in the neural crest were studied using a bottom-up approach, where individual candidate genes were targeted and their effect on downstream effector genes was assayed in an effort to establish regulatory linkages between them (Betancur et al., 2010b; Gammill and Bronner-Fraser, 2003; Sauka-Spengler and Bronner-Fraser, 2008). Moreover, identification of cis-regulatory elements was restricted to intergenic regions that were highly conserved between related species (Barembaum and Bronner, 2013; Betancur et al., 2011; Simões-Costa et al., 2012). The advent of ATAC-seq at the bulk and single-cell level has greatly expanded identification and dissection of cis-regulatory elements that are critical for normal neural crest development.

Using a combination of epigenomic and transcriptional profiling coupled with perturbations, Williams et al. (2019) provided the first comprehensive global gene regulatory network underlying the avian cranial neural crest development. They identified novel neural crest transcriptional inputs, enhancers [Figure 4A-D] and super-enhancers

[Figure 4A] that contribute to neural crest cell fate decisions to provide a thorough analysis of the regulatory interactions that help shape cranial neural crest identity.

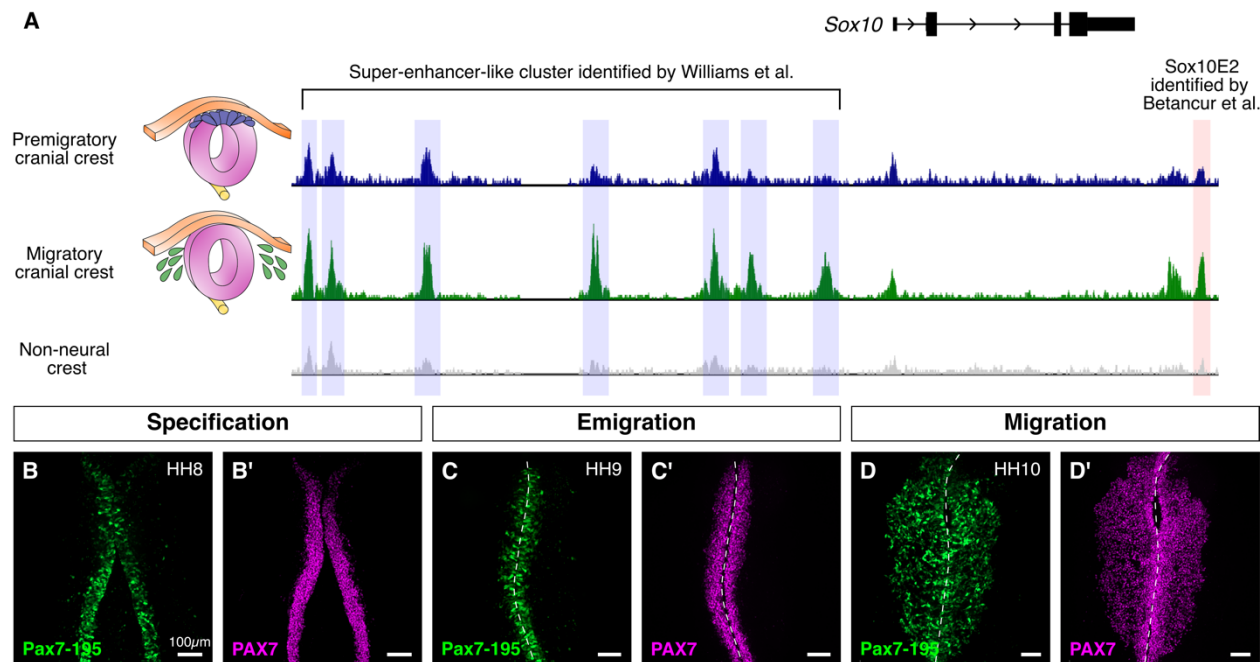


Figure 4. Application of high-throughput sequencing technologies to decipher gene regulatory networks. A. The genomic locus of the avian neural crest specifier gene *Sox10*. Cranial neural crest cells isolated by Fluorescence-activated cell sorting (FACS) at premigratory and migratory stages for characterization of their chromatin accessibility using ATAC-seq. The cis-regulatory landscape surrounding *Sox10* contained a super-enhancer-like cluster proximal to the *Sox10* promoter. This super-enhancer region was upstream of the *Sox10* enhancer element E2, which was identified by (Betancur et al., 2010) using sequence conservation between vertebrates. **B-D'**. An example of an intronic enhancer for the gene *Pax7*. This enhancer element recapitulates endogenous PAX7 expression in the dorsal neural folds during neural crest specification and emigration, as well as in migratory cranial neural crest cells. Raw data for (A) from (Williams et al., 2019).

Chromatin-modifying enzymes and remodelers are not the only class of genes that can modulate chromatin accessibility. A class of transcription factors, referred to as pioneer factors, has recently gained attention (Iwafuchi-Doi and Zaret, 2016). Pioneer factors are proteins that bimodally function as transcriptional activators as well as chromatin modifiers within a given genetic context. More importantly, they can selectively bind to condensed chromatin prior to the occupation of these cis-regulatory elements by other transactivation complexes. FoxA and GATA factors were among the first group of gene families that were identified as “pioneer factors” in the context of liver development (reviewed in (Zaret and Carroll, 2011)). In the neural crest, Lukoseviciute et al. (2018)

established the role of the neural crest specifier gene *foxd3* as a pioneer factor. Using zebrafish as a model, they demonstrated that loss of *foxd3* in premigratory neural crest cells resulted in a broad downregulation of neural crest specification markers, including *sox10*, *snai1b*, *sox9b*, and *twist1b*. However, at migratory stages, they observed upregulation of genes associated with neural crest differentiation into ectomesenchymal (*bmp5/6*, *col2a1b*) and neuronal (*robo4*, *slit1a/b*) derivatives. These genes were absent in wild type migratory neural crest cells, suggesting that *foxd3* functionally represses a premature differentiation program in migrating neural crest cells. Enhancers in the vicinity of several genes that were differentially up- or down-regulated in *foxd3* mutant embryos were directly occupied by *foxd3*. Moreover, in contrast to the depleted accessibility of these enhancers in the absence of *foxd3*, ectopic expression of *foxd3* resulted in an increase in chromatin accessibility. Together, the results suggest that activation of the neural crest program and repression of the differentiation program occurs simultaneously in a *foxd3*-dependent mechanism.

As another example of pioneer transcription factor activity in neural crest development, Rothstein and Simões-Costa (2020) explored the heterodimerization of TFAP2 family of transcription factors as a regulatory mechanism for neural crest specification. One of five paralogs, *Tfap2a* is important for both neural crest induction and neural crest specification (De Croz e et al., 2011; Knight et al., 2003; Luo et al., 2003), first expressed in neural crest precursors in gastrula stage embryos as a member of the neural plate border specification gene regulatory network. There, its expression overlaps with *Tfap2c*. As neurulation proceeds and presumptive neural crest cells are localized within the dorsal neural tube, the expression of *Tfap2b* comes on in the neural crest, while *Tfap2c* is downregulated. By mapping the regulatory targets of *Tfap2a*, *Tfap2b*, and *Tfap2c* using Cut&Run (Skene and Henikoff, 2017), Rothstein and Simões-Costa proposed a model whereby *Tfap2a* associates with *Tfap2c* to first control neural crest induction. Once neural crest induction is complete, *Tfap2a* switches its dimerizing partner to interact with *Tfap2b* to drive neural crest specification. As a case in point, when the coding sequence of *Tfap2b* was expressed using a *Tfap2a* enhancer element that

specifically functions in the neural crest, the timing of neural crest specification was altered, resulting in premature activation of neural crest specifier genes *Sox9* and *Snai2*. These results demonstrate that pioneer transcription factors can add additional layers of regulation over cell state transitions during neural crest development.

Identification of open enhancers that regulate expression of important cell fate determinants and may be critical for tissue morphogenesis is particularly important given that mutations in non-coding regions can result in their inactivation. In fact, several congenital birth defect-causing mutations, including neurocristopathies, exist in the non-coding regions of the genome, which accounts for more than 98% of the human genome. For example, deletions in the non-coding regions of the SRY-related HMG box transcription factor *Sox9*, an important member of the neural crest specification gene regulatory network, have been associated with Pierre Robin Sequence (PRS), which results in an underdevelopment of the lower jaw.

Long et al. (2020) used a combination of *in vitro* and *in vivo* methods to classify clusters of enhancers within the *Sox9* topologically-associating domain (TAD). These enhancers were selectively accessible within cranial-neural-crest-derived human craniofacial tissues, and their activity coincided with the onset of *Sox9* expression that resulted in the transition of Human embryonic stem cells into cranial neural crest cells. Using Capture-C, they presented evidence for long-range interactions between the *Sox9* promoter and the clusters of *Sox9* enhancers. Using a luciferase reporter gene assay, they demonstrated selective activity of these enhancers in neural crest cells, as compared to undifferentiated hESCs or even neural crest cells differentiated into chondrocytes. At E9.5 and E11.5, the enhancers recapitulated the expression of *Sox9* within the mandibular branchial arch. One of these enhancers was evolutionarily conserved across several vertebrate species, and ChIP-seq experiments revealed that the bHLH transcription factor *Twist1* regulated its activity in a sequence-dependent manner. Finally, using the *Wnt1^{Cre2}* mice for selective knockout of *Sox9* and/or the mouse orthologous enhancer, they showed that loss of the enhancer exacerbated defects in mandibular arch development in a dose-dependent manner.

8.8.2 Acquisition of a broad developmental potential

The early blastula segregates into the three germ layers designated ectoderm, mesoderm, and endoderm. While neural crest cells are derived from the ectodermal layer, they have the unique ability to form both ectodermal (e.g. neurons, glia) and mesodermal (e.g. cartilage, bone, smooth muscle of the cardiac outflow tract) type derivatives (Le Douarin, 1982). For this reason, the neural crest is sometimes referred to as the “fourth germ layer” (Le Douarin and Dupin, 2014; Glenn Northcutt, 2005). What underlies this broad developmental potential [Sidebar 2]? Two possible hypotheses have been proposed: 1) retention of developmental programs active in the early blastula, hereby referred to as the “retention model,” or 2) redeployment of pluripotency programs after neural crest induction, hereby referred to as the “reacquisition model.”

8.8.2.1 The retention model

Buitrago-Delgado et al. (2015) argued in favor of the retention model hypothesis, positing that neural crest cells retain a subset of genetic programs that are otherwise active in blastula cells of the early *Xenopus* embryo. Through *in situ* hybridization, they found that the neural crest gene regulatory network factors such as *Tfap2*, *Ets1*, and *FoxD3* were co-expressed with the core pluripotency markers *Oct60* (*Pou5F3.3*), *Sox3*, and *Vent2*. As the embryo developed, the expression of *Vent2* was retained in gastrula stages, whereas *Oct60* and *Sox3* were downregulated. When they knocked down the neural crest gene *Snai1* in the animal pole of blastula embryos, the expression of other neural crest markers as well as pluripotency genes was lost, suggesting that neural crest genes are required to maintain expression of pluripotency factors in the inducing neural crest. Loss of *Snai1* also resulted in reduced developmental potential of the animal pole, such that *Snai1* mutant cells failed to express markers associated with either the mesoderm derivatives (*Brachyury* and *MyoD*) or endodermal derivatives (*Endodermin* and *Sox17*). Snail proteins are absent from the endodermal lineage, therefore linking the loss of *Snai1* to a general lack of potency. Conferring a neural plate border identity through the expression of *Pax3* and *Zic1* onto animal pole cells expanded their

developmental potential at gastrula stages, in contrast to untreated animal pole cells, which lost the ability to form mesodermal and endodermal derivatives at gastrula stages. Finally, the treatment of neural plate border cells isolated from neurula stage embryos with high concentrations of activin was sufficient to induce expression of endodermal markers *Endodermin* and *Sox17*, despite the fact that neural crest cells do not endogenously form endodermal derivatives. Through this work, Buitrago-Delgado et al. (2015) demonstrated that neural crest cells maintain their broad developmental potential by retaining programs normally active at blastula stages.

In order to interrogate the lineage relationships between early embryonic precursors and their progeny, Briggs et al. (2018) took advantage of their optimized microfluidics method to profile 136,966 single-cell transcriptomes obtained from 10 individual timepoints representing early *Xenopus* development, with stages ranging from zygotic genome activation to early organogenesis. Using a computational approach, they demonstrated that the fate choices can be mapped as a tree-like model. Rather than step-wise transitions to distinct cell states, they found several transitions occurring as a transcriptional continuum. Their dataset uncovered 87 distinct cellular identities, out of which 69 corresponded to known anatomical states. This dataset also allowed them to investigate the correlation between computational occurrence of a cell state and experimental evidence for when the state is first observed. As a consequence, they identified several cell states that appeared in their dataset much earlier than previously recognized. For example, an endothelial/hemangioblast progenitor appeared at stage 18, as compared to previously published work, which suggested that the hemangioblast cell first appeared at stage 26 (Walmsley et al., 2002). By contrast, experimental evidence suggested that endothelial cells only appeared at stage 31 (Liu et al., 2008). They also provided insights into the concept of multi-lineage priming (Laslo et al., 2006), where uncommitted cells co-express transcription factors associated with multiple terminal cell fates, similar to the co-expression of neural (*Sox2*) and neural crest (*Pax7*) markers at the neural plate border. Interestingly, the depth of their data allowed them to revisit the question of what imbues neural crest cells with their broad developmental potential. They

supplemented their whole-organism data with cells dissected from the neural plate border to enrich neural crest precursors.

In contrast to the results of Buitrago-Delgado et al. (2015), Briggs et al. (2018) failed to uncover a cluster of cells with enriched expression of pluripotency markers. Instead, their data suggested that the transition from a blastula to gastrula stage embryo follows conventional trajectories, with the pluripotent blastula transitioning through intermediate neuroectodermal states before committing to the neural crest lineage. Interestingly, they found that the pluripotency genes were not specifically expressed in the neural plate border but were broadly present across all three germ layers. While this goes against the retention model, one caveat remains the reliance on transcriptional data to understand cell fate choices and developmental trajectories. It is possible that additional layers of non-transcriptional regulation, such as epigenetic modifications of enhancers regulating the expression of pluripotency genes, or post-translational modifications of pluripotency proteins, could still allow blastula cells to retain a pluripotency state following induction of the neural crest. However, as far as a transcriptional program underlying the retention model is concerned, they found little evidence to support it.

8.8.2.2 The reacquisition model

In a recent study, Zalc et al. (2021) revisited the “acquisition model” of neural crest cells’ broad developmental potential. Using *Wnt1^{Cre};Rosa26^{TdTomato}* mice, they collected neural crest cells at four distinct timepoints of development ranging from four to ten somites stage, corresponding to cranial neural crest precursors in the dorsal neural folds (four somites), and delaminating (six somites), migrating (eight somites), and differentiating (ten somites) cranial neural crest. As expected, cells isolated from the dorsal neural folds expressed markers characteristic of specified neural plate border cells, with high expression of neural markers such as *Sox2*, *Otx2*, and *Gbx2*. Six somite stage was marked by the onset of neural crest specifier genes *FoxD3*, *Sox10*, *Ets1*, and *Twist1*. Cells belonging to the eight and ten-somite stage expressed migratory neural crest

markers, and segregated into committed lineages, including ectomesenchymal, glial, and neural progenitors. While cells from the four-somite stage further segregated into anterior and posterior populations, this segregation was lost once the cells delaminated, suggesting that following their epithelial to mesenchymal transition, the cells represent a homogenous population of migrating neural crest cells that diversify into distinct lineages in response to specific environment cues.

Interestingly, cells within the earliest $Wnt1^{Cre+}$ cranial neural crest precursor cluster expressed pluripotency genes *Oct4*, *Sox2*, *Nanog*, and *Klf4*. *Oct4* levels were distinctively higher than the other three factors, although the expression of *Nanog* and *Klf4* was restricted to this cell cluster. At the six-somite stage, *Oct4* was notably downregulated within the $Wnt1^{Cre}/Otx2+$ cells, which mark the anterior boundary of the neural plate border. On the other hand, *Oct4* expression was increased within the $Wnt1^{Cre}/Gbx2+$ cells, which mark the posterior boundary of the neural plate border. This dynamic regulation of *Oct4* within the dorsal neural folds occurred in an anterior-posterior wave, coinciding with the timing of cranial neural crest delamination. Spatiotemporal expression of *Oct4* was assayed using *Oct4*-GFP embryos, which revealed that while *Oct4* was expressed in the whole epiblast at E7.5, it was absent in the developing head fold. Following somitogenesis, *Oct4* expression re-appeared in the most anterior part of the embryo. They also performed lineage tracing using an inducible $Oct4^{CreER/+};Rosa26^{TdT/+}$ line and showed that the proportion of cranial neural crest derivatives labeled directly correlated with the stage at which tamoxifen was administered, such that induction at one-somite stage positively labeled cells in the frontonasal mass and branchial arch 1, whereas induction at six-somite stage only labeled cells within the branchial arches 1, 2, and the glossopharyngeal nerve complex. Diphtheria toxin-mediated ablation of *Oct4* between E7.5 and E8 resulted in a complete absence of the frontonasal mass, even though neural folds were present in the embryos, mimicking the phenotype observed in avian embryos following the extirpation of the cranial neural crest (D'amico-Martel and Noden, 1983; Noden, 1975). Consistent with the transient shift of *Oct4* expression along the anterior-posterior axis, ablation of *Oct4* at E8.5 had no effect on the frontonasal mass;

however, the posterior derivatives, such as the nasal processes, were absent. Loss of *Oct4* mainly resulted in a downregulation of genes associated with the ectomesenchymal potential of the cranial neural crest, such as *Sox9* and *A/x4*, with no effect on *Sox10* expression. ATAC-seq of *Oct4*+ cells revealed that the non-coding regions surrounding cranial neural crest-specific cis-regulatory elements were accessible at six-somite stage, even though the expression of those genes peaked at ten-somite stage, as would be expected if the enhancers regulating the expression of these genes were primed to drive gene expression prior to when the genes were functionally relevant. Cis-regulatory priming has been observed across several systems (Huang et al., 2007; Laslo et al., 2006), and demonstrates the importance of following a multimodal approach to understand how transcriptional activation coordinates with chromatin accessibility to drive cell fate decisions.

The finding that the premigratory neural crest domain in mice expresses pluripotency factors is consistent with reports in the chick that reveal a neural crest stem cell niche in the dorsal midbrain with high expression of neural crest genes, pluripotency factors, and lineage markers (Lignell et al., 2017). Similarly, profiling of zebrafish *foxd3* positive cells revealed an early pluripotency signature that is down-regulated and then re-expressed in neural crest precursors prior to migration (Lukoseviciute et al., 2018). These results may suggest that the reacquisition model may reflect a pan-vertebrate trait.

8.9 Conclusions

This is an exciting time in developmental biology, when new methodologies have opened up the possibility to explore developmental cell fate choices at unprecedented resolution and across numerous species. The neural crest represents an interesting cell type for this type of analysis due to its broad developmental potential, extensive migratory ability and importance from a clinical perspective. In particular, the cranial and cardiac/vagal neural crest give rise to numerous cell types that are prone to mistakes leading to debilitating birth defects. The use of modern genomic approaches has allowed an ever deeper examination of the mechanisms underlying neural crest development and

has opened up the possibilities to dig deeper into some of the fundamental questions in neural crest biology: What triggers the cell-fate decision at the neural plate border? What mechanistic differences govern collective versus individual cell migration of the neural crest? Are there molecular signatures that govern neural crest migration across different species? What triggers the compensatory response of neural crest cells? Can their stem cell-like properties play a role in tissue replacement therapy? With 150 years of neural crest research behind us and exciting emerging technologies in front of us, the next century promises to help unravel the answers to these enduring questions.

8.10 References

Ahrens, K., and Schlosser, G. (2005). Tissues and signals involved in the induction of placodal Six1 expression in *Xenopus laevis*. *Dev. Biol.* *288*, 40–59.

Albazerchi, A., and Stern, C.D. (2007). A role for the hypoblast (AVE) in the initiation of neural induction, independent of its ability to position the primitive streak. *Dev. Biol.* *301*, 489–503.

Alföldi, J., Di Palma, F., Grabherr, M., Williams, C., Kong, L., Mauceli, E., Russell, P., Lowe, C.B., Glor, R.E., Jaffe, J.D., et al. (2011). The genome of the green anole lizard and a comparative analysis with birds and mammals. *Nature* *477*, 587–591.

Bajpai, R., Chen, D.A., Rada-Iglesias, A., Zhang, J., Xiong, Y., Helms, J., Chang, C.P., Zhao, Y., Swigut, T., and Wysocka, J. (2010). CHD7 cooperates with PBAF to control multipotent neural crest formation. *Nature* *463*, 958–962.

Barembaum, M., and Bronner-Fraser, M. (2005). Early steps in neural crest specification. *Semin. Cell Dev. Biol.* *16*, 642–646.

Barembaum, M., and Bronner, M.E. (2013). Identification and dissection of a key enhancer mediating cranial neural crest specific expression of transcription factor, *Ets-1*. *Dev. Biol.* *382*, 567–575.

Barlow, A.J., Wallace, A.S., Thapar, N., and Burns, A.J. (2008). Critical numbers of neural crest cells are required in the pathways from the neural tube to the foregut to ensure complete enteric nervous system formation. *Development* *135*, 1681–1691.

Basch, M.L., Bronner-Fraser, M., and García-Castro, M.I. (2006). Specification of the neural crest occurs during gastrulation and requires Pax7. *Nature* *441*, 218–222.

Betancur, P., Bronner-Fraser, M., and Sauka-Spengler, T. (2010a). Genomic code for Sox10 activation reveals a key regulatory enhancer for cranial neural crest. *Proc. Natl Acad. Sci. USA* *107*, 3570–3575.

Betancur, P., Bronner-Fraser, M., and Sauka-Spengler, T. (2010b). Assembling Neural Crest Regulatory Circuits into a Gene Regulatory Network. *Annu. Rev. Cell Dev. Biol.* *26*, 581–603.

Betancur, P., Sauka-Spengler, T., and Bronner, M. (2011). A Sox10 enhancer element common to the otic placode and neural crest is activated by tissue-specific paralogs. *Development* *138*, 3689–3698.

Bockman, D.E., Redmond, M.E., Waldo, K., Davis, H., and Kirby, M.L. (1987). Effect of neural crest ablation on development of the heart and arch arteries in the chick. *Am. J. Anat.* *180*, 332–341.

Bogni, S., Trainor, P., Natarajan, D., Krumlauf, R., and Pachnis, V. (2008). Non-cell-autonomous effects of Ret deletion in early enteric neurogenesis. *Development* *135*, 3007–3011.

Briggs, J.A., Weinreb, C., Wagner, D.E., Megason, S., Peshkin, L., Kirschner, M.W., and Klein, A.M. (2018). The dynamics of gene expression in vertebrate embryogenesis at single-cell resolution. *Science* *360*.

Bronner-Fraser, M. (1986). Analysis of the early stages of trunk neural crest migration in avian embryos using monoclonal antibody HNK-1. *Dev. Biol.* *115*, 44–55.

Bronner, M.E., and LeDouarin, N.M. (2012). Development and evolution of the neural crest: An overview. *Dev. Biol.* *366*, 2–9.

Brunskill, E.W., Park, J.S., Chung, E., Chen, F., Magella, B., and Potter, S.S. (2014). Single cell dissection of early kidney development: Multilineage priming. *Development* *141*, 3093–3101.

Buitrago-Delgado, E., Nordin, K., Rao, A., Geary, L., and LaBonne, C. (2015). Shared regulatory programs suggest retention of blastula-stage potential in neural crest cells. *Science* *348*, 1332–1335.

Burns, A.J., Champeval, D., and Le Douarin, N.M. (2000). Sacral neural crest cells colonise aganglionic hindgut in vivo but fail to compensate for lack of enteric ganglia. *Dev. Biol.* *219*, 30–43.

Burstyn-Cohen, T., Stanleigh, J., Sela-Donenfeld, D., and Kalcheim, C. (2004). Canonical Wnt activity regulates trunk neural crest delamination linking BMP/noggin signaling with G1/S transition. *Development* *131*, 5327–5339.

Copeland, J., and Simões-Costa, M. (2021). Post-transcriptional tuning of FGF signaling mediates neural crest induction. *Proc. Natl Acad. Sci. USA* *117*, 33305–33316.

Couly, G.F., Coltey, P.M., and Le Douarin, N.M. (1992). The developmental fate of the cephalic mesoderm in quail-chick chimeras. *Development* *114*, 1–15.

Couly, G.F., Coltey, P.M., and Le Douarin, N.M. (1993). The triple origin of skull in higher vertebrates: A study in quail-chick chimeras. *Development* *117*, 409–429.

Creazzo, T.L., Godt, R.E., Leatherbury, L., Conway, S.J., and Kirby, M.L. (1998). Role of Cardiac Neural Crest Cells in Cardiovascular Development. *Annu. Rev. Physiol.* *60*, 267–286.

De Croz , N., Maczkowiak, F., and Monsoro-Burq, A.H. (2011). Reiterative AP2a activity controls sequential steps in the neural crest gene regulatory network. *Proc. Natl Acad. Sci. USA* 108, 155–160.

D'amico-Martel, A., and Noden, D.M. (1983). Contributions of placodal and neural crest cells to avian cranial peripheral ganglia. *Am. J. Anat.* 166, 445–468.

Davidson, E.H. (1991). Spatial mechanisms of gene regulation in metazoan embryos. *Development* 113, 1–26.

Le Douarin, N.M. (1982). The neural crest, source of mesenchymal cells. *The Neural Crest* 54–86.

Le Douarin, N.M., and Dupin, E. (2014). The Neural Crest, a Fourth Germ Layer of the Vertebrate Embryo: Significance in Chordate Evolution. In *Neural Crest Cells: Evolution, Development and Disease*, pp. 3–26.

Le Douarin, N.M., and Kalcheim, C. (1982). *The Neural Crest*.

Le Douarin, N.M., and Teillet, M.A. (1973). The migration of neural crest cells to the wall of the digestive tract in avian embryo. *J. Embryol. Exp. Morphol.* 30, 31–48.

Le Douarin, N.M., and Teillet, M.A. (1974). Experimental analysis of the migration and differentiation of neuroblasts of the autonomic nervous system and of neurectodermal mesenchymal derivatives, using a biological cell marking technique. *Dev. Biol.* 41, 162–184.

Dupin, E., Creuzet, S., and Le Douarin, N.M. (2006). The contribution of the neural crest to the vertebrate body. In *Advances in Experimental Medicine and Biology*, pp. 96–119.

Epstein, M.L., Mikawa, T., Brown, A.M.C., and McFarlin, D.R. (1994). Mapping the origin of the avian enteric nervous system with a retroviral marker. *Dev. Dyn.* 201, 236–244.

Escot, S., Blavet, C., Härtle, S., Duband, J.L., and Fournier-Thibault, C. (2013). Misregulation of SDF1-CXCR4 signaling impairs early cardiac neural crest cell migration leading to conotruncal defects. *Circ. Res.* *113*, 505–516.

Espinosa-Medina, I., Jevans, B., Boismoreau, F., Chettouh, Z., Enomoto, H., Müller, T., Birchmeier, C., Burns, A.J., and Brunet, J.F. (2017). Dual origin of enteric neurons in vagal Schwann cell precursors and the sympathetic neural crest. *Proc. Natl Acad. Sci. USA* *114*, 11980–11985.

Ezin, A.M., Sechrist, J.W., Zah, A., Bronner, M., and Fraser, S.E. (2011). Early regulative ability of the neuroepithelium to form cardiac neural crest. *Dev. Biol.* *349*, 238–249.

Fedele, M., Fidanza, V., Battista, S., Pentimalli, F., Klein-Szanto, A.J.P., Visone, R., De Martino, I., Curcio, A., Morisco, C., Del Vecchio, L., et al. (2006). Haploinsufficiency of the *Hmga1* gene causes cardiac hypertrophy and myelo-lymphoproliferative disorders in mice. *Cancer Res.* *66*, 2536–2543.

Fernández-Garre, P., Rodriguez-Gallardo, L., Gallego-Diaz, V., Alvarez, I.S., and Puelles, L. (2002). Fate map of the chicken neural plate at stage 4. *Development* *129*, 2807–2822.

Gammill, L.S., and Bronner-Fraser, M. (2002). Genomic analysis of neural crest induction. *Development* *129*, 5731–5741.

Gammill, L.S., and Bronner-Fraser, M. (2003). Neural crest specification: migrating into genomics. *Nat. Rev. Neurosci.* *4*, 795–805.

Gandhi, S., and Bronner, M.E. (2018). Insights into neural crest development from studies of avian embryos. *Int. J. Dev. Biol.* *62*, 179–190.

Gandhi, S., Piacentino, M.L., Vieceli, F.M., and Bronner, M.E. (2017). Optimization of CRISPR/Cas9 genome editing for loss-of-function in the early chick embryo. *Dev. Biol.* *432*, 86–97.

Gandhi, S., Hutchins, E.J., Maruszko, K., Park, J.H., Thomson, M., and Bronner, M.E. (2020a). Bimodal function of chromatin remodeler *hmga1* in neural crest induction and *wnt*-dependent emigration. *ELife* *9*, e57779.

Gandhi, S., Ezin, M., and Bronner, M.E. (2020b). Reprogramming Axial Level Identity to Rescue Neural-Crest-Related Congenital Heart Defects. *Dev. Cell* *53*, 300-315.e4.

Gandhi, S., Li, Y., Tang, W., Christensen, J.B., Urrutia, H.A., Vieceli, F.M., Piacentino, M.L., and Bronner, M.E. (2021). A single-plasmid approach for genome editing coupled with long-term lineage analysis in chick embryos. *Development* *148*, dev.193565.

Gans, C., and Northcutt, R.G. (1983). Neural crest and the origin of vertebrates: a new head. *Science* *220*, 268–273.

Gao, Z., Kim, G.H., Mackinnon, A.C., Flagg, A.E., Bassett, B., Earley, J.U., and Svensson, E.C. (2010). *Ets1* is required for proper migration and differentiation of the cardiac neural crest. *Development* *137*, 1543–1551.

George, R.M., Maldonado-Velez, G., and Firulli, A.B. (2020). The heart of the neural crest: cardiac neural crest cells in development and regeneration. *Development* *147*, dev188706.

Glenn Northcutt, R. (2005). The new head hypothesis revisited. *J. Exp. Zool. Part B Mol. Dev. Evol.* *304B*, 274–297.

Gouti, M., Tsakiridis, A., Wymeersch, F.J., Huang, Y., Kleinjung, J., Wilson, V., and Briscoe, J. (2014). In Vitro Generation of Neuromesodermal Progenitors Reveals Distinct Roles for Wnt Signalling in the Specification of Spinal Cord and Paraxial Mesoderm Identity. *PLoS Biol.* *12*, e1001937.

Green, S.A., Simões-Costa, M., and Bronner, M.E. (2015). Evolution of vertebrates as viewed from the crest. *Nature* *520*, 474–482.

Grossfeld, P.D., Mattina, T., Lai, Z., Favier, R., Lyons Jones, K., Cotter, F., and Jones, C. (2004). The 11q Terminal Deletion Disorder: A Prospective Study of 110 Cases. *Am. J. Med. Genet.* *129*, 51–61.

Hall, B.K. (2000). The neural crest as a fourth germ layer and vertebrates as quadroblastic not triploblastic. *Evol. Dev.* *2*, 3–5.

Hanchate, N.K., Kondoh, K., Lu, Z., Kuang, D., Ye, X., Qiu, X., Pachter, L., Trapnell, C., and Buck, L.B. (2015). Single-cell transcriptomics reveals receptor transformations during olfactory neurogenesis. *Science* *350*, 1251–1255.

Hillier, L.W., Miller, W., Birney, E., Warren, W., Hardison, R.C., Ponting, C.P., Bork, P., Burt, D.W., Groenen, M.A.M., Delany, M.E., et al. (2004). Sequence and comparative analysis of the chicken genome provide unique perspectives on vertebrate evolution. *Nature* *432*, 695–716.

Hu, N., Strobl-Mazzulla, P., Sauka-Spengler, T., and Bronner, M.E. (2012). DNA methyltransferase3A as a molecular switch mediating the neural tube-to-neural crest fate transition. *Genes Dev.* *26*, 2380–2385.

Hu, N., Strobl-Mazzulla, P.H., and Bronner, M.E. (2014). Epigenetic regulation in neural crest development. *Dev. Biol.* *396*, 159–168.

Huang, S., Guo, Y.P., May, G., and Enver, T. (2007). Bifurcation dynamics in lineage-commitment in bipotent progenitor cells. *Dev. Biol.* *305*, 695–713.

Huang, Z.P., Chen, J.F., Regan, J.N., Maguire, C.T., Tang, R.H., Rong Dong, X., Majesky, M.W., and Wang, D.Z. (2010). Loss of MicroRNAs in neural crest leads to cardiovascular syndromes resembling human congenital heart defects. *Arterioscler. Thromb. Vasc. Biol.* *30*, 2575–2586.

Hutchins, E.J., and Bronner, M.E. (2018). Draxin acts as a molecular rheostat of canonical Wnt signaling to control cranial neural crest EMT. *J. Cell Biol.* *217*, 3683–3697.

Hutchins, E.J., and Bronner, M.E. (2019). Draxin alters laminin organization during basement membrane remodeling to control cranial neural crest EMT. *Dev. Biol.* *446*, 151–158.

Hutchins, E.J., Chacon, J., and Bronner, M.E. (2020). RNA-binding protein Elavl1/HuR is required for maintenance of cranial neural crest specification. *BioRxiv* 2020.10.14.338715.

Hutson, M.R., and Kirby, M.L. (2003). Neural crest and cardiovascular development: A 20-year perspective. *Birth Defects Res. Part C - Embryo Today Rev.* *69*, 2–13.

Hutson, M.R., and Kirby, M.L. (2007). Model systems for the study of heart development and disease. Cardiac neural crest and conotruncal malformations. *Semin. Cell Dev. Biol.* *18*, 101–110.

Iwafuchi-Doi, M., and Zaret, K.S. (2016). Cell fate control by pioneer transcription factors. *Development* *143*, 1833–1837.

Iwashita, T., Kruger, G.M., Pardal, R., Kiel, M.J., and Morrison, S.J. (2003). Hirschsprung disease is linked to defects in neural crest stem cell function. *Science* *301*, 972–976.

Jiang, X., Rowitch, D.H., Soriano, P., McMahon, A.P., and Sucov, H.M. (2000). Fate of the mammalian cardiac neural crest. *Development* *127*, 1607–1616.

Kerosuo, L., and Bronner, M.E. (2016). cMyc Regulates the Size of the Premigratory Neural Crest Stem Cell Pool. *Cell Rep.* *17*, 2648–2659.

Kirby, M.L. (1989). Plasticity and predetermination of mesencephalic and trunk neural crest transplanted into the region of the cardiac neural crest. *Dev. Biol.* *134*, 402–412.

Kirby, M.L., and Stewart, D.E. (1983). Neural crest origin of cardiac ganglion cells in the chick embryo: Identification and extirpation. *Dev. Biol.* *97*, 433–443.

Kirby, M.L., Gale, T.F., and Stewart, D.E. (1983). Neural crest cells contribute to normal aorticopulmonary septation. *Science* *220*, 1059–1061.

Kirby, M.L., Turnage, K.L., and Hays, B.M. (1985). Characterization of conotruncal malformations following ablation of “cardiac” neural crest. *Anat. Rec.* *213*, 87–93.

Knight, R.D., Nair, S., Nelson, S.S., Afshar, A., Javidan, Y., Geisler, R., Rauch, G.J., and Schilling, T.F. (2003). Lockjaw encodes a zebrafish *tfap2a* required for early neural crest development. *Development* *130*, 5755–5768.

Knight, R.D., Javidan, Y., Zhang, T., Nelson, S., and Schilling, T.F. (2005). AP2-dependent signals from the ectoderm regulate craniofacial development in the zebrafish embryo. *Development* *132*, 3127–3138.

Kuo, B.R., and Erickson, C.A. (2010). Regional differences in neural crest morphogenesis. *Cell Adhes. Migr.* *4*, 567–585.

Kuo, B.R., and Erickson, C.A. (2011). Vagal neural crest cell migratory behavior: A transition between the cranial and trunk crest. *Dev. Dyn.* *240*, 2084–2100.

Laslo, P., Spooner, C.J., Warmflash, A., Lancki, D.W., Lee, H.J., Sciammas, R., Gantner, B.N., Dinner, A.R., and Singh, H. (2006). Multilineage Transcriptional Priming and Determination of Alternate Hematopoietic Cell Fates. *Cell* *126*, 755–766.

Lignell, A., Kerosuo, L., Streichan, S.J., Cai, L., and Bronner, M.E. (2017). Identification of a neural crest stem cell niche by Spatial Genomic Analysis. *Nat. Commun.* *8*, 1–11.

Lindblad-Toh, K., Garber, M., Zuk, O., Lin, M.F., Parker, B.J., Washietl, S., Kheradpour, P., Ernst, J., Jordan, G., Mauceli, E., et al. (2011). A high-resolution map of human evolutionary constraint using 29 mammals. *Nature* *478*, 476–482.

Ling, I.T.C., and Sauka-Spengler, T. (2019). Early chromatin shaping predetermines multipotent vagal neural crest into neural, neuronal and mesenchymal lineages. *Nat. Cell Biol.* *21*, 1504–1517.

Liu, F., Walmsley, M., Rodaway, A., and Patient, R. (2008). Fli1 Acts at the Top of the Transcriptional Network Driving Blood and Endothelial Development. *Curr. Biol.* *18*, 1234–1240.

Long, H.K., Osterwalder, M., Welsh, I.C., Hansen, K., Davies, J.O.J., Liu, Y.E., Koska, M., Adams, A.T., Aho, R.J., Arora, N., et al. (2020). Loss of Extreme Long-Range Enhancers in Human Neural Crest Drives a Craniofacial Disorder. *Cell Stem Cell* *27*, 765–783.e14.

Lukoseviciute, M., Gavriouchkina, D., Williams, R.M., Hochgreb-Hagele, T., Senanayake, U., Chong-Morrison, V., Thongjuea, S., Repapi, E., Mead, A., and Sauka-Spengler, T. (2018). From Pioneer to Repressor: Bimodal foxd3 Activity Dynamically Remodels Neural Crest Regulatory Landscape In Vivo. *Dev. Cell* *47*, 608–628.e6.

Luo, T., Lee, Y.H., Saint-Jeannet, J.P., and Sargent, T.D. (2003). Induction of neural crest in *Xenopus* by transcription factor AP2 α . *Proc. Natl Acad. Sci. USA* *100*, 532–537.

Martik, M.L., and Bronner, M.E. (2017). Regulatory logic underlying diversification of the neural crest. *Trends Genet.* *33*, 715–727.

Martik, M.L., Gandhi, S., Uy, B.R., Gillis, J.A., Green, S.A., Simões-Costa, M., and Bronner, M.E. (2019). Evolution of the new head by gradual acquisition of neural crest regulatory circuits. *Nature* *574*, 675–678.

Mikkelsen, T.S., Wakefield, M.J., Aken, B., Amemiya, C.T., Chang, J.L., Duke, S., Garber, M., Gentles, A.J., Goodstadt, L., Heger, A., et al. (2007). Genome of the marsupial *Monodelphis domestica* reveals innovation in non-coding sequences. *Nature* *447*, 167–177.

Nakamura, H., and Ayer-Le Lievre, C.S. (1982). Mesectodermal capabilities of the trunk neural crest of birds. *J. Embryol. Exp. Morphol.* *70*, 1–18.

Neeb, Z., Lajiness, J.D., Bolanis, E., and Conway, S.J. (2013). Cardiac outflow tract anomalies. *Wiley Interdiscip. Rev. Dev. Biol.* 2, 499–530.

Nie, X., Wang, Q., and Jiao, K. (2011). Dicer activity in neural crest cells is essential for craniofacial organogenesis and pharyngeal arch artery morphogenesis. *Mech. Dev.* 128, 200–207.

Nieto, M.A., Sargent, M.G., Wilkinson, D.G., and Cooke, J. (1994). Control of cell behavior during vertebrate development by Slug, a zinc finger gene. *Science* 264, 835–839.

Noden, D.M. (1975). An analysis of the migratory behavior of avian cephalic neural crest cells. *Dev. Biol.* 42, 106–130.

Noden, D.M. (1978). The control of avian cephalic neural crest cytodifferentiation. I. Skeletal and connective tissues. *Dev. Biol.* 67, 296–312.

O'Donnell, M., Hong, C.-S., Huang, X., Delnicki, R.J., and Saint-Jeannet, J.-P. (2006). Functional analysis of Sox8 during neural crest development in *Xenopus*. *Development* 133, 3817–3826.

Osorio, L., Teillet, M.-A., and Catala, M. (2009). Role of noggin as an upstream signal in the lack of neuronal derivatives found in the avian caudal-most neural crest. *Development* 136, 1717–1726.

Pattyn, A., Morin, X., Cremer, H., Golidis, C., and Brunet, J.F. (1999). The homeobox gene Phox2b is essential for the development of autonomic neural crest derivatives. *Nature* 399, 366–370.

Pieper, M., Ahrens, K., Rink, E., Peter, A., and Schlosser, G. (2012). Differential distribution of competence for panplacodal and neural crest induction to non-neural and neural ectoderm. *Development* 139, 1175–1187.

Powell, D.R., Blasky, A.J., Britt, S.G., and Artinger, K.B. (2013). Riding the crest of the wave: Parallels between the neural crest and cancer in epithelial-to-mesenchymal transition and migration. *Wiley Interdiscip. Rev. Syst. Biol. Med.* *5*, 511–522.

Rabadán, M.A., Herrera, A., Fanlo, L., Usieto, S., Carmona-Fontaine, C., Barriga, E.H., Mayor, R., Pons, S., and Martí, E. (2016). Delamination of neural crest cells requires transient and reversible Wnt inhibition mediated by Dact1/2. *Development* *143*, 2194–2205.

Reeves, R., and Beckerbauer, L. (2001). HMGI/Y proteins: Flexible regulators of transcription and chromatin structure. *Biochim. Biophys. Acta - Gene Struct. Expr.* *1519*, 13–29.

Resar, L., Chia, L., and Xian, L. (2018). Lessons from the crypt: HMGA1 — amping up wnt for stem cells and tumor progression. *Cancer Res.* *78*, 1890–1897.

Rex, M., Orme, A., Uwanogho, D., Tointon, K., Wigmore, P.M., Sharpe, P.T., and Scotting, P.J. (1997). Dynamic expression of chicken Sox2 and Sox3 genes in ectoderm induced to form neural tissue. *Dev. Dyn.* *209*, 323–332.

Rickmann, M., Fawcett, J.W., and Keynes, R.J. (1985). The migration of neural crest cells and the growth of motor axons through the rostral half of the chick somite. *J. Embryol. Exp. Morphol.* *90*, 437–455.

Roellig, D., Tan-Cabugao, J., Esaian, S., and Bronner, M.E. (2017). Dynamic transcriptional signature and cell fate analysis reveals plasticity of individual neural plate border cells. *ELife* *6*, e21620.

Rogers, C.D., Ferzli, G.S., and Casey, E.S. (2011). The response of early neural genes to FGF signaling or inhibition of BMP indicate the absence of a conserved neural induction module. *BMC Dev. Biol.* *11*, 74.

Rothstein, M., and Simões-Costa, M. (2020). Heterodimerization of TFAP2 pioneer factors drives epigenomic remodeling during neural crest specification. *Genome Res.* *30*, 35–48.

Rothstein, M., Bhattacharya, D., and Simões-Costa, M. (2018). The molecular basis of neural crest axial identity. *Dev. Biol.* *444*, S170–S180.

Sauka-Spengler, T., and Bronner-Fraser, M. (2008). A gene regulatory network orchestrates neural crest formation. *Nat. Rev. Mol. Cell Biol.* *9*, 557–568.

Schoenwolf, G.C., and Sheard, P. (1990). Fate mapping the avian epiblast with focal injections of a fluorescent-histochemical marker: Ectodermal derivatives. *J. Exp. Zool.* *255*, 323–339.

Shah, S.N., and Resar, L.M.S. (2012). High mobility Group A1 and cancer: Potential biomarker and therapeutic target. *Histol. Histopathol.* *27*, 567–579.

Simões-Costa, M., and Bronner, M.E. (2015). Establishing neural crest identity: a gene regulatory recipe. *Development* *142*, 242–257.

Simões-Costa, M., and Bronner, M.E. (2016). Reprogramming of avian neural crest axial identity and cell fate. *Science* *352*, 1570–1573.

Simões-Costa, M., McKeown, S.J., Tan-Cabugao, J., Sauka-Spengler, T., and Bronner, M.E. (2012). Dynamic and differential regulation of stem cell factor FoxD3 in the neural crest is encrypted in the genome. *PLoS Genet.* *8*, e1003142.

Simões-Costa, M., Tan-Cabugao, J., Antoshechkin, I., Sauka-Spengler, T., and Bronner, M.E. (2014). Transcriptome analysis reveals novel players in the cranial neural crest gene regulatory network. *Genome Res.* *24*, 281–290.

Simões-Costa, M., Stone, M., and Bronner, M.E. (2015). Axud1 Integrates Wnt Signaling and Transcriptional Inputs to Drive Neural Crest Formation. *Dev. Cell* *34*, 544–554.

Skene, P.J., and Henikoff, S. (2017). An efficient targeted nuclease strategy for high-resolution mapping of DNA binding sites. *ELife* 6, e21856.

Smith, J. (1990). The avian neural crest as a model system for the study of cell lineages. *Int. J. Dev. Biol.* 34, 157–162.

Snider, P., Olaopa, M., Firulli, A.B., and Conway, S.J. (2007). Cardiovascular Development and the Colonizing Cardiac Neural Crest Lineage. *Sci. World J.* 7, 1090–1113.

Soldatov, R., Kaucka, M., Kastriti, M.E., Petersen, J., Chontorotzea, T., Englmaier, L., Akkuratova, N., Yang, Y., Häring, M., Dyachuk, V., et al. (2019). Spatiotemporal structure of cell fate decisions in murine neural crest. *Science* 364.

Stern, C.D., and Downs, K.M. (2012). The hypoblast (visceral endoderm): An evo-devo perspective. *Development* 139, 1059–1069.

Stoller, J.Z., and Epstein, J.A. (2005). Cardiac neural crest. *Semin. Cell Dev. Biol.* 16, 704–715.

Streit, A. (2002). Extensive cell movements accompany formation of the otic placode. *Dev. Biol.* 249, 237–254.

Streit, A., and Stern, C.D. (1999). Establishment and maintenance of the border of the neural plate in the chick: Involvement of FGF and BMP activity. *Mech. Dev.* 82, 51–66.

Streit, A., Berliner, A.J., Papanayotou, C., Slrulnik, A., and Stern, C.D. (2000). Initiation of neural induction by FGF signalling before gastrulation. *Nature* 406, 74–78.

Tang, W., and Bronner, M.E. (2020). Neural crest lineage analysis: from past to future trajectory. *Development* 147.

Tang, W., Martik, M.L., Li, Y., and Bronner, M.E. (2019a). Cardiac neural crest contributes to cardiomyocytes in amniotes and heart regeneration in zebrafish. *ELife* 8, e47929.

Tang, W., Li, Y., Gandhi, S., and Bronner, M.E. (2019b). Multiplex clonal analysis in the chick embryo using retrovirally-mediated combinatorial labeling. *Dev. Biol.* *450*, 1–8.

Tang, W., Li, Y., Li, A., and Bronner, M.E. (2021). Clonal analysis and dynamic imaging identify multipotency of individual *Gallus gallus* caudal hindbrain neural crest cells toward cardiac and enteric fates. *Nat. Commun.* *12*, 1–13.

Tani-Matsuhana, S., Vieceli, F.M., Gandhi, S., Inoue, K., and Bronner, M.E. (2018). Transcriptome profiling of the cardiac neural crest reveals a critical role for MafB. *Dev. Biol.* *444*, S209–S218.

Thawani, A., and Groves, A.K. (2020). Building the Border: Development of the Chordate Neural Plate Border Region and Its Derivatives. *Front. Physiol.* *11*, 608880.

Théveneau, E., Duband, J.-L., Altabef, M., Fauquette, W., and Pollet, I. (2007). Ets-1 Confers Cranial Features on Neural Crest Delamination. *PLoS One* *2*, e1142.

Treutlein, B., Brownfield, D.G., Wu, A.R., Neff, N.F., Mantalas, G.L., Espinoza, F.H., Desai, T.J., Krasnow, M.A., and Quake, S.R. (2014). Reconstructing lineage hierarchies of the distal lung epithelium using single-cell RNA-seq. *Nature* *509*, 371–375.

Tucker, R.P. (2004). Neural crest cells: a model for invasive behavior. *Int. J. Biochem. Cell Biol.* *36*, 173–177.

Vega-Lopez, G.A., Cerrizuela, S., and Aybar, M.J. (2017). Trunk neural crest cells: Formation, migration and beyond. *Int. J. Dev. Biol.* *61*, 5–15.

Vincentz, J.W., Firulli, B.A., Lin, A., Spicer, D.B., Howard, M.J., and Firulli, A.B. (2013). Twist1 Controls a Cell-Specification Switch Governing Cell Fate Decisions within the Cardiac Neural Crest. *PLoS Genet.* *9*, e1003405.

Waldo, K.L., and Kirby, M.L. (1993). Cardiac neural crest contribution to the pulmonary artery and sixth aortic arch artery complex in chick embryos aged 6 to 18 days. *Anat. Rec.* *237*, 385–399.

Waldo, K., Miyagawa-Tomita, S., Kumiski, D., and Kirby, M.L. (1998). Cardiac neural crest cells provide new insight into septation of the cardiac outflow tract: Aortic sac to ventricular septal closure. *Dev. Biol.* *196*, 129–144.

Walmsley, M., Ciau-Uitz, A., and Patient, R. (2002). Adult and embryonic blood and endothelium derive from distinct precursor populations which are differentially programmed by BMP in *Xenopus*. *Development* *129*, 5683–5695.

Williams, R.M., Candido-Ferreira, I., Repapi, E., Gavriouchkina, D., Senanayake, U., Ling, I.T.C., Telenius, J., Taylor, S., Hughes, J., and Sauka-Spengler, T. (2019). Reconstruction of the Global Neural Crest Gene Regulatory Network In Vivo. *Dev. Cell* *51*, 255-276 e7.

Xi, J., Wu, Y., Li, G., Ma, L., Feng, K., Guo, X., Jia, W., Wang, G., Yang, G., Li, P., et al. (2017). Mir-29b Mediates the Neural Tube versus Neural Crest Fate Decision during Embryonic Stem Cell Neural Differentiation. *Stem Cell Reports* *9*, 571–586.

Xian, L., Georgess, D., Huso, T., Cope, L., Belton, A., Chang, Y.-T., Kuang, W., Gu, Q., Zhang, X., Senger, S., et al. (2017). HMGA1 amplifies Wnt signalling and expands the intestinal stem cell compartment and Paneth cell niche. *Nat. Commun.* *8*, 15008.

Ye, M., Coldren, C., Liang, X., Mattina, T., Goldmuntz, E., Benson, D.W., Ivy, D., Perryman, M.B., Garrett-Sinha, L.A., and Grossfeld, P. (2009). Deletion of ETS-1, a gene in the Jacobsen syndrome critical region, causes ventricular septal defects and abnormal ventricular morphology in mice. *Hum. Mol. Genet.* *19*, 648–656.

Ye, M., Yin, Y., Fukatsu, K., and Grossfeld, P. (2016). Evidence that deletion of ETS-1, a gene in the Jacobsen syndrome (11q-) cardiac critical region, causes congenital heart defects through impaired cardiac neural crest cell function. In *Etiology and Morphogenesis of Congenital Heart Disease: From Gene Function and Cellular Interaction to Morphology*, (Springer Japan), pp. 361–369.

Zalc, A., Sinha, R., Gulati, G.S., Wesche, D.J., Daszczuk, P., Swigut, T., Weissman, I.L., and Wysocka, J. (2021). Reactivation of the pluripotency program precedes formation of the cranial neural crest. *Science* 371, eabb4776.

Zaret, K.S., and Carroll, J.S. (2011). Pioneer transcription factors: Establishing competence for gene expression. *Genes Dev.* 25, 2227–2241.

Zhu, Q., Song, L., Peng, G., Sun, N., Chen, J., Zhang, T., Sheng, N., Tang, W., Qian, C., Qiao, Y., et al. (2014). The transcription factor Pou3f1 promotes neural fate commitment via activation of neural lineage genes and inhibition of external signaling pathways. *ELife* 3, e02224.

Appendix A

Protocol for cloning gRNAs downstream of the U6 promoter

Authors' recommendations for gRNA design for chicken embryos:

Ideal targets for knock out: early in gene, mutations near the start codon and/or mutations in an early splice acceptor site

Splice sites: NNNN<exon>NNNN~~gt~~ --- <intron> – ~~ag~~NNNN<exon>NNNN

PAM sequence: NGG

PAMs with C and T at the N position are better than A or G.

CGG or TGG > AGG or GGG

The authors recommend using an online tool to identify all possible protospacers within a 250nt target region. These tools can rank gRNA protospacers based on their potential off-target activity with the chicken genome.

To design targets manually:

Open target sequence in your favorite sequence visualizing software (such as ApE or SnapGene).

Search the genomic locus for the sequence “NNNNNNNNNNNNNNNNNNNNNNNGG.” Allow the sequence software to search the reverse complement sequence for “CCN” targets.

Locate the PAM sequence. The 6 nucleotides in the protospacer immediately adjacent to the PAM are the PAM-proximal nucleotides (PAM-PNs). The GC% for PAM-PNs should be as high as possible, preferably at least 66%.

G[19nt]NGG

Avoid TTT-T_n

CCN[19nt]C

Avoid AAA-A_n

Underlined: spacer gRNA sequence, PAM is not a part of the protospacer.

Look for off-target sites in the genome by doing a BLAST search for the first 13nt of the protospacer (from the PAM) sequence against the chicken genome. If you use an online tool to design gRNAs, this is already done by the algorithm, so select one of the top hits if possible.

The U6 promoter requires a G at the 5' end of the protospacer for RNA Pol-III-mediated transcription. If the protospacer sequence selected does not have a G in the front, just replace the first nucleotide with a 'G.'

Step 1: Order the following oligos:

Primers: Target: 5' [CGAGAAGGTTGGCTGGGTG] CGG 3'

Forward: ggatg [19nt]

Reverse: aaac [revcomp19nt] c

Order: For: 5' - ggatg [CGAGAAGGTTGGCTGGGTG] -3'

Rev: 5' - aaac [CACCCAGCCAACCTTCTCG] c -3'

For CCN PAMs, take the reverse complement of the protospacer+PAM and paste in a new window. Now use the above-mentioned strategy to design the oligos.

Step 2: Set up the following annealing reaction:

5 μ l 100 μ M Forward Primer
 5 μ l 100 μ M Reverse Primer
 5 μ l NEB 10x T4 DNA Ligase Buffer
 35 μ l dH₂O
 50 μ l

Heat to 95°C for 5 minutes. Bring to room temperature on your bench for 30-45 minutes.

Annealed: For: 5' - ggatgCGAGAAGGTTGGCTGGGTG -3'
 |||
 Rev: 3' - cGCTCTTCCAACCGACCCACcaaa -5'

Dilute this annealed oligo reaction 1:1000. This is your insert.

Step 3: Set up the following digestion:

Digest U6.3>empty gRNA overnight with BsaI-HF.

x μ l	Empty gRNA plasmid
2 μ l	Bsa-I HF
6 μ l	10x Cutsmart Buffer
<u>(52-x) μl</u>	dH ₂ O
60 μ l	

Gel extract the vector. 5'-GGAT-3' and 3'-CAAA-5' overhangs will allow you to clone this annealed oligo in your linearized vector using this recipe:

Step 4: Set up the following ligation:

1 μ l	BsaI-digested vector
2.5 μ l	1:1000 diluted annealed oligos
2 μ l	NEB 10x T4 DNA Ligase Buffer
1 μ l	T4 DNA Ligase
<u>13.5 μl</u>	dH ₂ O
20 μ l	

Incubate at room temperature for 20 minutes, then transform 25 μ l competent cells using 5 μ l ligation reaction [Maintain 1:5 ratio of ligation reaction to competent cells].

Add 37.5 μ l SOC media [1.5x transformation volume] for 15 minute recovery at 37°C. Plate full volume on LB+Amp plates. For first use after digesting vector, perform a “vector only” control to test for digestion efficiency. After transformation, test for successful inserts by colony PCR using U6 sequencing primer + gRNA reverse primer.

ex ovo electroporations:

Its ideal to electroporate multiple gRNAs, but ensure that the targets are no closer than 108nt to one another in the genome.

Electroporation recipe: 2 μ g/ μ l Cas9 + 1.5 μ g/ μ l (gRNA₁ + gRNA₂ + ... + gRNA_n) + 2 μ g/ μ l pCIG or H2B-RFP

Appendix B

Molecular cloning of single-CRISPR plasmid

Step 1: Order the following oligos:

Example target: 5' ...**CCGAGAAGGTTGGCTGGGTGCGG**... 3'

Forward primer: **cgtc**[20nt protospacer]

Reverse primer: **aaac**[reverse complement of 20nt protospacer]

Order:

gRNA-TOP: 5' - **cgtcCCGAGAAGGTTGGCTGGGTG** - 3'

gRNA-BOT: 5' - **aaacCACCCAGCCAACCTTCTCGG** - 3'

EcoRI-HH-<Gene>-Fwd: 5' -**aaaGAATTC**<NNNNNN>**CTGATGAGTCCGTGAGGACG**-3'

This primer will be specific to each gRNA. <NNNNNN> is the reverse complement of the first 6 nucleotides of the gRNA protospacer. For the CCGAGAAGGTTGGCTGGGTG gRNA, this sequence will be <TCTCGG>, and the 'EcoRI-HH-<Gene>-Fwd' primer will be

5' -aaaGAATTCtctcggCTGATGAGTCCGTGAGGACG-3' .

The following primers are common for all constructs:

HDV-NotI-Rev: 5' - **aaagcggccgcGTCCCATTCGCCATGCCGAA** - 3'

Citrine-ColonyPCR-Fwd: 5' - **CACAAGCTGGAGTACAATA** - 3'

T7-seq-Rev: 5' - **taatacgactcactataggg** - 3'

Order and store 100µM/10µM dilutions at -20°C.

Step 2: Set up the gRNA protospacer annealing reaction:

5 μ L	100 μ M gRNA TOP
5 μ L	100 μ M gRNA BOT
5 μ L	NEB 10x T4 DNA Ligase Buffer
35 μ L	Water
50 μ L	Total volume

Heat to 95°C for 5 minutes. Bring to room temperature on the bench for 30-45 minutes.

Annealed oligos: 5' - **cgtcCCGAGAAGGTTGGCTGGGTG** - 3'
 |||
 3' - **GGCTCTTCCAACCGACCCAC**caaa - 5'

Dilute this reaction 1:1000. This is your insert.

Step 3: Digest the shuttle vector plasmid:

x μ L	6 μ g of DNA
6 μ L	10x Cutsmart Buffer
2 μ L	BsaI-HF enzyme
(52-x) μ L	Water
60 μ L	Total volume

Digest at 37°C overnight (16-18 hours at least). Gel extract to obtain your shuttle vector.

Do not CIP-treat. Ensure the vector concentration after elution is less than 50ng/ μ L (dilute if necessary).

Step 4: Ligate annealed oligos into the Shuttle vector:

1 μ L	Linearized Shuttle vector
2.5 μ L	gRNA annealed primers (1:1000 dilution from above)
2 μ L	NEB 10x T4 DNA Ligase Buffer
1 μ L	T4 DNA Ligase
13.5 μ L	Water
20 μ L	Total Volume

Incubate at room temperature for 20 minutes, then transform 25 μ L competent cells (*our lab uses homegrown competent cells*) with 5 μ L of ligation reaction (*This can be changed to maintain a 1:5 ratio of ligation mix to competent cells*). Add 37.5 μ L SOC medium (1.5x

volume of competent cells used) and recover for 15 minutes at 37°C. Plate full volume on LB+Amp plates. Incubate plates at 37°C overnight.

(For first use after digesting the Shuttle vector, perform a “Shuttle vector only” negative control to test for digestion efficiency. Make sure you don’t get any colonies. Repeat digestion if necessary.)

Step 5: Amplification of HH-gRNAf+e-HDV precursor:

Pick individual colonies and swirl in 10 μ L of SOC (in a PCR strip tube). Set up the following reactions:

Reaction 1

2.5 μ L	Swirled Culture
5 μ L	EcoRI-HH-<Gene>-Fwd
5 μ L	HDV-NotI-Rev
2.5 μ L	Taq Buffer
1 μ L	dNTPs
1.5 μ L	DMSO
0.5 μ L	Taq Polymerase
32 μ L	Water
50 μ L	Total Volume

In parallel, set up the following colony PCR to verify successful integration of the protospacer:

Reaction 2

1 μ L	Swirled Culture
2 μ L	gRNA-TOP (10 μ M dilution)
2 μ L	T7 seq Reverse
1 μ L	Taq Buffer
0.4 μ L	dNTPs
0.6 μ L	DMSO
0.2 μ L	Taq Polymerase
12.8 μ L	Water
20 μ L	Total Volume

Run $2\mu\text{L}$ of Reaction 1 and $20\mu\text{L}$ of Reaction 2 on a gel. Reaction 1 should yield a $\sim 215\text{bp}$ product, while Reaction 2 should yield a 690bp product (if the protospacer was successfully integrated into the shuttle vector). PCR purify the remaining $48\mu\text{L}$ of Reaction 1 (for colonies that have a positive band for Reaction 2) and elute in $52\mu\text{L}$. Set up the following digestion reaction:

$52\mu\text{L}$	PCR-purified product
$6\mu\text{L}$	10x Cutsmart Buffer
$1\mu\text{L}$	EcoRI-HF enzyme
$1\mu\text{L}$	NotI-HF enzyme
$60\mu\text{L}$	Total volume

Digest for 2 hours at 37°C . Gel extract. This is your “EcoRI-HH-gRNA-HDV-NotI” insert.

Step 6: Clone HH-gRNAf+e-HDV precursor into single CRISPR plasmid:

Set up the following digestion reaction:

$x\mu\text{L}$	$6\mu\text{g}$ of single CRISPR plasmid
$6\mu\text{L}$	10x Cutsmart Buffer
$1\mu\text{L}$	EcoRI-HF enzyme
$1\mu\text{L}$	NotI-HF enzyme
$(52-x)\mu\text{L}$	Water
$60\mu\text{L}$	Total volume

Digest at 37°C overnight. Gel extract to obtain the CRISPR destination vector. Set up ligation at 1:3 molar ratio using this vector and the insert obtained in Step 5.

$x\mu\text{L}$	Linearized CRISPR destination vector
$y\mu\text{L}$	Digested and purified HH-gRNA-HDV insert (from Step 5)
$2\mu\text{L}$	NEB 10x T4 DNA Ligase Buffer
$1\mu\text{L}$	T4 DNA Ligase
$(20-x-y)\mu\text{L}$	Water
$20\mu\text{L}$	Total Volume

Ligate for 2 hours at room temperature. Transform $25\mu\text{L}$ competent cells (*our lab uses homegrown competent cells*) with $5\mu\text{L}$ of ligation reaction (*This can be changed to maintain a 1:5 ratio of ligation mix to competent cells*). Add $37.5\mu\text{L}$ SOC medium ($1.5\times$

volume of competent cells used) and recover for 1 hour at 37°C. Plate and incubate at 37°C overnight.

The next day, validate colonies by colony PCR using Citrine-ColonyPCR-Fwd and 10 μ M dilution of gRNA-BOT primers. Validate insert by sequencing and electroporate chick embryos at 2.5 μ g/ μ L concentration.

Appendix C

Synthesizing high-titer RIA retroviruses

Day 1

1. Coat 15cm plates with 0.1% gelatin solution before use. DF1 cells are maintained in DMEM with 10% FBS supplemented with 1% Penstrep.
2. On the day of transfection, cells should reach 80% confluency for optimal transfection.

(In our experience, this density permits cells to attach with each other in order to survive, but still have space to divide.)

3. Remove old media and replace with 15ml fresh DMEM with 10% FBS.
4. Prepare 'Tube 1' by mixing 96 μ L of PEI with 1.2mL of OPTI-MEM prewarmed to room temperature. Vortex.

(To make working stock of PEI, dissolve PEI in water at 1mg/mL and filter-sterilize. The solution can be stored at 4°C for up to 3 months. Keep on ice when it is being used.)

5. Prepare 'Tube 2' by mixing 20 μ g of RIA-CRISPR plasmid and 5 μ g of VSVG plasmid with 1.2mL of room-temperature OPTI-MEM. Vortex.
6. Transfer all solution from 'Tube 1' to 'Tube 2.' Vortex. Let the mixture sit at room temperature for 30 mins.
7. Add the DNA/PEI mixture (2.4mL) into DF1 cells by dripping uniformly onto the plate. Gently swirl the plate to mix. Place the plate back in the incubator.
8. 2-3 hours later, replace the old media with 24mL fresh DMEM with 10% FBS. Place the plate back in the incubator overnight.

Day 2

1. 16 hours later, add 240 μ L of sodium butyrate and mix by gently swirling the plate. Incubate the cells for 6 hours.

(Make sodium butyrate by mixing 0.1g sodium butyrate in 1ml 1xPBS. Filter-sterilize before use.)

Note: make sure that the transfected cells are healthy and growing; otherwise, redo the transfection by adjusting the amounts of RIA-CRISPR and VSVG plasmids used. The optimal concentration will be variable for different recombinant RIA plasmids.

2. Remove the old media, wash twice with 10mL 1XPBS. Add 16mL fresh DMEM with 10% FBS. Place the cells back in the incubator overnight.

(Now, the cells will start producing the virus. Since sodium butyrate affects normal cell growth, it is expected that some cells will die. If too many cells die, then readjust the concentration of and/or treatment duration with sodium butyrate.)

Day 3-7

1. Collect 12ml media (*supernatant contains the viral particles*) in 15ml conical tube. Replenish the plate by adding 12mL fresh DMEM with 10% FBS. Freeze the supernatant at -80°C immediately.
2. Repeat this collection step every 12 hours for 4 days if possible, or every 24 hours for 4 days.

(In total, this will yield about 96mL or 48mL supernatant containing viral particles for concentration. Some media will be lost to evaporation during the 12-hour incubation, so adjust the media volume accordingly. Caution: Do not add excess volume of media since this might dilute the supernatant.)

3. Monitor the cells during collection. If the cells look extremely healthy, the transfection may not have been successful. Some deterioration in health is expected. If the cells are very confluent, switch to DMEM with 1% FBS to prevent the cells from falling off.

Day of injection

1. Take out 4 tubes of supernatant collected from transfection (48mL) and thaw at 37°C in a water bath. Invert the tube frequently to ensure proper mixing, and put immediately on ice when thawed.

(The virus is extremely sensitive and should not be subjected to room temperature.)

2. Centrifuge the tubes at 6000g for 10 minutes to clean up cell debris.
3. In the Tissue Culture hood, gently pour the supernatant into a 45µm filter. Collect the filtered solution.
4. Pipet the filtered solution into ultracentrifuge tubes. Be careful to avoid making bubbles. Balance with DMEM if necessary.
5. Centrifuge at 26000rpm for 1.5 hours at 4°C.

(~75500g for a 10cm rotor. Using a swinging bucket is critical to collect the pellet at the bottom.)

6. Decant the supernatant.

(At the bottom of the tube, there should be a yellowish-white pellet which contains the viral particles).

7. Use an autoclaved glass pipet and aspirate to remove the residual media in the tube. Leave around 30µL. Seal the centrifuge tube with parafilm and tin foil. Nutate at 4°C for 3 hours.

(The virus is sensitive to light, so protect it by wrapping the tube in foil.)

8. Remove the parafilm and foil. Pipet up and down 100 times to resuspend the virus.
(Do not make bubbles at this step, since the virus can die when in contact with air.)
9. Make 2 μ L aliquots. Use the virus the same day or store at -80°C. Only take out when ready to use. The viral titer drops after a few weeks.

(During the injection, add a small volume of 2% food dye so as to not dilute the virus too much. Only load 1 μ L in the injection needle at a time. Keep the rest of the virus on ice. If the virus has to be diluted, use DMEM.)

Appendix D

Dissociating embryonic tissue into a single-cell suspension

This protocol has been optimized for chicken embryos and is designed for **Fluorescence-activated cell sorting**. For each experiment, you will need to take the following solutions to the sorting facility:

1. Single-cell suspension of cells of interest.
2. Single-cell suspension of cells with individual fluorophores you are sorting for (Do not use RFP as a control for mCherry).
3. Single-cell suspension of wild-type cells (preferably from the same anatomical area as your cells of interest).
4. Live-dead cell staining dye (**Sytox Blue** if sorting mCherry+ cells, **7AAD** if sorting GFP+ cells).
5. Low-binding microcentrifuge tubes with 100 μ L of Hank's-EDTA.
6. Falcon tube with Hank's-MgCl₂ (Hank's-BSA for scRNA-seq).

For single-cell RNA-sequencing without FACS, use variations of the protocol as highlighted wherever appropriate.

Materials

- 1X DPBS – Make 50mL aliquots and store on bench. Stock bottles at stored 4°C.
- 10X Hank's Balanced Salt Solution (HBSS) – no calcium, no magnesium, no phenol red. Make 50mL aliquots and store at room temperature. Stock bottles stored at 4°C.
- Accumax – Stored at -20°C. Make 750 μ L aliquots and store them in the freezer. Avoid multiple freeze-thaw cycles. Activity of the enzyme-mix declines with more than 2-3 freeze-thaw cycles.
- 1M MgCl₂ – Autoclaved and stored at room temperature.

- 1M HEPES (pH 7.0) – Filter (0.22um) sterilized and stored at room temperature.
- 0.5M EDTA – Autoclaved and stored at room temperature.
- Bovine Serum Albumin (Sigma Aldrich) – Stored at 4°C.
- 40um cell strainers
- RQ1 DNase-I – RNase-free, stored at -20°C.
- Sytox blue – Live-dead stain for sorting red FP, stored at -20°C. **Cover aliquots in foil.**
- 20µm nylon strainer (for single-cell RNA-seq suspension) – Millipore.
- Low-binding 1.7mL Eppendorf tubes.
- 15mL falcon tubes – One tube per sample you are dissociating.
- 50mL falcon tubes – One tube per sample you are dissociating.
- 5mL polystyrene round bottom tubes – One tube per sample you are dissociating.

Procedure

Embryo dissection and pre-dissociation washes

1. Have an ice bucket with 1X DPBS, 10X HBSS, low-binding microcentrifuge tubes with 500µL ringers for each tissue type, and Accumax.

Thaw Accumax on ice while dissecting the tissue, then at room temperature during PBS washes.

2. Dissect the tissue and transfer it into the microcentrifuge tubes with ringers **on ice** ASAP.

The longer the tissue stays at room temperature, the more cell debris you will get later on.

3. Remove Ringer's solution from the tube and replace with 1 mL of chilled 1X DPBS. Allow the dissected tissues to settle at the bottom of the tube.
4. Wash with 1X DPBS thrice. At this point, keep Accumax in your hands to facilitate thawing. Once thawed, pipette up and down a couple of times and spin down to collect.

Tissue dissociation

5. Carefully remove as much 1X DPBS as possible and replace it with 750 μ L of Accumax. Transfer tubes to 37°C heat block. Start your timer counting up. **The goal is to dissociate cells for no longer than 15 minutes.**

If you have several tubes, then add Accumax to each tube and keep the tube on ice. The enzymatic activity starts at 37°C, so your cells are safe on ice.

6. Check dissociation by pipetting up and down every 5 minutes. Be gentle.

Use blue filter tips since they have a wider opening. My rule of thumb is to pipette 15 times against the wall of the tube.

7. While the cells are dissociating, prepare Hank's buffers using the following recipes:

Hank's- MgCl ₂ (for 40mL)		Hank's-EDTA (for 10mL)	
10X HBSS	4 mL	10X HBSS	1 mL
HEPES (pH=7)	1 mL	HEPES (pH=7)	250 μ L
BSA	100 mg	BSA	25 mg
1M MgCl ₂	400 μ L	EDTA	20 μ L
Water	34.6 mL	Water	8.75 mL

Add BSA at the very end and nutate for 5 minutes to ensure proper mixing. Hank's-MgCl₂ will be used to do the next couple of washes. Hank's-EDTA is the collection buffer

in which you will collect cells at the sorting facility. EDTA chelates divalent ions and hence inhibits the activity of DNase-I.

8. If you are dissociating cells to directly load them on the 10X Genomics controller, use this recipe instead:

Hank's recipe for scRNA-seq		
Hank's-BSA	(for 40mL)	for 10mL
10X HBSS	4mL	1mL
HEPES (pH=7)	1mL	250 μ L
BSA	100mg	25mg
Water	35mL	8.75mL

MgCl₂ interferes with the reverse transcription step of the scRNA-seq protocol by 10X Genomics, so it is important not to use Hank's-MgCl₂.

9. After 15 minutes, load 10 μ L of the suspension on a microscope slide and check under the cell-culture microscope.

If your dissected tissue contains the neural tube, be extremely careful. Cells at the periphery (including neural crest cells) are already in a single-cell suspension, while parts of the neural tube might be visible as threads floating in the sample. Over-dissociating can potentially lyse cells of interest. While checking the cells under the microscope, transfer tubes on ice.

10. Keep Hank's-MgCl₂ (Hank's-BSA for scRNA-seq) and Hank's-EDTA on ice. Transfer 5mL Hank's-MgCl₂ (Hank's- BSA for scRNA-seq) in a 15mL conical tube per sample and keep on ice.

Post-dissociation washes

11. Once the tissue is dissociated as required, transfer the suspension to chilled 15ml falcon that already has 5ml of chilled fresh Hank's-MgCl₂ (Hank's-BSA for scRNA-seq).

Wash original Eppendorf with some Hank's-MgCl₂ (Hank's-BSA for scRNA-seq) from the conical to ensure all cells are in the 15mL falcon tube.

12. Spin down at 4°C at 300 rcf for 4 mins in 15mL falcons.

While the cells are in the centrifuge, get 40um cell strainers (20µm filters for scRNA-seq) and 50mL falcons for each dissociated sample. Label the tubes and put them on ice.

13. Carefully remove supernatant and resuspend pellet in 1mL Hank's-MgCl₂ (Hank's-BSA for scRNA-seq). Be extremely gentle.

The cells at this point have (theoretically) clumped at the bottom of the falcon. It is important to release the cells back into a single-cell suspension before passing it through the filter in the next step. My rule of thumb is to pipette 10 times very gently against the wall of the tube.

14. Filter the 1mL suspension through the 40µm cell strainer (20µm filter for scRNA-seq) into the 50ml conical tube on ice.

Pipette the solution into a P1000 filter tip. Place the pipette such that the tip touches the strainer. Release the solution in one smooth motion without stopping. Use the 20µm filter in the TC hood.

15. Centrifuge the 50mL falcons at 4°C for 3 mins at 300 rcf. Leave the cell strainer on the top of the falcon.

For scRNA-seq, when using the 20µm nylon filters from Millipore, discard the filter after passing the cell suspension through it.

16. Remove the supernatant as much as possible without disturbing the pellet and replace with 50-250µl Hank's-MgCl₂ (Hank's-BSA for scRNA-seq) depending on how much starting material you had. Resuspend the pellet very carefully.

A good rule of thumb is to pipette up and down 10 times extremely gently against the wall of the tube. Keep additional Hank's-MgCl₂ buffer (Hank's-BSA for scRNA-seq) on ice in case cell density is very high. Sometimes, the pellet might be too small to be seen. If that's the case, just be very careful when removing the supernatant.

17. Transfer the cells to a 5mL culture tube. Label and keep on ice. Check cell viability using Trypan Blue and count live cells.

Add 10 μ L cells (or a 1:10 dilution depending on the size of pellet observed at the beginning of step 15) to 10 μ L trypan blue. Load 10 μ L of this mixture on chamber-slide in the tissue-culture room. Cell viability should be at least 85% if not more.

18. Add 15 μ L of RQ1 DNase-I to each tube. Pipette up and down gently. To collect sorted cells, transfer 100 μ L of Hank's-EDTA to low-bind Eppendorf tubes (one per replicate) and keep them on ice.



19. For scRNA-seq applications, **skip steps 17 and 18**. Instead, transfer your single-cell suspension in Hank's-BSA to a low-bind Eppendorf tube. Spin at 300g for 5 minutes at 4°C and resuspend in ~38 μ L of Hank's-BSA buffer. You are ready to load your cells on the 10X controller chip.

This volume is variable. Please check the volume of cells you would load on the controller chip in the scRNA-seq protocol by 10X Genomics.